

# COUPLING RHEOLOGY AND SEGREGATION FOR GRANULAR FLOWS IN ROTATING DRUMS

A THESIS SUBMITTED TO THE UNIVERSITY OF MANCHESTER  
FOR THE DEGREE OF DOCTOR OF PHILOSOPHY  
IN THE FACULTY OF SCIENCE AND ENGINEERING

2022

**Eoin Maguire**

School of Natural Sciences

Department of Mathematics

# Contents

<b>Abstract</b>	<b>7</b>
<b>Declaration</b>	<b>8</b>
<b>Copyright Statement</b>	<b>9</b>
<b>Acknowledgements</b>	<b>10</b>
<b>Contributors</b>	<b>11</b>
<b>1 Introduction</b>	<b>13</b>
1.1 Granular material . . . . .	13
1.2 Rheology of dense granular flows . . . . .	16
1.2.1 The Coulomb friction model . . . . .	16
1.2.2 Development of the $\mu(I)$ -rheology . . . . .	18
1.3 Particle-size segregation . . . . .	27
1.3.1 Segregation mechanisms . . . . .	28
1.3.2 Continuum modelling of particle-size segregation . . . . .	31
1.3.3 Rotating drums . . . . .	36
1.4 The finite volume method in OpenFOAM . . . . .	39
1.4.1 Discretisation procedure . . . . .	39
1.4.2 Boundary conditions . . . . .	42
1.4.3 Governing equations . . . . .	43
1.4.4 Derivation of the pressure equation . . . . .	44
1.4.5 The PISO algorithm . . . . .	45
1.5 Thesis structure . . . . .	46

<b>2</b>	<b>Coupling rheology and segregation in granular flows</b>	<b>49</b>
<b>3</b>	<b>Particle-size segregation in triangular rotating drums with sidewall friction</b>	<b>115</b>
<b>4</b>	<b>Conclusions</b>	<b>190</b>

# List of Figures

- 1.1 Examples of different granular materials. On the left, an assortment of whole-grains, image courtesy of World Grain magazine. On the top right, dense liquid-like granular flow triggered by human footsteps on the side of a desert sand dune (Barale, 2015). On the bottom right, household waste being poured into a landfill from a rubbish truck, image courtesy of Resource magazine. . . . . 14
- 1.2 Schematic diagram of a granular flow with shear and normal stresses, illustrating (a) the macroscopic timescale for deformation  $T_\gamma = 1/\dot{\gamma}$  in the presence of a shear rate  $\dot{\gamma}$ , and (b) the microscopic timescale for grain rearrangement  $T_p = d\sqrt{\rho_*/p}$ , under the application of pressure  $p$ . The inertial number  $I$  can be interpreted as the ratio of these two timescales. . . . . 21
- 1.3 Plot of the Bagnold velocity profile (1.2.18) for steady uniform flow down an incline. The flowing layer has constant thickness  $h = 1$  cm, the slope is inclined at an angle  $\zeta = 21^\circ$ , the grains have diameter  $d = 0.1$  cm and the solids volume fraction  $\Phi = 0.6$ . . . . . 23



- 1.4 Plot of  $\mu(I)$ , for the original  $\mu(I)$  curve given by (1.2.21) (blue line) and the partially regularised form given by (1.2.23) (red line), for parameters  $\mu_s = 0.404$ ,  $\mu_s = 0.675$ ,  $\mu_\infty = 0.04$ ,  $I_0 = 0.249$ , and  $\alpha = 1.9$ . The vertical dashed blue lines represent the lower and upper limits of well-posedness for the original  $\mu(I)$  curve. The lower limit is also very close to the point of transition between the two branches of (1.2.23) since the  $\mu_\infty I^2$  term in (1.2.23) is dominated by the other terms in the region where  $I < 1$ . While the original curve decays to  $\mu_s$  for  $I = 0$  and asymptotically approaches  $\mu_d$  for  $I \rightarrow \infty$ , the partially regularised form enters a creep regime as  $I \rightarrow 0$  which decays to  $\mu(I = 0) = 0$ , and has no upper bound. The vertical red dashed line represents the upper limit of well-posedness for the partially regularised  $\mu(I)$ -rheology, which for the given parameters is at  $I = 17.0189$ . . . . . 25
- 1.5 Schematic diagram of gravity-driven size segregation in a shear flow between two plates, where gravity is assumed to point downwards. As the initially well-mixed flow is sheared, smaller particles preferentially fall through void spaces in the granular material and squeeze the larger particles upwards, resulting in the inversely graded layer depicted in the second graphic. . . . . 29
- 1.6 Examples of two polydisperse shallow granular flows. On the top, a geophysical snow avalanche bounded by levees (Edwards *et al.*, 2017). On the bottom, a photograph of an experiment with segregation-induced fingering instabilities at the flow front, with larger brown particles advected to the sides to form levees for each finger (Baker *et al.*, 2016). . . 35

1.7	Experimental images of different flows in a circular rotating drum. Clockwise from top left; a continuously avalanching drum flow filled with three particle species (red small, white medium, and green large particles) (Gray & Ancey, 2011), a petal pattern in a half filled drum with small white and large red particles (Zuriguel <i>et al.</i> , 2006), a baffled drum inhibiting segregation between small white and large red particles (McCarthy, 2009), and a Catherine wheel pattern formed by an intermittent avalanche for small black and large white particles (Gray & Hutter, 1997).	37
-----	--	----

# The University of Manchester

Eoin Maguire

Doctor of Philosophy

**Coupling rheology and segregation for granular flows in rotating drums**

**December 9, 2022**

Granular materials exhibit behaviours reminiscent of solids, liquids and gasses, and typically contain particles with various sizes, densities and shapes. In dense liquid-like flows, particles are sorted efficiently by size, producing inversely graded layers of large particles above small, since smaller particles are more likely to fall through void spaces. Size segregation in geophysical avalanches may increase run-out distance and destructive capacity. Granular materials are also handled in many industries, and rotating drum flows in which two or more granular materials are tossed together provide an eminent example of size segregation. Here, segregation is confined to a thin free-surface avalanche through which material is continuously entrained, resulting in an extraordinary variety of pattern formations and presenting a formidable obstacle to mixture uniformity. In this thesis, a theoretical and numerical method for coupling rheology and size segregation in polydisperse granular flows is developed, using the partially regularised  $\mu(I)$ -rheology (adapted to reflect the sizes and frictional properties of the local mixture composition) in an incompressible Navier-Stokes framework, along with segregation and diffusion rates tied to the bulk flow properties. The numerical method is tested using inclined plane flow simulations and the DEM data of Tripathi & Khakhar (2011), before the petal-like pattern in a square rotating drum is computed. The segregation and diffusion dependencies confine particle redistribution to the free-surface avalanche, and the drum simulation gives promising qualitative results. Triangular rotating drum experiments with varying fill fractions and mean particle concentrations are then performed with bidisperse mixtures. The mixtures are enclosed in a thin channel by clear lateral sidewalls which exert a frictional force on the flow, producing a very thin avalanche which induces intense segregation. This is incorporated into the theoretical and numerical model using width-averaged mass and momentum balance equations with Coulomb slip assumed on the sidewalls, resulting in a two-dimensional system with an additional momentum term representing sidewall friction. The adapted numerical method is tested using an enclosed infinite shear cell and used to compute triangular drum flows with parameters matched to the experiments. The pattern formations and timescales of the simulations give excellent qualitative agreement with the experiments. A novel method for quantitative analysis is used to project a concentration field onto laboratory images based on pixel intensities, and strong quantitative agreement between the segregation intensities of the experiments and simulations is observed. Complex rheology-segregation feedback interactions are identified and clarified using the experimental and numerical results. A tridisperse triangular drum flow is then computed, correctly predicting the pattern formation observed experimentally. These results suggest that all the key features of continuously avalanching rotating drum flows may be captured in a fully coupled, incompressible continuum framework. Furthermore, by unifying previously disparate theories for rheology and segregation, this research provides a powerful tool for extending understanding of polydisperse granular flows in general.

# Declaration

No portion of the work referred to in the thesis has been submitted in support of an application for another degree or qualification of this or any other university or other institute of learning.

# Copyright Statement

- i. The author of this thesis (including any appendices and/or schedules to this thesis) owns certain copyright or related rights in it (the “Copyright”) and s/he has given The University of Manchester certain rights to use such Copyright, including for administrative purposes.
- ii. Copies of this thesis, either in full or in extracts and whether in hard or electronic copy, may be made **only** in accordance with the Copyright, Designs and Patents Act 1988 (as amended) and regulations issued under it or, where appropriate, in accordance with licensing agreements which the University has from time to time. This page must form part of any such copies made.
- iii. The ownership of certain Copyright, patents, designs, trade marks and other intellectual property (the “Intellectual Property”) and any reproductions of copyright works in the thesis, for example graphs and tables (“Reproductions”), which may be described in this thesis, may not be owned by the author and may be owned by third parties. Such Intellectual Property and Reproductions cannot and must not be made available for use without the prior written permission of the owner(s) of the relevant Intellectual Property and/or Reproductions.
- iv. Further information on the conditions under which disclosure, publication and commercialisation of this thesis, the Copyright and any Intellectual Property and/or Reproductions described in it may take place is available in the University IP Policy (see <http://documents.manchester.ac.uk/DocuInfo.aspx?DocID=24420>), in any relevant Thesis restriction declarations deposited in the University Library, The University Library’s regulations (see <http://www.manchester.ac.uk/library/about/regulations/>) and in The University’s Policy on Presentation of Theses.

# Acknowledgements

I take this opportunity to thank my supervisor Nico Gray for his guidance, feedback and encouragement over the course of my research, and for giving me the opportunity to travel to international conferences (in the pre-Covid age). I would also like to thank my co-supervisor Chris Johnson for his occasional but always clarifying technical insights into the inevitable problems which arise throughout a PhD. If not for my regular discussions with Tom Barker, who happily answered all of my confused questions, the early stages of this process would have been far more difficult. My friends in office 1.134, 5-a-side and the whole granular research group provided relief from research and helped make the past few years truly enjoyable despite the trying times. Finally, thank you to anyone bothering to read this thesis.

# Contributors

This thesis is presented in alternative format, meaning the two main chapters take the form of collaborative journal papers. The following is a list of the contributing authors:

- Thomas Barker (TB), School of Mathematics, University of Cardiff.
- Matthias Rauter (MR), Department of Water Management, Office of the Tyrolean Regional Government.
- Chris Johnson (CG), Department of Mathematics and Manchester Centre for Nonlinear Dynamics, The University of Manchester.
- Nico Gray (NG), Department of Mathematics and Manchester Centre for Nonlinear Dynamics, The University of Manchester.

An overview of the individual author contributions to each chapter will now be provided. For chapter 2, “Coupling rheology and segregation in granular flows”, the coupling theory was developed collaboratively by Eoin Maguire (EM), TB and NG. EM researched the appropriate granular diffusion scaling and parameters, and the method for incorporating a different diffusion rate for the air phase. The numerical implementation of the coupling theory in OpenFOAM was done by EM, TB and MR, led by the technical expertise of MR. In particular, the numerical implementation of Trewthell *et al.*’s (2021) segregation scaling law, the diffusion scaling law, as well as the numerical calculation of the concentration-weighted grain diameter and the dependence of the rheological model and the segregation and diffusion rates on this variable was done by EM. EM also investigated the trapping of air bubbles across different flow geometries to build understanding of this numerical issue, identified the grid-dependence of the bubble size, and determined the optimal direction and

magnitude for air segregation in both the inclined plane and rotating drum geometries. The section on the numerical implementation was written by MR, and the comparison to the DEM data of Tripathi & Khakhar (2011) was performed and written by NG. EM performed the fully coupled rotating drum simulations, including the grid convergence study, and wrote this section, including production of all the figures. The remainder of the paper was written by TB, who also performed the various inclined plane flow simulations and produced these figures. CG and NG supervised this process.

Chapter 3, “Particle-size segregation in triangular rotating drums with sidewall friction”, was written by EM who performed all the theoretical work, simulations and experiments, including the quantitative analysis, and produced all of the figures. EM derived the width-averaged equations and modified the numerical code to include the wall friction term corrected for a moving mesh, and also modified the numerical implementation of the coupling theory to include the reduction factor in the segregation scaling law. MR wrote the code for tetrahedral mesh generation in OpenFOAM, and CG provided the outline of the idea for the quantitative analysis. NG provided supervision and guidance.



# Chapter 1

## Introduction

### 1.1 Granular material

Grains come in many shapes and sizes. For the purposes of this thesis, grains are defined as macroscopic solid particles with diameter greater than  $100\text{ }\mu\text{m}$ ; a grain of sand, a grain of salt, a coin, a boulder, or an asteroid. Smaller particles are characterised as powders or colloids, and different forms of inter-particle interaction then become important (Andreotti *et al.*, 2013). A granular material is a collection of such grains, surrounded by some interstitial fluid, typically air or water. This collection could take the mathematically convenient form of near-identical spherical marbles with uniform radius or, more problematically, a heterogeneous pile of rubbish in a landfill. Granular materials are frequently handled in some capacity in many industries, across sectors such as food, agriculture, and pharmaceuticals. They are also ubiquitous across the Earth’s many terrains; snow, sand and soil are all granular materials, while granular avalanches, always a potentially destructive natural force, are also a common hazard for peripheral urban settlements in many major cities (Davis, 2006). These industrial and geophysical categories often overlap, in mining or the construction of roads, for example. See figure 1.1 for some examples of different granular materials.

When static (or quasi-static), a granular material mimics the solid state of its particulate constituents. However, under application of an external force a granular material can exhibit properties typical of a liquid, or even a gas. Consider a static desert sand dune: the grains are jammed together, but disturb the sand with sufficient force and material at the free-surface may fail and avalanche downslope, before settling



Figure 1.1: Examples of different granular materials. On the left, an assortment of whole-grains, image courtesy of World Grain magazine. On the top right, dense liquid-like granular flow triggered by human footsteps on the side of a desert sand dune (Barale, 2015). On the bottom right, household waste being poured into a landfill from a rubbish truck, image courtesy of Resource magazine.

again into a static, solid-like state. Light winds may blow grains out from the mound in a gaseous form; extreme desert conditions could even lead to a sandstorm. The sand has apparently passed through three states of matter without any alteration in the atomic-level structure. These contrasting phenomena are indeed a precondition of sand dune formation and transportation (Andreotti *et al.*, 2013), and it is not unusual for a single granular flow to encompass all three quasi-states simultaneously.

Under closer scrutiny however, granular materials reveal unique properties which

elude any of these classifications. Grains do not experience Brownian motion. Solid-like granular materials can sustain a stress without undergoing plastic (irreversible) deformation but are bound together by frictional interactions between grains rather than attractive forces. The fluid regime on the other hand is dominated by inelastic, strongly dissipative collisions between grains and enduring frictional contacts, without significant thermal fluctuation due to the macroscopic particle sizes. Inter-particle collisions can be long lasting in the liquid regime, or instantaneous in the gaseous regime (Armanini *et al.*, 2014). Granular materials are compressible, and may also be characterised as existing in the limit of zero surface tension (Cheng *et al.*, 2008). It is therefore unsurprising when it is suggested that granular materials may be said to constitute their own unique state of matter (Jaeger *et al.*, 1996).

Theoretical and numerical modelling of such multifarious behaviours is necessarily very challenging. DEM (discrete element method) modelling simulates interactions between individually tracked particles subject to external and collisional forces, but these numerical computations quickly become very costly as the number of particles increases - a mere handful of sand contains around 10,000 grains. Moreover, a unified continuum theory encapsulating granular matter in its entirety remains a distant goal, and until this is achieved, continuum approaches must be limited to some subset of granular flows. For this thesis, the focus is upon dry (i.e. where the interstitial fluid is air), dense sheared granular flows in the liquid-like regime, and where necessary also the solid-like regime. This scope encompasses both geophysical avalanches and industrial particulate handling involving silos and rotating mixers or drums. In many of these flows polydispersity (the property of granular flows containing particles of different sizes) is an important feature with consequences for the flow dynamics. The central aim of this thesis is the development of a fully coupled continuum model for the bulk flow and evolving particle-size distribution in transient polydisperse flows, and the application of this coupled approach to rotating drum flows specifically. A fully coupled theory can be used to understand and predict the complex interplay between rheology and segregation within a continuum framework. The concepts of coupling and particle-size segregation will be developed in detail from §1.3.

## 1.2 Rheology of dense granular flows

### 1.2.1 The Coulomb friction model

The genesis of theoretical modelling for dense granular flows is arguably Charles-Augustin de Coulomb’s seminal 1773 work, “Essay on the Application of the Rules of Maxima and Minima to Statical Problems Relating to Architecture” (de Coulomb, 1773, see Heyman & de Coulomb (1972) for an English translation). This memoir-essay details theories developed during the construction of Fort Desaix (initially known as Fort Bourbon during the pre-revolutionary era) on the island of Martinique, where Coulomb served as a military engineer amid territorial struggles between the imperial powers of France and Britain. Coulomb studied earth fortifications, and was able to predict the maximum slope angle of a static pile of granular material, postulating that the material yields when the shear stress  $\tau$  reaches or exceeds a critical (scalar) value  $\tau_c$ , so that for a yielding material

$$\tau \geq \tau_c = \sigma_n \tan \delta + c, \quad (1.2.1)$$

where  $\sigma_n$  represents the normal stress,  $\tan \delta$  is the internal friction coefficient with  $\delta$  the angle of repose of the pile, and  $c$  is the cohesion between grains. When  $\tau < \tau_c$ , the granular material will not yield. For the dry granular flows to be studied here there is no cohesion, and therefore  $c = 0$ . The relation (1.2.1) without cohesion is analogous to the sliding block problem studied by Leonardo da Vinci centuries earlier in his pioneering work on friction.

Alongside further constitutive assumptions, the ideas of Coulomb can be expressed in a form more useful to the theory of modern fluid mechanics by re-writing (1.2.1) in tensorial form (Drucker & Prager, 1952), where for a yielding material

$$\|\boldsymbol{\tau}\| = \mu p, \quad (1.2.2)$$

where  $\mu$  is the dimensionless constant internal friction coefficient,  $p$  is the pressure, related to the normal stress in tensorial form by  $\boldsymbol{\sigma}_n = -p\mathbf{1}$  where  $\mathbf{1}$  is the identity matrix, and  $\boldsymbol{\tau}$  is the shear (or deviatoric) stress tensor, with  $\|\boldsymbol{\tau}\|$  denoting its second invariant. In terms of plasticity theory, this is a Drucker-Prager type yield condition (Yu, 2007). Note that the second invariant of some trace-free tensor  $\|\mathbf{T}\|$  is defined

here in terms of the trace of its square,

$$\|\mathbf{T}\| = \sqrt{\frac{1}{2}\text{tr}(\mathbf{T}^2)}. \quad (1.2.3)$$

The shear and normal stresses can be expressed as components of the decomposed Cauchy stress tensor,

$$\boldsymbol{\sigma} = -p\mathbf{1} + \boldsymbol{\tau}. \quad (1.2.4)$$

It is interesting to note as an aside that in the Napoleonic era the young Cauchy was, like Coulomb, a military engineer, assisting with the construction of a naval base before dedicating himself to his mathematical career.

It is further assumed the the shear stress tensor is aligned with the strain-rate tensor (Savage, 1983; Goddard, 1986), where the strain-rate tensor for a continuous medium undergoing deformation is given by

$$\mathbf{D} = \frac{1}{2}(\nabla \mathbf{u} + (\nabla \mathbf{u})^T), \quad (1.2.5)$$

for bulk velocity  $\mathbf{u}$  and the gradient operator  $\nabla$ . The alignment condition is then expressed as

$$\frac{\boldsymbol{\tau}}{\|\boldsymbol{\tau}\|} = \frac{\mathbf{D}}{\|\mathbf{D}\|}, \quad (1.2.6)$$

where  $\text{tr}(\mathbf{D}) = \nabla \cdot \mathbf{u} = 0$  for an incompressible flow field (see immediately below), and the definition of the second tensor invariant (1.2.3) then means that  $\|\mathbf{D}\|$  has the same dimensions as the shear rate. Combining the alignment condition (1.2.6) with the yield condition (1.2.2) gives an expression for the shear stress,

$$\boldsymbol{\tau} = \mu p \frac{\mathbf{D}}{\|\mathbf{D}\|}. \quad (1.2.7)$$

For a dense granular flow, variations in the solids volume fraction  $\Phi$  are small (GDR-MiDi, 2004), and so the flow may be treated as incompressible. In this case, the bulk density  $\rho$  is a constant, and conservation of mass is given by

$$\nabla \cdot \mathbf{u} = 0. \quad (1.2.8)$$

The expressions for the Cauchy stress tensor (1.2.4) and the shear stress (1.2.7) may be substituted into the Cauchy momentum equation to give

$$\rho \left( \frac{\partial \mathbf{u}}{\partial t} + \mathbf{u} \cdot \nabla \mathbf{u} \right) = -\nabla p + \nabla \cdot (2\eta \mathbf{D}) + \rho \mathbf{g}, \quad (1.2.9)$$

where  $t$  represents time, ‘ $\cdot$ ’ denotes the scalar product operator, the bulk density  $\rho$  is related to the intrinsic grain density  $\rho_*$  by  $\rho = \Phi\rho_*$ ,  $\mathbf{g}$  is the gravitational acceleration vector, and the internal friction coefficient  $\mu$  appears through the granular viscosity  $\eta$ , given by

$$\eta = \frac{\mu p}{2\|\mathbf{D}\|}. \quad (1.2.10)$$

The momentum conservation equation (1.2.9) bears a strong resemblance to the incompressible Navier-Stokes equation, and alongside the incompressible mass balance equation (1.2.8) provides a powerful theoretical framework for modelling the plastic deformation of yielding dense granular materials, i.e. those in the liquid-like regime. Unfortunately, Schaeffer (1987) showed that when the internal friction  $\mu$  is a constant, this system of equations is unconditionally ill-posed. In this context, mathematical ill-posedness means that short wavelength perturbations away from a base state solution exhibit unbounded growth. This is both physically unrealistic and problematic for numerical computations, where noise can lead to violent, grid dependent instabilities in the results, which do not converge upon a well defined solution with increasing grid resolution. Ill-posedness strongly implies that important physics is missing from the theory.

### 1.2.2 Development of the $\mu(I)$ -rheology

Instead, for the theory to correspond more closely to the real physics of dense granular flows within an incompressible framework, it is necessary to express the dimensionless internal friction  $\mu$  as a function of the other available non-dimensional physical quantities. It was observed from experimental measurements of shallow flows down a rough inclined plane (Pouliquen, 1999a; Pouliquen & Forterre, 2002) that steady uniform flows develop only between two critical inclination angles, the static angle  $\zeta_s$  and the dynamic angle  $\zeta_d$ , with no flow when the inclination angle  $\zeta < \zeta_s$  and accelerating flow when  $\zeta > \zeta_d$ . Based upon empirical measurements, Pouliquen & Forterre (2002) then proposed a form for the basal friction coefficient  $\mu_b$ , given by

$$\mu_b = \mu_s + \frac{\mu_d - \mu_s}{\beta h / (\mathcal{L} Fr) + 1}, \quad (1.2.11)$$

where  $\mu_s = \tan(\zeta_s)$  is the static friction coefficient,  $\mu_d = \tan(\zeta_d)$  is the dynamic friction coefficient,  $h$  is the flowing depth,  $\beta$  and  $\mathcal{L}$  are material constants to be measured

empirically, and  $Fr$  is the Froude number, given by

$$Fr = \frac{\bar{u}}{\sqrt{gh \cos \zeta}}, \quad (1.2.12)$$

where  $\bar{u}$  is the depth-averaged velocity, defined as

$$\bar{u} = \frac{1}{h} \int_0^h u(z) dz. \quad (1.2.13)$$

The basal friction law (1.2.11) and later modifications (Edwards *et al.*, 2017, 2019) are very powerful tools for the study of shallow granular flows within a depth-averaged framework. However, the basal friction law (1.2.11) is only valid at the base of the flowing layer, in the dynamic regime when steady uniform flows are possible, defined by  $Fr \geq \beta$ , and for the geometries to be studied in this thesis the shallowness assumption does not necessarily hold.

The Groupement De Recherche Milieux Divisés (GDR-MiDi, 2004) used experiments and DEM simulations to investigate dense granular flows in six different steady-state geometries, encompassing plane shear, annular shear, vertical chute flow, inclined plane flow, heap flow from a discharging silo, and a circular rotating drum. Using dimensional analysis, they proposed that for flow in the dense regime, the friction  $\mu$  is a function of a single parameter only, known as the inertial number  $I$ , defined as

$$I = \frac{2d\|\mathbf{D}\|}{\sqrt{p/\rho_*}}, \quad (1.2.14)$$

where  $d$  is the grain diameter, and then the constitutive law (1.2.2) can be re-expressed as

$$\frac{\|\boldsymbol{\tau}\|}{p} = \mu(I). \quad (1.2.15)$$

The inertial number is the square root of the Savage or Coulomb number (Savage & Sayed, 1984; Ancy *et al.*, 1999). The relation (1.2.15) is equivalent to the assumption of a local rheology, meaning that the stresses and shear rate at a given flow location have a one to one relation (GDR-MiDi, 2004). The rheology is then considered to be non-local when  $\|\boldsymbol{\tau}\|/p$  depends on the shear rate at other locations or on another field with unspecified governing equations. The local rheology hypothesis is supported by the collapse of DEM and experimental data across a variety of flow configurations onto a single  $\mu(I)$  curve (GDR-MiDi, 2004; Da Cruz *et al.*, 2005; Andreotti *et al.*, 2013). Non-local effects may still arise under a variety of circumstances (Kamrin, 2019); of

particular concern in this thesis is non-locality in rotating drum flows, where material deep in the quasi-static substrate undergoes creeping flow induced by the avalanching free-surface. Nevertheless, this quasi-static region is unimportant for the avalanche dynamics and particle segregation patterns investigated here and indeed, as will be demonstrated in chapter 3, rotating drum flows can be accurately modelled with viscous Newtonian fluid flow assumed (for the purposes of numerical regularisation) in the deeper creeping region. Therefore, although a part of the full physics of granular flows, current evidence does not suggest that non-locality is necessary for useful predictive modelling of rotating drum flows, and so the assumption of a local rheology will be retained here for its greater simplicity.

GDR-MiDi (2004) offer a physical interpretation of  $I$  as the ratio between two timescales, illustrated in figure 1.2. Consider two layers of flowing grains, confined by a pressure  $p$  with shear rate  $\dot{\gamma} = 2\|\mathbf{D}\|$  between the upper and lower layers. The upper layer moves relative to the lower layer with velocity  $\dot{\gamma}d$ , and so the time taken for one layer to travel a single grain width  $d$  in relation to the other is  $d/\dot{\gamma}d$ . This defines the deformation or macroscopic timescale, given by  $T_\gamma = 1/\dot{\gamma}$ . After a grain in the upper layer has travelled over a grain in the lower layer, the confinement or microscopic timescale  $T_p$  is the time taken for the grain in the upper layer to drop back into a position nested between grains in the lower layer due to the confining pressure. This can be derived using Newton's law in the normal direction, written  $F = m d^2 z / dt^2$ . The mass  $m \propto \rho d^3$ , the force  $F \propto \rho d^2$ , and the acceleration  $d^2 z / dt^2 \propto d/t^2$ . Combining these relations and rearranging gives the expression for the microscopic timescale as  $T_p = d\sqrt{\rho_*/p}$ .

The inertial number can then be used to characterise the flowing regime (GDR-MiDi, 2004; Da Cruz *et al.*, 2005; Andreotti *et al.*, 2013), with  $10^{-3} < I < 1$  approximately corresponding to the liquid-like or inertial regime,  $I < 10^{-3}$  representing the solid-like or quasi-static regime, and  $I > 1$  representing the gaseous or collisional regime, where the assumption of dense flow breaks down and a coefficient of restitution becomes important. This interpretation also hints at one of the difficulties in applying continuum theories to granular materials: the lack of clear scale separation between the macroscopic and microscopic length scales, since granular flows are often only a few grain diameters in thickness. Although the focus of this thesis is primarily on the



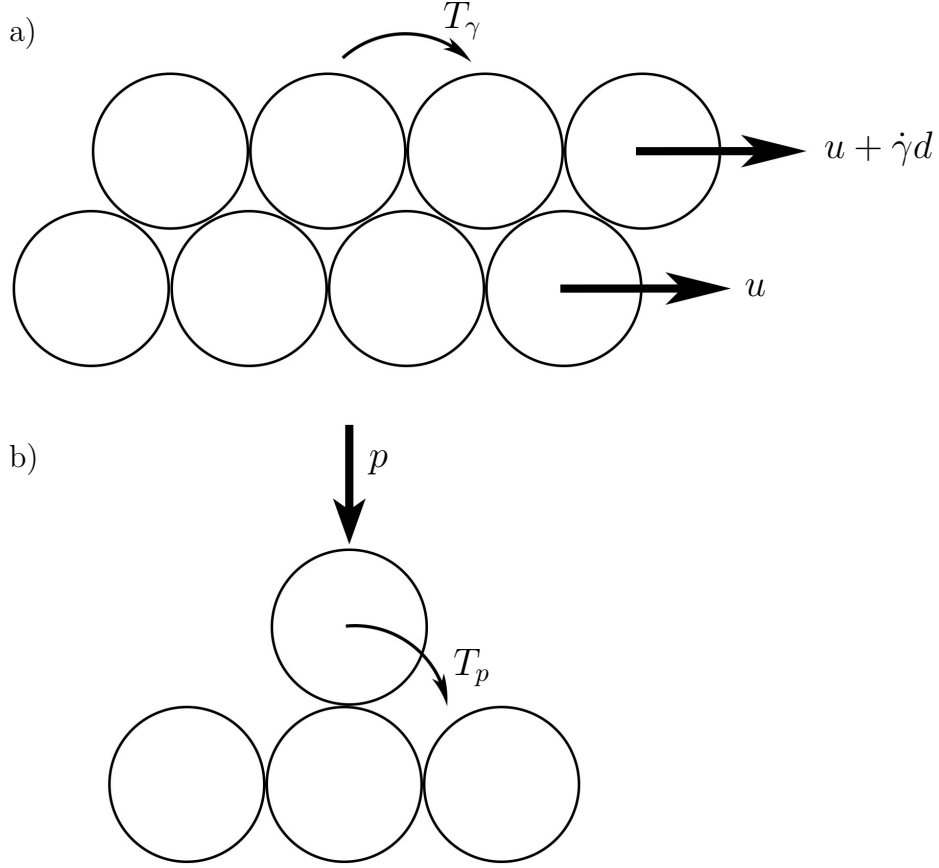


Figure 1.2: Schematic diagram of a granular flow with shear and normal stresses, illustrating (a) the macroscopic timescale for deformation  $T_\gamma = 1/\dot{\gamma}$  in the presence of a shear rate  $\dot{\gamma}$ , and (b) the microscopic timescale for grain rearrangement  $T_p = d\sqrt{\rho_*/p}$ , under the application of pressure  $p$ . The inertial number  $I$  can be interpreted as the ratio of these two timescales.

inertial and quasi-static regimes, the behaviour of granular material in the collisional regime has been described using kinetic theory (see e.g. Campbell, 1990; Lun, 1991; Armanini *et al.*, 2014).

An explicit functional form for the constitutive law (1.2.15) was derived by Jop *et al.* (2005) by comparison with the basal friction law (1.2.11). For a steady uniform flow on a plane inclined at an angle  $\zeta$ , the normal component of the momentum balance (1.2.9) gives

$$p = \rho g(h - z) \cos \zeta, \quad (1.2.16)$$

where  $z$  is the normal co-ordinate and  $h$  is the flowing depth, assuming zero pressure at the free-surface where  $z = h$ . The downslope component of the momentum balance (1.2.9) then reduces to  $\mu = \tan \zeta$ , implying that  $\mu(I)$  and hence  $I = I_\zeta$  is constant

through the layer and depends only on the inclination angle  $\zeta$ . Since  $\partial u/\partial z$  is the only non-zero velocity gradient, in this geometry the second invariant of the strain-rate tensor is

$$\|\mathbf{D}\| = \frac{1}{2} \frac{\partial u}{\partial z}. \quad (1.2.17)$$

Invoking the definition of the inertial number (1.2.14) and using the pressure scaling (1.2.16) therefore gives an ordinary differential equation (ODE) for the downslope velocity profile  $u(z)$ , with the exact solution

$$u(z) = \frac{2I_\zeta}{3d} \sqrt{\Phi g \cos \zeta} (h^{3/2} - (h - z)^{3/2}), \quad (1.2.18)$$

using  $\rho/\rho_* = \Phi$ . This is known as Bagnold's velocity profile (Bagnold, 1954), after Ralph Bagnold, and is plotted in figure 1.3. Another military engineer and geologist, Bagnold served for the British Empire in North Africa and the Indian subcontinent during the interwar period. His explorations of the Libyan Desert in particular were crucial to the formation of a scientific understanding of aeolian transport and granular flows more generally, which he continued to develop through field research, experiments and theoretical modelling throughout much of the 20th century.

The Bagnold velocity profile (1.2.18) can be integrated to give the depth-averaged velocity profile defined by (1.2.13),

$$\bar{u} = \frac{2I_\zeta}{5d} \sqrt{\Phi g \cos \zeta} h^{3/2}. \quad (1.2.19)$$

The depth-averaged Bagnold velocity (1.2.19) can then be substituted into the definition for the Froude number (1.2.12) to give an explicit expression for the Froude number,

$$Fr = \frac{2I_\zeta}{5d} \sqrt{\Phi} h. \quad (1.2.20)$$

Since the internal friction is constant through the flowing depth, the region of validity for the basal friction law (1.2.11) can be extended by substituting (1.2.20) and re-writing (1.2.11) in terms of the inertial number  $I$ , as

$$\mu(I) = \mu_s + \frac{\mu_d - \mu_s}{I_0/I + 1}, \quad (1.2.21)$$

where  $I_0$  is related to the constants  $\beta$  and  $\mathcal{L}$  by

$$I_0 = \frac{5\beta d}{2\sqrt{\Phi}\mathcal{L}}. \quad (1.2.22)$$

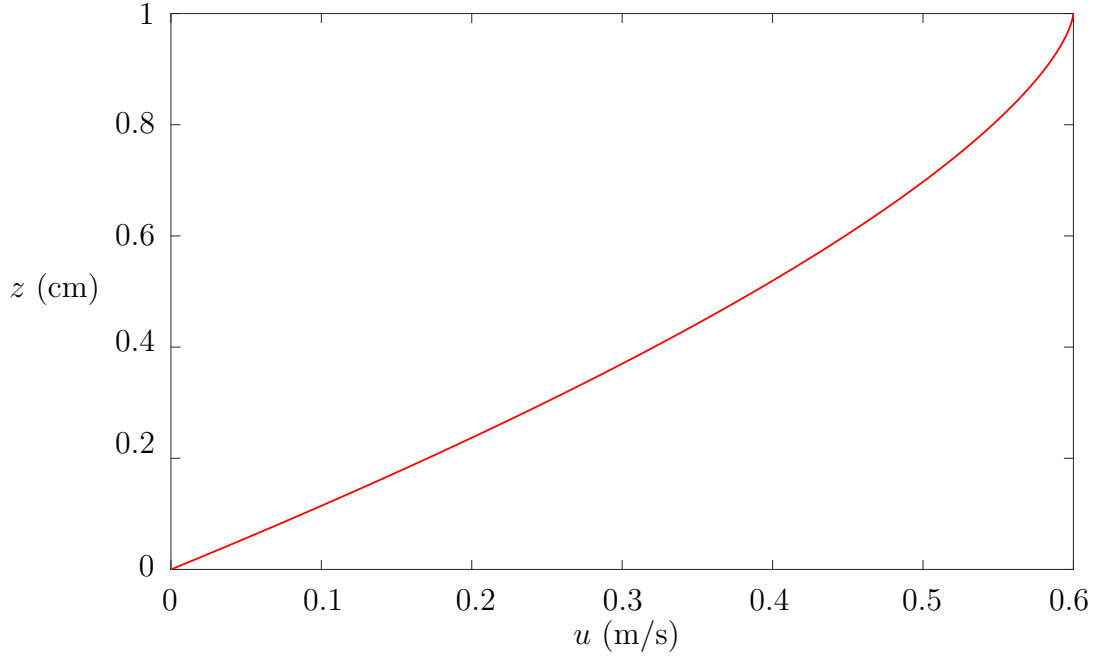


Figure 1.3: Plot of the Bagnold velocity profile (1.2.18) for steady uniform flow down an incline. The flowing layer has constant thickness  $h = 1$  cm, the slope is inclined at an angle  $\zeta = 21^\circ$ , the grains have diameter  $d = 0.1$  cm and the solids volume fraction  $\Phi = 0.6$ .

Note that  $\mathcal{L}$  is a length scale considered to be linear in the particle size  $d$  (Jop *et al.*, 2005), and so  $I_0$  does not vary with  $d$  and is simply a material constant. The functional form (1.2.21) expresses a local rheology based upon the constitutive laws (1.2.14) and (1.2.15), known as the  $\mu(I)$ -rheology.

The establishment of the  $\mu(I)$ -rheology represented a major breakthrough in the study of dense granular flows. It has been used to describe velocity profiles for granular flow on a pile between rough sidewalls, giving strong quantitative agreement with experimental measurements (Jop *et al.*, 2006). Furthermore, although its origin lies in observations of steady-state flows (GDR-MiDi, 2004; Jop *et al.*, 2005), strong evidence was provided by Lacaze & Kerswell (2009) that the validity of the rheology extends beyond this into dynamic, highly transient flows. They demonstrated that data extracted from three-dimensional DEM modelling of a cylindrical granular column collapse matched very accurately with the  $\mu(I)$  curve (1.2.21). Later, the incompressible Navier-Stokes-like mass (1.2.8) and momentum balance equations (1.2.9), with the

constant friction coefficient replaced by (1.2.21) in the definition of the granular viscosity (1.2.10), were used to compute full two-dimensional numerical simulations of a column collapse (Lagrée *et al.*, 2011) and discharge from a silo (Staron *et al.*, 2012, 2014), with promising qualitative results.

The  $\mu(I)$ -rheology is able to capture both flowing and solid-like dense regimes, with transition between the two modelled using the static friction coefficient  $\mu_s$  attained at  $I = 0$ , and static material predicted below the minimum yield stress of  $\|\boldsymbol{\tau}\| = \mu_s p$ , whereafter the functional form (1.2.21) is no longer valid. There is however evidence from free-surface flows over a heap (Komatsu *et al.*, 2001; Crassous *et al.*, 2008) suggesting that the solid-like regime for shear flows is instead characterised by quasi-static creeping flow which tails off exponentially with depth below a flowing layer.

Furthermore, the problem of ill-posedness related to the Coulomb friction model (1.2.2) remains relevant to the  $\mu(I)$ -rheology. Barker *et al.* (2015) showed that (1.2.21) leads to ill-posedness in both the small and large inertial number limits, but is well posed for intermediate values of  $I$ . This is a significant advance from the Coulomb friction model which was always ill-posed, and implies that the validity of (1.2.21) roughly corresponds to the dense flow or inertial regime, with additional important physics present in the quasi-static and collisional regimes, along with the solid-liquid and liquid-gas transitions.

Barker & Gray (2017) noted that  $\mu(I = 0) = 0$  is a necessary condition for well-posedness throughout the quasi-static regime, and proposed a new functional form which is well-posed for small  $I$  by introducing a creep state derived by inverting the neutral stability curves, and a continuous transition with the inertial regime at the point where the latter becomes ill-posed. They were also able to extend the maximum well-posed inertial number up to a very high upper limit by having  $\mu \propto I$  as  $I \rightarrow \infty$ , as suggested by high speed chute flow experiments (Holyoake & McElwaine, 2012; Barker & Gray, 2017). This new functional form, known as the partially regularised  $\mu(I)$ -rheology, is given by

$$\mu = \begin{cases} \sqrt{\frac{\alpha}{\log\left(\frac{A}{I}\right)}}, & \text{for } I \leq I_1, \\ \frac{\mu_s I_0 + \mu_d I + \mu_\infty I^2}{I_0 + I}, & \text{for } I > I_1, \end{cases} \quad (1.2.23)$$

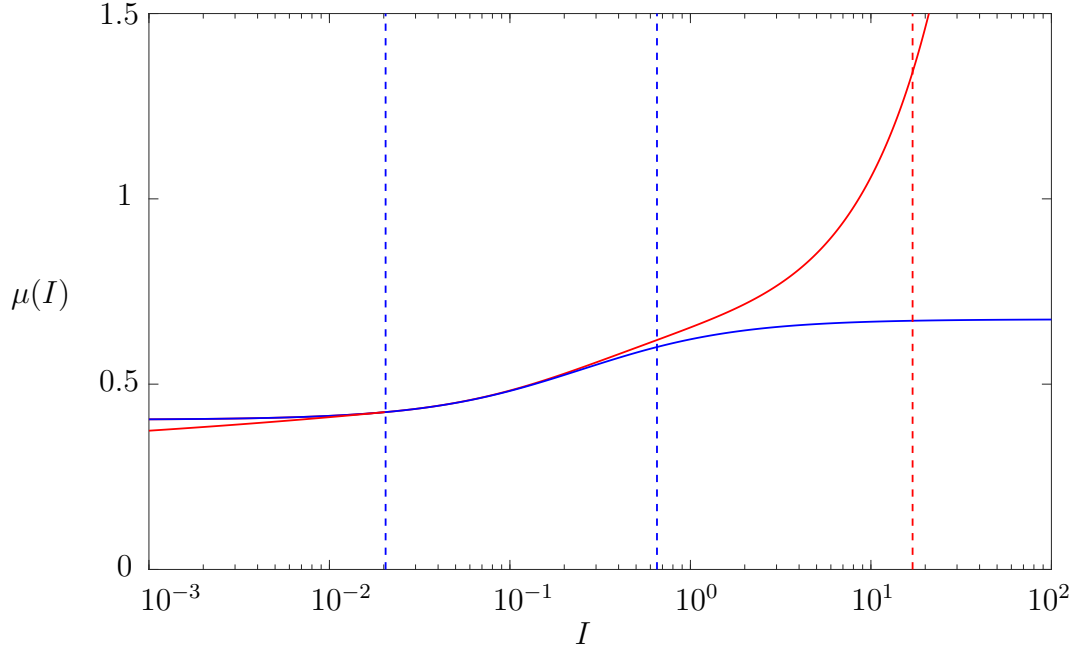


Figure 1.4: Plot of  $\mu(I)$ , for the original  $\mu(I)$  curve given by (1.2.21) (blue line) and the partially regularised form given by (1.2.23) (red line), for parameters  $\mu_s = 0.404$ ,  $\mu_s = 0.675$ ,  $\mu_\infty = 0.04$ ,  $I_0 = 0.249$ , and  $\alpha = 1.9$ . The vertical dashed blue lines represent the lower and upper limits of well-posedness for the original  $\mu(I)$  curve. The lower limit is also very close to the point of transition between the two branches of (1.2.23) since the  $\mu_\infty I^2$  term in (1.2.23) is dominated by the other terms in the region where  $I < 1$ . While the original curve decays to  $\mu_s$  for  $I = 0$  and asymptotically approaches  $\mu_d$  for  $I \rightarrow \infty$ , the partially regularised form enters a creep regime as  $I \rightarrow 0$  which decays to  $\mu(I = 0) = 0$ , and has no upper bound. The vertical red dashed line represents the upper limit of well-posedness for the partially regularised  $\mu(I)$ -rheology, which for the given parameters is at  $I = 17.0189$ .

where  $\alpha \lesssim 2$  ensures the creep state remains within the well-posed region,  $\mu_\infty$  is a constant characterising collisional dissipation for large  $I$  (Barker & Gray, 2017), and

$$A = I_1 \exp \left( \frac{\alpha(I_0 + I_1)^2}{(\mu_s I_0 + \mu_d I_1 + \mu_\infty I_1^2)^2} \right) \quad (1.2.24)$$

gives continuity between the two branches at the point of transition  $I = I_1$ , below which the upper branch would become ill-posed. The partially regularised formulation (1.2.23) guarantees well-posedness throughout the quasi-static and inertial regimes, and with an appropriate choice of  $\mu_\infty$ , for a subset of the collisional regime, up to some extreme maximum value depending on the particular choice of parameters. The partially regularised  $\mu(I)$ -rheology and the original curve of Jop *et al.* (2005) are

plotted in figure 1.4, showing close agreement between the two in the region of well-posedness for the original curve.

Although the  $\mu(I)$ -rheology can only reasonably be expected to provide an accurate approximation of the physics in the inertial regime due to its specific empirical origins (GDR-MiDi, 2004), the small  $I$  creep state introduced in the partially regularised formulation means that solid and liquid-like material can be modelled simultaneously without ill-posedness. For the relevant physics in the quasi-static regime as well as the transition between inertial and quasi-static regimes to be reflected more accurately in the theory, important phenomena such as frictional hysteresis (Edwards *et al.*, 2017, 2019) or non-locality (Pouliquen & Forterre, 2009; Kamrin & Koval, 2012; Kamrin, 2019) must be included. In the collisional regime designated here by large  $I$  the coefficient of restitution becomes relevant since collisions between grains are inelastic (Jenkins, 2007; Jenkins & Berzi, 2010; Armanini *et al.*, 2014). Variation in the solids volume fraction  $\Phi$  also becomes increasingly important, and hence the assumption of incompressibility breaks down, and so kinetic theory models include some  $\Phi$  dependence. Attempts at modelling compressibility in the inertial regime have been made by introducing  $\Phi(I)$  dependence into the original  $\mu(I)$ -rheology (GDR-MiDi, 2004; Forterre & Pouliquen, 2008), which have recently been extended into forms which can regularise the rheology (Heyman *et al.*, 2017; Goddard & Lee, 2018; Schaeffer *et al.*, 2019). In particular, Schaeffer *et al.* (2019) showed that compressible theories can include a yield stress and remain unconditionally well-posed.

Despite this, here the partially regularised incompressible  $\mu(I)$ -rheology is preferred to these alternative approaches. In rotating drum flows, as discussed above non-locality should be introduced into the model for an accurate physical approximation of the quasi-static creep regime below the flowing layer, but since segregation in polydisperse drum flows is confined to the inertial avalanching region, non-locality is overlooked here in favour of a simpler approach centred on the inertial regime. As a lower order effect, compressibility is also neglected to simplify the numerical computations and ensure the rheological approach is compatible with pre-existing incompressible segregation theories. Furthermore, drum flows cannot be depth-averaged since they do not have a shallow dimension, and modelling frictional hysteresis with non-monotonic  $\mu(I)$  curves leads to ill-posedness in non-depth-averaged frameworks.

Hysteresis is likely necessary for physical modelling of intermittently avalanching rotating drum flows (Gray & Hutter, 1997) and so its omission here imposes a limitation on the theory in the context of rotating drums. DEM approaches to modelling drum flows are also currently infeasible for direct comparison to experimental data due to the computational expense incurred when using particle numbers typical for experiments or industrial mixers. Therefore, at the time of writing the partially regularised incompressible  $\mu(I)$ -rheology is an appropriate approach for numerical modelling of the complex transient dense flows of interest in this thesis.

### 1.3 Particle-size segregation

The rheological modelling in §1.2 is formulated on the assumption of monodisperse flows of uniform density (1.2.14), but in reality all granular flows contain some level of variation in size (polydispersity), density or shape. This is perhaps most pronounced in a geophysical context, where individual grains are formed as the result of sensitive natural processes such as weathering, erosion or crystallisation. Furthermore, handling of dissimilar classes of particles is important in mining, food manufacture, the chemical and pharmaceutical industries, and agriculture, and the earliest research into segregation was driven by these industrial interests, where particles may be mixed to improve product uniformity or control chemical reactions, for example (Cooke *et al.*, 1976). Despite the pragmatism of early work, particle segregation has gained traction as an exciting field of research in its own right due to the limited current understanding which belies the ubiquity of segregation and its importance across varied flow phenomena, and due to the arresting variety of pattern formations possible under different flow configurations (Hill *et al.*, 1999; McCarthy, 2009; Gray, 2018), with particle species typically distinguished by colour.

For geophysical avalanche flows or those occurring during industrial mixing or transportation, as well as tumbled or vibrated flows, segregation between different particle classes inevitably occurs, exacerbating the already considerable difficulty associated with handling granular materials. This may result in wastage due to the inherent difficulty of obtaining desired mixture compositions, or geophysical avalanches with unpredictable run-out distances and flow behaviours (Johnson *et al.*, 2012). The

scale of the problem is such that factories utilising granular materials typically suffer much longer start-up times than those dealing exclusively with fluids (Shinbrot & Muzzio, 2000). Developing theories for particle segregation is therefore an important, ongoing aim within granular flow modelling, and although a general theory remains elusive (as in the case of rheology), recent advances in understanding of segregation dependencies in the inertial regime (Trewhele *et al.*, 2021; Bancroft & Johnson, 2021) give rise to the possibility of the full rheology-segregation coupling which is developed in this thesis.

### 1.3.1 Segregation mechanisms

Early breakthroughs in experimental and theoretical studies of particle segregation in cohesionless granular materials were led by John Bridgwater, with some overview provided by Bridgwater (1994). Scott & Bridgwater (1975) discussed problems related to the industrial mixing of polydisperse granular materials, noting the difficulty in obtaining uniformly mixed materials, and even reliable data on particle distribution with existing experimental or industrial methods. A limited physical explanation of this phenomenon was given using the process of spontaneous percolation, and it was suggested that the underlying mechanism for segregation was partially gravity driven. They designed a simple shear cell experiment involving large particles of diameter  $d^l$  and smaller particles of diameter  $d^s < d^l$  which gave reliable results without the need for a laborious sampling process, through which a relationship between strain-rate and particle percolation time was ascertained. In their experiments the particle size ratio  $R = d^l/d^s$  was the most important independent variable, while variations in particle shape and density played a less significant role. The predominance of size segregation over density-driven segregation in dense shear flows was later reaffirmed by Vallance & Savage (2000); density variation between species also introduces compressibility into theoretical models (Tripathi & Khakhar, 2013; Gray & Ancey, 2015), and will therefore be convenient to overlook in later sections.

Over time a clearer picture of the mechanisms driving particle-size segregation has emerged. Savage & Lun (1988) observed slow motion recordings of bidisperse (mixtures containing two species distinguished by particle size) inclined plane flows in the inertial regime confined between glass sidewalls, and used their observations



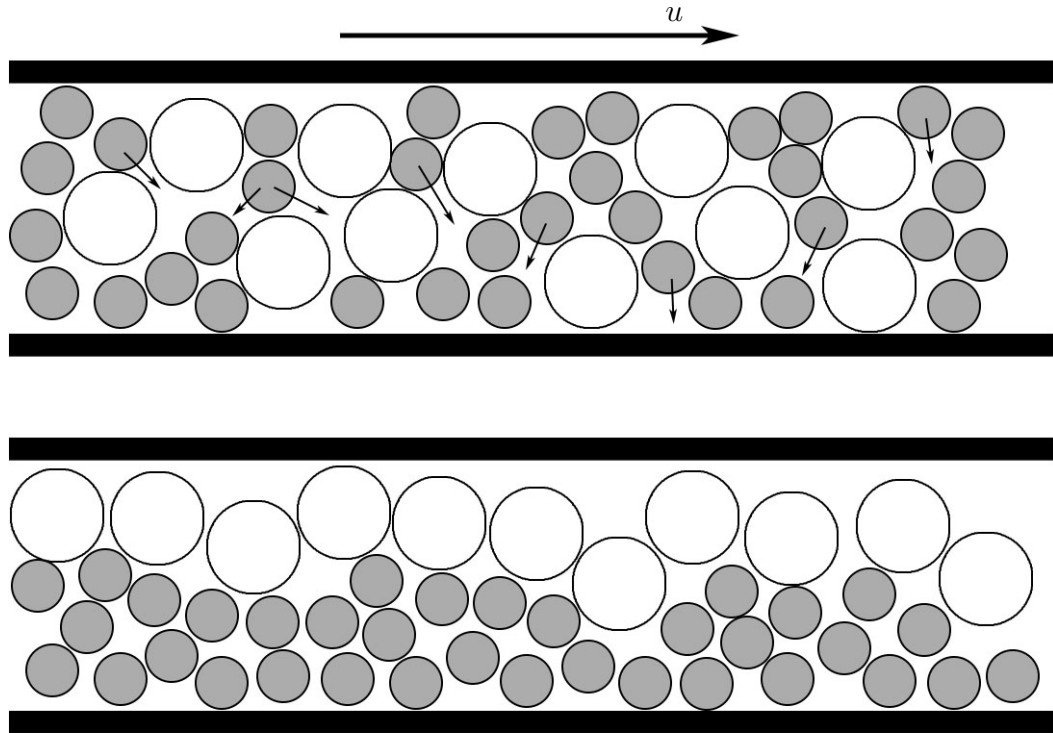


Figure 1.5: Schematic diagram of gravity-driven size segregation in a shear flow between two plates, where gravity is assumed to point downwards. As the initially well-mixed flow is sheared, smaller particles preferentially fall through void spaces in the granular material and squeeze the larger particles upwards, resulting in the inversely graded layer depicted in the second graphic.

to discern the nature of size segregation at the inter-particle level. When a granular material undergoes shear, the distribution in void spaces throughout the material continuously changes, and if a void space is sufficiently large a particle from an upper layer can drop down to occupy it (Shinohara *et al.*, 1970). This is more likely to happen for smaller particles. This process, known as ‘kinetic sieving’ (Savage & Lun, 1988) and illustrated in figure 1.5, is fundamentally gravity-driven and results in inversely graded layers with smaller particles concentrated towards the base of a flowing layer. In a geophysical context, inversely graded sediment layers (Middleton, 1970) are observed in which finer particles collect towards the base of flow deposits. A second, more subtle mechanism was also apparent in the recordings, whereby a force imbalance on an individual particle pushes it upwards into an adjacent layer, so that there is no net mass flux in the direction normal to the inclined plane. This process, termed ‘squeeze expulsion’, is not gravity driven or size preferential, and acts as a counterpart to

kinetic sieving. Taken together, these two processes have been termed ‘gravity-driven segregation’ (Gray, 2018). The propensity of larger particles to accumulate near the top of a shaken granular material is commonly known as the Brazil nut effect.

Other mechanisms driving particle-size segregation include convection cycles in vibrated granular materials (Knight *et al.*, 1993; Ehrichs *et al.*, 1995), trajectory segregation induced by greater sensitivity to air resistance in smaller particles (Schulze, 2008), and fluidisation or condensation of one species before another (Hong *et al.*, 2001; Schröter *et al.*, 2006) related to differences in granular temperature, which measures the kinetic energy of random particle motion and is important in kinetic theory (see e.g. Brilliantov & Pöschel, 2004). Condensation (the transition of fluid-like granular material to a solid-like state, inducing segregation towards the bottom of a flowing layer) can act against kinetic sieving in excited systems in a so-called reverse Brazil nut effect (Hong *et al.*, 2001). Alongside kinetic sieving/squeeze expulsion, these mechanisms have been designated as the most important and widely researched (McCarthy, 2009), although there are many others (see e.g. Gray, 2018).

For dense sheared flows in the inertial regime, gravity-driven segregation has usually been identified as the most important (Savage & Lun, 1988; Gray, 2018); trajectory induced segregation can occur via discharge from an inclined chute, but in this case the material is likely to have already formed an inversely graded layer due to gravity, and convection induced segregation is mainly important in vibrating materials. Condensation induced segregation appears to occur only in externally excited systems with fluidised grains in the gaseous regime (Breu *et al.*, 2003; Hong *et al.*, 2001) rather than in dense shear flows, and it can only override gravity-driven segregation under specific conditions related to the density ratio, size ratio, and the excitation of the system. Nevertheless, Hill & Tan (2014) demonstrated that gradients in the kinetic stresses or granular temperature may drive segregation in dense rotating drum flows, although these granular temperature gradients were ultimately induced by gravity and for particle species of equal density the net result remains an inversely graded layer.

Conway *et al.* (2006) showed that in sparse dry systems or in particle suspensions a shear rate gradient may drive segregation, with large particles segregated towards regions of low shear rate. However, it has been observed that shear-induced kinetic stress gradients may also drive segregation in certain dense flow regimes (Fan & Hill,

2010, 2011; Hill & Tan, 2014), and even oppose gravity-driven segregation. Fan & Hill (2011) used DEM simulations in which large and small grains were allowed to fall between parallel plates to show that a kinetic stress gradient induced by a gradient of shear rate alone could drive segregation. Large particles were segregated towards the plates and small particles towards the middle of the chute by a kinetic sieving mechanism acting in a direction normal to gravity, with large particles now segregated towards regions of higher shear rate. This result seemingly contradicts observations that in inclined plane flows with Bagnold-like velocity profiles (see figure 1.3), large particles segregate towards the free-surface where the shear rate is lowest. In practice, for gravity-driven flows contributions from both kinetic stress gradients arising from shear rate gradients and gravity may drive segregation, but the relative importance of these competing mechanisms is difficult to ascertain precisely (Staron & Phillips, 2015). The evidence across different dense flow geometries suggests that gravity plays the pivotal role in the presence of a gravity-induced pressure gradient, but in certain geometries which induce a shear-aligned pressure gradient normal to gravity the segregation can be orientated normal to gravity. The pressure gradient is therefore a versatile indicator of the correct alignment of the segregation direction.

Since this thesis is concerned with avalanche-type flows of dense granular materials in the inertial or quasi-static regimes in which large particles are known to segregate towards the low-shear free-surface region, it is reasonable to subsume segregation driven by shear rate gradients as an underlying constraint within a gravity-driven segregation theory. The opposing effect of shear rate gradients can then be considered to be implicitly incorporated into the segregation scaling derived by Trehwela *et al.* (2021) in a simplified form as a background process feeding into parameter measurements.

### 1.3.2 Continuum modelling of particle-size segregation

A continuum model for size segregation and diffusion in dense regimes was first developed by Bridgwater *et al.* (1985) for a polydisperse mixture in a uniform flow, and subsequent theories generally share a similar structure. Consider a polydisperse flow where each component of the mixture  $\nu$  is identified with a constant particle size  $d^\nu$ . Each component or species has a concentration  $\phi^\nu$  defined as a proportion of the overall

solids volume fraction  $\Phi$ , and so by definition,

$$\sum_{\forall \nu} \phi^\nu = 1, \quad (1.3.1)$$

for an arbitrary number of particle species. Gray & Ancey (2011) derived a multi-component mixture theory for shallow granular avalanches with explicit expressions for the normal velocity of each phase based upon a species interaction law (Gray & Chugunov, 2006) and a hydrostatic pressure scaling (Gray & Thornton, 2005). In a more general form, by analogy with standard mixture theory (Morland, 1992), each species has a volume fraction weighted partial density given by

$$\rho^\nu = \phi^\nu \rho, \quad (1.3.2)$$

where the constant bulk density is related to the intrinsic grain density by  $\rho = \Phi \rho_*$  for each species as in §1.2. The continuity equation is then

$$\frac{\partial \rho^\nu}{\partial t} + \nabla \cdot (\rho^\nu \mathbf{u}^\nu), \quad (1.3.3)$$

where  $\mathbf{u}^\nu$  is the velocity of species  $\nu$ . This only reduces to the incompressibility condition (1.2.8) when summed over each of the phases, since

$$\sum_{\forall \nu} \rho^\nu = \rho \sum_{\forall \nu} \phi^\nu = \rho. \quad (1.3.4)$$

Substituting the partial density definition (1.3.2) into the mass continuity equation (1.3.3) trivially results in the concentration continuity equation,

$$\frac{\partial \phi^\nu}{\partial t} + \nabla \cdot (\phi^\nu \mathbf{u}^\nu). \quad (1.3.5)$$

Following Bridgwater *et al.* (1985), the species flux  $\mathbf{q}^\nu = \phi^\nu \mathbf{u}^\nu$  may be split into contributions from the bulk velocity, segregation and diffusion, resulting in a generalised multi-component advection-segregation-diffusion equation, of the form

$$\frac{\partial \phi^\nu}{\partial t} + \nabla \cdot (\phi^\nu \mathbf{u}) + \nabla \cdot \mathbf{F}^\nu = \nabla \cdot \mathbf{D}^\nu, \quad (1.3.6)$$

where  $\mathbf{F}^\nu$  is the segregation flux and  $\mathbf{D}^\nu$  is the diffusive flux. This represents a generalisation of the one-dimensional continuity equation derived by Bridgwater *et al.* (1985), which included contributions to the normal species velocity from segregation

and diffusion but discarded the advective term using the assumption of uniform flow. By imposing the constraint that the segregation and diffusive fluxes sum to zero,

$$\sum_{\forall \nu} \mathbf{F}^\nu = 0, \quad \sum_{\forall \nu} \mathbf{D}^\nu = 0, \quad (1.3.7a,b)$$

the incompressible mass balance (1.2.8) is recovered by summation of the advection-segregation-diffusion equation (1.3.6) over each phase.

Another model of the general form (1.3.6) was proposed by Dolgunin & Ukolov (1995) for an explicitly bidisperse mixture including an advection term along with segregation and diffusion. For a mixture containing small and large particles with  $\nu = s$  and  $\nu = l$  respectively, the concentration summation constraint (1.3.1) requires that  $\phi^l = 1 - \phi^s$ , and so particle redistribution can be described using a single equation of the form (1.3.6). The segregation flux function in two or three dimensions is a vector  $\mathbf{F}^\nu = F^\nu \mathbf{e}_{\nu\lambda}$ , where  $\mathbf{e}_{\nu\lambda}$  is a unit vector determining the direction of segregation, and the diffusive flux similarly is a vector  $\mathbf{D}^\nu$  related to concentration gradients. For gravity-driven segregation,

$$\mathbf{F}^s = F^s \frac{\mathbf{g}}{|\mathbf{g}|}, \quad \mathbf{F}^l = -F^l \frac{\mathbf{g}}{|\mathbf{g}|}, \quad (1.3.8a,b)$$

and the summation constraint for the segregation fluxes (1.3.7a) is satisfied as long as  $F^s = F^l$ . Since it is necessary that no segregation should occur when  $\phi^\nu = 0$  or 1, the cubic function

$$F^s = F^l = f_{sl} \phi^s (1 - \phi^s)^2, \quad (1.3.9)$$

was suggested by Bridgwater *et al.* (1985) as an arbitrary functional form for the bidisperse segregation flux satisfying these requirements, where  $f_{sl}$  represents the bidisperse segregation coefficient. Dolgunin & Ukolov (1995) instead used a simpler quadratic dependence,

$$F^s = F^l = f_{sl} \phi^s (1 - \phi^s), \quad (1.3.10)$$

which is the simplest form satisfying  $F^\nu = 0$  at  $\phi^\nu = 0$  or 1. Either the cubic (1.3.9) or quadratic (1.3.10) formulations may be generalised for an arbitrary number of particle species by assuming that each species flux function is the sum of the relevant bidisperse flux functions (Gray & Ancy, 2011) where the segregation coefficient for arbitrary species  $\nu$  and  $\lambda$  is denoted by  $f_{\nu\lambda}$ . A generalised asymmetric cubic function has also been suggested based upon observations of shear box experiments (Gajjar &

Gray, 2014; van der Vaart *et al.*, 2015). The asymmetric flux function (1.3.9) is able to capture the phenomenon that a single small particle intruder percolates down through a body of large particles faster than a single large intruder is able to be squeezed upwards through a body of small particles (Golick & Daniels, 2009; van der Vaart *et al.*, 2015).

For an asymmetric dependency of the form (1.3.9) with no concentration dependency in the segregation coefficients  $f_{\nu\lambda}$ , care must be taken with a polydisperse mixture to ensure that each bidisperse flux function is linear in the smaller particle concentration and quadratic in larger particle concentration in order to satisfy the segregation flux summation constraint (1.3.7a). For this reason, ultimately it is simpler to choose the symmetric flux function (1.3.10) and confine the asymmetry discussed by Gajjar & Gray (2014) to the segregation rate  $f_{\nu\lambda}$ , as will be seen in chapter 2.

Various analytic and numerical solutions of the advection-segregation-diffusion equation (1.3.6) in a reduced form have been found, with boundary conditions formulated at concentration shocks (discontinuities), for mixtures with two or three distinct particle sizes with or without diffusion (Bridgwater *et al.*, 1985; Dolgunin & Ukolov, 1995; Gray & Thornton, 2005; Thornton *et al.*, 2006; Gray & Chugunov, 2006; Thornton & Gray, 2008; Gray & Ancey, 2011; Gajjar & Gray, 2014; Gray & Ancey, 2015). Considerable complexity may be captured using analytic solutions where the segregation coefficient  $f_{\nu\lambda}$  is held constant. For example, when large particles have been segregated towards the free-surface of a bidisperse avalanche, they are preferentially transported towards the flow front (Pouliquen *et al.*, 1997) where they may be overrun and recirculated in a breaking size-segregation wave (Thornton & Gray, 2008; van der Vaart *et al.*, 2018), inside a complex lens structure formed by a pair of expansion fans (see e.g. Roshko & Liepmann, 1957) containing a mix of small and large particles. Ultimately however, these segregation models are limited by a level of arbitrariness in selection of a constant segregation or diffusion coefficient, and prescription of a bulk velocity profile, when in reality there is strong two-way interaction between the bulk flow properties and the mixing process (for more detail see chapter 2).

One approach to coupling the bulk flow and evolving particle distribution for inclined plane flows is to exploit their shallowness by coupling depth-averaged mass (1.2.8) and momentum balances (1.2.9), including the  $\mu(I)$ -rheology (1.2.21), and a



Figure 1.6: Examples of two polydisperse shallow granular flows. On the top, a geophysical snow avalanche bounded by levees (Edwards *et al.*, 2017). On the bottom, a photograph of an experiment with segregation-induced fingering instabilities at the flow front, with larger brown particles advected to the sides to form levees for each finger (Baker *et al.*, 2016).

bidisperse segregation-advection-diffusion equation (1.3.6), itself depth-averaged with an assumed shear profile and inversely graded layer (Gray & Kokelaar, 2010*b*; Baker *et al.*, 2016). Feedback of the particle distribution onto the bulk flow is achieved by incorporating frictional differences between small and large particles into a concentration-dependent basal friction coefficient (Pouliquen & Vallance, 1999; Woodhouse *et al.*, 2012), and feedback of the bulk flow onto the particle distribution occurs through advection only, rather than the functional dependencies of the segregation and diffusion rates. For this reason the depth-averaged segregation equation is known as the large

particle transport equation (Gray & Kokelaar, 2010a).

Using the large particle transport equation, the complex structure of the breaking size-segregation wave is transformed into a simpler propagating concentration shock (Baker *et al.*, 2016). This framework has been able to predict widely observed geophysical phenomena related to size segregation (see figure 1.6 for some examples), such as levee formation (Iverson, 1997; Félix & Thomas, 2004; Bartelt *et al.*, 2012), in which predominantly large particles advected to the sides of a flow form stationary lateral barriers confining an inner channel of flowing material and extending run-out distances (Johnson *et al.*, 2012); fingering instabilities (Pouliquen & Vallance, 1999) in a large particle rich flow front themselves bounded by levees (Woodhouse *et al.*, 2012; Baker *et al.*, 2016); and bulbous head formation (Denissen *et al.*, 2019), in which the more frictional large particles advected to the flow front bulge relative to material upstream. Depth-averaged approaches are attractive for the simplicity by which they can illuminate important geophysical phenomena without recourse to a fully coupled theory, but their application is limited to shallow flows, and in non-shallow geometries such as rotating drums or storage silos there is a more complex interaction between the bulk flow properties and the evolving particle distribution than can be captured using the large particle transport equation. To be applicable to such geometries, a general segregation theory for dense flows must incorporate segregation and diffusion rates dependent on the strain-rate, pressure, gravity and other relevant parameters in conjunction with frictional feedback from the mixture composition onto the bulk flow.

### 1.3.3 Rotating drums

Rotating drums are an industrial mechanism widely used for mixing distinct species of solid particles, and have long been the subject of academic investigation (for a review of early literature on rotating drums, see e.g. Cooke *et al.*, 1976). As the drums rotate, particle species tend to segregate out into regions of high concentration, often in direct opposition to the intended and desired result. In some more recent studies (Metcalf *et al.*, 1995; Khakhar *et al.*, 1997; Hill *et al.*, 1999; Khakhar *et al.*, 1999; Gray, 2001; Zuriguel *et al.*, 2006), these large three-dimensional industrial mixers have been replaced by an experimental analogue; a quasi-two-dimensional drum which minimises the importance of axial segregation, with transparent lateral sidewalls through which



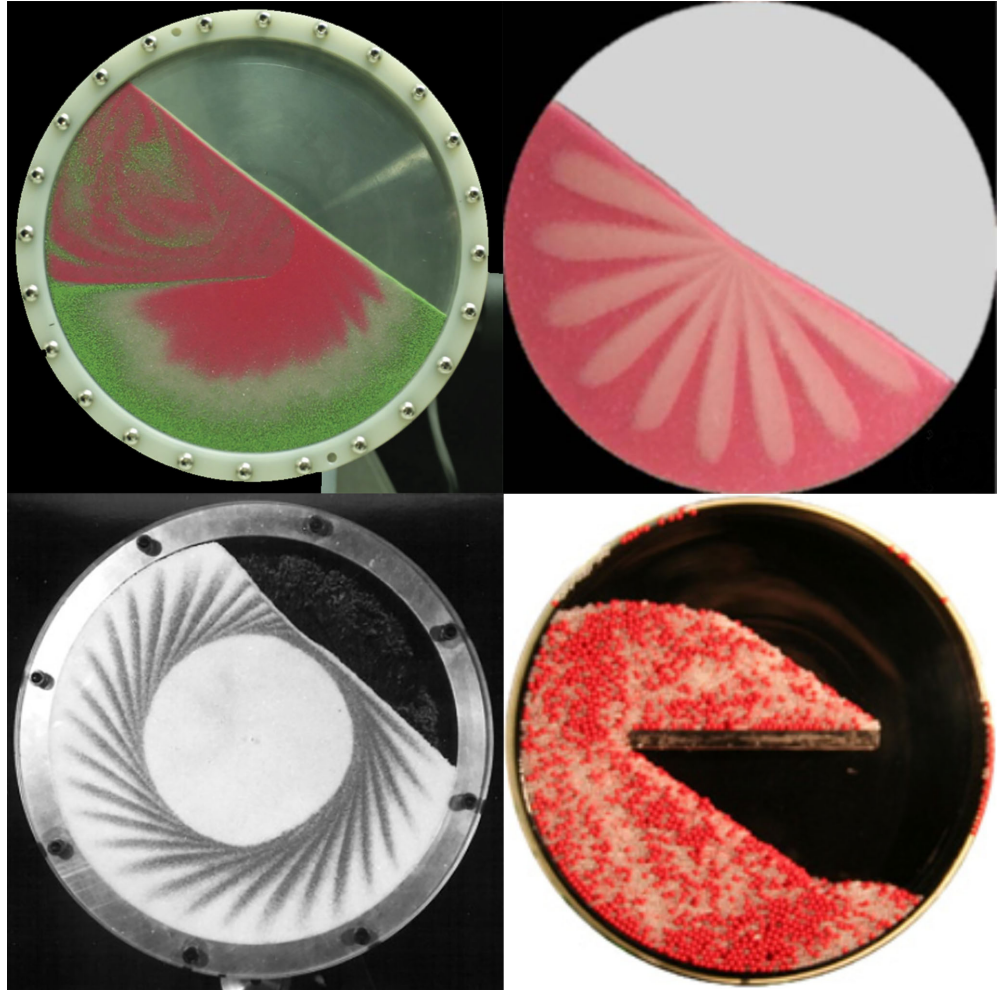


Figure 1.7: Experimental images of different flows in a circular rotating drum. Clock-wise from top left; a continuously avalanching drum flow filled with three particle species (red small, white medium, and green large particles) (Gray & Ancey, 2011), a petal pattern in a half filled drum with small white and large red particles (Zuriguuel *et al.*, 2006), a baffled drum inhibiting segregation between small white and large red particles (McCarthy, 2009), and a Catherine wheel pattern formed by an intermittent avalanche for small black and large white particles (Gray & Hutter, 1997).

emerging particle patterns can be observed. Particle species are typically colour-coded so that the particle-size distribution can be easily tracked, resulting in a stunning variety of patterns, some of which are shown in figure 1.7. The particle pattern formation depends on many variables, such as the particle properties, the fill level of the container, the relative quantity of each particle species, the drum shape and drum rotation speed (see e.g. Rajchenbach, 1990; Hill *et al.*, 1999; Mounty, 2007).

Although many flow regimes are possible (Rajchenbach, 1990), the most commonly

studied and easily produced is the continuously avalanching or rolling regime, characterised by a thin, continuously flowing free-surface avalanche above a substrate of quasi-static material performing solid body rotation, which may assume a steady-state for circular drums. When drums are slightly over half-filled, complex mobility feedback interactions between the particle distribution and bulk flow can produce radial streaks or petals (Hill *et al.*, 1999; Khakhar *et al.*, 2001; Hill *et al.*, 2004; Zuriguel *et al.*, 2006) highly sensitive to the rotation speed. At slower rotation rates, intermittent avalanches form which may result in Catherine wheel patterns (Gray & Hutter, 1997). For non-circular drums, chaotic advection is possible (Khakhar *et al.*, 1999; Ottino & Khakhar, 2000), and such drums have been described as the simplest experimental demonstration of competition between chaotic advection and (segregation-induced) order (Hill *et al.*, 1999).

Despite the complexity of the underlying physical mechanisms governing segregation, various methods have by necessity been developed for its avoidance or minimisation (Tang & Puri, 2004; Schulze, 2008; McCarthy, 2009). Inter-particle cohesion generated by an interstitial fluid can inhibit segregation if the grains are sufficiently saturated (Samadani & Kudrolli, 2000; Li & McCarthy, 2005). Shi *et al.* (2007) demonstrated that insertion of a centrally located baffle into a rotating drum flow can drastically reduce the intensity of segregation by periodically varying the direction of segregation in relation to streamlines. For engineers tasked with devising new methods for segregation reduction, the ability to quantitatively model rotating drum flows is an invaluable tool, and continuum approaches can help characterise flow phenomena according to their underlying physics while providing new insight into the relationship between segregation and the bulk flow dynamics. Additionally, the sensitivity and astonishing diversity of pattern formations and flow behaviours in rotating drums means they are both an attractive research topic and a useful benchmark against which to test and understand granular flow models. Much of the remainder of this thesis is dedicated to establishing a method for fully coupling the bulk flow rheology and a theory for particle-size segregation, in essence unifying the approaches described in these two introductory sections, and then utilising this method to investigate rotating drum flows. A more comprehensive description of the dynamics within rotating drums is left for chapters 2 and, in particular, 3.

## 1.4 The finite volume method in OpenFOAM

The coupling framework developed in this thesis leads to a non-linear set of governing equations which cannot be solved analytically, except in certain highly reduced cases. Numerical solutions are instead calculated using the finite volume method, with a custom multiphase fluid solver implemented in the open source computational fluid dynamics toolbox OpenFOAM. While the precise method used for rheology-segregation coupling is deferred until Chapter 2, details of the general numerical method will be provided here.

### 1.4.1 Discretisation procedure

The finite volume method is based on the integral form of conservation equations. A general advection-diffusion equation for a conservative scalar property  $\psi(\mathbf{x}, t)$  takes the form

$$\underbrace{\frac{\partial \psi}{\partial t}}_{\text{temporal derivative}} + \underbrace{\nabla \cdot (\psi \mathbf{u})}_{\text{advective term}} + \underbrace{\nabla \cdot (D_\psi \nabla \psi)}_{\text{diffusive term}} = \underbrace{S_\psi}_{\text{source term}}. \quad (1.4.1)$$

The spatial domain is discretised by a polygonal mesh of finite volume cells which do not overlap and completely fill the domain. The transport equation (1.4.1) is then expressed in the form of an integral over a finite volume  $V_P$ , corresponding to the volume of the cell  $P$  with geometric centre  $\mathbf{x}_P$ , as

$$\frac{\partial}{\partial t} \int_{V_P} \psi \, dV + \int_{V_P} \nabla \cdot (\psi \mathbf{u}) \, dV + \int_{V_P} \nabla \cdot (D_\psi \nabla \psi) \, dV = \int_{V_P} S_\psi \, dV. \quad (1.4.2)$$

This can then be transformed using the divergence theorem to become

$$\frac{\partial}{\partial t} \int_{V_P} \psi \, dV + \oint_{\partial V_P} \mathbf{n} \cdot (\psi \mathbf{u}) \, dS + \oint_{\partial V_P} \mathbf{n} \cdot (D_\psi \nabla \psi) \, dS = \int_{V_P} S_\psi \, dV, \quad (1.4.3)$$

where  $\partial V_P$  is the closed surface bounding the volume  $V_P$ , and  $dS$  represents an infinitesimal surface element with outward pointing normal  $\mathbf{n}$ . The surface  $\partial V_P$  consists of a finite number of faces  $f$  with geometric centres  $\mathbf{x}_f$  and surface areas  $S_f$ . The geometric centres or centroids  $\mathbf{x}_P$  and  $\mathbf{x}_f$  for the faces  $f$  of a given cell  $P$  are calculated by decomposing each polygonal face into triangles sharing apex points  $A_f$ , defined as the mean of the face vertices. The area  $S_T$  and the centroid  $\mathbf{x}_T$  for each triangle on a particular face can then be calculated from the vertices using known formulae, and

used to give expressions for the face area  $S_f = \sum_{T \in f} S_T$  and the face centroid

$$\mathbf{x}_f = \frac{1}{S_f} \sum_{T \in f} S_T \mathbf{x}_T. \quad (1.4.4)$$

The cell centroid is then calculated using the expression

$$\mathbf{x}_P = \frac{1}{2V_P} \sum_f S_f |\mathbf{x}_f|^2. \quad (1.4.5)$$

Full derivations for the centroid expressions can be found in Greenshields & Weller (2022).

A second order accurate approximation of the property  $\psi$  within the cell  $P$  with assumed linear spatial variation (Jasak, 1996) is given by

$$\psi(\mathbf{x}, t) = \psi_P(t) + (\mathbf{x} - \mathbf{x}_P) \cdot \nabla \psi_P(t), \quad (1.4.6)$$

where  $\psi_P(t) = \psi(\mathbf{x}_P, t)$ , and  $\nabla \psi_P(t)$  is uniform inside the cell since it refers to the gradient at the cell centre only. The volume integral of  $\psi(\mathbf{x}, t)$  over cell  $P$  is then

$$\begin{aligned} \int_{V_P} \psi(\mathbf{x}, t) \, dV &= \int_{V_P} \psi_P(t) + (\mathbf{x} - \mathbf{x}_P) \cdot \nabla \psi_P(t) \, dV \\ &= \psi_P(t) \int_{V_P} dV + \left( \int_{V_P} (\mathbf{x} - \mathbf{x}_P) \, dV \right) \cdot \nabla \psi_P(t) \\ &= \psi_P(t) V_P, \end{aligned} \quad (1.4.7)$$

where the second integral term vanishes since  $\mathbf{x}_P$  is the centre point of the cell. Similarly, closed surface integrals can be expressed as the sum of integrals over faces,

$$\begin{aligned} \oint_{\partial V_P} \psi(\mathbf{x}, t) \, dS &= \sum_f \left[ \int_f \psi_f(t) + (\mathbf{x} - \mathbf{x}_f) \cdot \nabla \psi_f(t) \, dS \right] \\ &= \sum_f \left[ \psi_f(t) \int_f dS + \left( \int_f (\mathbf{x} - \mathbf{x}_f) \, dS \right) \cdot \nabla \psi_f(t) \right] \\ &= \sum_f \psi_f(t) S_f, \end{aligned} \quad (1.4.8)$$

where  $\psi_f(t) = \psi(\mathbf{x}_f, t)$ , which is approximated using a linear interpolation of the values of  $\psi$  on cell centres,

$$\psi_f = \alpha \psi_P + (1 - \alpha) \psi_N, \quad (1.4.9)$$

where  $N$  denotes the neighbouring cell sharing face  $f$  with cell  $P$ . OpenFOAM uses a blended interpolation scheme combining upwind and central differencing, full details of

which can be found in Jasak *et al.* (1999). The interpolation rule (1.4.9) is replaced at boundary faces with an expression reflecting the specified boundary conditions. Note that, since the divergence theorem states that

$$\int_{V_P} \nabla \cdot \mathbf{a} \, dV = \oint_{\partial V_P} \mathbf{n} \cdot \mathbf{a} \, dS, \quad (1.4.10)$$

for some arbitrary vector property  $\mathbf{a}$ , making use of analogous discretisations for volume (1.4.7) and surface integrals (1.4.8) gives a second order discretised form of the divergence theorem:

$$(\nabla \cdot \mathbf{a})V_P = \sum_f (\mathbf{n}_f \cdot \mathbf{a}_f)S_f, \quad (1.4.11)$$

with an analogous expression for an arbitrary scalar property.

The diffusive term in the transport equation (1.4.3) can be discretised using (1.4.8),

$$\oint_{\partial V_P} \mathbf{n} \cdot (D_\psi \nabla \psi) \, dS = \sum_f \mathbf{n}_f \cdot D_{\psi,f} (\nabla \psi)_f S_f, \quad (1.4.12)$$

which, assuming mesh orthogonality, can be simplified using the second order approximation

$$\mathbf{n}_f \cdot (\nabla \psi)_f = \frac{\psi_N - \psi_P}{|\mathbf{x}_N - \mathbf{x}_P|}. \quad (1.4.13)$$

For non-orthogonal meshes, a correction term must be introduced to the approximation (1.4.13) (see e.g. Jasak, 1996). Temporal discretisation is achieved using the implicit Euler method, so that

$$\frac{\partial \psi_P^i}{\partial t} = \frac{\psi_P^i - \psi_P^{i-1}}{\Delta t}, \quad (1.4.14)$$

where the superscript  $i$  denotes evaluation at time  $t^i = t^{i-1} + \Delta t$ . This approximation has first order temporal accuracy. The transport equation (1.4.3) can then be written as

$$\frac{\psi_P^i - \psi_P^{i-1}}{\Delta t} V_P + \sum_f \mathbf{n}_f \cdot \psi_f^i \mathbf{u}_f^i S_f + \sum_f D_{\psi,f} \frac{\psi_N^i - \psi_P^i}{|\mathbf{x}_N - \mathbf{x}_P|} S_f = S_{\psi,P} V_P. \quad (1.4.15)$$

Applying the interpolation rule (1.4.9) gives the implicit, fully discretised system of equations for each cell:

$$\begin{aligned} \frac{\psi_P^i - \psi_P^{i-1}}{\Delta t} V_P + \sum_f \mathbf{n}_f \cdot (\alpha \psi_P^i + (1 - \alpha) \psi_N^i) \mathbf{u}_f^i S_f + \\ \sum_f D_{\psi,f} \frac{\psi_N^i - \psi_P^i}{|\mathbf{x}_N - \mathbf{x}_P|} S_f = S_{\psi,P} V_P. \end{aligned} \quad (1.4.16)$$

This can be expressed as the algebraic equation

$$a_P \psi_P^i + \sum_N a_N \psi_N^i = b_P^i. \quad (1.4.17)$$

An equation of this form is solved for every cell  $P$ . This describes the discretisation process for a simple advection-diffusion equation.

### 1.4.2 Boundary conditions

The two fundamental types of boundary condition used in OpenFOAM are Dirichlet and Neumann, from which other more specialised types are derived. Dirichlet conditions take the form

$$\psi = \psi_b \quad (1.4.18)$$

on a boundary face  $b$ . Discretisation of the advective term gives

$$\int_{V_P} \nabla \cdot (\psi \mathbf{u}) \, dV = \sum_f \mathbf{n}_f \cdot \psi_f \mathbf{u}_f S_f, \quad (1.4.19)$$

and the term for the boundary face is then

$$\mathbf{n}_b \cdot \psi_b \mathbf{u}_b S_b. \quad (1.4.20)$$

For the diffusive term the discretisation is

$$\int_{V_P} \nabla \cdot (D_\psi \nabla \psi) \, dV = \sum_f \mathbf{n}_f \cdot D_{\psi,f} (\nabla \psi)_f S_f. \quad (1.4.21)$$

The face gradient at the boundary is calculated from the given boundary value and the value at the cell centre:

$$\mathbf{n}_b \cdot (\nabla \psi)_b = \frac{\psi_b - \psi_P}{|\mathbf{d}_b|}, \quad (1.4.22)$$

where  $\mathbf{d}_b$  is the vector from the cell centre  $P$  to the boundary face which is normal to the face. For orthogonal boundaries,  $|\mathbf{d}_b| = |\mathbf{x}_b - \mathbf{x}_P|$ .

Neumann conditions are specified on the gradient of the given property at the boundary, expressed as

$$\mathbf{n}_b \cdot (\nabla \psi)_b = g_b, \quad (1.4.23)$$

where  $g_b$  is the prescribed condition. For the advective term, the boundary value  $\psi_b$  is calculated from the value at the cell centre and the prescribed gradient, as

$$\psi_b = \psi_P + |\mathbf{d}_b|g_b. \quad (1.4.24)$$

For the diffusive term the boundary condition can be applied directly,

$$\mathbf{n}_b \cdot (\nabla \psi)_b S_b = g_b S_b. \quad (1.4.25)$$

### 1.4.3 Governing equations

For the geometries of interest in this thesis, as discussed above the mass and momentum balance equations take the form of Navier-Stokes-like equations, which can be expressed in conservative form as

$$\nabla \cdot \mathbf{u} = 0, \quad (1.4.26)$$

$$\frac{\partial}{\partial t}(\rho \mathbf{u}) + \nabla \cdot (\rho \mathbf{u} \otimes \mathbf{u}) = -\nabla p + \nabla \cdot (2\eta \mathbf{D}) + \rho \mathbf{g}. \quad (1.4.27)$$

Additionally, segregation-advection-diffusion equations for an arbitrary number of particle phases with respective concentrations  $\phi^\nu$  must also be solved, taking the form

$$\frac{\partial \phi^\nu}{\partial t} + \nabla \cdot (\phi^\nu \mathbf{u}) + \nabla \cdot \mathbf{F}^\nu = \nabla \cdot \mathbf{D}^\nu. \quad (1.4.28)$$

The transport equation procedure in § 1.4.1 gives the general method for discretisation of the terms in the governing equations (1.4.26)-(1.4.28), using analogous statements of the divergence theorem. The segregation-advection-diffusion equations are solved in OpenFOAM using an implementation of flux corrected transport theory (Zalesak, 1979) known as MULES (Multidimensional Universal Limiter for Explicit Solution) (see Damián, 2013, for the full algorithm), which limits the respective phase fluxes to ensure solutions remain bounded within  $\phi^\nu \in [0, 1]$ , with  $\sum_\nu \phi^\nu = 1$ .

When solving equations (1.4.26) and (1.4.27), particular care must be taken over the discretisation of the non-linear term

$$\nabla \cdot (\rho \mathbf{u} \otimes \mathbf{u}). \quad (1.4.29)$$

Using the discretised divergence theorem (1.4.11) and evaluating at time  $t^i$  gives

$$\nabla \cdot (\rho \mathbf{u} \otimes \mathbf{u}) = \frac{1}{V_P} \sum_f (\mathbf{n}_f \cdot \rho \mathbf{u}_f^i) \mathbf{u}_f^i S_f. \quad (1.4.30)$$

This is linearised using the assumption  $\mathbf{u}_f^i \cong \mathbf{u}_f^{i-1}$ , which holds for small Courant–Friedrichs–Lewy (CFL) numbers (Jasak, 1996), where the CFL number is

$$\text{CFL} = \frac{|\mathbf{u}| \Delta t}{\Delta x} + \frac{\eta \Delta t}{\rho \Delta x^2}. \quad (1.4.31)$$

Adaptive time stepping is used, where the time step  $\Delta t$  is determined by applying a constraint on the magnitude of the CFL number to ensure it remains appropriately small. The equation (1.4.30) can then be linearised:

$$\begin{aligned} \nabla \cdot (\rho \mathbf{u} \otimes \mathbf{u}) &\cong \frac{1}{V_P} \sum_f (\mathbf{n}_f \cdot \rho \mathbf{u}_f^{i-1}) \mathbf{u}_f^i S_f \\ &= a_P \mathbf{u}_P^i + \sum_N a_N \mathbf{u}_N^i, \end{aligned} \quad (1.4.32)$$

where  $\mathbf{u}_f^{i-1}$  is known from the previous time step. The viscous momentum term is similarly linearised by calculating the granular viscosity  $\eta = \mu(I)p/2\|\mathbf{D}\|$  using values for the velocity and pressure from the previous time step.

#### 1.4.4 Derivation of the pressure equation

A semi-discretised form of the momentum equation (1.4.27) can be written in the form

$$a_P \mathbf{u}_P = \mathbf{H}(\mathbf{u}) - \nabla p, \quad (1.4.33)$$

where  $\mathbf{H}(\mathbf{u})$  includes contributions from neighbouring cells and source terms excluding the pressure gradient. The cell centre velocity  $\mathbf{u}_P$  as expressed by (1.4.33) can be interpolated at faces to give

$$\mathbf{u}_f = \left( \frac{\mathbf{H}(\mathbf{u})}{a_P} \right)_f - \left( \frac{1}{a_P} \right)_f (\nabla p)_f, \quad (1.4.34)$$

and discretising the mass balance equation (1.4.26) gives

$$\nabla \cdot \mathbf{u} = \sum_f \mathbf{n}_f \cdot \mathbf{u}_f S_f = 0. \quad (1.4.35)$$

The set of discretised equations deriving from the mass and momentum balance equations (1.4.26) and (1.4.27) is then

$$a_P \mathbf{u}_P = \mathbf{H}(\mathbf{u}) - \sum_f \mathbf{S}(p)_f, \quad (1.4.36)$$

$$\sum_f \mathbf{n}_f \cdot \left( \left( \frac{1}{a_P} \right)_f (\nabla p)_f \right) S_f = \sum_f \mathbf{n}_f \cdot \left( \frac{\mathbf{H}(\mathbf{u})}{a_P} \right)_f S_f, \quad (1.4.37)$$



where  $\mathbf{S}(p)$  is a pressure gradient source term. Momentum conservation is represented by (1.4.36), while the pressure equation (1.4.37) is obtained by substituting the face velocity (1.4.34) into the mass conservation equation (1.4.35). The face flux  $F$  is derived from (1.4.34) to give

$$F = \mathbf{n}_f \cdot \mathbf{u}_f S_f = \mathbf{n}_f \cdot \left[ \left( \frac{\mathbf{H}(\mathbf{u})}{a_P} \right)_f - \left( \frac{1}{a_P} \right)_f (\nabla p)_f \right] S_f. \quad (1.4.38)$$

### 1.4.5 The PISO algorithm

The system (1.4.36) and (1.4.37) is expressed in a form which can be solved in OpenFOAM using the PISO (Pressure-Implicit with Splitting of Operators) algorithm proposed by Issa (1986). The PISO algorithm solves the pressure-velocity coupling expressed by this system using a segregated approach in which the equations are solved in sequence. This operates as follows:

1. The momentum equation (1.4.36) is solved to give an approximation of the velocity field, where the pressure field from the previous time step is used since the pressure gradient source term  $\mathbf{S}(p)$  is not yet known, and the advective term in  $\mathbf{H}(\mathbf{u})$  is linearised as in (1.4.32).
2. The pressure equation (1.4.37) is assembled and solved using the approximated velocity field.
3. The face fluxes are calculated using (1.4.38).
4. The velocity is corrected for the new pressure field using (1.4.33) in the form

$$\mathbf{u}_P = \frac{\mathbf{H}(\mathbf{u})}{a_P} - \frac{\nabla p}{a_P}. \quad (1.4.39)$$

5. Return to step 2; this process is repeated for a pre-specified number of iterations.

This introductory section details the finite volume discretisation and solution technique employed in OpenFOAM and used extensively throughout this thesis. Numerical solutions to the Navier-Stokes-like equations (1.4.26) and (1.4.27) produced below are calculated using the PISO algorithm. While the pressure-velocity coupling is calculated in the PISO loop, other inter-equation couplings, such as rheology-segregation coupling, are lagged, and hence in the coupling framework developed in Chapter 2 the

segregation-advection-diffusion equations (1.4.28) are solved prior to the momentum predictor stage (step 1 in the above description) at each time step.

Numerical errors in the discretisation procedure may be expected to result from discretisation of terms to below second order accuracy, and the discretisation of the solution domain, i.e. mesh generation. In the latter case, the assumed linear variation of a property within a cell  $P$  may diffuse important grid-scale effects. Rotating drum simulations have been computed at different resolutions with the aim of demonstrating grid converging solutions and identifying the appropriate refinement level for minimising error due to insufficient mesh resolution. Error due to sub-second order discretisation may be expected to result from the implicit Euler method (1.4.14), which only gives first order temporal accuracy. Other temporal discretisation methods with second order accuracy, such as the Crank-Nicholson method, are available as built-in features of OpenFOAM, but the first order scheme was preferred because it guarantees boundedness of the solution (Hirsch, 2007). A full treatment of numerical error and its estimation in the finite volume implementation of OpenFOAM is provided by Jasak (1996).

## 1.5 Thesis structure

This thesis is presented in alternative format, meaning that the chapters are presented in the style of journal articles. It is made up of one paper published in *The Journal of Fluid Mechanics* and another in preparation for submission to the same journal. Each paper is a self-contained work, and so there is necessarily some overlap in content between them due to their related topics. They each conform to their own internal section, figure, equation and table numbering with independent bibliographies, but page numbering has been adapted to be consistent over the whole thesis.

The main content of the thesis is divided into two chapters. As alluded to above, chapter 2, *Coupling rheology and segregation in granular flows*, develops a generalised framework for coupling particle-size segregation mechanics to flow rheology and vice versa. A specific theory coupling a strain-rate dependent diffusion coefficient and a segregation theory developed by Trewhela *et al.* (2021) to the partially regularised  $\mu(I)$ -rheology (Barker & Gray, 2017) detailed in §1.2.2 is then described. This results

in a system of governing equations for the bulk velocity, pressure and species concentrations, and it is shown how inclusion of an excess air phase segregating away from the granular material is advantageous for numerical schemes involving interface tracking. The numerical implementation is tested against known exact solutions of concentration shocks, steady-state concentration profiles and the Bagnold velocity profile, and computations of inclined plane flows are also able to predict breaking size-segregation waves, the frontal shape implied by depth-averaged equations, and segregation mobility feedback resulting in the formation of a large particle-rich bulbous head. The coupled model also shows good agreement with the DEM data of Tripathi & Khakhar (2011). Finally, a fully coupled numerical simulation of a square rotating drum is computed to demonstrate the possibilities of the model. The results are impressive and qualitatively similar to those observed in experiments, but the lack of lateral sidewall friction in the theory imposes a limitation on quantitative comparison to experiments.

Chapter 3, *Particle-size segregation in triangular rotating drums with sidewall friction*, uses the coupling method described in the previous chapter to investigate triangular drum flows, with a full experimental comparison. Friction from confining lateral sidewalls is incorporated into the model by integrating three-dimensional mass and momentum balance equations through the width with Coulomb slip boundary conditions applied at the sidewalls, resulting in an additional term in the two-dimensional momentum balance equation modelling sidewall friction. An adapted segregation scaling law suggested by Trehwela *et al.* (2021) is used which reproduces the result that segregation intensity in rotating drums is maximal near particle-size ratios of  $R = 2$ . The extended numerical model is tested against an analytic solution for a shear cell with sidewall friction, providing a very precise match.

Experiments are then performed for triangular rotating drums containing bidisperse mixtures with various fill levels and mean small particle concentrations. Equivalent numerical simulations for each case are then computed, with no fitting parameters, and an excellent congruence between all the features of the experiments and simulations is demonstrated across the entire timescale of segregation. This is only possible due to the inclusion of lateral sidewall friction in the numerical model, which produces a thin, rapidly flowing free-surface avalanche where the segregation is very intense. All the particle redistribution occurs in this avalanching region, which acts as a thin

boundary-layer and can only be fully resolved using a fine numerical mesh. A method of quantitative analysis is devised, using pixel intensity data from experimental images of drums with known mean particle concentration to project a particle-size distribution onto the images of more complex pattern evolutions. This data is then used to calculate an intensity of segregation, which matches closely with the intensity of segregation in the simulations. Finally, a tridisperse rotating drum flow is computed, giving a good qualitative match to experiments and revealing a mechanism by which the intermediate particle species is simultaneously segregated in opposing directions by the small and large species.

## Chapter 2

# Coupling rheology and segregation in granular flows

This chapter is a reproduction of the journal article “Coupling rheology and segregation in granular flows”, which was published in volume 909, A22 of the *Journal of Fluid Mechanics* (2021). The digital object identifier (DOI) for this article is: <https://doi.org/10.1017/jfm.2020.973>. The supplementary material for the article is also available from this address. Permission for reproduction was granted from Cambridge University Press.

# Coupling rheology and segregation in granular flows

**T. Barker<sup>1,2</sup>, M. Rauter<sup>3,4</sup>, E.S.F. Maguire<sup>1</sup>, C.G. Johnson<sup>1</sup> & J.M.N.T. Gray<sup>1</sup>**

<sup>1</sup>Department of Mathematics and Manchester Centre for Nonlinear Dynamics,  
University of Manchester, Oxford Road, Manchester, M13 9PL, UK

<sup>2</sup>School of GeoSciences and Institute for Infrastructure and Environment, University of  
Edinburgh, King's Buildings, Edinburgh, EH9 3JL, UK

<sup>3</sup>Department of Natural Hazards, Norwegian Geotechnical Institute, Oslo, N-0806,  
Norway

<sup>4</sup>Department of Mathematics, University of Oslo, Oslo, N-0851, Norway

(Received 6 March 2020; revised 19 October 2020; accepted 2 November 2020)

During the last fifteen years there has been a paradigm shift in the continuum modelling of granular materials; most notably with the development of rheological models, such as the  $\mu(I)$ -rheology, but also with significant advances in theories for particle segregation. This paper details theoretical and numerical frameworks (based on OpenFOAM<sup>®</sup>) which unify these currently disconnected endeavours. Coupling the segregation with the flow, and vice-versa, is not only vital for a complete theory of granular materials, but is also beneficial for developing numerical methods to handle evolving free-surfaces. This general approach is based on the partially-regularised incompressible  $\mu(I)$ -rheology, which is coupled to the gravity-driven segregation theory of Gray & Ancey (*J. Fluid Mech.*, vol. 678, 2011, 353–588). These advection-diffusion-segregation equations describe the evolving concentrations of the constituents, which then couple back to the variable viscosity in the incompressible Navier-Stokes equations. A novel feature of this approach is that any number of differently sized phases may be included, which may have disparate frictional properties. Further inclusion of an excess air phase, which segregates away from the granular material, then allows the complex evolution of the free-surface to be captured simultaneously. Three primary coupling mechanisms are identified; (i) advection of the particle concentrations by the

bulk velocity, (ii) feedback of the particle-size and/or frictional properties on the bulk flow field and (iii) influence of the shear rate, pressure, gravity, particle size and particle-size ratio on the locally evolving segregation and diffusion rates. The numerical method is extensively tested in one-way coupled computations, before the fully coupled model is compared to the DEM simulations of Tripathi & Khakhar (*Phys. Fluids*, vol. 23, 2011, 113302) and used to compute the petal-like segregation pattern that spontaneously develops in a square rotating drum.

## 1. Introduction

Despite nearly all natural and man-made granular materials being composed of grains of varying size, shape and frictional properties, the majority of continuum flow modelling has largely been restricted to perfectly monodisperse aggregates. The purpose of this work is therefore to extend the current granular flow models by introducing multiple phases, with different properties, and to model inter-phase segregation. Coupling the flow rheology to the local constituent concentrations is important because the mobility of a granular flow is strongly affected by the local frictional properties of the grains. In turn, the bulk flow controls the strength and direction of the segregation as well as the advection of the granular phases.

Striking examples of segregation induced feedback on the bulk flow are found during levee formation (Iverson & Vallance 2001; Johnson *et al.* 2012; Kokeelaar *et al.* 2014) and fingering instabilities (Pouliquen, Delour & Savage 1997; Pouliquen & Vallance 1999; Woodhouse *et al.* 2012; Baker, Johnson & Gray 2016*b*), which commonly occur during the run-out of pyroclastic density currents, debris flows and snow avalanches. Many other examples of segregation-flow coupling occur in industrial settings (Williams 1968; Makse *et al.* 1997; Gray & Hutter 1997; Hill, Khakhar, Gilchrist, McCarthy & Ottino 1999; Ottino & Khakhar 2000; Zuriguel *et al.* 2006). Storage silo filling and emptying, stirring mixers and rotating tumblers all have the common features of cyclic deformation and an ambition of generating well mixed material. However, experiments consistently suggest that these processes have a tendency to promote local segregation, which can feedback on the bulk flow velocities. Considering the inherent destructive potential of geophysical phenomena and the implications of poor efficiency in

industrial mixing, a continuum theory which captures the important physics of flow and of segregation simultaneously is therefore highly desirable.

To date, the leading approaches for solving coupled flow and segregation have come from either discrete particle simulations (Tripathi & Khakhar 2011; Thornton *et al.* 2012) or from depth-averaged equations (Woodhouse *et al.* 2012; Baker *et al.* 2016*b*; Viroulet *et al.* 2018). Particle simulations, using the discrete element method (DEM), provide important rheological information as evolving velocities, stresses and constituent concentrations can be directly computed given only minimal approximations. Such results can then be used to motivate models for the bulk flow (GDR MiDi 2004; Jop, Forterre & Pouliquen 2006; Singh *et al.* 2015) and also to form connections between flow and segregation processes (Hill & Fan 2008; Staron & Phillips 2015). Unfortunately, the discrete particle approach is naturally limited by computational expense as many flows of interest include such a large number of particles that direct DEM calculations are unfeasible. Recently efforts have been made to overcome this limitation with the development of hybrid schemes (e.g. Yue *et al.* 2018; Xiao *et al.* 2019) which couple discrete particle dynamics to continuum solvers, but these approaches naturally invoke additional complexity and new assumptions are required in order to map properly and consistently between the somewhat disparate approaches.

Depth-averaged models, which reduce the full three-dimensional flow to two dimensions by integrating through the depth and assuming shallowness, lead to efficient numerical codes which are widely used in geophysical modelling (see e.g. Grigorian, Eglit & Iakimov 1967; Savage & Hutter 1989; Iverson 1997; Gray, Wieland & Hutter 1999; Pouliquen & Forterre 2002; Sheridan *et al.* 2005; Mangeney *et al.* 2007; Christen, Kowalski & Bartelt 2010; Gray & Edwards 2014; Delannay *et al.* 2017; Rauter & Tuković 2018; Rocha *et al.* 2019). However, depth-averaged approaches are limited to geometries in which there is a clear dimension that remains shallow throughout the dynamics. This approximation holds well for thin flows on inclined planes and for flows over certain gradually varying terrain, but breaks down in many flows of practical interest, such as those in hoppers, silos and rotating drums.

Historical attempts to construct three-dimensional continuum models for monodisperse granular materials focused on quasi-static deformations and lead to



elasto-plastic formulations of models such as the Drucker-Prager yield condition (Lubliner 2008) and Critical State Soil Mechanics (Schofield & Wroth 1968). Despite successes in modelling the point of failure of materials under load, calculations of the subsequent time-dependent flow proved to be problematic, because the results are grid mesh-size dependent. Schaeffer (1987) showed that this was because the underlying equations are mathematically ill-posed, i.e. in the small wavelength limit the growth rate of linear instabilities becomes unbounded in certain directions.

Despite the Mohr-Coulomb/Drucker-Prager plasticity theory being designed for the flow of monodisperse grains, the grain diameter  $d$  does not appear in the constitutive model. It can be incorporated by making the friction  $\mu$  a function of the non-dimensional inertial number, which is defined as

$$I = \frac{d\dot{\gamma}}{\sqrt{p/\rho_*}}, \quad (1.1)$$

where  $\dot{\gamma}$  is the shear rate,  $p$  is the pressure and  $\rho_*$  is the intrinsic grain density (Savage 1984; Ancey, Coussot & Evesque 1999; GDR MiDi 2004). Jop *et al.* (2006) generalized the scalar  $\mu(I)$ -rheology to tensorial form. The resultant incompressible  $\mu(I)$ -rheology leads to a significantly better posed system of equations (Barker *et al.* 2015). For the  $\mu(I)$  curve suggested by Jop, Forterre & Pouliquen (2005), the equations are well-posed for a large range of intermediate values of  $I$  and are only ill-posed for very low or relatively high inertial numbers.

Barker & Gray (2017) derived a new functional form for the  $\mu(I)$  relation, which is known as the partially regularised  $\mu(I)$ -rheology. This ensures well-posedness for  $0 < I < I_{\max}$ , where  $I_{\max}$  is a very large value, and leads to stable and reliable numerical schemes. It also provides a better fit to experimental (Holyoake & McElwaine 2012; Barker & Gray 2017) and DEM data (Kamrin & Koval 2012) than the original  $\mu(I)$  curve, but also introduces a creep state (i.e.  $\mu = 0$  when  $I = 0$ ) so the granular material no longer has a yield stress. It is possible to formulate well-posed models with a yield stress by introducing bulk compressibility (Barker, Schaeffer, Shearer & Gray 2017; Schaeffer *et al.* 2019) or non-locality (Henann & Kamrin 2013). However, in this paper the partially regularised  $\mu(I)$ -rheology

is chosen for the bulk flow, both for simplicity and because it is most readily compatible with existing numerical methods and particle segregation models.

Initially well mixed granular materials have a strong propensity of ordering spatially when they undergo flow. Chief among these effects is that of particle size segregation, made famous through the moniker “the Brazil nut effect” (Rosato, Strandburg, Prinz & Swendsen 1987), whereby particles move relative to the bulk flow based on their size compared to their neighbours. The resultant vertical distribution, in which larger particles are often concentrated at the surface of a flow, can also be observed in many geophysical mass flows, forming so-called inversely graded deposits (e.g. Middleton 1970; Festa *et al.* 2015). The origin of this effect was explained through statistical entropic arguments by Savage & Lun (1988) who proposed a means of “kinetic sieving” (Middleton 1970) in which smaller grains are more likely to fall (by gravity) into voids that are created as layers of particles are sheared over one another. Force imbalances then drive particles out of the denser layer, which is known as “squeeze expulsion”. The combination of kinetic sieving and squeeze expulsion produces a net upward motion of large particles as the smaller grains percolate downwards. These concepts formed the basis of the theory of Gray & Thornton (2005) who focused on this form of gravity driven segregation in granular free-surface flows. The theory was later extended by Gray & Chugunov (2006), in order to account for diffusive mixing, and has been successfully applied to a range of gravity-driven flows (Gray 2018). However, Fan & Hill (2011) found that the direction of segregation was not always aligned with the vector of gravitational acceleration. Instead gradients in kinetic stress were found to drive and orient segregation in a range of geometries (Hill & Tan 2014). These findings have since inspired many investigations into the micromechanical origin of size segregation (Staron & Phillips 2015; Guillard, Forterre & Pouliquen 2016; van der Vaart *et al.* 2018), but a unified and compelling theory is still lacking.

In order to accommodate different models for size segregation and different flow rheologies, this paper first introduces a very general framework for multi-component flows in §2. In particular, the multicomponent segregation theory of Gray & Ancey (2011) is generalized to allow submixtures to segregate in different directions and with differing diffusion rates. In §3 the three primary coupling

mechanisms are discussed in detail. §4 documents the general numerical method, which is then extensively tested against the one-way coupled simulations in §5. Two-way fully coupled simulations are then presented for flow down an inclined plane, in §6, and in §7 simulations are performed for a square rotating drum. The new experimental segregation law of Trehwela, Ancy & Gray (2021) is tested against the steady-state DEM solutions of Tripathi & Khakhar (2011) in §6.3 and then used in §7 for the rotating drum simulations, which are able to spontaneously generate petal-like patterns that have previously been seen in the experiments of Hill *et al.* (1999), Ottino & Khakhar (2000) and Mounty (2007).

## 2. Governing equations

### 2.1. The partially regularized $\mu(I)$ -rheology for the bulk flow

The granular material is assumed to be composed of a mixture of particles that may differ in size, shape and surface properties, but have the same intrinsic particle density  $\rho_*$ . If the solids volume fraction  $\Phi$  is constant, which is a reasonable first approximation (GDR MiDi 2004; Tripathi & Khakhar 2011; Thornton *et al.* 2012), then the bulk density  $\rho = \Phi\rho_*$  is constant and uniform throughout the material. Mass balance then implies that the bulk velocity field  $\mathbf{u}$  is incompressible

$$\nabla \cdot \mathbf{u} = 0. \quad (2.1)$$

where  $\nabla$  is the gradient and  $\cdot$  is the dot product. The momentum balance is

$$\rho \left( \frac{\partial \mathbf{u}}{\partial t} + \mathbf{u} \cdot \nabla \mathbf{u} \right) = -\nabla p + \nabla \cdot (2\eta \mathbf{D}) + \rho \mathbf{g}, \quad (2.2)$$

where  $p$  is the pressure,  $\eta$  is the viscosity,  $\mathbf{D} = \frac{1}{2} (\nabla \mathbf{u} + (\nabla \mathbf{u})^T)$  is the strain-rate tensor and  $\mathbf{g}$  is the gravitational acceleration. Assuming alignment of the shear-stress and strain-rate tensors the  $\mu(I)$ -rheology (Jop *et al.* 2006) implies that the granular viscosity is

$$\eta = \frac{\mu(I)p}{2||\mathbf{D}||}, \quad (2.3)$$

where the second invariant of the strain-rate tensor is defined as

$$||\mathbf{D}|| = \sqrt{\frac{1}{2} \text{tr}(\mathbf{D}^2)}, \quad (2.4)$$

---

$\mu_s = 0.342,$	$\mu_d = 0.557,$	$\mu_\infty = 0.05,$	$I_0 = 0.069,$
$\alpha = 1.9,$	$I_1 = 0.004,$	$d = 0.5 \times 10^{-3} \text{ m},$	$\rho_* = 2500 \text{ kg/m}^3$
$\Phi = 0.6$	$\varrho_*^a = 1 \text{ kg/m}^3$	$\eta_*^a = 10^{-3} \text{ kg/(ms)}$	

---

TABLE 1. The frictional parameters  $\mu_s$ ,  $\mu_d$ ,  $\mu_\infty$ ,  $I_0$  and  $\alpha$  in Barker & Gray’s (2017) friction law, which were measured for 143 micron glass beads. The value  $I_1 \simeq I_1^N$  is set by the lower bound for well posedness in Jop *et al.*’s (2006) friction law using the parameters above. Unless stated otherwise, the remaining parameters are the values chosen in the numerical simulations. Note that the air viscosity is higher than the physical value of  $\eta_*^a = 1.81 \times 10^{-5} \text{ kg/(ms)}$  to prevent the convective Courant number limiting the time-step size.

---

and the inertial number, defined in (1.1), in this notation becomes

$$I = \frac{2d\|\mathbf{D}\|}{\sqrt{p/\rho_*}}. \quad (2.5)$$

The meaning of the particle size  $d$  in a polydisperse mixture will be clarified in §3.2. Note that this paper is restricted to two-dimensional deformations with an isotropic Drucker-Prager yield surface. However, as shown by Rauter, Barker & Fellin (2020), this framework can be extended to include three-dimensional deformations through further modification of the granular viscosity i.e. dependence on  $\det(\mathbf{D})$ .

The viscosity (2.3) is a highly non-linear function of the inertial number dependent friction  $\mu = \mu(I)$ , pressure  $p$  and the second invariant of the strain-rate  $\|\mathbf{D}\|$ . Barker *et al.* (2015) examined the linear instability of the system, to show that the growth rate becomes unbounded in the high wavenumber limit, and hence the incompressible  $\mu(I)$ -rheology is mathematically ill-posed, when the inequality

$$4 \left( \frac{I\mu'}{\mu} \right)^2 - 4 \left( \frac{I\mu'}{\mu} \right) + \mu^2 \left( 1 - \frac{I\mu'}{2\mu} \right) > 0, \quad (2.6)$$

is satisfied, where  $\mu' = \partial\mu/\partial I$ . Ill-posedness of this type is not only unphysical, but results in two-dimensional time-dependent numerical computations that do not converge with mesh refinement (see e.g. Barker *et al.* 2015; Martin, Ionescu, Mangeney, Bouchut & Farin 2017; Barker & Gray 2017). If the friction is not inertial number dependent ( $\mu = \text{const}$ ) the ill-posedness condition (2.6) is satisfied for all inertial numbers and the system of equations is always ill-posed (Schaeffer 1987). The equations are also ill-posed if the friction  $\mu$  is a decreasing function of  $I$ , since all the terms in (2.6) are strictly positive.

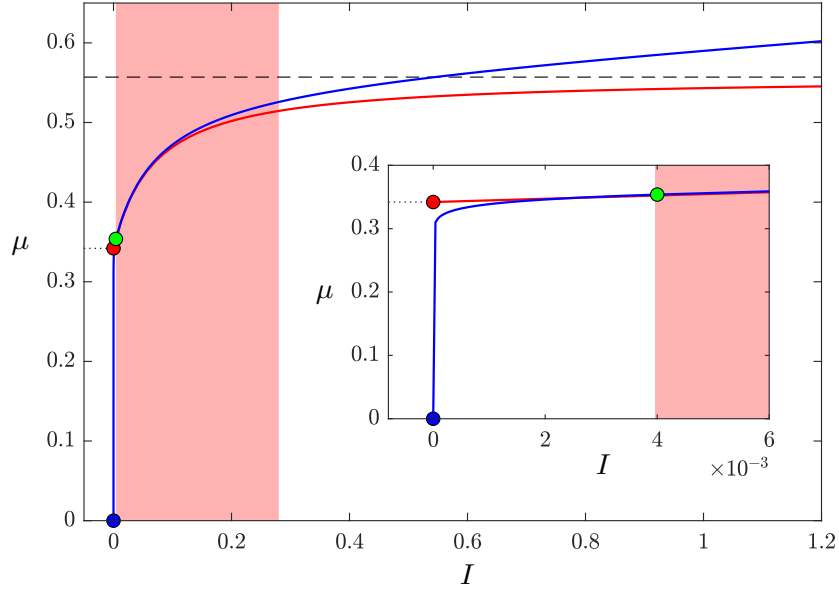


FIGURE 1. Comparison between the friction law of Jop *et al.* (2006) (red line) and the partially regularized law of Barker & Gray (2017) (blue line). The Jop *et al.* (2006) curve has a finite yield stress  $\mu_s$  (red dot) and asymptotes to  $\mu_d$  at large inertial number (dashed line). For the parameters summarized in table 1, it is well-posed in the range  $[I_1^N, I_2^N] = [0.00397, 0.28016]$  (red shaded region). A necessary condition for well posedness is that the friction  $\mu$  is zero at  $I = 0$  (blue dot). Barker & Gray's (2017) curve therefore introduces a creep state for  $I \in [0, I_1]$  to the left of the green dot (see inset) and becomes linear at large inertial numbers. The value of  $I_1 = 0.004$  is chosen to be very slightly larger than  $I_1^N$ . The resulting partially regularized law is well-posed for  $I \in [0, 16.9918]$ .

The original form of the  $\mu(I)$ -curve proposed by Jop *et al.* (2005) is a monotonically increasing function of  $I$  starting at  $\mu_s$  at  $I = 0$  and asymptoting to  $\mu_d$  at large  $I$ ,

$$\mu(I) = \frac{\mu_s I_0 + \mu_d I}{I_0 + I}, \quad (2.7)$$

where  $I_0$  is a material specific constant. The inertial number dependence in (2.7) gives the rheology considerably better properties than the original, constant friction coefficient, Mohr-Coulomb/Drucker-Prager theory. Provided  $\mu_d - \mu_s$  is large enough, the system is well-posed when the inertial number lies in a large intermediate range of inertial numbers  $I \in [I_1^N, I_2^N]$ . The equations are, however, ill-posed if either the inertial number is too low  $I < I_1^N$  or too high  $I > I_2^N$ , or if  $\mu_d - \mu_s$  is not large enough. For the parameter values given in table 1 the  $\mu(I)$  rheology is well posed for  $I \in [0.00397, 0.28016]$ .

The range of well-posedness was extended by Barker & Gray (2017) to  $0 \leq I \leq I_{\max}$ , where  $I_{\max}$  is a large maximal value, by changing the shape of the

$\mu(I)$ -curve. This paper uses the  $\mu(I)$ -curve proposed by Barker & Gray (2017)

$$\mu = \begin{cases} \sqrt{\frac{\alpha}{\log\left(\frac{A}{I}\right)}}, & \text{for } I \leq I_1, \\ \frac{\mu_s I_0 + \mu_d I + \mu_\infty I^2}{I_0 + I}, & \text{for } I > I_1, \end{cases} \quad (2.8)$$

where  $\alpha$  and  $\mu_\infty$  are new material constants and

$$A = I_1 \exp\left(\frac{\alpha(I_0 + I_1)^2}{(\mu_s I_0 + \mu_d I_1 + \mu_\infty I_1^2)^2}\right), \quad (2.9)$$

is chosen to ensure continuity between the two branches at  $I = I_1$ . As shown in figure 1 this curve stays close to (2.7) in the well-posed region of parameter space, but passes through  $\mu = 0$  at  $I = 0$  and is asymptotically linear in  $I$  at large inertial numbers. For the parameters given in table 1, the matching occurs at  $I_1 = 0.004$  (which is very slightly larger than  $I_1^N$ ) and the maximum well-posed inertial number is  $I_{\max} = 16.9918$ .

The partially regularised  $\mu(I)$ -rheology not only ensures well-posedness for  $I < I_{\max}$ , but it also provides better fitting to experimental and DEM results. For instance, relative to (2.7) the new  $\mu(I)$ -curve (2.8) predicts higher viscosities for large values of  $I$ , as seen in the chute flow experiments of Holyoake & McElwaine (2012) and Barker & Gray (2017). For low values of  $I$ , the partially regularised  $\mu(I)$ -rheology predicts very slow creeping flow, since  $\mu \rightarrow 0$  as  $I \rightarrow 0$ . This behaviour is seen, to a certain extent, in DEM simulations (Kamrin & Koval 2012; Singh *et al.* 2015) and has been postulated by Jerolmack & Daniels (2019) to play an important role in soil creep. The lack of a yield stress may, however, be viewed as a disadvantage of the theory. It is important to note that by allowing some bulk compressibility, it is possible to formulate granular rheologies that are always well-posed mathematically (Barker *et al.* 2017; Heyman *et al.* 2017; Goddard & Lee 2018; Schaeffer *et al.* 2019) and support a yield stress.

## 2.2. Generalized polydisperse segregation theory

The granular material is assumed to be composed of a finite number of grain size classes, or species  $\nu$ , which have different sizes  $d^\nu$ , but all have the same intrinsic density  $\rho_*^\nu = \rho_*$ . Note that the inclusion of density differences between the particles implies that the bulk velocity field is compressible, which significantly

complicates the theory (Tripathi & Khakhar 2013; Gray & Ancey 2015; Gilberg & Steiner 2020) and is therefore neglected. Even for a bidisperse mixture of particles of the same density, the grains can pack slightly denser in a mixed state than in a segregated one (Golick & Daniels 2009). However, the DEM simulations (Tripathi & Khakhar 2011; Thornton *et al.* 2012) suggest these packing effects are small, and for simplicity, and compatibility with the incompressible  $\mu(I)$ -rheology, these solids volume fraction changes are neglected. Each grain-size class is therefore assumed to occupy a volume fraction  $\phi^\nu \in [0, 1]$  per unit granular volume, and the sum over all grain sizes therefore equals unity

$$\sum_{\forall \nu} \phi^\nu = 1. \quad (2.10)$$

Many models to describe particle segregation have been proposed (see e.g. Bridgwater, Foo & Stephens 1985; Savage & Lun 1988; Dolgunin & Ukolov 1995; Khakhar, Orpe & Hajra 2003; Gray & Thornton 2005; Gray & Chugunov 2006; Fan & Hill 2011; Gray & Ancey 2011; Schlick, Fan, Umbanhowar, Ottino & Lueptow 2015) and these all have the general form of an advection-segregation-diffusion equation

$$\frac{\partial \phi^\nu}{\partial t} + \nabla \cdot (\phi^\nu \mathbf{u}) + \nabla \cdot \mathbf{F}^\nu = \nabla \cdot \mathbf{D}^\nu, \quad (2.11)$$

where  $\mathbf{F}^\nu$  is the segregation flux and  $\mathbf{D}^\nu$  is the diffusive flux. Provided that these fluxes are independent, this formulation is compatible with the bulk incompressibility provided

$$\sum_{\forall \nu} \mathbf{F}^\nu = 0, \quad \text{and} \quad \sum_{\forall \nu} \mathbf{D}^\nu = 0. \quad (2.12)$$

The form of the segregation flux is motivated by early bidisperse models (Bridgwater *et al.* 1985; Dolgunin & Ukolov 1995; Gray & Thornton 2005). These all had the property that the segregation shut off when the volume fraction of either species reached zero. This is satisfied if the segregation flux for species  $\nu$  and  $\lambda$  is proportional to  $\phi^\nu \phi^\lambda$ . In polydisperse systems, Gray & Ancey (2011) proposed that the segregation flux for species  $\nu$  was simply the sum of the bidisperse segregation fluxes with all the remaining constituents  $\lambda$ . This paper proposes a significant generalization of this concept, by allowing the local direction of segregation to be different for each bidisperse sub-mixture, so that the segregation

flux takes the general polydisperse form

$$\mathbf{F}^\nu = \sum_{\forall \lambda \neq \nu} f_{\nu\lambda} \phi^\nu \phi^\lambda \mathbf{e}_{\nu\lambda}, \quad (2.13)$$

where  $f_{\nu\lambda}$  is the segregation velocity magnitude and  $\mathbf{e}_{\nu\lambda}$  is the unit vector in the direction of segregation, for species  $\nu$  relative to species  $\lambda$ . This segregation flux function satisfies the summation constraint (2.12) provided

$$f_{\nu\lambda} = f_{\lambda\nu}, \quad \text{and} \quad \mathbf{e}_{\nu\lambda} = -\mathbf{e}_{\lambda\nu}. \quad (2.14)$$

In contrast to the theory of Gray & Ancy (2011) the segregation velocity magnitude is the same for species  $\nu$  with species  $\lambda$  and species  $\lambda$  with species  $\nu$ , and it is instead the direction of segregation that now points in the opposite sense. This approach has the property that individual sub-mixtures may segregate in different directions, which allows the theory to be applied to polydisperse problems where gravity driven segregation (e.g. Gray 2018) competes against segregation driven by gradients in kinetic stress (Fan & Hill 2011). This would require the constituent vector momentum balance to be solved in order to determine the resultant magnitude and direction of segregation (Hill & Tan 2014; Tunuguntla, Weinhart & Thornton 2017). In this paper the inter-particle segregation is always assumed to align with gravity. However, the direction of segregation for the particles and air can be chosen to be different. This proves to be advantageous in the numerical method that will be developed to solve the coupled system of equations in §4.

It is also very useful in the numerical method to allow the rate of diffusion between the various sub-mixtures to be different. By direct analogy with the Maxwell–Stefan equations (Maxwell 1867) for multi-component gas diffusion, the diffusive flux vector is therefore assumed to take the form

$$\mathcal{D}^\nu = \sum_{\forall \lambda \neq \nu} \mathcal{D}_{\nu\lambda} (\phi^\lambda \nabla \phi^\nu - \phi^\nu \nabla \phi^\lambda), \quad (2.15)$$

where  $\mathcal{D}_{\nu\lambda}$  is the diffusion coefficient of species  $\nu$  with species  $\lambda$ . Equation (2.15) satisfies the summation constraint (2.12), provided  $\mathcal{D}_{\nu\lambda} = \mathcal{D}_{\lambda\nu}$ , and reduces to the usual Fickian diffusion for the case of bidisperse mixtures (see e.g. Gray & Chugunov 2006). For a mixture of  $n$  distinct species, it is necessary to solve  $n - 1$



separate equations of the form (2.11) together with the summation constraint (2.10) for the  $n$  concentrations  $\phi^\nu$ , assuming that the bulk velocity field  $\mathbf{u}$  is given.

In the absence of diffusion, concentration shocks form naturally in the system (see e.g. Gray & Thornton 2005; Thornton, Gray & Hogg 2006; Gray & Ancey 2011). The jumps in concentration across such boundaries can be determined using jump conditions that are derived from the conservation law (2.11) (see e.g. Chadwick 1976). These jump conditions are also useful when formulating boundary conditions with diffusion. The most general form of the jump condition for species  $\nu$  is

$$\llbracket \phi^\nu (\mathbf{u} \cdot \mathbf{n} - v_n) \rrbracket + \left\llbracket \sum_{\forall \lambda \neq \nu} f_{\nu\lambda} \phi^\nu \phi^\lambda \mathbf{e}_{\nu\lambda} \cdot \mathbf{n} \right\llbracket = \left\llbracket \sum_{\forall \lambda \neq \nu} \mathcal{D}_{\nu\lambda} (\phi^\lambda \nabla \phi^\nu - \phi^\nu \nabla \phi^\lambda) \cdot \mathbf{n} \right\llbracket, \quad (2.16)$$

where  $\mathbf{n}$  is the normal to the shock,  $v_n$  is the normal speed of the shock and the jump bracket  $\llbracket \cdot \rrbracket$  is the difference of the enclosed quantity on the forward and rearward sides of the shock. In particular, if the flow is moving parallel to a solid stationary wall, then the jump condition reduces to the one-sided boundary condition

$$\sum_{\forall \lambda \neq \nu} f_{\nu\lambda} \phi^\nu \phi^\lambda \mathbf{e}_{\nu\lambda} \cdot \mathbf{n} = \sum_{\forall \lambda \neq \nu} \mathcal{D}_{\nu\lambda} (\phi^\lambda \nabla \phi^\nu - \phi^\nu \nabla \phi^\lambda) \cdot \mathbf{n}. \quad (2.17)$$

This implies that the segregation and diffusive fluxes balance and that there is no mass lost or gained through the wall.

### 2.3. Reduction to the bidisperse case

For the case of a mixture of large and small particles, which will be referred to by the constituent letters  $\nu = s, l$  respectively, the summation constraint (2.10) becomes

$$\phi^s + \phi^l = 1. \quad (2.18)$$

Assuming that the gravitational acceleration vector  $\mathbf{g}$  points downwards and that the segregation aligns with this direction, the concentration equation (2.11) for

small particles reduces to

$$\frac{\partial \phi^s}{\partial t} + \nabla \cdot (\phi^s \mathbf{u}) + \nabla \cdot \left( f_{sl} \phi^s \phi^l \frac{\mathbf{g}}{|\mathbf{g}|} \right) = \nabla \cdot (\mathcal{D}_{sl} \nabla \phi^s). \quad (2.19)$$

where  $f_{sl}$  is the segregation velocity magnitude and  $\mathcal{D}_{sl}$  is the diffusivity of the small and large particles. The functional dependence of these quantities on the shear rate, pressure, gravity, particle size and the particle-size ratio, will be discussed in detail in §3.3.

### 3. Coupling the bulk flow with the segregation

One of the key advances of this paper is to develop a coupled framework that solves for the bulk velocity field  $\mathbf{u}$ , the pressure  $p$  and the particle concentrations  $\phi^v$  at the same time. This framework allows us to explore some of the intimate couplings between the segregation and the bulk flow. A variety of couplings are envisaged, that may act singly or all at once, to generate very complex behaviour. The models fall into two classes: (i) one-way coupled and (ii) two-way coupled, and both forms of coupling are investigated in this paper.

#### 3.1. *Advection by the bulk flow field*

Many important practical segregation problems involve a time dependent spatially evolving bulk flow that can not easily be prescribed or determined from DEM simulations. Since the particle concentrations are advected by the bulk velocity  $\mathbf{u}$ , the most basic one-way coupling involves the solution of the mass (2.1) and momentum (2.2) balances to determine this velocity field. This enables the segregation equation (2.11) to be solved within a physically relevant flow field, provided the segregation velocity magnitudes and diffusivities are prescribed. Computations of this nature may give a good indication of where differently sized particles are transported, in a flow field that does not experience strong frictional feedback from the evolving species concentrations. This simplification implicitly assumes that an essentially monodisperse flow field provides a reasonable approximation for the dynamics of a much more complex polydisperse mixture of particles, and that there is no feedback of this local flow field on the segregation and diffusion rates. This simple coupling is investigated in §5 for a time-dependent spatially evolving flow down an inclined plane. Importantly, this simple one-way

coupling also enables the accuracy of the numerical method to be tested against known exact travelling wave and steady-state solutions for the bulk flow field and the particle concentrations. In general, the particle concentrations are always transported by the bulk flow field, so this mechanism is also active in models with more complex couplings, which will be investigated in §6 and §7.

### 3.2. Segregation induced frictional feedback on the bulk flow

Each distinct granular phase may have differing particle size, shapes or surface properties, that lead to different macroscopic friction and/or rheological parameters. In this next stage of coupling these rheological differences are built into the model, so that the evolving particle concentrations feedback on the bulk flow through the evolving macroscopic friction of the mixture. There are two basic ways to introduce this coupling.

A key finding of the  $\mu(I)$ -rheology (GDR MiDi 2004) was that the inertial number (2.5) is a function of the particle size  $d$ . This is clearly defined in a monodisperse mixture, but an important generalization is needed for polydisperse systems. Based on DEM simulations of bidisperse two-dimensional assemblies of disks, Rognon *et al.* (2007) proposed an inertial number in which the particle size  $d$  was replaced by the local volume fraction weighted average particle size  $\bar{d}$ . The same law was also proposed by Tripathi & Khakhar (2011) and shown to agree with three-dimensional DEM simulations of spheres. Generalizing this concept to polydisperse systems, implies that the average particle size

$$\bar{d} = \sum_{\forall \nu} \phi^\nu d^\nu, \quad (3.1)$$

evolves as the local concentrations  $\phi^\nu$  of each particle species change. As a result, given the same local shear rate  $2\|\mathbf{D}\|$ , pressure  $p$  and intrinsic grain density  $\rho_*$ , the new inertial number

$$I = \frac{2\bar{d}\|\mathbf{D}\|}{\sqrt{p/\rho_*}}. \quad (3.2)$$

will be larger for a mixture composed of larger particles than one made of smaller grains.

As well as differences in size, the particles may also differ in shape and/or surface properties. A prime example of this are segregation induced fingering instabilities,

which develop with large angular (resistive) particles and finer spherical particles (Pouliquen *et al.* 1997; Pouliquen & Vallance 1999; Woodhouse *et al.* 2012; Baker *et al.* 2016*b*). The effect of particle shape and surface properties can certainly be modelled in monodisperse flows by changing the assumed macroscopic frictional parameters (see e.g. Pouliquen & Forterre 2002; Forterre 2006; Edwards *et al.* 2019; Rocha *et al.* 2019). Furthermore, the results of Baker *et al.*'s (2016*b*) granular fingering model suggest that a good approach is to assume that each phase satisfies a monodisperse friction law  $\mu^\nu = \mu^\nu(I)$  of the form (2.8) and then compute the effective friction by the weighted sum of these laws, i.e.

$$\bar{\mu} = \sum_{\forall \nu} \phi^\nu \mu^\nu. \quad (3.3)$$

On the other hand, it is also possible to assume that there is a single  $\mu(I)$ -curve, given by (2.8), but that the parameters in it evolve as the mixture composition changes, i.e.

$$\bar{\mu}_s = \sum_{\forall \nu} \phi^\nu \mu_s^\nu, \quad \bar{\mu}_d = \sum_{\forall \nu} \phi^\nu \mu_d^\nu, \quad \bar{\mu}_\infty = \sum_{\forall \nu} \phi^\nu \mu_\infty^\nu, \quad \bar{I}_0 = \sum_{\forall \nu} \phi^\nu I_0^\nu, \quad (3.4)$$

where  $\mu_s^\nu$ ,  $\mu_d^\nu$ ,  $\mu_\infty^\nu$  and  $I_0^\nu$  are the frictional parameters for a pure phase of constituent  $\nu$ . There is clearly potential for a great deal of complexity here that needs to be explored. However, to the best of our knowledge there are no DEM studies that measure the effective frictional properties of mixtures of particles of different sizes, shapes and surface properties that could further guide the model formulation. Segregation mobility feedback on the bulk flow will be investigated further in §6.

### 3.3. Feedback of the bulk flow on the segregation rate and diffusivity

The shear rate  $\dot{\gamma} = 2\|\mathbf{D}\|$ , the pressure  $p$ , gravity  $g$  and the particle properties also enter the equations more subtly through the functional dependence of the segregation velocity magnitude  $f_{\nu\lambda}$  and diffusivity  $\mathcal{D}_{\nu\lambda}$  in the fluxes (2.13) and (2.15). Even in bidisperse granular mixtures very little is known about their precise functional dependencies. However, dimensional analysis is very helpful in constraining the allowable forms.

Consider a bidisperse mixture of large and small grains of sizes  $d^l$  and  $d^s$ ,

respectively, which have the same intrinsic density  $\rho_*$ . The small particles occupy a volume fraction  $\phi^s = 1 - \phi^l$  per unit granular volume and the total solids volume fraction is  $\Phi$ . The system is subject to a bulk shear stress  $\tau$ , a pressure  $p$  and gravity  $g$ , which results in a shear rate  $\dot{\gamma}$ . Even though these variables are spatially varying, they are considered here as inputs to the system, whereas the segregation velocity magnitude  $f_{sl}$  and the diffusivity  $\mathcal{D}_{sl}$  are outputs. Since there are nine variables, with three primary dimensions (mass, length and time), dimensional analysis implies that there are six independent non-dimensional quantities

$$\mu = \frac{\tau}{p}, \quad I = \frac{\dot{\gamma}\bar{d}}{\sqrt{p/\rho_*}}, \quad \Phi, \quad P = \frac{p}{\rho_*g\bar{d}}, \quad R = \frac{d^l}{d^s}, \quad \phi^s, \quad (3.5)$$

where  $\bar{d}$  is the volume fraction weighted average grain size defined in (3.1),  $P$  is the non-dimensional pressure and  $R$  is the grain-size ratio. For a monodisperse system in the absence of gravity, only the first three quantities are relevant and GDR MiDi (2004) made a strong case for the friction  $\mu$  being purely a function of the inertial number  $I$ . This led to the development of the incompressible  $\mu(I)$ -rheology (GDR MiDi 2004; Jop *et al.* 2006; Barker & Gray 2017), which is used in this paper.

Using the monodisperse scalings, it follows that in the absence of gravity the self diffusion of grains should scale as

$$\mathcal{D} \sim \dot{\gamma}\bar{d}^2 \mathcal{F}(\mu, I, \Phi), \quad (3.6)$$

where  $\mathcal{F}$  is an arbitrary function of the friction, the inertial number and the solids volume fraction, and with no dependence on  $P$ ,  $R$  and  $\phi^s$ . In both the incompressible and compressible  $\mu(I)$ -rheologies (GDR MiDi 2004; da Cruz *et al.* 2005; Jop *et al.* 2006; Forterre & Pouliquen 2008) the friction  $\mu$  and the solids volume fraction  $\Phi$  are rigidly bound to the inertial number  $I$ , so it is not necessary to retain their dependence in (3.6). However, in the latest well-posed compressible theories (e.g. Barker & Gray 2017; Heyman *et al.* 2017; Schaeffer *et al.* 2019) the  $\mu = \mu(I)$  and  $\Phi = \Phi(I)$  laws only hold at steady-state, and so the general form of the diffusivity (3.6) applies.

Utter & Behringer (2004) showed experimentally that the self-diffusion coefficient scaled with the shear rate and the particle size squared. This suggests that

the simplest model for the diffusion of the grains in a polydisperse system is

$$\mathcal{D}_{\nu\mu} = \mathcal{A}\dot{\gamma}\bar{d}^2, \quad (3.7)$$

where  $\mathcal{A} = 0.108$  is a universal constant (Utter & Behringer 2004) and  $\bar{d}$  is now interpreted as the average, locally evolving, particle size defined in (3.1). Some evidence for this is provided by the experiments of Trewela *et al.* (2021) which show that a single small intruder in a matrix of large grains performs larger random walks than a single large intruder in a matrix of fine grains. In general, however, the diffusivity could be multiplied by an arbitrary function of the other non-dimensional quantities in (3.5).

Gravity driven percolation (kinetic sieving) and squeeze expulsion (Middleton 1970; Bridgwater *et al.* 1985; Savage & Lun 1988; Gray & Thornton 2005; Gray 2018) combine to create the dominant mechanism for segregation in dense sheared granular flows. Assuming that the segregation is independent of the diffusion, dimensional analysis suggests that the segregation velocity magnitude in a bidisperse mixture of large and small particles should scale as

$$f_{sl} \sim \dot{\gamma}\bar{d}\mathcal{G}(\mu, I, \Phi, P, R, \phi^s), \quad (3.8)$$

where  $\mathcal{G}$  is an arbitrary function. It has long been known that the segregation velocity magnitude  $f_{sl}$  is strongly dependent on the strain-rate and the particle size ratio (see e.g. Bridgwater *et al.* 1985; Savage & Lun 1988). Gray & Thornton (2005) also suggested that there should be a dependence on gravity. Evidence for this is provided by the fact that granular segregation experiments, with a density matched interstitial fluid, do not segregate (Vallance & Savage 2000; Thornton *et al.* 2006), i.e. when gravity is effectively reduced, so is the rate of segregation. Inclusion of the gravitational acceleration suggests that the segregation velocity magnitude should also be pressure dependent, since  $g$  only appears in the non-dimensional pressure  $P$ . This is supported by the experiments of Golick & Daniels (2009), who observed a dramatic slowing in the segregation rate when they applied a normal force on their ring shear cell. This pressure dependent suppression of segregation has been investigated further in the DEM simulations of Fry *et al.* (2018), who suggested that the segregation velocity magnitude should scale with

the reciprocal of the square root of the pressure. When this is combined with the shear rate dependence this implies that  $f_{sl}$  is linear in the inertial number.

In this paper, the segregation velocity magnitude is based on the refractive index matched shear box experiments of Trewhela *et al.* (2021). They measured the trajectories of (i) a single large and (ii) a single small intruder for a wide range of shear rates  $\dot{\gamma} \in [0.26, 2.3]$  and size ratios  $R \in [1.17, 4.17]$ . Trewhela *et al.* (2021) made four key observations (a-d below) that allowed them to collapse all their data. (a) Both the large and small intruder data showed a linear dependence of  $f_{sl}$  on the shear rate  $\dot{\gamma}$ . (b) Large intruders have a linear dependence on the size ratio that shuts off when  $R$  equals unity, i.e. linear in  $(R - 1)$ , while (c) small intruders have the same linear dependence at small size ratios, but develop a quadratic dependence on  $(R - 1)$  at larger size ratios. Finally, (d) both large and small intruders do not move linearly through the depth of the cell, but describe approximately quadratic curves as they rise up, or percolate down, through it. Since the pressure is linear with depth, this suggests a  $1/(\mathcal{C} + P)$  dependence, where the non-dimensional constant  $\mathcal{C}$  is introduced to prevent a singularity when the pressure is equal to zero. Trewhela *et al.* (2021) therefore suggested that the segregation velocity magnitude had the form

$$f_{sl} = \frac{\mathcal{B}\rho_*g\dot{\gamma}\bar{d}^2}{\mathcal{C}\rho_*g\bar{d} + p} [(R - 1) + \mathcal{E}\phi^l(R - 1)^2], \quad (3.9)$$

where  $\mathcal{B}$ ,  $\mathcal{C}$  and  $\mathcal{E}$  are universal constants. This expression encapsulates the key processes of gravity, shear and pressure, which drive the dominant mechanism for gravity driven segregation of particles of different sizes and size ratios in shear flows. Moreover, as a consequence of the  $\bar{d}^2$  dependence, equation (3.9) automatically gives rise to asymmetric flux functions (Gajjar & Gray 2014; van der Vaart *et al.* 2015), whose asymmetry is size ratio dependent (Trewhela *et al.* 2021). The function (3.9) not only collapses all the single intruder experiments of Trewhela *et al.* (2021), but it also quantitatively matches the time and spatial evolution of van der Vaart *et al.*'s (2015) shear box experiments, with a 50:50 mix of 4 mm and 8 mm glass beads, using the same values of  $\mathcal{B}$ ,  $\mathcal{C}$  and  $\mathcal{E}$  and the generalized diffusion law (3.7). The values of all the non-dimensional parameters are given in table 2. Note that, since the segregation velocity magnitude (3.9) is pressure

---


$$\mathcal{A} = 0.108, \quad \mathcal{B} = 0.3744, \quad \mathcal{C} = 0.2712, \quad \mathcal{E} = 2.0957,$$

TABLE 2. Non-dimensional constants  $\mathcal{A}$ ,  $\mathcal{B}$ ,  $\mathcal{C}$  and  $\mathcal{E}$  in the diffusion (3.7) and segregation laws (3.9) of Trewela *et al.* (2021).

---

dependent, but the generalized diffusivity (3.7) is not, Trewela *et al.*'s (2021) theory also exhibits the segregation suppression with increased pressure, observed by Golick & Daniels (2009) and Fry *et al.* (2018). The formula (3.9) can not be pushed too far, because, for size ratios greater than five, spontaneous percolation is known to occur for low small particle concentrations (Cooke, Bridgwater & Scott 1978), while isolated large intruders may exhibit intermediate or reverse segregation (Thomas 2000; Thomas & D'Ortona 2018).

#### 4. Numerical method

In order to solve the coupled system of equations the mass and momentum equations (2.1)–(2.2) are written in conservative form

$$\nabla \cdot \mathbf{u} = 0, \quad (4.1)$$

$$\frac{\partial}{\partial t} (\varrho \mathbf{u}) + \nabla \cdot (\varrho \mathbf{u} \otimes \mathbf{u}) = -\nabla p + \nabla \cdot (2\eta \mathbf{D}) + \varrho \mathbf{g}, \quad (4.2)$$

where  $\varrho$  is now the mixture density and  $\otimes$  is the dyadic product. This paper focuses on solving fully coupled bidisperse segregation problems with an evolving free-surface using a multiphase approach based on the segregation theory of §2.2.

The method assumes that there are three coexisting phases; large particles, small particles and excess air, which occupy volume fractions  $\varphi^l$ ,  $\varphi^s$  and  $\varphi^a$  per unit mixture volume, respectively. In this representation the granular phases are implicitly assumed to retain some air between the grains, so that the overall solids volume fraction in a purely granular state is still  $\Phi$  as before. Assuming that there is no diffusion of the excess air phase with respect to the particles (i.e  $\mathcal{D}_{al} = \mathcal{D}_{as} = 0$ ) the three conservation laws (2.11) for large particles, small particles and excess air are

$$\frac{\partial \varphi^l}{\partial t} + \nabla \cdot (\varphi^l \mathbf{u}) + \nabla \cdot \left( -f_{ls} \varphi^l \varphi^s \frac{\mathbf{g}}{|\mathbf{g}|} - f_{ag} \varphi^l \varphi^a \mathbf{e} \right) = \nabla \cdot \left( \mathcal{D}_{ls} (\varphi^s \nabla \varphi^l - \varphi^l \nabla \varphi^s) \right), \quad (4.3)$$



$$\frac{\partial \varphi^s}{\partial t} + \nabla \cdot (\varphi^s \mathbf{u}) + \nabla \cdot \left( f_{sl} \varphi^s \varphi^l \frac{\mathbf{g}}{|\mathbf{g}|} - f_{ag} \varphi^s \varphi^a \mathbf{e} \right) = \nabla \cdot \left( \mathcal{D}_{sl} (\varphi^l \nabla \varphi^s - \varphi^s \nabla \varphi^l) \right), \quad (4.4)$$

$$\frac{\partial \varphi^a}{\partial t} + \nabla \cdot (\varphi^a \mathbf{u}) + \nabla \cdot (f_{ag} \varphi^a \varphi^g \mathbf{e}) = 0, \quad (4.5)$$

respectively, where the concentration of grains is defined as

$$\varphi^g = \varphi^l + \varphi^s = 1 - \varphi^a. \quad (4.6)$$

When  $\varphi^a = 0$ , both the large and small particle segregation equations, (4.3) and (4.4), reduce to the bidisperse segregation equation (2.19), and equation (4.5) is trivially satisfied. As will be demonstrated in §5, this approach provides a simple and effective way of segregating the large and small particles from one another, while simultaneously expelling unwanted air bubbles and sharpening the free-surface interface.

The excess air is assumed to segregate from the grains with constant segregation velocity magnitude  $f_{ag}$  along the direction  $\mathbf{e}$ . The excess air segregation velocity magnitude has no physical significance and the approach should be thought of as a convenient numerical interface sharpening method. The rate is chosen to expel the excess air quickly enough to prevent bubble trapping. For the inclined plane simulations in §§5 and 6, the direction  $\mathbf{e}$  is chosen to be the upwards pointing normal to the plane in order to avoid air being segregated through the advancing front. This is not a concern in the rotating drum simulations in §7 and the direction  $\mathbf{e}$  is therefore chosen to point in the opposite direction to gravity  $\mathbf{g}$ .

The system of equations (4.1)–(4.5) is solved numerically with OpenFOAM assuming that the density and viscosity are given by the local volume fraction weighted averaged values

$$\varrho = \sum_{\forall \nu} \varphi^\nu \varrho_*^\nu, \quad \eta = \sum_{\forall \nu} \varphi^\nu \eta_*^\nu. \quad (4.7)$$

The intrinsic density of the air  $\varrho_*^a$  is equal to a constant and the intrinsic densities of the large and small particles are both constant and equal to one another, i.e.  $\varrho_*^l = \varrho_*^s = \Phi \rho_* \gg \varrho_*^a$ , where the solids volume fraction  $\Phi$  accounts for the interstitial air that is always present in the granular matrix. The intrinsic viscosity of the air  $\eta_*^a$  is also assumed to be constant, while the intrinsic viscosity of the grains is calculated from the viscosity (2.3) of the  $\mu(I)$ -rheology, with the friction

---


$$f_{sl} = 7 \times 10^{-3} \text{ m/s}, \quad f_{al} = f_{as} = 0.1 \text{ m/s},$$

$$\mathcal{D}_{sl} = 1 \times 10^{-6} \text{ m}^2/\text{s}, \quad \mathcal{D}_{al} = \mathcal{D}_{as} = 0 \text{ m}^2/\text{s}, \quad h = 5 \times 10^{-3} \text{ m},$$


---

TABLE 3. Constant segregation velocities and diffusivities between the different phases, as well as the inflow thickness  $h$  for the inclined flow simulations presented in §5 and §6.

---

$\mu$  and inertial number  $I$  calculated using the couplings discussed in §3.2. The parameters used in the simulations in §5 and §6 are summarized in tables 1 and 3.

Equations (4.1) and (4.2) are of the form of the incompressible Navier-Stokes equations and the pressure-velocity coupling is solved by the PISO algorithm (Issa 1986). The MULES algorithm (multi-dimensionalsal limiter for explicit solution, Weller 2006) is used to solve the concentration equations (4.4)–(4.5). The first two terms in equations (4.4)–(4.5) are the same as those in classic multiphase flow problems, and the inclusion of segregation actually simplifies the problem, as it provides a physical mechanism to counteract the inherent and unwanted numerical diffusion. The numerical treatment of the segregation flux can yield phase fractions outside the interval  $[0, 1]$ . Limiting of the respective fluxes (to avoid this discrepancy) is accomplished with the MULES algorithm. The diffusive flux in polydisperse flows is numerically unproblematic and is treated in a similar way to the convective flux, but without a limiter. The coupling of phase fractions with the bulk flow equations for the velocity and pressure is achieved with iterative coupling (Picard iteration) through the respective calculation of local viscosity and density in equations (4.7).

Numerical diffusion leads to a smearing of the free-surface interface, which has to be suppressed by the numerical scheme. These issues are not limited to the present problem but appear in similar form in many multiphase problems (e.g. Marschall *et al.* 2012). In OpenFOAM, this effect is normally corrected with an artificial flux, that compresses the interface (Rusche 2002; Weller 2008). For a general multiphase mixture the interface sharpening equation for phase fraction  $\varphi^\nu$  is

$$\frac{\partial \varphi^\nu}{\partial t} + \nabla \cdot (\varphi^\nu \mathbf{u}) + \sum_{\forall \lambda \neq \nu} \nabla \cdot (\mathbf{u}_{\nu\lambda} \varphi^\nu \varphi^\lambda) = 0, \quad (4.8)$$

where  $\mathbf{u}_{\nu\lambda}$  is the relative velocity between phases  $\nu$  and  $\lambda$ . This relative velocity is specifically constructed to be similar in magnitude to the bulk velocity and directed towards regions of higher concentration of phase  $\nu$ , i.e.

$$\mathbf{u}_{\nu\lambda} = c_{\nu\lambda} |\mathbf{u}| \frac{\varphi^\lambda \nabla \varphi^\nu - \varphi^\nu \nabla \varphi^\lambda}{|\varphi^\lambda \nabla \varphi^\nu - \varphi^\nu \nabla \varphi^\lambda|}. \quad (4.9)$$

The parameter  $c_{\nu\lambda}$  is usually chosen to be of order 1 and regulates the amount of counter gradient transport between phases  $\nu$  and  $\lambda$ . The counter gradient flux sharpens the interface, but can lead to results that are outside the range  $[0, 1]$  and the MULES algorithm is used again to keep all cell values within this interval.

For the case of a mixture of air and grains, equations (4.8) and (4.9) reduce to

$$\frac{\partial \varphi^a}{\partial t} + \nabla \cdot (\varphi^a \mathbf{u}) + \nabla \cdot \left( c_{ag} |\mathbf{u}| \varphi^a \varphi^g \frac{\nabla \varphi^a}{|\nabla \varphi^a|} \right) = 0, \quad (4.10)$$

which has the same  $\phi^a \phi^g$  structure to the air concentration equation (4.5). The key difference, is that (4.5) allows the user to choose the direction  $\mathbf{e}$  and magnitude  $f_{ag}$  of the air segregation, rather than being constrained to the counter-gradient direction. Since many problems of practical interest involve dense granular free-surface flows, with a region of air above them, choosing the direction to segregate the air is not difficult, and completely avoids the unfortunate tendency of interface sharpening methods to create bubbles of air within the body of grains that may remain permanently stuck. The magnitude of the air segregation velocity magnitude may also be chosen to parameterize the typical timescales over which excess air is physically expelled from the body of grains. The polydisperse segregation theory, developed in §2.2, provides a promising general method of interface sharpening that can be applied to a wide range of problems.

Time stepping is conducted in the ordinary time marching manner. However, special consideration is required due to the spatially varying and high viscosity. In OpenFOAM, each velocity component is solved individually and coupling is achieved explicitly (in a numerically segregated approach). The explicit terms introduce a strict CFL criterion which incorporates the local viscosity (Moukalled, Mangani & Darwish 2016). The CFL number is defined as

$$\text{CFL} = \frac{|\mathbf{u}| \Delta t}{\Delta x} + \frac{\eta \Delta t}{\rho \Delta x^2}, \quad (4.11)$$

and should be limited to a value that is characteristic for the time integration scheme (e.g. 1 for forward Euler). In most multiphase flows the first term (convection) dominates and the second term (viscosity or diffusion) is neglected. In granular flows with stationary zones, the opposite is the case, since the granular viscosity tends towards infinity in the limit  $\|\mathbf{D}\| \rightarrow 0$ . To avoid infinitely small time steps, the granular viscosity is therefore limited to a reasonably high value (see e.g. Lagr  e, Staron & Popinet 2011; Staron, Lagr  e & Popinet 2012), i.e.

$$\eta = \min(\eta_{max}, \eta), \quad (4.12)$$

so that  $\eta_{max}$  is the maximum viscosity when the pressure is large and/or the strain-rate is small. This is a purely numerical regularisation rather than a physically motivated one (see e.g. Barker & Gray 2017). The viscous part is still the dominating contribution in the CFL number and granular flow simulations require much smaller time steps than comparable simulations with low viscosity liquids. Note that computations can be sped up considerably by giving the air phase an artificially high viscosity. This reduces inertial effects in the air, whilst still resulting in a negligible influence of the air on the grains.

The general multi-component segregation-diffusion equations have been implemented into a custom solver based on the OpenFOAM solver `multiphaseInterFoam`, and which makes extensive use of the MULES algorithm provided in the OpenFOAM library. The original solver implements a system of multiple immiscible phases. The system requires an additional diffusion term and replaces the counter gradient transport term with the segregation fluxes. The granular rheology is implemented in a separate library, making use of the respective OpenFOAM programming interface. A similar interface has been created to allow for different expressions for segregation and diffusion coefficients.

## 5. Segregation in an uncoupled bulk flow down an inclined plane

The various couplings and feedbacks between segregation and the bulk flow, discussed in §3, are now explored in more detail. In order to test the numerical method against known steady-state and travelling wave solutions, §5 examines the

one-way coupled model, in which the segregation velocity magnitudes and diffusivities are prescribed, and the bulk flow field is computed with a monodisperse model (as described in §3.1). The parameters for the bulk flow are summarized in table 1 and are based on the monodisperse glass bead experiments of Barker & Gray (2017). The segregation velocity magnitudes and diffusivities are given in table 3 and are chosen to rapidly segregate the air from the grains to produce a sharp free-surface, whilst simultaneously allowing a diffuse inversely-graded steady-state segregation profile to develop (see e.g. Wiederseiner *et al.* 2011).

### 5.1. Inflow conditions and boundary conditions

A rectangular Cartesian coordinate system is defined with the  $x$ -axis pointing down the slope, which is inclined at  $\zeta = 24^\circ$  to the horizontal, and the  $z$ -axis being the upward pointing slope normal. The unit vectors in each of these directions are  $\mathbf{e}_x$  and  $\mathbf{e}_z$ , respectively. Numerical simulations are performed on a rectangular grid in the region  $0 \leq x \leq L_x$ ,  $0 \leq z \leq L_z$ , where  $L_x$  and  $L_z$  define the box size. In order to represent an initially empty domain, a Newtonian air phase  $\nu = a$  is used, which initially fills the box and is stationary, so that  $\varphi^a = 1$  and  $\mathbf{u} = \mathbf{0}$  everywhere at time  $t = 0$ . Granular material, composed of a bidisperse mixture of large  $\nu = l$  and small  $\nu = s$  grains, is then injected at the left boundary using Dirichlet conditions on the velocity

$$\mathbf{u}|_{x=0} = \begin{cases} \mathbf{u}^a(z), & \text{for } h < z \leq L_z, \\ \mathbf{u}^g(z), & \text{for } 0 \leq z \leq h, \end{cases} \quad (5.1)$$

and on the constituent volume fractions

$$(\varphi^a, \varphi^s, \varphi^l)|_{x=0} = \begin{cases} (1, 0, 0) & \text{for } h < z \leq L_z, \\ (0, \frac{1}{2}, \frac{1}{2}) & \text{for } 0 \leq z \leq h, \end{cases} \quad (5.2)$$

where  $h$  is the height of the interface between air and grains at the inflow, and  $\mathbf{u}^a$  and  $\mathbf{u}^g = \mathbf{u}^s = \mathbf{u}^l$  are prescribed air and grain velocities. This corresponds to a 50:50 mix by volume of large and small grains, with an air phase above. Along the solid base of the chute ( $z = 0$ ) the no slip and no penetration condition  $\mathbf{u} = \mathbf{0}$  is enforced, as well as the no normal flux condition (2.17) for all of the phases. At the outlet wall at  $x = L_x$  a free outlet condition is applied. This means that

there is free outflow (i.e. zero gradient) unless the velocity vector points into the domain (inflow). If inflow is predicted, then the condition switches to Dirichlet and  $(\varphi^a, \varphi^s, \varphi^l) = (1, 0, 0)$  i.e. there is only air inflow and not granular inflow. A similar free-outflow condition applies for the concentration on the top boundary,  $z = L_z$ . Here the normal velocity has zero gradient, but the pressure is prescribed to be a small constant (Barker & Gray 2017). Simulations have been performed with  $p(L_z) = 10^{-3} \text{ N/m}^2$  and  $10^{-6} \text{ N/m}^2$  and are insensitive to this change.

### 5.2. Steady-uniform bulk flow velocity

As this becomes an effectively monodisperse problem for the bulk flow  $\mathbf{u}$  and pressure  $p$ , fully developed steady uniform flow should correspond to the Bagnold flow solution (see e.g. Silbert *et al.* 2001; GDR MiDi 2004; Gray & Edwards 2014; Barker *et al.* 2015). Assuming a flow of thickness  $h$ , the exact solution to the  $\mu(I)$ -rheology implies that the pressure is lithostatic

$$p = \rho_* \Phi g (h - z) \cos \zeta, \quad (5.3)$$

the downslope velocity is given by the Bagnold profile

$$u_{Bagnold}(z) = \frac{2I_\zeta}{3d} \sqrt{\Phi g \cos \zeta} \left( h^{\frac{3}{2}} - (h - z)^{\frac{3}{2}} \right), \quad (5.4)$$

and the inertial number  $I$  is equal to the constant

$$I_\zeta = \mu^{-1}(\tan \zeta). \quad (5.5)$$

For the partially regularized form of the friction law (2.8) used in this paper, it follows, that for  $\mu_\infty > 0$  and  $I > I_1^N$ , the inertial number is equal to

$$I_\zeta = \frac{\tan \zeta - \mu_d + \sqrt{(\mu_d - \tan \zeta)^2 + 4(\tan \zeta - \mu_s)\mu_\infty I_0}}{2\mu_\infty}. \quad (5.6)$$

The granular inflow velocity is therefore set to  $\mathbf{u}^g = u_{Bagnold} \mathbf{e}_x$ . The velocity in the air phase above is set to the Newtonian flow solution  $\mathbf{u}^a = u_p(z) \mathbf{e}_x$ , where the Poiseuille profile is

$$u_p(z) = \frac{g\rho_*^a \cos \zeta}{\eta^a} (2L_z(z - h) + h^2 - z^2) + u_{Bagnold}(h). \quad (5.7)$$

This implicitly assumes no slip at the lower free-surface interface with the moving grains, i.e.  $u_p(h) = u_{Bagnold}(h)$ .

### 5.3. Comparison between the different methods of interface tracking

For this simple case, it is instructive to compare the alternative interface sharpening techniques that were discussed in §4. As shown in figure 2(a), when there is no interface sharpening, numerical diffusion leads to a very wide diffuse layer between the air and the grains, rather than a sharp free-surface. In addition, a large vortex of dilute granular material is thrown into the air at the front and a thin layer of air is trapped next to the basal solid wall. This trapping of air next to the boundary is a serious problem, because it prevents direct contact of the grains with the lower boundary and consequently affects the effective friction experienced by the grains as they flow downslope. In reality, any air that is trapped adjacent to the lower wall is free to percolate up through the pore space between the particles and escapes. This unphysical air trapping is also observed in the simulation with active counter gradient transport as shown in figure 2(b). Although the free-surface is much shaper than before, there is a tendency for the trapped air to form bubbles. This effect is especially strong in high viscosity flows because the bubbles become stuck and are unable to escape. The results, both with and without interface sharpening, are also found to be sensitive to the numerical mesh and time step used in the calculation. Figure 2(c) shows the new method of tracking the interface using equations (4.4)–(4.5) assuming that trapped air is segregated upwards, i.e.  $\mathbf{e} = \mathbf{e}_z$ . The segregation velocity magnitude and diffusion coefficients (see table 3) are chosen to give diffuse segregation inside the granular mixture, but also to generate a sharp interface between the granular phases and the air above. It is clear from figure 2(c) that with this method there is no trapped air next to the basal boundary, the free-surface interface is sharp and there is no vortex shedding at the flow front. Moreover, the results are grid-converged. The new method of treating the free-surface is therefore very promising, and provides a simple way of parameterizing the physics that is actually taking place.

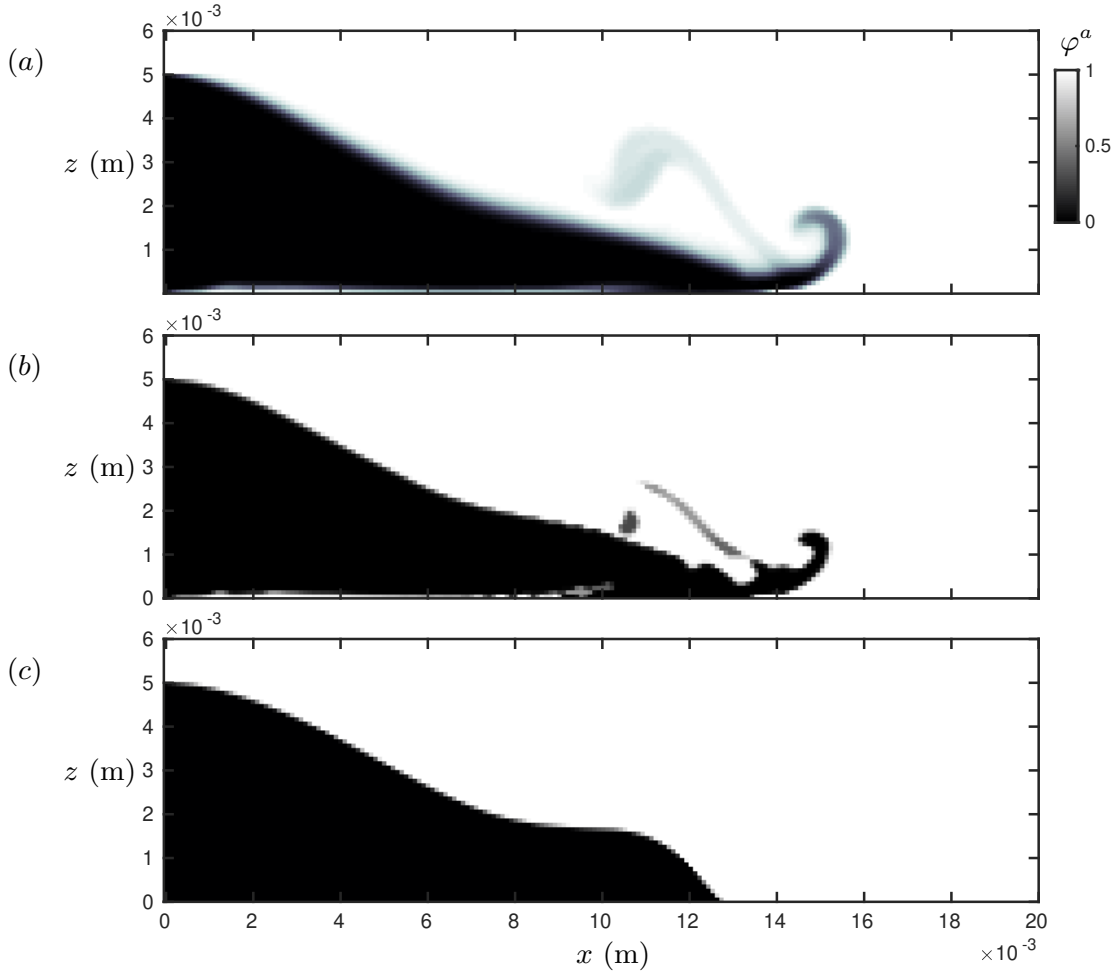


FIGURE 2. The air fraction  $\varphi^a$  after  $t = 0.05$  s of injection of granular material onto a frictional plane inclined at  $\zeta = 24^\circ$ . Case (a) uses no interface sharpening whereas case (b) uses the usual counter gradient transport method often employed in OpenFOAM. For the same initial and boundary conditions, the air segregation method proposed in §4 gives the constituent distribution shown in panel (c), using the parameters in table 3.

#### 5.4. Numerical simulation of the bulk flow and the segregation

Armed with this improved and reliable method of interface capture, the full transient evolution of the travelling front can be explored. Figure 3 shows the results of a calculation performed in a long aspect ratio domain with dimensions  $(L_x, L_z) = (0.62, 6.2 \times 10^{-3})$  m i.e. 100 : 1. As the front progresses into the domain, there is dynamic evolution of both the front shape and the distribution of the granular phases. In particular, a steadily travelling front forms with a well defined shape (Pouliquen 1999a; Gray & Ancey 2009; Saingier, Deboeuf & Lagr  e 2016). Behind the advancing front, the initially evenly mixed concentration of large and small grains is swept downstream from the inflow and is gradually eroded by a growing layer of large particles at the surface and a growing layer of



finer grains adjacent to the base of the flow. By 20 cm downstream the homogeneously mixed region completely disappears and further downstream there is a thin layer with high concentrations of large grains at the surface and a thicker layer with high concentrations of fine grains at the base. This is known as an inversely graded particle-size distribution. The difference in thickness is due to the large particles being concentrated in the faster moving region of the flow, so a much thinner layer can transport the same mass flux as the thick, slow moving layer beneath, which contains high concentrations of fines.

An immediate consequence of the large particles being segregated into the faster moving near surface layers is that they are preferentially transported to the flow front, as shown in figure 3(b,c,d). As large grains reach the front, they are overrun, but can rise back towards the surface again by particle segregation, to form a recirculating frontal cell of large particles that grows in size with increasing time (Pierson 1986; Pouliquen *et al.* 1997; Iverson & Vallance 2001; Gray & Kokelaar 2010*b,a*; Johnson *et al.* 2012; Woodhouse *et al.* 2012; Baker *et al.* 2016*b*; Denissen *et al.* 2019). The large particle rich flow front and the inversely graded body of the flow are connected by what is known as a breaking size-segregation wave (Thornton & Gray 2008; Johnson *et al.* 2012; Gajjar, van der Vaart, Thornton, Johnson, Ancey & Gray 2016). This travels steadily downslope, but at a slower speed than the front. It is this wave that segregates the large slow moving particles, close to the base of the flow, up into faster moving regions allowing them to be recirculated, and conversely, allows fast moving small grains to percolate down into slower moving basal layers. The breaking wave shown here includes the effects of diffusion as well as segregation for the first time. Eventually the flow front and the breaking-size segregation wave propagate out of the domain, to leave the approximately steady uniform flow shown in figure 3(e). For comparison, Gray & Thornton's (2005) concentration shock solution (see appendix A) is also plotted in figure 3(e) using the Bagnold velocity profile (5.4). For an inflow small particle concentration  $\varphi_0^s = 0.5$  this accurately predicts the position of the centre of the final steady-state height of the inversely graded layer, with the large particles occupying a thinner faster moving region than the fines. However, the solution neglects diffusion in both the downslope and slope normal directions, and only

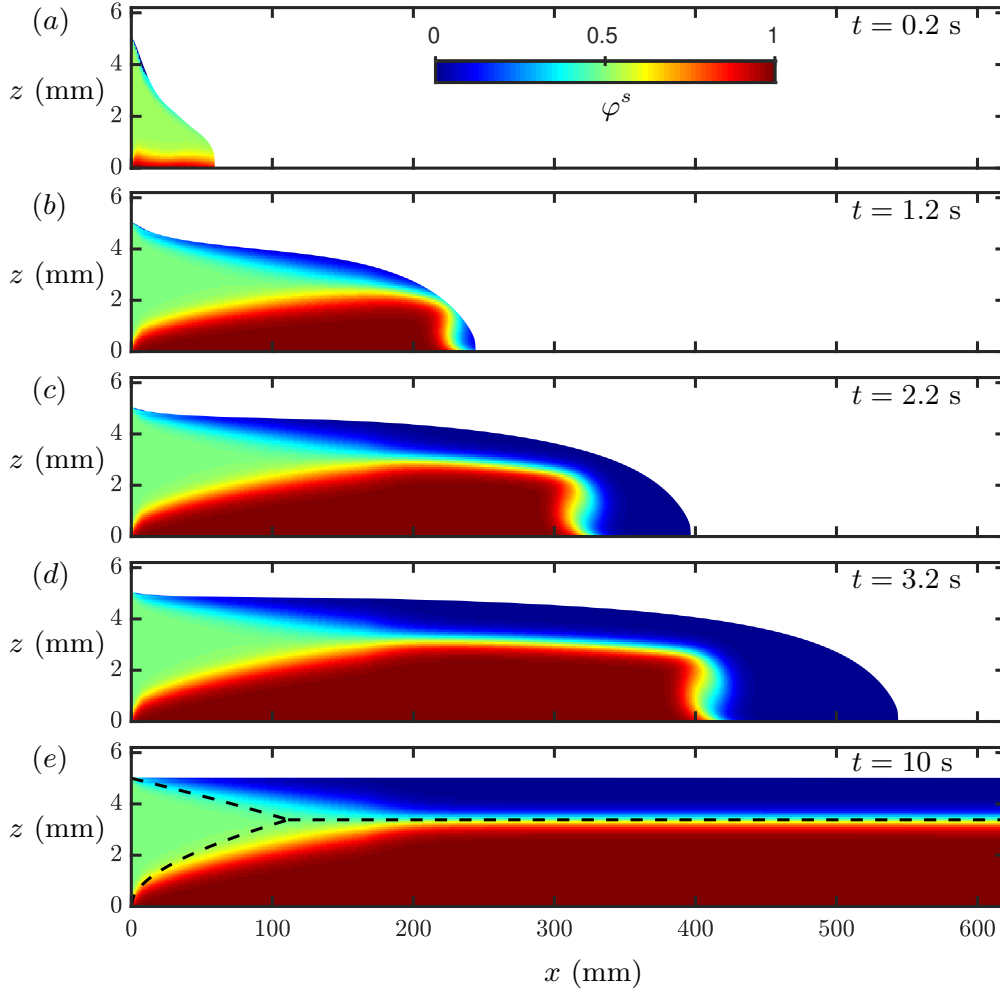


FIGURE 3. Evolution of a granular flow front down a frictional plane inclined at  $\zeta = 24^\circ$ . The flow consists of a bidisperse mixture with both small and large particles having identical rheological properties (listed in table 1) and no feedback from the local particle size. Here the concentration of small particles  $\varphi^s$  is plotted inside the granular material at 5 successive times. The plots are stretched vertically in order to provide greater detail of the concentration distribution. Panel (e), which is the plot of a late time at  $t = 10$  s, is indicative of the long-time steady dynamics after which no further evolution is observed in the simulations. The dashed lines in (e) show the corresponding shock solutions of Gray & Thornton (2005), which assume that there is no diffusion and resolve only the normal component of the segregation flux. The parameters are summarized in tables 1 and 3. A video is available in the online supplementary material showing the full dynamics of the flow front.

resolves the segregation flux in the slope normal direction, so it does not capture the precise point at which the solution reaches steady state.

### 5.5. *Comparison with steady uniform solutions for the bulk flow and the segregation*

Figure 4(a) shows excellent agreement between the computed two-dimensional steady uniform flow solution for the downslope velocity  $u$  and the Bagnold velocity

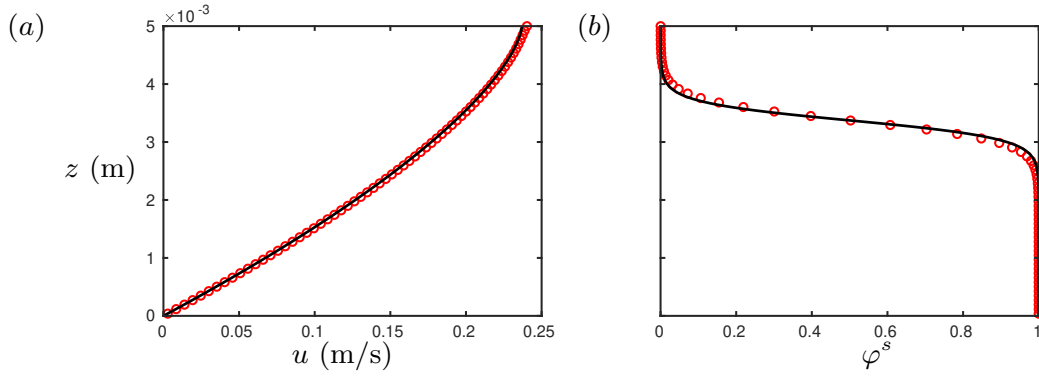


FIGURE 4. Long-time downstream velocity and small particle concentration. Open circles are from the numerical simulation, at the outflow boundary  $x = L_x$  at  $t = 10$  s, and the solid curve in (a) is the Bagnold velocity profile (5.4) and in (b) the solid line is the exact solution (5.8)–(5.11) of Gray & Chugunov (2006). The parameters are summarized in tables 1 and 3.

profile (5.4). The only slight difference occurs near the free-surface, where the weight of the column of air above produces the largest relative change in the pressure within the granular material. With the  $\mu(I)$ -rheology, this changes the balances in the inertial number and hence the computed velocity profile. For steady uniform flows, Gray & Chugunov (2006) derived an exact solution for the small particle concentration, assuming that the segregation and diffusion rates were constant. This solution takes the form

$$\varphi^s = \frac{1}{1 + A_{GC} \exp(Pe \hat{z})}, \quad (5.8)$$

where  $A_{GC}$  is a constant and  $Pe$  is the Peclet number for segregation. Note that in this solution the  $z$ -coordinate has been non-dimensionalized using the scaling  $z = h\hat{z}$ , where  $h$  is the slope normal flow depth. In terms of the dimensional segregation and diffusion rates, given in table 3, the Peclet number is defined as

$$Pe = \frac{f_{sl} h \cos \zeta}{\mathcal{D}_{sl}}, \quad (5.9)$$

where the factor  $\cos \zeta$  arises from the fact that the segregation is inclined at an angle  $\zeta$  to the slope normal  $z$ -axis, i.e.  $\mathbf{e}_z \cdot \mathbf{g}/|\mathbf{g}| = -\cos \zeta$ . The constant  $A_{GC}$  alters the position of the transition between large and small particles in the solution. If the depth averaged concentration is equal to

$$\overline{\varphi^s} = \frac{1}{h} \int_0^h \varphi(z) dz = \int_0^1 \varphi(\hat{z}) d\hat{z}, \quad (5.10)$$

then

$$A_{GC} = \frac{\exp(-Pe \overline{\varphi^s}) - \exp(-Pe)}{1 - \exp(-Pe \overline{\varphi^s})}. \quad (5.11)$$

The depth-averaged flux of small particles is the same at all downstream positions at steady state. It follows that the upstream inflow conditions can be used to determine the constant  $A_{GC}$  in the final steady-state (see e.g. Wiederseiner *et al.* 2011; van der Vaart *et al.* 2015). For the inflow concentration  $\varphi_0^s = 0.5$  and Bagnold velocity (5.4), the depth-averaged concentration  $\overline{\varphi^s} = 0.6744$ , which is very close to the value of  $\overline{\varphi^s} = 0.6746$  for the computed solution shown in figure 4(b). For the parameters chosen in table 3, the Peclet number  $Pe = 31.97$ , so the particles are quite sharply segregated. The close match between the Bagnold solution and Gray & Chugunov's (2006) results provides a clear indication that the numerical method and implementation are appropriate and precise. In particular, the bulk flow requires a delicate balance of stresses over a relatively long distance and any significant numerical diffusion would likely disrupt this.

### 5.6. Comparison of the frontal shape with depth-averaged solutions

The basal friction law of Pouliquen (1999b) predates the full tensorial  $\mu(I)$ -rheology and was designed to model the frictional source term in the shallow avalanche equations of Savage & Hutter (1989) on chutes with rough bases. The fully developed numerical front solution, shown in figure 3, is indeed very shallow, so it is appropriate to compare it to solutions of these reduced equations. The depth-averaged theory provides a very simple means of predicting the shape of a steadily travelling granular flow front (Pouliquen 1999a; Gray & Ancey 2009; Saingier *et al.* 2016). In a frame  $\xi = x - u_F t$  moving with the front speed  $u_F$  the steady-state depth-averaged mass and momentum balances are

$$\frac{d}{d\xi} (h(\overline{u} - u_F)) = 0, \quad (5.12)$$

$$\frac{d}{d\xi} (\chi h \overline{u^2} - h \overline{u} u_F) + \frac{d}{d\xi} \left( \frac{1}{2} g h^2 \cos \zeta \right) = h g \cos \zeta (\tan \zeta - \mu), \quad (5.13)$$

where  $h$  is the avalanche thickness, and the depth-averaged velocity  $\overline{u}$ , the depth-average of the velocity squared  $\overline{u^2}$  and the shape factor  $\chi$  are defined as

$$\overline{u} = \frac{1}{h} \int_0^h u \, dz, \quad \overline{u^2} = \frac{1}{h} \int_0^h u^2 \, dz, \quad \chi = \frac{\overline{u^2}}{\overline{u}^2}, \quad (5.14)$$

respectively. Many theories assume that the shape factor  $\chi = 1$ , which corresponds to plug flow, and which dramatically simplifies the characteristic structure of this hyperbolic system of equations. For the Bagnold velocity profile (5.4), the shape factor  $\chi = 5/4$ . Saingier *et al.* (2016) showed that with Pouliquen & Forterre's (2002) effective basal friction law this led to the formation of a thin precursor layer ahead of the main front that extended to infinity, which is unphysical.

The depth-averaged mass balance equation (5.12) can be integrated directly, subject to the condition that the thickness is zero at the flow front, to show that for non-trivial solutions the depth-averaged velocity is equal to the front speed, i.e.

$$\bar{u} = u_F, \quad (5.15)$$

everywhere in the flow. Far upstream the flow is steady and uniform. The front speed can therefore be determined by integrating the Bagnold solution (5.4) through the avalanche depth to show that

$$u_F = \bar{u}_\infty = \frac{2I\zeta}{5d} \sqrt{\Phi g \cos \zeta} h_\infty^{3/2}, \quad (5.16)$$

where  $h_\infty$  and  $\bar{u}_\infty$  are the steady-uniform thickness and downslope velocity far upstream. Expanding (5.13), dividing through by  $hg \cos \zeta$  and using (5.15) yields an ordinary differential equation (ODE) for the flow thickness

$$\left[ (\chi - 1) Fr_\infty^2 \frac{h_\infty}{h} + 1 \right] \frac{dh}{d\xi} = \tan \zeta - \mu, \quad (5.17)$$

where  $Fr_\infty$  is the Froude number far upstream, i.e.

$$Fr_\infty = \frac{\bar{u}_\infty}{\sqrt{gh_\infty \cos \zeta}}. \quad (5.18)$$

In order to solve the ODE (5.17) it is necessary to convert the new friction law (2.8) into an effective basal friction law. This is done by assuming that Bagnold flow holds everywhere in the flow and hence the depth-averaged downslope velocity  $\bar{u}$  satisfies

$$\bar{u} = \frac{2I}{5d} \sqrt{\Phi g \cos \zeta} h^{3/2}. \quad (5.19)$$

Since, the depth-averaged velocity is the same as the front velocity (5.15) everywhere in the flow, equations (5.16) and (5.19) can be equated to determine the

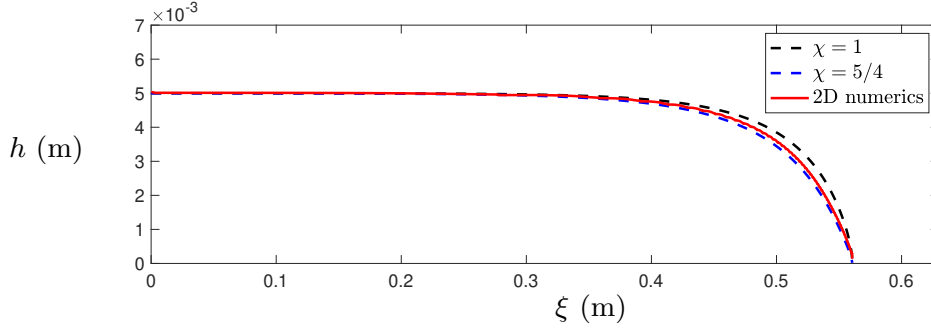


FIGURE 5. Comparison of the two-dimensional computed steady travelling free-surface profile (red line), with solutions of the depth-averaged equations using the regularised effective basal friction law (5.21) with a plug-flow shape factor  $\chi = 1$  (black dashed line) and Bagnold flow shape factor  $\chi = 5/4$  (blue dashed line). The free-surface from the full two-dimensional numerics, after  $t = 10$  s in a moving frame, is calculated by interpolating the contour of  $\varphi^a = 0$ . The parameters are summarized in table 1.

inertial number

$$I(\xi) = I_\zeta \left( \frac{h_\infty}{h(\xi)} \right)^{3/2}, \quad (5.20)$$

at a general position  $\xi$ . Substituting this expression into the high- $I$  branch of the full  $\mu(I)$  curve (2.8) gives the regularised depth-averaged basal friction

$$\mu(h) = \frac{\mu_s I_0 h^{3/2} + \mu_d I_\zeta h_\infty^{3/2} + \mu_\infty I_\zeta^2 \left( \frac{h_\infty}{\sqrt{h}} \right)^3}{I_0 h^{3/2} + I_\zeta h_\infty^{3/2}}. \quad (5.21)$$

The significance of this expression is made clear by taking the limit as  $h \rightarrow 0$ . Unlike for the previous expression for  $\mu$ , in which  $\mu_\infty = 0$ , the friction now tends to infinity for vanishingly thin layers. This means that the ODE (5.17) naturally predicts an infinite slope and therefore the front always pins to the boundary and this system is guaranteed to preclude infinite precursor layers.

The front shape predicted by this newly derived regularised depth-averaged formulation is compared with the full two-dimensional numerics in figure 5. In order to guarantee that the full solution does indeed correspond to a steady travelling front, the simulation is continued from  $t = 4$  s in a moving frame. This change is applied simply by shifting all the velocities and the boundary conditions by the depth-averaged velocity (5.16) i.e.  $\mathbf{u}^{\text{new}} = \mathbf{u}(t = 4\text{s}) - \bar{u}\mathbf{e}_x$  everywhere. The following analysis applies to the long-time solution in this moving frame, which is found to be numerically invariant of time after another  $\sim 5$  s of simulation. Upstream of the front (for low values of  $\xi$ ) the flow is almost uniform, so the Bagnold solution, which has a shape factor  $\chi = 5/4$ , is observed as expected.

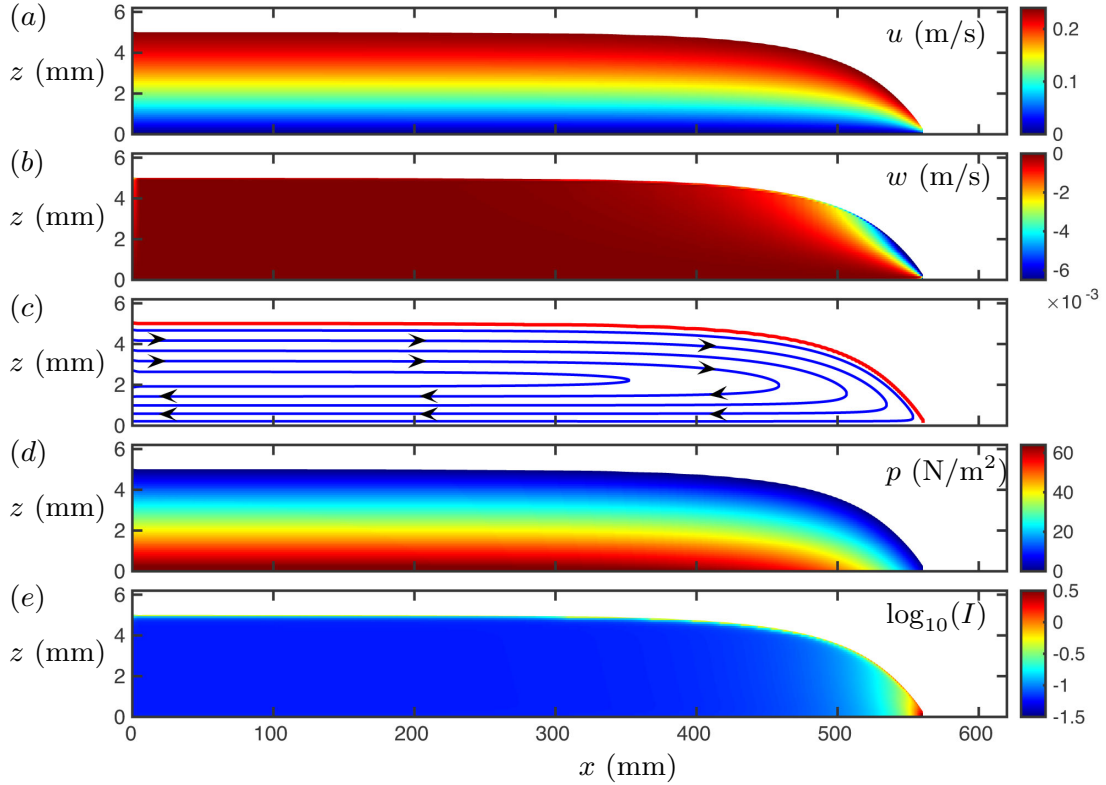


FIGURE 6. Flow fields inside the granular flow front after 10 s in a moving frame. Panels (a) and (b) show the velocity components and panel (c) is a selection of the corresponding streamlines. The pressure and the base 10 logarithm of the inertial number  $I$  are shown in (d) and (e) respectively. Note that the downstream velocity in panel (a) has been shifted by the front velocity (5.16) in order to give values in the frame of the frictional base. The parameters are summarized in table 1.

However, closer to the flow front the assumption of uniformity breaks down and the two solutions differ. As shown in figure 5, the front computed with the multiphase approach lies between the depth averaged solution with  $\chi = 5/4$  and that with  $\chi = 1$ , which corresponds to pure plug flow, where  $u$  no longer depends on  $z$ . This comparison therefore highlights the expected discrepancies between full two-dimensional theories and depth-averaged equivalents when dynamics vary in a non-shallow manner.

### 5.7. The two-dimensional internal flow fields in the moving frame

Given that the two-dimensional transient flow front has developed into a steady travelling state, the detailed flow fields inside the granular material are of particular interest. These are plotted in figure 6. Figure 6(a) shows the downstream velocity, shifted back to the lab-frame by adding  $\bar{u}\mathbf{e}_x$ , which is monotonically

increasing in  $z$  for all  $x$  in a similar manner to the Bagnold velocity profile. Only at the tip of the front is the vertical velocity non-zero (figure 6b) and there is a downwards motion. As these two velocity components define a steady travelling front, the streamlines which result from them coincide with the particle paths. However, these trajectories, which are plotted in figure 6(c), only correspond to the paths of monodisperse particles. The large and small particle trajectories, which couple to these flow fields, but not vice-versa, are not steady in this frame, or any frame of reference as the large particle recirculation region at the head is forever growing in size. Just like the similarity to the Bagnold velocity solution, the pressure field in figure 6(d) is close to the lithostatic profile (5.3) except that the flow thickness is not constant. Similarly, the inertial number (figure 6e) takes its steady uniform value upstream, but gets larger as the front is approached, as predicted by (5.20). It should be noted that any potential issues of ill-posedness at high inertial numbers, close to the very tip of the flow, are suppressed by the maximum viscosity cutoff (4.12) in the numerical method.

## 6. Segregation mobility feedback on the bulk flow

The one-way coupled simulations in §5 demonstrate the effectiveness of the numerical method developed in §4, and also show qualitatively how large and small particles are advected, segregated and diffused within the bulk flow field. To produce quantitative results, it is necessary to couple the evolving particle size distribution to the bulk flow dynamics, as discussed in §3.2. There are essentially two ways of producing frictional feedback; namely (i) indirectly through the evolving average local grain size, which changes the inertial number and hence the friction, and (ii) directly through the modification of the frictional parameters associated with each of the species. Both couplings are investigated in this section, and the results of the inertial number coupling are compared directly to the DEM simulations of Tripathi & Khakhar (2011).

### 6.1. *Steady uniform flow down an inclined plane with segregation mobility feedback*

Consider once again a steady uniform flow down an inclined plane, but this time incorporating feedback of the steady-state concentration distribution. If the



segregation and diffusion rates are constant, then the volume fractions  $\varphi^\nu = \varphi^\nu(z)$  can be solved for with the polydisperse theory in §2.2, completely independently of the bulk flow. These concentrations will therefore be assumed to be known in what follows. The normal component of the momentum balance then implies that the pressure is lithostatic (5.3). The only difference to the classical Bagnold solution (Silbert *et al.* 2001; GDR MiDi 2004; Gray & Edwards 2014) is that, with the volume fraction weighted friction (3.3), the downslope momentum balance reduces to

$$\sum_{\forall \nu} \varphi^\nu \mu^\nu(I) = \tan \zeta, \quad (6.1)$$

where  $\mu^\nu$  is the friction law for constituent  $\nu$ . For the purposes of illustration, let us assume that each phase satisfies the classical  $\mu(I)$  friction law, which is of the form

$$\mu^\nu = \mu_s^\nu + \frac{\mu_d^\nu - \mu_s^\nu}{I_0/I + 1}, \quad (6.2)$$

where  $I_0$  is assumed to be the same for all the phases. Substituting (6.2) into (6.1) and solving for the inertial number, it follows that

$$I = I_0 \left( \frac{\tan \zeta - \bar{\mu}_s}{\bar{\mu}_d - \tan \zeta} \right), \quad (6.3)$$

where  $\bar{\mu}_s$  and  $\bar{\mu}_d$  are now the volume fraction weighted averages that are depth dependent

$$\bar{\mu}_s(z) = \sum_{\forall \nu} \varphi^\nu(z) \mu_s^\nu, \quad \bar{\mu}_d(z) = \sum_{\forall \nu} \varphi^\nu(z) \mu_d^\nu. \quad (6.4)$$

Importantly, equation (6.3) shows that, if there are frictional differences between the particles, then the inertial number is dependent on the normal coordinate  $z$  rather than being equal to the constant  $I_\zeta$  defined in (5.5). Using the definition of the generalized inertial number for polydisperse systems (3.2) and assuming steady uniform flow, it follows that the ODE for the velocity profile is

$$\frac{du}{dz} = \frac{I_0}{\bar{d}} \sqrt{\Phi g \cos \zeta} (h - z)^{\frac{1}{2}} \left( \frac{\tan \zeta - \bar{\mu}_s}{\bar{\mu}_d - \tan \zeta} \right) \quad (6.5)$$

where  $\bar{d}$  is the local average particle size, which is also depth-dependent

$$\bar{d}(z) = \sum_{\forall \nu} \varphi^\nu(z) d^\nu. \quad (6.6)$$

This averaged particle size-dependence is important, because even if the particles have the same shape and the same effective frictional properties, the velocity profile will no longer be the classical Bagnold solution (5.4), but will depend on the local changes in particle size.

Figure 7 shows a specific example of the qualitative types of solution that are generated for a bidisperse mixture of large and small particles. The solutions assume Gray & Chugunov's (2006) exact solution for the concentration profile (5.8)–(5.11) using the same constant segregation velocity magnitude  $f_{sl}$ , constant diffusivity  $\mathcal{D}_{sl}$ , flow depth  $h$  as in table 3, as well as the same slope angle  $\zeta = 24^\circ$ . The only difference is that the depth-averaged concentration  $\overline{\varphi^s}$  is chosen to be equal to 50% in order to produce flowing layers of large and small particles that are the same depth. For consistency with the assumed friction law (6.2),  $\mu_\infty^\nu = 0$  for both the large and small particles. All the other parameters are the same for both species, and identical to those given in table 1, except that  $\mu_s^l = 1.2\mu_s$ . This small change is sufficient to make the inertial number (6.3) depth-dependent as shown in figure 7(a). The increase in  $\mu_s^l$  for the large particles decreases the inertial number in the near surface regions, where the large particles are located. Integrating the ODE (6.5) through the flow depth, subject to the no slip condition at the base, gives the velocity profile in figure 7(b). The solution lies between the velocity profiles for pure large and for pure small particles, and closely follows the small particle velocity profile in the lower part of the flow, where the small particles are concentrated. In the upper part of the flow it rapidly transitions onto a curve that is parallel to that of the pure large particles, but they attain a much higher speed than if there were no small particles in the flow. Or indeed, if the particles were evenly mixed throughout the column with  $\varphi^s = 1/2$  everywhere. The small particles therefore provide an important lubricating mechanism that can significantly increase flow speeds and the overall run-out (Kokelaar *et al.* 2014).

## 6.2. Formation of a large rich bulbous flow front on an inclined plane

Given the steady solution in §6.1, it is also interesting to consider the transient behaviour of a granular flow front when the large particles are more frictional than the fines. Analogously to the DEM study of Denissen *et al.* (2019), the solution

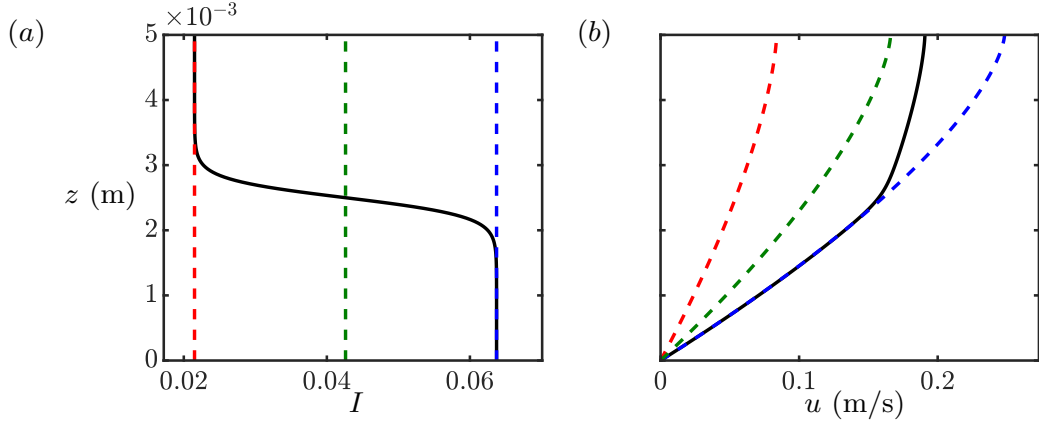


FIGURE 7. Exact solutions for (a) the inertial number and (b) the downstream velocity for a bidisperse mixture of large and small particles (black lines) on a slope inclined at  $\zeta = 24^\circ$  to the horizontal. The solutions assume a small particle concentration profile given by Gray & Chugunov’s (2006) exact solution in equations (5.8)–(5.11), with  $\overline{\varphi^s} = 0.5$  and using the parameters in table 3. Here all bulk flow parameters are identical to those in table 1 except that the large particles have  $\mu_s^l = 1.2\mu_s$  and  $\mu_\infty^\nu = 0$  for both phases. The dashed lines indicate uniform concentration solutions with red corresponding to pure large, blue corresponding to pure small particles and green being the solution for a mixture with  $\varphi^s = 0.5$  everywhere.

detailed in figure 7 is used as the boundary condition at the inlet wall  $x = 0$ , so that material entering the domain is already stratified and well-developed. All parameters are the same as those in §6.1. As shown in figure 8(a), the two-dimensional transient dynamics generates a bulbous head of large particles in front of an approximately uniform thickness upstream flow. This bulging of the surface differs from the monotonically decreasing free-surface shape, observed when there is no feedback of the segregation on the bulk, as shown in §5 and figures 3–6. The fundamental cause of this effect is that pure regions of large particles are much less mobile than the inversely graded flows behind, which are lubricated by the fine particles at the base. The preferential transport of large particles to the front, where they recirculate and accumulate (by a combination of the bulk flow field and particle segregation) causes the front to grow in size and become increasingly resistive. This causes it to bulge upwards until it either (i) stops and blocks the flow, (ii) permanently deposits some of the large grains on the substrate and flows over them (Gray & Ancey 2009), (iii) pushes some of the large particles to the side to form static levees (Pierson 1986; Pouliquen *et al.* 1997; Pouliquen & Vallance 1999; Iverson & Vallance 2001; Woodhouse *et al.* 2012; Kokelaar *et al.* 2014; Baker, Barker & Gray 2016a) or (iv) becomes sufficiently thick that a flow of large particles can form that moves slightly faster than the

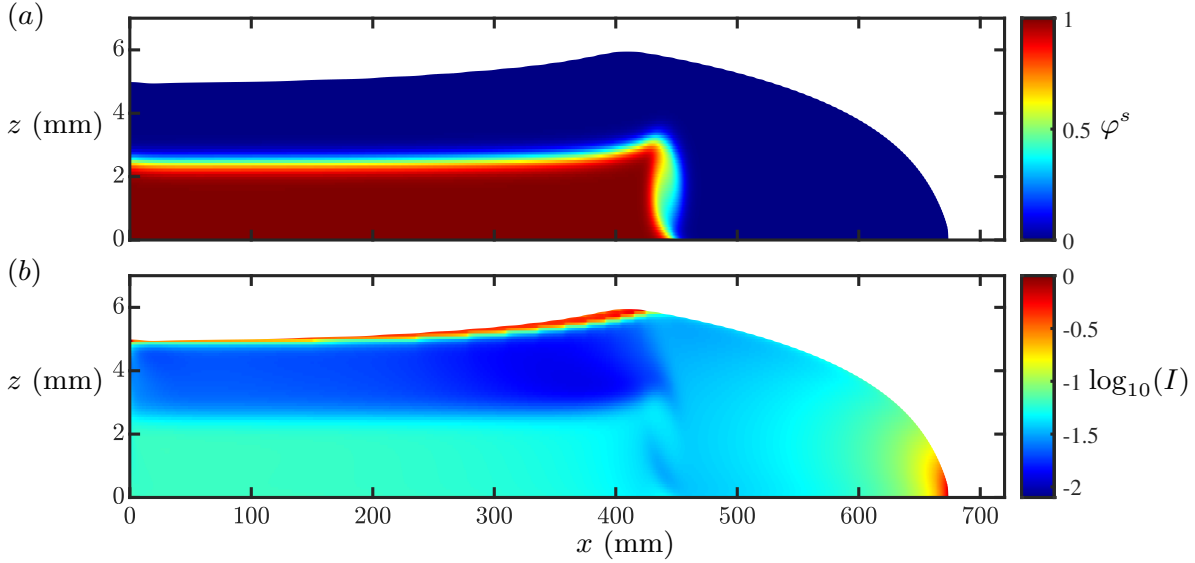


FIGURE 8. Contour plots of (a) the concentration of small particles and (b) the base 10 logarithm of the inertial number at  $t = 5.2$  s for a flow in which the large particles are more frictional than the fines. Here, as in figure 7, the parameters for each species are identical to those in table 1 except that  $\mu_{s*}^l = 1.2\mu_s$  and  $\mu_\infty^\nu = 0$  for both species. The inflow concentration is assumed to be a steady-uniform solution (5.8) of the segregation equations assuming the parameters in table 3 and with  $\bar{\varphi}^s = 0.5$ . A video of the full dynamics is available in the online supplementary material.

thinner upstream inversely-graded layer behind, to accommodate the continued supply of large particles to the front (Denissen *et al.* 2019).

This problem therefore has a very strong two-way coupling between the bulk flow and the segregation. As shown in figure 8(b), the inertial number in the flow front provides a clear demonstration of this coupling. Upstream of the head, where the flow is uniform,  $I$  approximately matches the two-layer solution from figure 7(a) and close to the flow head the fields are reminiscent of the monodisperse case detailed in figure 6(e). A diffuse breaking size segregation wave (Thornton & Gray 2008; Johnson *et al.* 2012; Gajjar *et al.* 2016) allows the two regions to connect to one another. It is located at  $x \simeq 450$  mm and is clearly evident in both the small particle concentration distribution as well as in the inertial number distribution. This is therefore the first fully coupled breaking size segregation wave to be computed.

### 6.3. Comparison to the steady-state DEM solutions of Tripathi & Khakhar (2011)

To provide a quantitative comparison for the steady-state behaviour, the theory is now compared to the bidisperse DEM simulations of Tripathi & Khakhar

(2011), using Trehwela *et al.*'s (2021) segregation velocity magnitude and the generalization of Utter & Behringer's (2004) diffusivity to bidisperse systems (rather than prescribed rates). The results shown in Tripathi & Khakhar's (2011) figure 9 correspond to flow down a plane inclined at an angle  $\zeta = 25^\circ$ , in which the large particle diameter is one and a half times the small grain diameter, i.e.  $d^l = 1.5d^s$ . The results are presented in non-dimensional form, where the length, time and velocity scalings

$$z = d^s \hat{z}, \quad h = d^s \hat{h}, \quad t = \sqrt{d^s/g} \hat{t}, \quad u = \sqrt{gd^s} \hat{u}, \quad (6.7)$$

are based on the small particle diameter  $d^s$  and gravity  $g$ . The layer depth  $h$  is assumed to be  $30d^s$ . The simulations are performed in a three-dimensional cell that is periodic in the down and cross slope directions, and has a fixed bed that is made rough with particles of diameter  $1.2d^s$ . The down and cross slope dimensions are  $20d^s \times 20d^s$ . Figure 9 shows Tripathi & Khakhar's (2011) computed small particle concentration and downslope velocity for five different depth-averaged concentrations, ranging from pure small to pure large.

For comparison, the bidisperse small particle concentration equation (2.19) is solved at steady-state, assuming the functional forms (3.7) and (3.9) for the segregation velocity magnitude and diffusivity, i.e.

$$f_{sl} = \frac{2\mathcal{B}\rho_*g||\mathbf{D}||\bar{d}^2}{\mathcal{C}\rho_*g\bar{d} + p} [(R-1) + \mathcal{E}\varphi^l(R-1)^2], \quad \mathcal{D}_{sl} = 2\mathcal{A}||\mathbf{D}||\bar{d}^2, \quad (6.8)$$

where  $\mathcal{A}$ ,  $\mathcal{B}$ ,  $\mathcal{C}$  and  $\mathcal{E}$  are non-dimensional constants and  $\dot{\gamma}$  has been replaced by its equivalent strain-rate invariant, i.e.  $2||\mathbf{D}||$ . Assuming that the downslope velocity and the small particle concentration are purely functions of the slope normal coordinate  $z$ , equation (2.19) can be integrated once with respect to  $z$ . Applying the no flux boundary condition (2.17) at the surface and/or base of the flow, the  $||\mathbf{D}||\bar{d}^2$  dependence in the segregation and diffusive terms cancels out. As a result the final steady-state ODE for the concentration is independent of the shear rate, uncoupling it from the downslope momentum balance.

The non-dimensional parameter  $\mathcal{C}$  is primarily introduced to remove the pressure singularity at the free-surface, and its measured value of  $\mathcal{C} = 0.2712$  makes very little difference to the shape of the concentration profile (Trehwela *et al.*

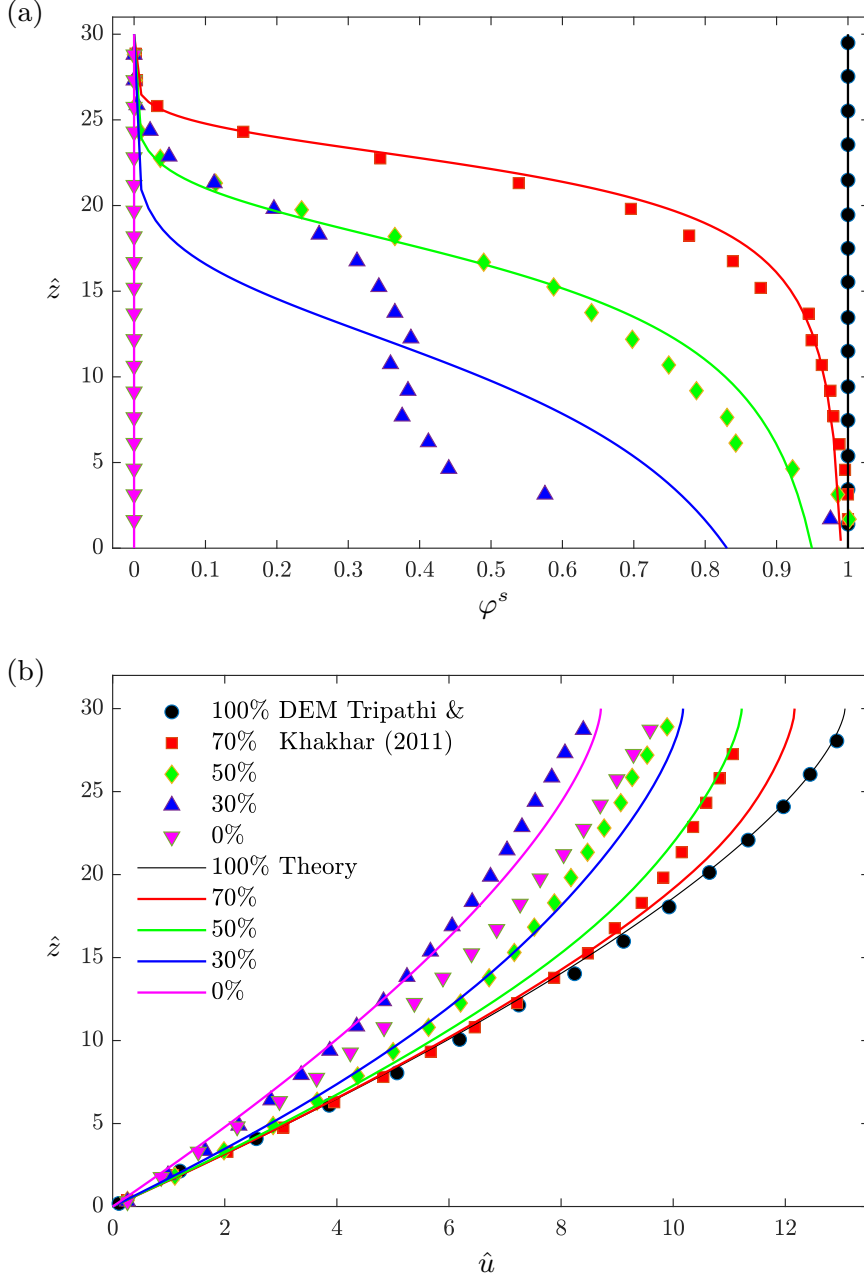


FIGURE 9. Comparison of Tripathi & Khakhar’s (2011) DEM simulations (markers) with theory (lines) for (a) the small particle concentration  $\varphi^s$  and (b) the downslope velocity  $u$  at different depth-averaged small particle concentration  $\bar{\varphi}^s = 0, 30, 50, 70$  and 100%. The non-dimensional segregation constants are summarized in table 2 and the velocity is calculated using Tripathi & Khakhar’s (2011) values of  $\mu_s = \tan(20.16^\circ)$  and  $\mu_d = \tan(37.65^\circ)$ , while  $I_0 = 0.5106$  is used to fit the steady-state 100% small particle velocity profile.

2021). If instead  $\mathcal{C}$  is assumed to be zero, and the pressure is lithostatic (5.3), then the intrinsic grain density  $\rho_*$ , gravity  $g$  and the slope angle  $\zeta$  cancel out, leaving a non-dimensional steady-state ODE for the concentration

$$\frac{d\varphi^s}{d\hat{z}} = -\frac{\mathcal{B}(R-1)\varphi^s\varphi^l(1+\mathcal{E}\varphi^l(R-1))}{\Phi\mathcal{A}(\hat{h}-\hat{z})}, \quad (6.9)$$

which is dependent purely on the grain-size ratio  $R$ . This is separable, and can

be integrated (Trehela *et al.* 2021) to give the exact solution

$$\hat{z} = \hat{h} - K(1 - \varphi^s)^{-\lambda_1}(1 + \mathcal{E}(1 - \varphi^s)(R - 1))^{\lambda_2}(\varphi^s)^{\lambda_3}, \quad (6.10)$$

where  $K$  is a constant of integration and the coefficients  $\lambda_1$ ,  $\lambda_2$  and  $\lambda_3$  are

$$\lambda_1 = \frac{\Phi\mathcal{A}}{\mathcal{B}(R - 1)}, \quad \lambda_2 = \frac{\Phi\mathcal{A}\mathcal{E}}{\mathcal{B}(1 + \mathcal{E}(R - 1))}, \quad \lambda_3 = \frac{\Phi\mathcal{A}}{\mathcal{B}(R - 1)(1 + \mathcal{E}(R - 1))}. \quad (6.11)$$

For a given depth-averaged small particle concentration  $\overline{\varphi^s}$  the constant of integration  $K$  can be determined iteratively. Figure 9(a) shows the comparison between these exact solutions and the DEM simulations of Tripathi & Khakhar (2011) for depth-averaged concentrations  $\overline{\varphi^s} = 0, 30, 50, 70$  and 100%. The agreement in the monodisperse limits of  $\overline{\varphi^s} = 0$  and 100% are guaranteed. There is also very good agreement at  $\overline{\varphi^s} = 50\%$  and 70% using exactly the same non-dimensional constants  $\mathcal{A}$ ,  $\mathcal{B}$  and  $\mathcal{E}$  determined experimentally by Trehela *et al.* (2021) and summarized in table 2. The theory therefore matches the stronger segregation at the surface than the base of the flow, as well as the gradient of the concentration profiles, without the need for any fitting parameters. This is strong evidence that Trehela *et al.*'s (2021) theory captures the essence of the segregation process. It also contrasts with Gray & Chugunov's (2006) solution, where the ratio of segregation to diffusion is uniform with depth. The agreement between Trehela *et al.*'s (2021) theory and Tripathi & Khakhar's (2011) DEM simulations is not as good at  $\overline{\varphi^s} = 30\%$ . The DEM results at  $\overline{\varphi^s} = 30\%$  look slightly odd, with a layer of almost pure small particles at the base of the cell and a much more diffuse profile higher up. It is therefore possible that, in this particular case, Tripathi & Khakhar's (2011) DEM simulations have not fully reached steady-state.

Figure 17 of Tripathi & Khakhar (2011) suggests that the friction in both their monodisperse and bidisperse systems was closely approximated by the classical  $\mu(I)$  law (2.7), using the generalized inertial number (3.2) with a local average grain size  $\bar{d}$ . To leading order, therefore, the macroscopic friction coefficients  $\mu_s$  and  $\mu_d$ , as well as the non-dimensional constant  $I_0$  are the same for the large and small particles. Tripathi & Khakhar (2011) suggested that a good overall fit to the data was provided by  $\mu_s = \tan(20.16^\circ)$ ,  $\mu_d = \tan(37.65^\circ)$  and  $I_0 = 0.434$ . These values are, however, not good for the particular set of simulations shown in

Tripathi & Khakhar's (2011) figure 9, and reproduced here in figure 9. To select a better fit, the Bagnold solution (5.4) has been non-dimensionalized using the scalings (6.7) to give

$$\hat{u}_{Bagnold} = \frac{2}{3} I_{\zeta} \sqrt{\Phi \cos \zeta} \left( \hat{h}^{\frac{3}{2}} - (\hat{h} - \hat{z})^{\frac{3}{2}} \right) \quad (6.12)$$

and then fitted to the small particle velocity DEM data using a least squares fit. This determines the value of  $I_{\zeta}$ , which for the classical friction law (2.7) of Jop *et al.* (2006) is defined as

$$I_{\zeta} = I_0 \left( \frac{\tan \zeta - \mu_s}{\mu_s - \tan \zeta} \right). \quad (6.13)$$

The values of  $\mu_s$ ,  $\mu_d$  and  $I_0$  can therefore be modified, while still fitting the data, provided the same value of  $I_{\zeta}$  is obtained. There are an infinite number of combinations that will do this. This paper therefore assumes that the values of  $\mu_s$  and  $\mu_d$  are the same as Tripathi & Khakhar (2011), but that  $I_0 = 0.5106$ . To solve for the velocity profiles at other concentrations it is necessary solve the ODE (6.5) in non-dimensional form, i.e.

$$\frac{d\hat{u}}{d\hat{z}} = \frac{I_{\zeta} \sqrt{\Phi \cos \zeta}}{(\varphi^s + R\varphi^l)} (\hat{h} - \hat{z})^{\frac{1}{2}}, \quad (6.14)$$

subject to a no-slip boundary condition at the base. In the ODE (6.14) the small particle concentration  $\varphi^s = 1 - \varphi^l$  is given by Trehwela *et al.*'s (2021) exact solution (6.10). The solutions are shown in figure 9(b). The 100% small particle solution agrees extremely well with the Bagnold solution (6.12), which is not too surprising as the parameters  $\mu_s$ ,  $\mu_d$  and  $I_0$  have been chosen specifically to match this curve. The monodisperse large particle solution also has a Bagnold like velocity profile, but the magnitude of the velocities are slightly underpredicted. In principle, the monodisperse small particle solution should be a factor  $R$  larger than the large particle solution. The fact that they are not, is an indication of either (i) the level of noise in Tripathi & Khakhar's (2011) system, or (ii) the basal roughness not scaling with the size of flowing particles (i.e. non-local effects). Since the deviations of the intermediate solutions from the DEM data are of a similar order of magnitude, it is probably unwise to read too much into the precise comparisons. The predicted velocity profiles at intermediate



concentrations monotonically decrease in magnitude as the small particle content decreases. This is broadly speaking what the DEM data shows, however, the case  $\overline{\varphi^s} = 30\%$  the DEM solution is again anomalous, being below the case of pure large particles (Tripathi & Khakhar 2011). To be sure that this is real behaviour, rather than an anomaly, more precise DEM solutions are required that average over significantly more than the approximately 4,000-12,000 particles used by Tripathi & Khakhar (2011).

## 7. Fully coupled rotating drum simulations

Particle segregation in non-circular rotating drums provides an ideal test case for the two-way coupled model, as the particles strongly segregate and diffuse in the near surface liquid-like avalanche, but not in the solid-like rotating body beneath. Computing the bulk flow field in a rotating drum is still a significant challenge. Indeed, recent segregation simulations in a circular rotating drum (Schlick *et al.* 2015) have prescribed the steady-state incompressible bulk velocity field based on fits to DEM simulations; a process that inherently relies on the steady-state nature and simple geometry of the circular drum. More complex models that do use a continuum approach to calculate the bulk flow in a circular drum (e.g. Liu *et al.* 2018, 2019), do so with rate-independent elasto-plastic constitutive laws which are prone to ill-posedness (Schaeffer 1987). This paper goes considerably further, by using the partially regularized  $\mu(I)$ -rheology and the recent segregation model of Trehwela *et al.* (2021) to simultaneously compute the fully two-way coupled bulk flow, segregation and diffusion in a square rotating drum.

### 7.1. Modelling the bulk flow, segregation and diffusion in a square rotating drum

It is useful to have two coordinate systems to simulate the flow in the drum. The first is a rectangular Cartesian coordinate system  $Oxz$  that is fixed and centred at the axis of rotation of the drum, which lies at the centre of the square. The  $z$  axis is aligned with the gravitational acceleration  $\mathbf{g}$ , but points upwards in the opposite sense. A second coordinate system  $OXZ$  is inclined at an angle  $\theta$  to  $Oxz$  and rotates with the drum. The axes are aligned with the drum walls, so the drum lies in the region  $-L \leq X \leq L$ ,  $-L \leq Z \leq L$ , where  $2L$  is the length of the walls.

Initially, the  $OXZ$  axes coincide with  $Oxz$  and the concentrations of excess air, small particles and large particles are

$$(\varphi^a, \varphi^s, \varphi^l)|_{t=0} = \begin{cases} (1, 0, 0), & \text{for } H < Z \leq L, \\ (0, \frac{1}{2}, \frac{1}{2}), & \text{for } -L \leq Z \leq H, \end{cases} \quad (7.1)$$

where  $L = 0.1$  m and  $H = 0.04$  m, implying a 70% fill fraction with a 50:50 mix of large and small particles of diameters  $d^l = 2$  mm and  $d^s = 1$  mm, respectively. A fill fraction above 50% is chosen so that an undisturbed core forms in the centre of the drum, consisting of material which never enters the avalanche (see e.g. Gray & Hutter 1997; Gray 2001). All the material is initially assumed to be in solid body rotation

$$\mathbf{u}_0 = \Omega r \boldsymbol{\theta}, \quad (7.2)$$

where  $\Omega$  is the rotation rate, the radial coordinate  $r = \sqrt{x^2 + z^2}$  and  $\boldsymbol{\theta}$  is the azimuthal unit vector. A constant rotation rate of  $\Omega = -\pi/5$  rad/s is specified, with the negative sign denoting clockwise rotation. This corresponds to one full revolution every 10 s, placing the flow at the upper end of rolling flow (Henein *et al.* 1983; Ding *et al.* 2002; Yang *et al.* 2008). This is also known as the continuous, or the continuously avalanching, regime (Rajchenbach 1990; Gray 2001) as a quasi steady-state avalanche forms, with continuous erosion and deposition occurring with the solid-rotating body of grains beneath. The frictional parameters are the same for the large and small particles, and the momentum coupling enters via the evolving local average particle size  $\bar{d}$  in the generalized inertial number (3.2). The values of  $\mu_s$ ,  $\mu_d$  and  $I_0$  are the same as those used to fit the DEM simulations of Tripathi & Khakhar (2011) (see fig. 9), and the theory is partially regularized (Barker & Gray 2017) by introducing a creep state at low inertial numbers and a linear friction regime at high inertial numbers. The values of all the frictional parameters are summarized in table 4, together with the particle sizes, and the air segregation and diffusion rates. The segregation of the particles is performed using the same non-dimensional constants  $\mathcal{A}$ ,  $\mathcal{B}$ ,  $\mathcal{C}$  and  $\mathcal{E}$  suggested by Trehwela *et al.* (2021) and summarized in table 2.

The velocity field  $\hat{\mathbf{u}}$  in the rotating frame is related to the velocity  $\mathbf{u}$  in the

---


$$\begin{array}{lll}
\mu_s = \tan(20.16^\circ), & \mu_d = \tan(37.65^\circ), & \mu_\infty = 0.03, \\
I_0 = 0.5106, & \alpha = 1.9, & I_1 = 0.01886 \\
d^l = 2 \text{ mm} & d^s = 1 \text{ mm} & R = 2, \\
f_{al} = f_{as} = 1 \text{ m/s}, & \mathcal{D}_{al} = \mathcal{D}_{as} = 0 \text{ m}^2/\text{s}, & \mathbf{e} = -\mathbf{g}/|\mathbf{g}| = \mathbf{k}.
\end{array}$$


---

TABLE 4. The fully coupled rotating drum simulations are performed with Barker & Gray’s (2017) partially regularized friction law with parameters that match the steady-state DEM simulations of Tripathi & Khakhar (2011) shown in figure 9. The value of  $\mu_\infty$  is chosen to insure that the equations remain well-posed up to a maximum inertial number  $I_{max} = 16.20$ , while  $I_1$  is the minimum well-posed inertial number in the unregularized law. To handle the evolving free-surface, the excess air segregates with a constant rate  $f_{al} = f_{as}$  from the large and small particles and does not diffuse with them. The air phase is assumed to segregate upwards in the direction of the unit vector  $\mathbf{k}$  along the  $z$ -axis, which this time is aligned with gravity.

---

fixed coordinate system by the relation

$$\hat{\mathbf{u}} = \mathbf{u} - \Omega r \boldsymbol{\theta}. \quad (7.3)$$

As the drum rotates the no-slip and no-penetration (no flux) conditions are enforced on the drum walls, which implies that

$$\hat{\mathbf{u}} = \mathbf{0}, \quad \text{on} \quad X = \pm L, \quad \text{and} \quad Z = \pm L. \quad (7.4)$$

These conditions are mapped back to the fixed coordinate system and applied on the moving mesh using OpenFOAM’s mesh-motion routines. The computations are performed on a regular  $N \times N$  mesh, with results presented for the finest resolution studied of  $N = 200$ . The simulation runs for 8 full revolutions.

### 7.2. Bulk velocity, pressure and inertial number in the square drum

Initially the free-surface is flat and the material is in solid body rotation, see equations (7.1) and (7.2). The entire body of grains is therefore quasi-static in the moving frame, and the high viscosity cut-off (4.12) remains active until the free-surface inclination nears the static angle of friction

$$\zeta_s = \tan^{-1}(\mu_s), \quad (7.5)$$

at which point the material near the free-surface fails and avalanches downslope. After the initial failure and slump, a continuously avalanching regime rapidly establishes itself, as shown in figure 10 and the supplementary online videos. There is a rapid liquid-like avalanche close to the free-surface and a solid-like quasi-static

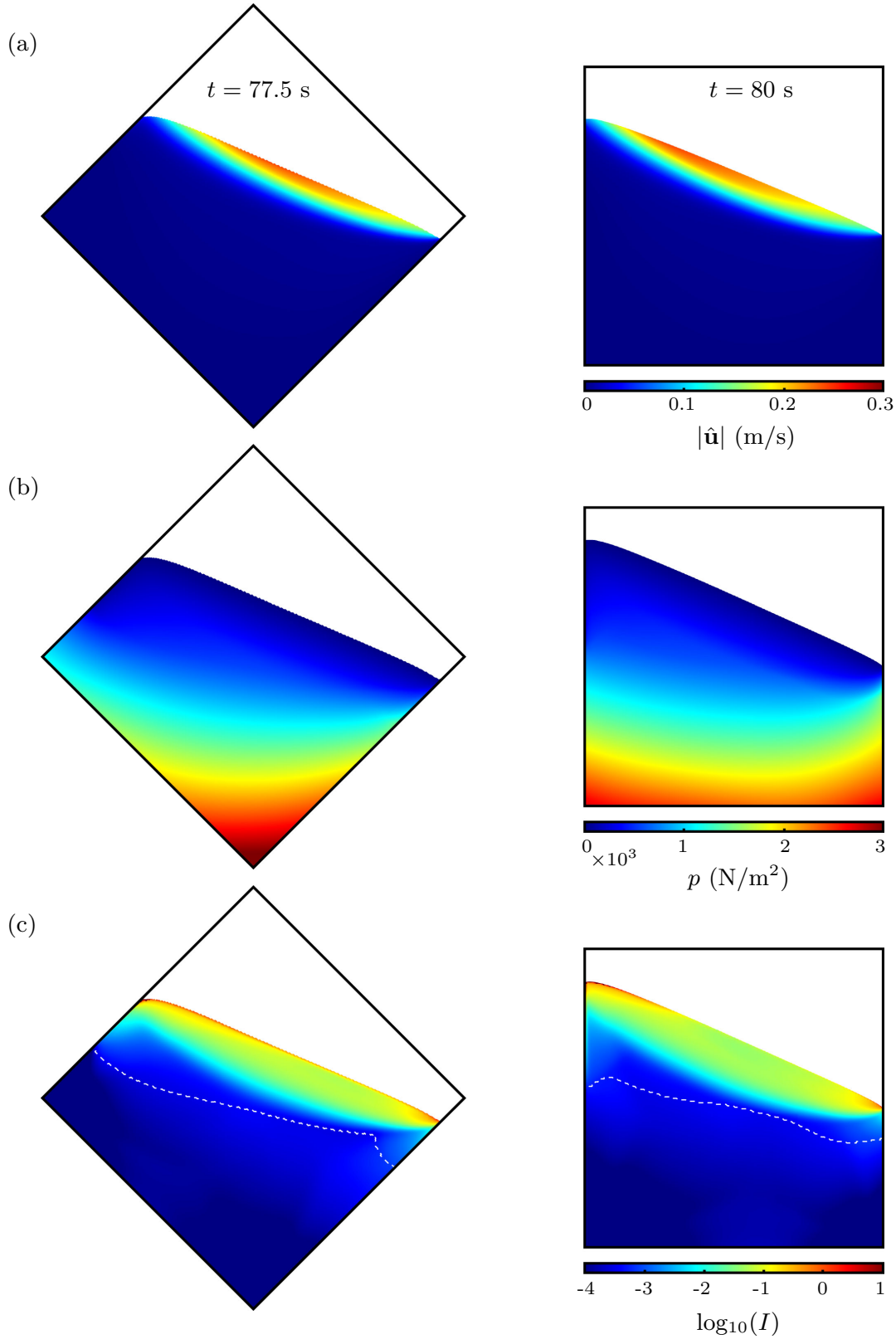


FIGURE 10. Periodic motion of the bulk flow shown at  $t = 78.75$  s (left column) and  $t = 80$  s (right column), for (a) velocity magnitude in the rotating frame (i.e. minus the solid body rotation), (b) pressure and (c) base 10 logarithm of the inertial number  $I$ . The dashed lines in (c) indicate the height below which the high viscosity cut-off becomes active. The parameters used to compute the bulk flow, segregation and diffusion are summarized in tables 2 and 4. Supplementary videos showing the full periodic solution are available in the online supplementary material.

region beneath (fig. 10a). The angle of the free-surface remains close to the static value  $\zeta_s$ , but the position of the free-surface subtly rises and falls as the finite volume of grains is incorporated into the constantly changing intersections with the shape of the drum during each quarter turn. The flow therefore has a quasi periodic pulsing behaviour, with peak surface velocities (at the centre and surface of the flow) changing in time, e.g. the peak free-surface velocity is faster at  $t = 80$  s than at  $t = 78.75$  s in figure 10(a). As shown in §6.3, the variations in velocity with the flow composition are subtle, and do not provide a strong feedback on the bulk flow at this fill height. However, the experiments of Zuriguel *et al.* (2006) imply that for fill levels close to 50% these subtle composition dependent velocity changes can cause the formation of petal-like structures in the deposit, and so can be very important.

As the flow pulses, the surface avalanche becomes deeper directly beneath the region where the peak velocities are attained. The avalanche depth also changes along its length, reaching a peak near its centre. Typically the main flow is confined to a layer with a maximum thickness of 1.6 cm, which gives the rapid free-surface flow a shallow aspect ratio, consistent with the assumptions underpinning theoretical models for avalanches (e.g. Savage & Hutter 1989; Gray 2001; Gray & Edwards 2014). Close to the free-surface the pressure is approximately lithostatic and is aligned with the free-surface (fig. 10b) as one might expect. However, lower down the pressure rises to much higher values and pulses as the overall volume of grains redistributes itself in the changing geometry of the walls that confine it. The base ten logarithm of the inertial number is shown in figure 10(c) and also identifies the near surface region where the failure occurs. The flow is in a creep state for  $I < I_1 = 0.01886$ . This region lies significantly higher in the flow than the Newtonian viscous region, which is activated by the numerical regularization (4.12) at high viscosities. The dominant rheology in the simulation is therefore the granular rheology, which involves regions of both creep and dynamic motion.

For fill levels above approximately 55% a solid core develops (Mounty 2007), within which particles are simply rotated around with the drum and undergo a small amount of creep when they are closer to the free-surface. The remaining grains pass through both the solid-like and fluid-like regions. These particles are rotated around with the drum in the solid-body region, until they approach

the near surface layers when they begin to creep downslope. As an individual particle is rotated further towards the free-surface the creep becomes progressively stronger, until finally it avalanches downslope in the liquid-like surface avalanche. As more particles are entrained into this avalanche it becomes deeper and flows faster, so peak velocities are reached midway down the slope, after which particles are deposited from the base of the flow, and the avalanche thins and slows. An individual particle therefore accelerates downslope in the first half of the avalanche and decelerates after the midway point, before being deposited into the slowly creeping body of rotating grains beneath. Unlike a circular drum, where monodisperse particles form closed streamlines, the changing geometry of the confining walls adds considerable complexity to the problem. This is because the underlying particle trajectories become chaotic even for monodisperse flows (Hill *et al.* 1999; Ottino & Khakhar 2000). Particle-size segregation, however, introduces a strong organizational influence on the resulting patterns that form.

### 7.3. *The particle size distribution in the square drum*

The dynamics of the mixing and segregation process are shown in figure 11 and the supplementary online video. As the drum rotates up to the static angle of friction there is no shear and hence no segregation or diffusion. However, as soon as the initial failure occurs, and the avalanche flows downslope, the particles begin to segregate with the large particles rising to the free-surface and the small particles percolating downwards. The linear shear rate dependence in equations (6.8) ensures that both the segregation and diffusion are confined to the thin avalanching layer close to the free-surface, with the additional pressure dependence ensuring that segregation shuts off more rapidly than the diffusion with increasing depth (Golick & Daniels 2009; Fry *et al.* 2018; Trewhela *et al.* 2021). This effect is compounded by the fact that particles near the free-surface travel the longest distance through the liquid-like avalanche, while those that are entrained at lower levels may move only a short distance before they are deposited back into the solid-like rotating body of grains beneath. As a result, after the first full rotation of the drum (at  $t = 10$  s) the clearest segregation can be seen in the large particles that are able to rise to the surface and collect at the top of the flow before being deposited near the drum wall. The rest of the grains remain quite well mixed.

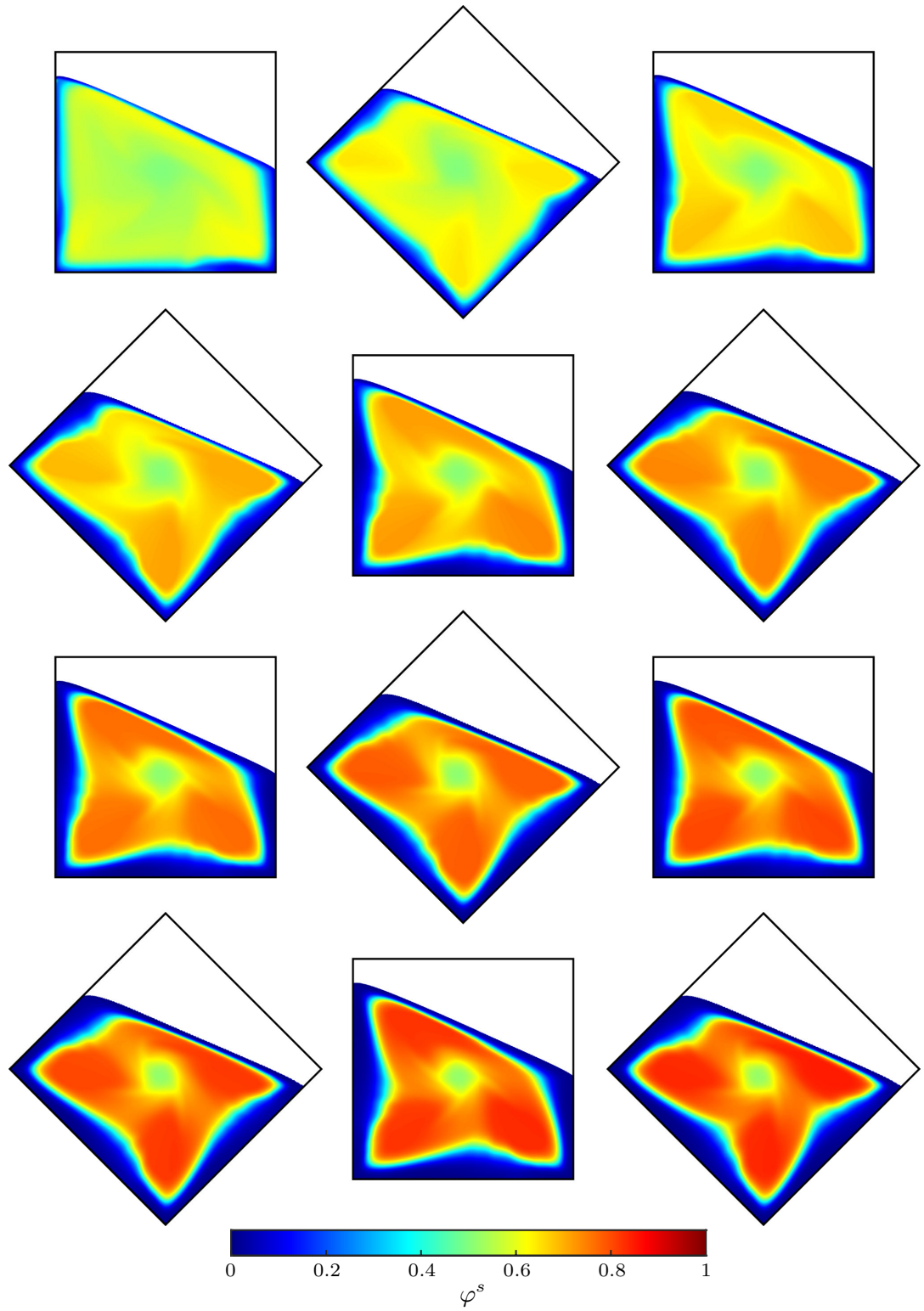


FIGURE 11. Fully coupled simulation of a bidisperse granular mixture in a square rotating drum using the parameters in tables 2 and 4. The drum walls are of length 0.2 m. The first panel plots  $\varphi^s$  at 10 s and subsequent panels correspond to a further 6.25 s of rotation, or 5/8 of a full revolution, up to 78.75 s. A video is available in the online supplementary material.

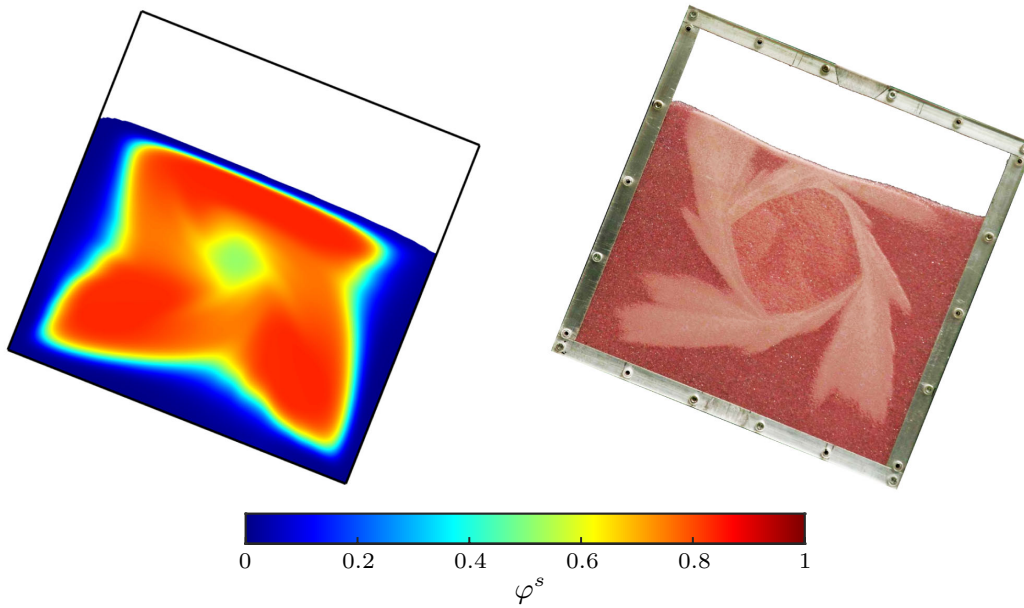


FIGURE 12. Computed particle size distribution after 78.1 seconds (left) and a comparable pattern formed in a rotating drum Mounty (2007) with small white particles ( $75\text{--}150\ \mu\text{m}$ ) and the large red particles ( $400\text{--}500\ \mu\text{m}$ ).

After approximately  $3/4$  of a drum revolution all the material that is able to pass through the surface avalanche has done so, and the material that is subsequently entrained is no longer homogeneously mixed. The large particles that were deposited next to the drum wall are rotated around and re-entrained into the avalanche right at the back of the flow, where the avalanche is thinnest. There is therefore no need for them to segregate towards the surface again, as they are naturally re-entrained on trajectories that pass through the surface layers of the avalanche. The particles that lie closer to the drum core are naturally entrained onto paths that take them through lower regions of the avalanche. They therefore get another chance to segregate again each time they pass through the avalanche. This process can be seen slowly sharpening the segregation in the successive panels of figure 11. With increasing time, the large particle region adjacent to the drum wall thickens up and regions with high concentrations of small particles start to emerge, as the avalanche at the surface becomes progressively more inversely graded. Complete separation of the large and small grains does not occur, however, because of the diffusive remixing process in equation (2.19).

The combination of particle segregation and the rising and falling of the free-surface height as the drum rotates leads to the spontaneous formation of three lobes with high concentrations of small particles, that are oriented towards the



corners of the drum. These lobes are interesting because they propagate around the drum faster than the drum rotates, with a period of approximately 7.5 s. The lobes are in qualitatively very good agreement with the experiments of Hill *et al.* (1999), Ottino & Khakhar (2000) and Mounty (2007), as shown in figure 12. The simulations also predict the formation of a central core within which the concentration is almost unchanged from its initial value. This core forms a shape that is almost square and lies at an angle of  $45^\circ$  to the square drum walls, which is also qualitatively in agreement with the experiments of Hill *et al.* (1999), Ottino & Khakhar (2000) and Mounty (2007). However, the simulated central core is about half the diameter of that in experiment. The reason for this is that the surface avalanche is much deeper in the simulations than in the experiments. This is not necessarily a deficiency of the model. The experiments are performed in drums with a narrow gap between the sidewalls; as a result the avalanche is thinner and faster than in a drum with a wide cross section (Jop *et al.* 2005) and hence the central core is larger.

One of the important consequences of the  $\|\mathbf{D}\|\bar{d}^2$  dependence in the segregation velocity magnitude and diffusivity in equations (6.8) is that the timescale for segregation and diffusion to occur is proportional to  $h^2/(\dot{\gamma}\bar{d}^2)$ . It therefore takes longer to segregate in a deeper avalanche, or with smaller average grain sizes. This makes direct comparison with the experiments difficult, as the depth and velocity of the surface avalanche is strongly influenced by sidewall friction. In principle, it is very easy to include the effect of sidewall friction in the simulations. However, the numerical method requires sufficient grid points to be located in the surface avalanche. For a regular grid this requires higher resolution throughout the drum, which dramatically increases the time necessary to produce grid converged results, and so this is not done here. Instead the grain sizes are made larger in order to get the pattern to form in the rotating drum simulations in a comparable timescale to that in the experiments.

The lobes do not appear to reach a quasi-periodic steady state, but have small protuberances that continue to evolve when tracking a particular lobe. This is also in accordance with experimental observation, as a non-homogeneous initial distribution of particles can lead to lobes of different sizes, which appear to persist indefinitely. Figure 11 also shows that over long periods of time the central core

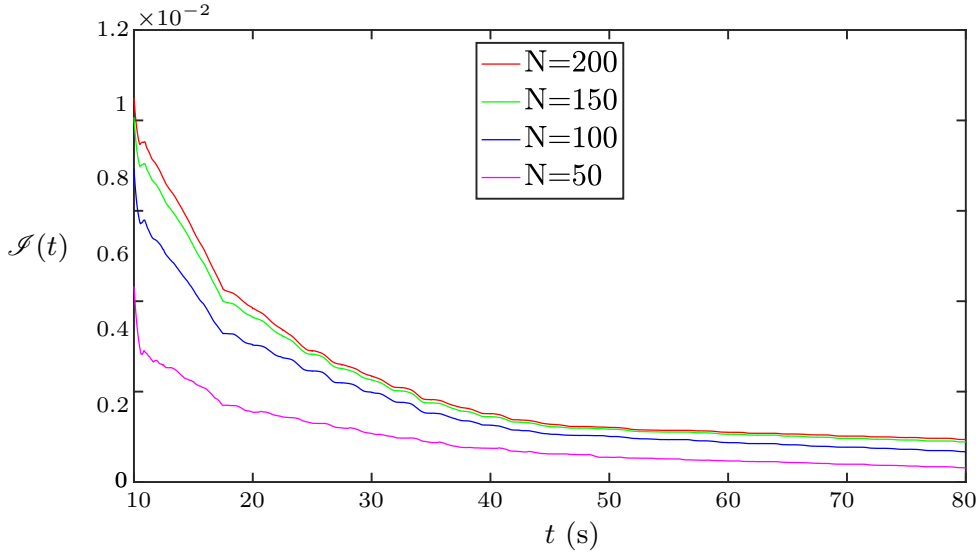


FIGURE 13. Integral  $\mathcal{J}(t)$  of the small particle concentration difference between the current state and the state of one full revolution earlier, as a function of time and for four different mesh resolutions  $N$  to demonstrate grid convergence of the numerical solution.

contracts towards the origin. This is due to the slow creep that occurs as the material in the solid body region is rotated through the near surface creeping zone, where both segregation and diffusion can act over very long timescales. This creep can be minimized either by (i) introducing sidewall friction or (ii) by using constitutive equations with a static yield stress. However, both of these require additional physics to be included in the model.

#### 7.4. Grid convergence

A grid convergence study was carried out for four different mesh refinements. Figure 13 shows the evolution over time of the integral  $\mathcal{J}(t)$ , defined as

$$\mathcal{J}(t) = \frac{1}{4L^2} \iint_{N^2} |\varphi^s(t, X, Z) - \varphi^s(t - T, X, Z)| dX dZ, \quad (7.6)$$

where  $T = 10$  s represents one full revolution of the drum and  $N^2$  is the number of grid cells in the domain. The quantity  $\mathcal{J}(t)$  measures the small particle concentration difference between the current state and the state a full rotation period earlier. The maximal value of  $\mathcal{J}(t)$  is unity. Numerical diffusion means that overall segregation is weaker when the flow is under resolved, and, at  $N = 50$ , regions of high concentration fail to coalesce. The increasing proximity of the curves with increasing grid resolution, and particularly the closeness of  $\mathcal{J}(t)$  for  $N = 150$  and  $N = 200$ , demonstrate numerical grid convergence. This relatively

high number of grid points is required to properly resolve the shallow avalanche at the free-surface of the flow where the segregation and diffusion predominantly occur. As noted earlier, higher grid resolutions will be necessary to resolve the thinner surface avalanches that develop in experiments with sidewall friction (Hill *et al.* 1999; Ottino & Khakhar 2000; Jop *et al.* 2005; Mounty 2007).

The integral  $\mathcal{J}(t)$  implies that the square drum does not approach a periodic quasi-steady solution, but settles down, after about four complete revolutions, to a state where  $d\mathcal{J}(t)/dt$  is small and  $\mathcal{J}(t)$  is non-zero. This represents a fully segregated mixture with time-dependent perturbations that propagate around the system.

## 8. Conclusions and discussion

This paper develops a general framework for simultaneously solving for the flow and segregation of polydisperse granular materials. At its heart lies the partially regularized incompressible  $\mu(I)$ -rheology of Barker & Gray (2017) and the polydisperse segregation theory of Gray & Ancy (2015), which is generalized here to allow for different diffusion rates and segregation directions between the constituents. The coupling between the models is crucial and can be very complex. Three primary coupling mechanisms are identified; (i) advection of the particle concentrations by the bulk velocity, (ii) feedback of the particle-size and/or frictional properties on the bulk flow field and (iii) influence of the shear rate, pressure, gravity, particle size and particle-size ratio on the locally evolving segregation (Trehwela *et al.* 2021) and diffusion rates (Utter & Behringer 2004).

A general numerical method is developed to solve the resulting system of equations, which is implemented in OpenFOAM. In order to solve free-surface flow problems that commonly arise in both geophysical and industrial contexts, a new interface sharpening procedure is developed that uses the multi-component segregation theory to segregate excess air out of the granular material. The new method generates a sharp interface between the grains and the air and prevents the formation of mesh-dependent trapped air bubbles or air layers, which form with standard interface sharpening techniques (Rusche 2002; Weller 2008). In fluid flows, bubbles may be realistic, but in granular flows they are not, because the

air can usually escape easily through the pore space. Bubble trapping in solid-like granular flows is a common problem, and the new segregation based approach to interface sharpening solves many of the issues when combining multiphase methods with granular flow theory and may be applicable to a wide range of problems.

The numerical method is used to investigate one-way coupled problems in §5 and two-way coupled problems in §6 and §7. The advantage of investigating one-way coupled problems is that it allows the numerical method to be extensively tested against exact solutions for (i) concentration shock wave development (fig. 3), (ii) steady-state Bagnold flow (fig. 4a), (iii) steady-state concentration profiles (fig. 4b), and (iv) the formation of steadily travelling flow fronts (figs. 5 and 6). These simple one-way coupled simulations also qualitatively show how large and small particles are advected in a spatially and temporally evolving bulk flow field, allowing, for instance, the formation of a large rich flow front to develop (fig. 3). When the large particles are more frictional than the fines (in §6) the large rich flow front slows down, and a bulbous head develops (see fig. 8) that is relevant for geophysical flows (Denissen *et al.* 2019).

To provide a quantitative test of the model, Trewhela *et al.*'s (2021) experimental scaling law for segregation is implemented together with a generalization of Utter & Behringer's (2004) diffusivity in §6.3. Figure 9(a) shows very good agreement with Tripathi & Khakhar's (2011) DEM simulation data for the steady-state concentration profiles with depth, without the need for any fitting parameters. The frictional feedback arises through the use of the generalized inertial number (3.2), which is based on the average local grain size  $\bar{d}$  defined in (3.1). For an inclined flow down a plane, this monotonically decreases the velocity at all heights as the proportion of large particles increases. This general trend is also seen in Tripathi & Khakhar's (2011) DEM data (fig. 9b), although the fits are not precise. The fact that Tripathi & Khakhar's (2011) pure large and pure small simulations do not obey the Bagnold scaling precisely, suggests that more accurate DEM simulations are required to fully test the model, in particular, there may be an influence from the basal roughness, which does not change as the mean grain size changes, and their data at 30% small particle concentration appears anomalous.

As a demonstration of the potential of the model, the fully coupled flow in a

square rotating drum is computed in §7. Such a configuration is a real challenge for current models, because the flow field is not steady and can not easily be prescribed or approximated from DEM simulations. The numerical simulations (figs. 10–12) show that the fully coupled model is able to compute the spatially evolving velocity, pressure and concentration fields as a function of time, and that a petal-like concentration pattern spontaneously forms in the rotating deposit, which is qualitatively very similar to that observed in the experiments of Hill *et al.* (1999), Ottino & Khakhar (2000) and Mounty (2007). Precise experimental comparison is not possible at this stage, however, because the experiments are strongly influenced by wall friction, making the free-surface avalanche thinner and faster than in the absence of sidewalls (Jop *et al.* 2005). Computations that include sidewall friction are possible, but will require finer meshes to resolve the segregation within the avalanche, and consequently will take much longer to run.

The examples investigated in this paper provide the briefest glimpse at what is possible within this powerful new theoretical and computational framework. There is still much work to be done to fully understand the feedbacks and how they can affect real world problems of practical interest. In some situations the feedback may be relatively subtle, i.e. the quantitative values for the velocity, pressure and concentrations are changed, but they don't have a big impact on the subsequent flow (see e.g. figs. 10–12). However, in other situations these (sometimes small) quantitative changes can induce fundamental qualitative change in the solutions. A prime example of this is the formation of a bulbous large rich head (Gray & Ancy 2009; Denissen *et al.* 2019), which is calculated in two-dimensions for the first time in §6.2 and shown in detail in the supplementary video to figure 8. In three-dimensions this solution can become unstable to span-wise perturbations and instead generates a series of leveed flow fingers (Pouliquen *et al.* 1997; Woodhouse *et al.* 2012; Baker *et al.* 2016b) that are directly relevant to the self-channelization of snow avalanches, debris flows and volcanic pyroclastic flows (Pierson 1986; Iverson & Vallance 2001; Johnson *et al.* 2012; Rocha *et al.* 2019). Much less is known about the feedbacks between segregation and flow in industrial problems, but they most definitely occur (see e.g. Zuriguel *et al.* 2006). It is hoped that our new found understanding can also be exploited in future to improve, and

control, the flowability of bulk solids as well as mitigate the worst effects of particle segregation.

## Acknowledgements

M.R. received funding from the European Union's Horizon 2020 research and innovation programme under the Marie Skłodowska-Curie grant agreement No. 721403. This research was also supported by NERC grants NE/E003206/1 and NE/K003011/1 as well as EPSRC grants EP/I019189/1, EP/K00428X/1 and EP/M022447/1. J.M.N.T.G. is a Royal Society Wolfson Research Merit Award holder (WM150058) and an EPSRC Established Career Fellow (EP/M022447/1).

## Declaration of Interests

The authors report no conflict of interest.

## Supplementary material

Supplementary videos are available at <https://doi.org/10.1017/jfm.2020.973>.

## Appendix A. Gray & Thornton's (2005) concentration shock solution

Gray & Thornton's (2005) concentration shock solution assumes that there is no diffusion (in any direction) and only resolves the slope normal component of the segregation flux. In this case there are three concentration shocks that have linear profiles when solved in streamfunction coordinates  $(\Psi, x)$ . The lower shock  $\psi_{lower}$  separates a pure region of small particles from the inflow small particle concentration  $\varphi_0^s$ , the upper shock  $\psi_{upper}$  separates the inflow concentration from a pure region of large grains and the final shock  $\psi_{final}$  separates a pure region of large grains from a pure region of fines. Assuming that the flow is of thickness  $h$  the equations for the three shocks are

$$\psi_{lower} = f_{sl}\varphi_0^s x \cos \zeta, \quad x < \psi(h)/(f_{sl} \cos \zeta), \quad (\text{A } 1)$$

$$\psi_{upper} = \psi(h) - f_{sl}(1 - \varphi_0^s)x \cos \zeta, \quad x < \psi(h)/(f_{sl} \cos \zeta), \quad (\text{A } 2)$$

$$\psi_{final} = \varphi_0^s \psi(h), \quad x > \psi(h)/(f_{sl} \cos \zeta), \quad (\text{A } 3)$$

where the streamfunction  $\psi$  for the Bagnold velocity profile (5.4) is

$$\psi(z) = \int_0^z u(z') dz' = \frac{2I_\zeta \sqrt{\Phi g \cos \zeta}}{15d} \left( 2(h-z)^{\frac{5}{2}} - 2h^{\frac{5}{2}} + 5h^{\frac{3}{2}}z \right). \quad (\text{A } 4)$$

## REFERENCES

- ANCEY, C., COUSSOT, P. & EVESQUE, P. 1999 A theoretical framework for granular suspensions in a steady simple shear flow. *J. Rheol.* **43**, 1673.
- BAKER, J. L., BARKER, T. & GRAY, J. M. N. T. 2016*a* A two-dimensional depth-averaged  $\mu(I)$ -rheology for dense granular avalanches. *J. Fluid Mech.* **787**, 367–395.
- BAKER, J. L., JOHNSON, C. G. & GRAY, J. M. N. T. 2016*b* Segregation-induced finger formation in granular free-surface flows. *J. Fluid Mech.* **809**, 168–212.
- BARKER, T. & GRAY, J. M. N. T. 2017 Partial regularisation of the incompressible  $\mu(I)$ -rheology for granular flow. *J. Fluid Mech.* **828**, 5–32.
- BARKER, T., SCHAEFFER, D. G., BOHORQUEZ, P. & GRAY, J. M. N. T. 2015 Well-posed and ill-posed behaviour of the  $\mu(I)$ -rheology for granular flow. *J. Fluid Mech.* **779**, 794–818.
- BARKER, T., SCHAEFFER, D. G., SHEARER, M. & GRAY, J. M. N. T. 2017 Well-posed continuum equations for granular flow with compressibility and  $\mu(I)$ -rheology. *Proc. Roy. Soc. A* **473** (2201).
- BRIDGWATER, J., FOO, W. & STEPHENS, D. 1985 Particle mixing and segregation in failure zones - theory and experiment. *Powder Technol.* **41**, 147–158.
- CHADWICK, P. 1976 *Continuum Mechanics. Concise theory and problems*. George Allen & Unwin.
- CHRISTEN, M., KOWALSKI, J. & BARTELT, P. 2010 Ramms: numerical simulation of dense snow avalanches in three-dimensional terrain. *Cold Reg. Sci. Tech.* **63**, 1–14.
- COOKE, M. H., BRIDGWATER, J. & SCOTT, A. M. 1978 Interparticle percolation: Lateral and axial diffusion coefficients. *Powder Tech.* **21**, 183–193.
- DA CRUZ, F., EMAM, S., PROCHNOW, M., ROUX, J. N. & CHEVOIR, F. 2005 Rheophysics of dense granular materials: Discrete simulation of plane shear flows. *Phys. Rev. E* **72**, 021309.
- DELANNAY, R., VALANCE, A., MANGENEY, A., ROCHE, O. & RICHARD, P. 2017 Granular and particle-laden flows: from laboratory experiments to field observations. *J. Phys. D: Appl. Phys.* **50**, 053001.
- DENISSEN, I. F. C., WEINHART, T., TE VOORTWIS, A., LUDING, S., GRAY, J. M.

- N. T. & THORNTON, A. R. 2019 Bulbous head formation in bidisperse shallow granular flow over an inclined plane. *J. Fluid Mech.* **866**, 263–297.
- DING, Y., FORSTER, R., SEVILLE, J. & PARKER, D. 2002 Granular motion in rotating drums: bed turnover time and slumping-rolling transition. *Powder Technol.* **124**, 18–27.
- DOLGUNIN, V. N. & UKOLOV, A. A. 1995 Segregation modeling of particle rapid gravity flow. *Powder Technol.* **83** (2), 95–103.
- EDWARDS, A. N., RUSSELL, A. S., JOHNSON, C. G. & GRAY, J. M. N. T. 2019 Frictional hysteresis and particle deposition in granular free-surface flows. *J. Fluid Mech.* **875**, 1058–1095.
- FAN, Y. & HILL, K. M. 2011 Theory for shear-induced segregation of dense granular mixtures. *New J. Phys.* **13** (9), 095009.
- FESTA, A., OGATA, K., PINI, G. A., DILEK, Y. & CODEGONE, G. 2015 Late Oligocene–early Miocene olistostromes (sedimentary mélanges) as tectono-stratigraphic constraints to the geodynamic evolution of the exhumed Ligurian accretionary complex (Northern Apennines, NW Italy). *Int. Geol. Rev.* **57** (5–8), 540–562.
- FORTERRE, Y. 2006 Kapiza waves as a test for three-dimensional granular flow rheology. *J. Fluid Mech.* **563**, 123–132.
- FORTERRE, Y. & POULIQUEN, O. 2008 Flows of dense granular media. *Ann. Rev. Fluid Mech.* **40**, 1–24.
- FRY, A. M., UMBANHOWAR, P. B., OTTINO, J. M. & LUEPTOW, R. M. 2018 Effect of pressure on segregation in granular shear flows. *Phys. Rev. E* **97** (6), 062906.
- GAJJAR, P. & GRAY, J. M. N. T. 2014 Asymmetric flux models for particle-size segregation in granular avalanches. *J. Fluid Mech.* **757**, 297–329.
- GAJJAR, P., VAN DER VAART, K., THORNTON, A. R., JOHNSON, C. G., ANCEY, C. & GRAY, J. M. N. T. 2016 Asymmetric breaking size-segregation waves in dense granular free-surface. *J. Fluid Mech.* **794**, 460–505.
- GDR MiDi 2004 On dense granular flows. *Eur. Phys. J. E* **14** (4), 341–365.
- GILBERG, D. & STEINER, K. 2020 Size segregation in compressible granular shear flows of binary particle systems. *Granul. Matter* **22**, 45.
- GODDARD, J. D. & LEE, J. 2018 Regularization by compressibility of the  $\mu(I)$  model of dense granular flow. *Phys. Fluids* **30**, 073302.
- GOLICK, L. A. & DANIELS, K. E. 2009 Mixing and segregation rates in sheared granular materials. *Phys. Rev. E* **80** (4), 042301.
- GRAY, J. M. N. T. 2001 Granular flow in partially filled slowly rotating drums. *J. Fluid Mech.* **441**, 1–29.
- GRAY, J. M. N. T. 2018 Particle segregation in dense granular flows. *Ann. Rev. Fluid Mech.* **50**, 407–433.



- GRAY, J. M. N. T. & ANCEY, C. 2009 Segregation, recirculation and deposition of coarse particles near two-dimensional avalanche fronts. *J. Fluid Mech.* **629**, 387–423.
- GRAY, J. M. N. T. & ANCEY, C. 2011 Multi-component particle-size segregation in shallow granular avalanches. *J. Fluid Mech.* **678**, 535–588.
- GRAY, J. M. N. T. & ANCEY, C. 2015 Particle-size and -density segregation in granular free-surface flows. *J. Fluid Mech.* **779**, 622–668.
- GRAY, J. M. N. T. & CHUGUNOV, V. A. 2006 Particle-size segregation and diffusive remixing in shallow granular avalanches. *J. Fluid Mech.* **569**, 365–398.
- GRAY, J. M. N. T. & EDWARDS, A. N. 2014 A depth-averaged  $\mu(I)$ -rheology for shallow granular free-surface flows. *J. Fluid Mech.* **755**, 503–534.
- GRAY, J. M. N. T. & HUTTER, K. 1997 Pattern formation in granular avalanches. *Contin. Mech. Thermodyn.* **9** (6), 341–345.
- GRAY, J. M. N. T. & KOKELAAR, B. P. 2010*a* Erratum large particle segregation, transport and accumulation in granular free-surface flows – erratum. *J. Fluid Mech.* **657**, 539.
- GRAY, J. M. N. T. & KOKELAAR, B. P. 2010*b* Large particle segregation, transport and accumulation in granular free-surface flows. *J. Fluid Mech.* **652**, 105–137.
- GRAY, J. M. N. T. & THORNTON, A. R. 2005 A theory for particle size segregation in shallow granular free-surface flows. *Proc. Royal Soc. A* **461**, 1447–1473.
- GRAY, J. M. N. T., WIELAND, M. & HUTTER, K. 1999 Free surface flow of cohesionless granular avalanches over complex basal topography. *Proc. Roy. Soc. A* **455**, 1841–1874.
- GRIGORIAN, S. S., EGLIT, M. E. & IAKIMOV, I. L. 1967 New statement and solution of the problem of the motion of snow avalanche. *Snow, Avalanches & Glaciers. Tr. Vysokogornogo Geofizich Inst* **12**, 104–113.
- GUILLARD, F., FORTERRE, Y. & POULIQUEN, O. 2016 Scaling laws for segregation forces in dense sheared granular flows. *J. Fluid Mech.* **807**.
- HENANN, D. L. & KAMRIN, K. 2013 A predictive, size-dependent continuum model for dense granular flows. *Proc. Natl. Acad. Sci. U.S.A.* **110**, 6730–6735.
- HENEIN, H., BRIMACOMBE, J. & WATKINSON, A. 1983 Experimental study of transverse bed motion in rotary kilns. *Metall Trans. B* **14**, 191–205.
- HEYMAN, J., DELANNAY, R., TABUTEAU, H. & VALANCE, A. 2017 Compressibility regularizes the  $\mu(I)$ -rheology for dense granular flows. *J. Fluid Mech.* **830**, 553–568.
- HILL, K. M. & FAN, Y. 2008 Isolating segregation mechanisms in a split-bottom cell. *Phys. Rev. Lett.* **101** (8), 088001.
- HILL, K. M., KHAKHAR, D. V., GILCHRIST, J. F., MCCARTHY, J. J. & OTTINO, J. M.

- 1999 Segregation-driven organization in chaotic granular flows. *Proceedings of the National Academy of Sciences* **96** (21), 11701–11706.
- HILL, K. M. & TAN, D. S. 2014 Segregation in dense sheared flows: gravity, temperature gradients, and stress partitioning. *J. Fluid Mech.* **756**, 54–88.
- HOLYOAKE, A. J. & MCELWAIN, J. N. 2012 High-speed granular chute flows. *J. Fluid Mech.* **710**, 35–71.
- ISSA, R. I. 1986 Solution of the implicitly discretised fluid flow equations by operator-splitting. *Journal of Computational Physics* **62** (1), 40–65.
- IVERSON, R. M. 1997 The physics of debris-flows. *Rev. Geophy.* **35**, 245–296.
- IVERSON, R. M. & VALLANCE, J. W. 2001 New views of granular mass flows. *Geology* **29** (2), 115–118.
- JEROLMACK, D. J. & DANIELS, K. E. 2019 Viewing earth’s surface as a soft-matter landscape. *Nat. Rev. Phys.* pp. 1–15.
- JOHNSON, C. G., KOKELAAR, B. P., IVERSON, R. M., LOGAN, M., LAHUSEN, R. & GRAY, J. M. N. T. 2012 Grain-size segregation and levee formation in geophysical mass flows. *J. Geophys. Res. Earth Surf.* **117** (F01032).
- JOP, P., FORTERRE, Y. & POULIQUEN, O. 2005 Crucial role of sidewalls in granular surface flows: consequences for the rheology. *J. Fluid Mech.* **541**, 167.
- JOP, P., FORTERRE, Y. & POULIQUEN, O. 2006 A constitutive relation for dense granular flows. *Nature* **44**, 727–730.
- KAMRIN, K. & KOVAL, G. 2012 Nonlocal constitutive relation for steady granular flow. *Phys. Rev. Lett.* **108** (17), 178301.
- KHAKHAR, D. V., ORPE, A. V. & HAJRA, S. K. 2003 Segregation of granular materials in rotating cylinders. *Physica A* **318**, 129–136.
- KOKELAAR, B. P., GRAHAM, R. L., GRAY, J. M. N. T. & VALLANCE, J. W. 2014 Fine-grained linings of leveed channels facilitate runout of granular flows. *Earth Planet. Sci. Lett.* **385**, 172–180.
- LAGRÉE, P.-Y., STARON, L. & POPINET, S. 2011 The granular column collapse as a continuum: validity of a two-dimensional Navier–Stokes model with a  $\mu(I)$ -rheology. *J. Fluid Mech.* **686**, 378–408.
- LIU, Y., GONZALEZ, M. & WASSGREN, C. 2018 Modeling granular material blending in a rotating drum using a finite element method and advection-diffusion equation multiscale model. *AIChE J.* **64** (9), 3277–3292.
- LIU, Y., GONZALEZ, M. & WASSGREN, C. 2019 Modeling granular material segregation using a combined finite element method and advection–diffusion–segregation equation model. *Powder Technol.* **346**, 38–48.
- LUBLINER, J. 2008 *Plasticity theory*. Courier Corporation.

- MAKSE, H. A., HAVLIN, S., KING, P. R. & STANLEY, H. E. 1997 Spontaneous stratification in granular mixtures. *Nature* **386**, 379–382.
- MANGENY, A., BOUCHUT, F., THOMAS, N., VILOTTE, J. P. & BRISTEAU, M. O. 2007 Numerical modeling of self-channeling granular flows and of their levee-channel deposits. *J. Geophys. Res.* **112**, F02017.
- MARSCHALL, H., HINTERBERGER, K., SCHÜLER, C., HABLA, F. & HINRICHSSEN, O. 2012 Numerical simulation of species transfer across fluid interfaces in free-surface flows using openfoam. *Chem. Eng. Sci.* **78**, 111–127.
- MARTIN, N., IONESCU, I. R., MANGENY, A., BOUCHUT, F. & FARIN, M. 2017 Continuum viscoplastic simulation of a granular column collapse on large slopes:  $\mu(I)$  rheology and lateral wall effects. *Phys. Fluids* **29**, 013301.
- MAXWELL, J. C. 1867 Iv. on the dynamical theory of gases. *Phil. Trans. Roy. Soc.* **157**, 49–88.
- MIDDLETON, G. V. 1970 Experimental studies related to problems of flysch sedimentation. In *Flysch Sedimentology in North America* (ed. J. Lajoie), pp. 253–272. Business and Economics Science Ltd, Toronto.
- MOUKALLED, F., MANGANI, L. & DARWISH, M. 2016 *The finite volume method in computational fluid dynamics*. Springer.
- MOUNTY, D. 2007 *Particle size-segregation in convex rotating drums*. PhD Thesis, The University of Manchester (United Kingdom).
- OTTINO, J. M. & KHAKHAR, D. V. 2000 Mixing and segregation of granular materials. *Annu. Rev. Fluid Mech.* **32**, 55–91.
- PIERSON, T. C. 1986 Flow behavior of channelized debris flows, Mount St. Helens, Washington. In *Hillslope Processes* (ed. A. D. Abrahams), pp. 269–296. Allen and Unwin, Winchester, Mass.
- POULIQUEN, O. 1999*a* On the shape of granular fronts down rough inclined planes. *Phys. Fluids* **11** (7), 1956–1958.
- POULIQUEN, O. 1999*b* Scaling laws in granular flows down rough inclined planes. *Phys. Fluids* **11** (3), 542–548.
- POULIQUEN, O., DELOUR, J. & SAVAGE, S. B. 1997 Fingering in granular flows. *Nature* **386**, 816–817.
- POULIQUEN, O. & FORTERRE, Y. 2002 Friction law for dense granular flows: application to the motion of a mass down a rough inclined plane. *J. Fluid Mech.* **453**, 133–151.
- POULIQUEN, O. & VALLANCE, J. W. 1999 Segregation induced instabilities of granular fronts. *Chaos* **9** (3), 621–630.
- RAJCHENBACH, J. 1990 Flow in powders: From discrete avalanches to continuous regime. *Phys. Rev. Lett.* **65** (18), 2221–2224.
- RAUTER, M., BARKER, T. & FELLIN, W. 2020 Granular viscosity from plastic yield

- surfaces: The role of the deformation type in granular flows. *Comput. Geotech.* **122**, 103492.
- RAUTER, M. & TUKOVIĆ, Ž. 2018 A finite area scheme for shallow granular flows on three-dimensional surfaces. *Comput. Fluids* **166**, 184–199.
- ROCHA, F. M., JOHNSON, C. G. & GRAY, J. M. N. T. 2019 Self-channelisation and levee formation in monodisperse granular flows. *J. Fluid Mech.* **876**, 591–641.
- ROGNON, P. G., ROUX, J.-N., NAAÏM, M. & CHEVOIR, F. 2007 Dense flows of bidisperse assemblies of disks down an inclined plane. *Phys. Fluids* **19** (5), 058101.
- ROSATO, A., STRANDBURG, K. J., PRINZ, F. & SWENDSEN, R. H. 1987 Why the brazil nuts are on top: Size segregation of particulate matter by shaking. *Phys. Rev. Lett.* **58** (10), 1038–1040.
- RUSCHE, H. 2002 *Computational fluid dynamics of dispersed two-phase flows at high phase fractions*. PhD Thesis, University of London.
- SAINGIER, G., DEBOEUF, S. & LAGRÉE, P.-Y. 2016 On the front shape of an inertial granular flow down a rough incline. *Phys. Fluids* **28** (5), 053302.
- SAVAGE, S. B. 1984 The mechanics of rapid granular flows. *Adv. Appl. Mech.* **24**, 289–366.
- SAVAGE, S. B. & HUTTER, K. 1989 The motion of a finite mass of granular material down a rough incline. *J. Fluid Mech.* **199**, 177–215.
- SAVAGE, S. B. & LUN, C. K. K. 1988 Particle size segregation in inclined chute flow of dry cohesionless granular solids. *J. Fluid Mech.* **189**, 311–335.
- SCHAEFFER, D. G. 1987 Instability in the evolution-equations describing incompressible granular flow. *J. Differ. Equ.* **66** (1), 19–50.
- SCHAEFFER, D. G., BARKER, T., TSUJI, D., GREMAUD, P., SHEARER, M. & GRAY, J. M. N. T. 2019 Constitutive relations for compressible granular flow in the inertial regime. *J. Fluid Mech.* **874**, 926–951.
- SCHLICK, C. P., FAN, Y., UMBANHOWAR, P. B., OTTINO, J. M. & LUEPTOW, R. M. 2015 Granular segregation in circular tumblers: theoretical model and scaling laws. *J. Fluid Mech.* **765**, 632–652.
- SCHOFIELD, A. & WROTH, P. 1968 *Critical state soil mechanics*. McGraw-Hill London.
- SHERIDAN, M. F., STINTON, A. J., PATRA, A., PITMAN, E. B., BAUER, A. & NICHITA, C. C. 2005 Evaluating Titan2D mass-flow model using the 1963 Little Tahoma peak avalanches, Mount Rainier, Washington. *J. Volcanol. Geotherm. Res.* **139** (1–2), 89–102.
- SILBERT, L. E., ERTAŞ, D., GREST, G. S., HALSEY, T. C., LEVINE, D. & PLIMPTON, S. J. 2001 Granular flow down an inclined plane: Bagnold scaling and rheology. *Phys. Rev. E* **64** (5), 051302.

- SINGH, A., MAGNANIMO, V., SAITOH, K. & LUDING, S. 2015 The role of gravity or pressure and contact stiffness in granular rheology. *New J. Phys.* **17** (4), 043028.
- STARON, L., LAGRÉE, P.-Y. & POPINET, S. 2012 The granular silo as a continuum plastic flow: The hour-glass vs the clepsydra. *Phys. Fluids* **24**, 103301.
- STARON, L. & PHILLIPS, J. C. 2015 Stress partition and microstructure in size-segregating granular flows. *Phys. Rev. E* **92** (2), 022210.
- THOMAS, N. 2000 Reverse and intermediate segregation of large beads in dry granular media. *Phys. Rev. E* **62**, 961–974.
- THOMAS, N. & D'ORTONA, U. 2018 Evidence of reverse and intermediate size segregation in dry granular flows down a rough incline. *Phys. Rev. E* **97**, 022903.
- THORNTON, A. R. & GRAY, J. M. N. T. 2008 Breaking size segregation waves and particle recirculation in granular avalanches. *J. Fluid Mech.* **596**, 261–284.
- THORNTON, A. R., GRAY, J. M. N. T. & HOGG, A. J. 2006 A three-phase mixture theory for particle size segregation in shallow granular free-surface flows. *J. Fluid Mech.* **550**, 1–25.
- THORNTON, A. R., WEINHART, T., LUDING, S. & BOKHOVE, O. 2012 Modeling of particle size segregation: calibration using the discrete particle method. *Int. J. Mod. Phys. C* **23** (08), 1240014.
- TREWHELA, T., ANCEY, C. & GRAY, J. 2021 Scalings laws for gravity driven particle size segregation in dense sheared granular flows. *J. Fluid Mech.* .
- TRIPATHI, A. & KHAKHAR, D. V. 2011 Rheology of binary granular mixtures in the dense flow regime. *Phys. Fluids* **23**, 113302.
- TRIPATHI, A. & KHAKHAR, D. V. 2013 Density difference-driven segregation in a dense granular flow. *J. Fluid Mech.* **717**, 643–669.
- TUNUGUNTALA, D. R., WEINHART, T. & THORNTON, A. R. 2017 Comparing and contrasting size-based particle segregation models. *Comput. Part. Mech.* **4** (4), 387–405.
- UTTER, B. & BEHRINGER, R. P. 2004 Self-diffusion in dense granular shear flows. *Phys. Rev. E* **69**, 031308.
- VAN DER VAART, K., GAJJAR, P., EPÉLY-CHAUVIN, G., ANDREINI, N., GRAY, J. M. N. T. & ANCEY, C. 2015 Underlying asymmetry within particle size segregation. *Phys. Rev. Lett.* **114** (23), 238001.
- VAN DER VAART, K., VAN SCHROJENSTEIN LANTMAN, M. P., WEINHART, T., LUDING, S., ANCEY, C. & THORNTON, A. R. 2018 Segregation of large particles in dense granular flows suggests a granular saffman effect. *Phys. Rev. Fluids* **3** (7), 074303.
- VALLANCE, J. W. & SAVAGE, S. B. 2000 Particle segregation in granular flows down chutes,. In *IUTAM Symposium on segregation in granular materials* (ed. A. D. Rosato & D. L. Blackmore). Kluwer.

- VIROULET, S., BAKER, J. L., ROCHA, F. M., JOHNSON, C. G., KOKELAAR, B. P. & GRAY, J. M. N. T. 2018 The kinematics of bidisperse granular roll waves. *J. Fluid Mech.* **848**, 836–875.
- WELLER, H. G. 2006 Bounded explicit and implicit second-order schemes for scalar transport, report tr/hgw/06. *Tech. Rep.*. OpenCFD Ltd.
- WELLER, H. G. 2008 A new approach to vof-based interface capturing methods for incompressible and compressible flow, report tr/hgw/04. *Tech. Rep.*. OpenCFD Ltd.
- WIEDERSEINER, S., ANDREINI, N., EPELY-CHAUVIN, G., MOSER, G., MONNEREAU, M., GRAY, J. M. N. T. & ANCEY, C. 2011 Experimental investigation into segregating granular flows down chutes. *Phys. Fluids* **23**, 013301.
- WILLIAMS, S. C. 1968 The mixing of dry powders. *Powder Technol.* **2**, 13–20.
- WOODHOUSE, M. J., THORNTON, A. R., JOHNSON, C. G., KOKELAAR, B. P. & GRAY, J. M. N. T. 2012 Segregation-induced fingering instabilities in granular free-surface flows. *J. Fluid Mech.* **709**, 543–580.
- XIAO, H., FAN, Y., JACOB, K. V., UMBANHOWAR, P. B., KODAM, M., KOCH, J. F. & LUEPTOW, R. M. 2019 Continuum modeling of granular segregation during hopper discharge. *Chem. Eng. Sci.* **193**, 188–204.
- YANG, R. Y., YU, A. B., MCELROY, L. & BAO, J. 2008 Numerical simulation of particle dynamics in different flow regimes in a rotating drum. *Powder Technol.* **188** (2), 170–177.
- YUE, Y., SMITH, B., CHEN, P. Y., CHANTHARAYUKHONTHORN, M., KAMRIN, K. & GRINSPUN, E. 2018 Hybrid grains: Adaptive coupling of discrete and continuum simulations of granular media. In *SIGGRAPH Asia 2018 Technical Papers*, p. 283. ACM.
- ZURIGUEL, I., GRAY, J. M. N. T., PEIXINHO, J. & MULLIN, T. 2006 Pattern selection by a granular wave in a rotating drum. *Phys. Rev. E* **73**, 061302.

## Chapter 3

# Particle-size segregation in triangular rotating drums with sidewall friction

This chapter is an article entitled “Particle-size segregation in triangular rotating drums with sidewall friction”, which at the time of writing is in preparation for submission to a journal. The supplementary material is available online at <https://doi.org/10.17632/b36kh3w7xf.1>.

# Particle-size segregation in triangular rotating drums with sidewall friction

**E.S.F. Maguire<sup>1</sup>, T. Barker<sup>1,2</sup>, M. Rauter<sup>3</sup>, C.G. Johnson<sup>1</sup> & J.M.N.T. Gray<sup>1</sup>**

<sup>1</sup>Department of Mathematics and Manchester Centre for Nonlinear Dynamics,  
University of Manchester, Oxford Road, Manchester, M13 9PL, UK

<sup>2</sup>School of Mathematics, University of Cardiff, Cardiff, CF10 3AT, UK

<sup>3</sup>Department of Water Management, Office of the Tyrolean Regional Government,  
Innsbruck, Austria.

The tendency of polydisperse granular flows in rotating drums to segregate efficiently by particle size into stunning geometrical patterns has been the subject of extensive research, but continuum models have yet to grasp the full interplay between the bulk flow and segregation in such flows. Recent theoretical and numerical developments provide a powerful tool for tackling problems with complex rheology-segregation feedback interactions within a continuum framework. In particular, the partially regularised incompressible  $\mu(I)$ -rheology has been coupled with complex functional dependencies for the particle-size segregation and diffusion rates. This method is fully coupled, in the sense that the bulk flow fields depend on the evolving particle distribution and the frictional properties of its constituents, while the segregation and diffusion rates depend upon the shear rate, gravity, pressure, particle concentration, particle size and particle-size ratio. In this paper, polydisperse triangular rotating drum flows are examined via a series of original experiments and fully coupled numerical simulations computed using OpenFOAM. Rotating drum flows are of practical relevance to industrial mixing procedures, and also present a lens through which to investigate the intricate relationship between rheology and segregation. They are confined within a thin channel by lateral sidewalls which exert a frictional force on the grains, and this is incorporated into a two-dimensional framework using width-averaged Navier-Stokes type equations with a Coulomb slip condition on the sidewalls. As



a test case for the numerical implementation, a simulation of an infinite shear-cell with confining sidewalls is compared to an exact solution. Bidisperse triangular rotating drum experiments and simulations are performed for a variety of drum fill fractions and mean particle concentrations. Friction from the sidewalls induces a very thin free-surface avalanche which acts as a boundary layer inside which all the segregation occurs, and which must be adequately resolved by the numerical mesh to predict the correct intensity of segregation. The bulk flow fields and particle pattern formations are examined, and subtle interactions between the two are discovered. A novel approach for processing images of the experimental results is used to project a particle concentration field onto laboratory images, facilitating quantitative comparison with the simulation data. Finally, a drum containing a tridisperse mixture is considered, where the intermediate species is segregated in opposite directions by the small and large particles, leading to a reduction in the net segregation rate.

## 1. Introduction

Polydisperse granular flows are ubiquitous throughout the natural world and industrial processes. They may take the form of geophysical mass flows such as rockfalls, debris flows, lahars, pyroclastic flows or snow avalanches, which all naturally encompass a wide distribution of particle sizes and shapes, or industrial procedures in which two or more distinct particle species are mixed together with the aim of attaining a homogeneous mixture. Segregation - the internal redistribution of polydisperse particle mixtures according to size, shape, density or other distinguishing features - can therefore present a major obstacle to efficiency in industrial processes. Research into the nature of segregation in industrial processes is often concerned with filling and emptying of storage silos (Williams 1968; Drahn & Bridgwater 1983; Gray & Hutter 1997; Makse *et al.* 1997; Staron, Lagr  e & Popinet 2012; Staron, Lagr  e & Popinet 2014), and rotating drums partially filled with granular material (Hill *et al.* 1999; Ottino & Khakhar 2000*a*; Gray 2001; Zuriguel *et al.* 2006; Gray & Chugunov 2006). Here, experiments are conducted using triangular rotating drums to mix (or segregate) glass beads of differing particle sizes, and the approach of Barker *et al.* (2021) and Trehwela, Ancey & Gray (2021) is used to produce continuum simulations of triangular rotating drums in which the rheology and the particle distribution are fully coupled. The segregation rate is dependent upon the local flow properties, and the frictional properties of the grains themselves in the evolving particle distribution feedback onto the mobility of the flow (Pouliquen, Delour & Savage 1997; Iverson & Vallance 2001; van der Vaart *et al.* 2018*b*; Barker *et al.* 2021). Friction from confining lateral sidewalls is an important feature of rotating drum experiments when the confined channel of granular material is narrow. Sidewall friction can then drastically alter the flow properties and particle pattern formation (Hill *et al.* 1999; Ottino & Khakhar 2000*a*; Jop, Forterre & Pouliquen 2005; Mounty 2007), and is introduced into the numerical model for the rotating drum simulations here to accurately reproduce the particle pattern evolution and segregation intensity observed in experiments.

Early attempts at continuum modelling of monodisperse granular flows were characterised by Coulomb friction models with a Drucker-Prager type yield surface

(Yu 2007), which were shown to be mathematically ill-posed in two dimensions by Schaeffer (1987), because the growth rate of infinitesimally small perturbations became unbounded in the small wavelength limit. Well-posed problems have a unique solution with a continuous dependence on the initial conditions; when a problem fails to meet these conditions, it is classified as ill-posed, or Hadamard unstable (Joseph & Saut 1990). A significant milestone was reached with the development of the incompressible  $\mu(I)$ -rheology (GDR MiDi 2004; Jop *et al.* 2005; Jop, Forterre & Pouliquen 2006) which ties the effective friction  $\mu$  to the non-dimensional inertial number  $I$ , which in turn depends upon the strain-rate, pressure, grain density and grain size. This formulation is well-posed for intermediate values of the inertial number but remains ill-posed for sufficiently small or large values (Barker *et al.* 2015). Barker & Gray (2017) developed a modified, partially regularised  $\mu(I)$  curve which greatly extends the region of well-posedness to include all values below an extreme high value limit of the inertial number, by forgoing a yield criterion and introducing a creep state for low  $I$ . For values of the inertial number towards the upper end of the well-posed parameter space, the partially regularised  $\mu(I)$ -rheology provides an improved match to experimental data and DEM (discrete element method) simulations (Holyoake & McElwaine 2012; Kamrin & Koval 2012; Barker & Gray 2017) relative to the original  $\mu(I)$  curve. It is possible to formulate unconditionally well-posed local continuum models with a yield stress by introducing compressibility (Barker & Gray 2017; Schaeffer *et al.* 2019), but significantly the partially regularised incompressible  $\mu(I)$ -rheology is compatible with established segregation models which share the assumption of incompressibility (Gray & Thornton 2005), and also fits into the framework of incompressible Navier-Stokes solvers.

When polydisperse granular materials undergo shear, vacant void spaces open up between particles which smaller particles are more likely to percolate through, in a gravity-driven process known as kinetic sieving (Middleton 1970; Savage & Lun 1988). A force imbalance in the lower, densely packed layer then leads to particles being driven upwards, which is known as squeeze expulsion (Savage & Lun 1988). The net impact of these combined effects, collectively known as gravity-driven segregation, is an inversely graded layer in which larger particles collect near the surface of the flow. There are many other mechanisms by which

segregation may occur (Scott & Bridgwater 1975; Ehrichs *et al.* 1995; Jenkins & Yoon 2002; Schröter *et al.* 2006; Schulze 2008; McCarthy 2009; Hill & Tan 2014; Gray & Ancey 2015), but kinetic sieving and squeeze expulsion are the dominant mechanisms in shallow granular avalanches (Gray 2018). Even for a relatively simple inclined plane flow of bidisperse granular material, segregation can lead to varied and complex phenomena. The shear profile through the flow depth in an inversely graded layer can also lead to the transportation of less mobile (Iverson 2003) large particles towards the flow front. A feedback affect onto the bulk flow due to frictional differences between the different particle species may result in the formation of a bulbous head at the flow front (Denissen *et al.* 2019), static levees (Pouliquen & Vallance 1999; Iverson 1997; Johnson *et al.* 2012), and fingering instabilities (Pouliquen *et al.* 1997; Pouliquen & Vallance 1999; Vallance & Savage 2000; Woodhouse *et al.* 2012; Baker, Johnson & Gray 2016*b*), or deposition of the particles from the front onto the underlying substrate (Gray & Ancey 2009).

Gray & Thornton (2005) proposed an advection-segregation equation which models the mixing process between two species with differing particle sizes, which was extended to include the effects of diffusive remixing by Gray & Chugunov (2006) and generalised for multiple particle phases by Gray & Ancey (2011). Fan & Hill (2011) found that segregation was not always orientated in the direction of gravity but may be aligned with kinetic stress gradients (Hill & Tan 2014), which inspired a generalised segregation-advection-diffusion equation (Barker *et al.* 2021) in which the segregation direction may be arbitrarily specified. The early shear box experiments of Scott & Bridgwater (1975) identified the grain-size ratio as the most important parameter in controlling the segregation rate, and it has long been suggested that the segregation rate should be an increasing function of the strain-rate (Bridgwater, Foo & Stephens 1985; May *et al.* 2010; Schlick *et al.* 2015). Trehela *et al.* (2021) used dimensional analysis and refractive-index matched oscillatory shear box experiments to derive a pressure and strain-rate dependent scaling law for the segregation velocity magnitude. This provides a natural route towards coupling segregation and diffusive remixing to the bulk flow properties (Barker *et al.* 2021) when used alongside a diffusivity scaling law suggested by dimensional analysis and experimental observation (see e.g. Utter & Behringer 2004), which scales with the second invariant of the strain-

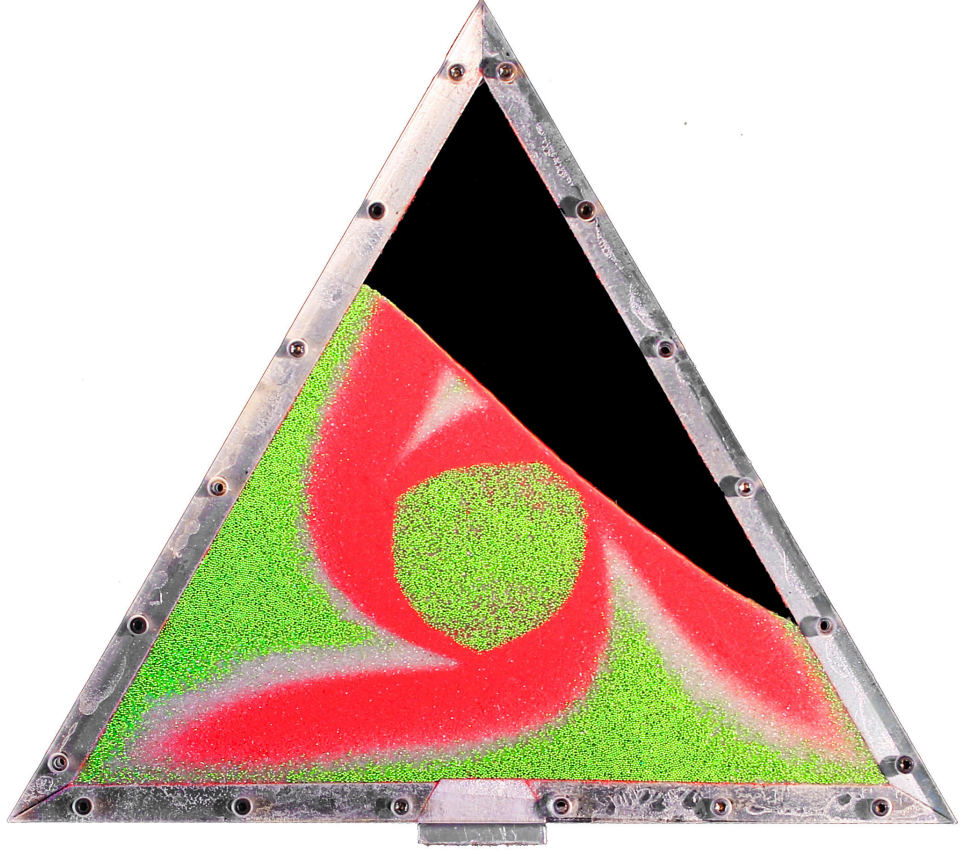


FIGURE 1. Image of a triangular rotating drum experiment 70% filled with particles of three different sizes; small red particles ( $125 - 160 \mu\text{m}$ ), medium white particles ( $400 - 500 \mu\text{m}$ ), and large green particles ( $600 - 800 \mu\text{m}$ ). The drum rotates clockwise with a rotation rate of  $\Omega = -\pi/48 \text{ rad/s}$ . Particles flowing down the thin free-surface avalanche segregate into an inversely graded layer, which is deposited into the underlying substrate and rotated back around the drum to be re-entrained into the avalanche, producing a stunning pattern of small and medium particle arms surrounding an undisturbed central core.

rate tensor and the grain size squared. Based upon the partially regularised  $\mu(I)$ -rheology, Barker *et al.* (2021) also established a method for determining the rheological parameters of an evolving polydisperse mixture by taking volume fraction weighted averages, resulting in a two-way coupled system capable of capturing the complex feedback interactions in polydisperse granular flows.

Rotating drums, in which lateral sidewalls confine a quasi-two-dimensional body of granular material inside a container, provide a simplified experimental counterpart to industrial mixing processes in which two or more substances are tumbled together in a rotating container with the aim of achieving either segregated or homogeneous mixtures. These quasi-two-dimensional drum experiments remove the additional complexity of axial segregation, which is observed in fully three-dimensional rotating drum flows (see e.g. Cooke, Stephens & Bridgwater

1976). Particle segregation presents an impediment to the attainment of uniform mixtures, as demonstrated in an extensive literature dedicated to the experimental study of spherical rotating drums (Metcalf *et al.* 1995; Hill *et al.* 1999; Ottino & Khakhar 2000*a*). Rajchenbach (1990) found that granular avalanches in rotating drum flows take the form of intermittent or continuous avalanches, which Henein *et al.* (1983) identified with corresponding regimes for slowly rotating drums which are sometimes known as the slumping and rolling regimes respectively. Mellmann (2001) identified additional regimes characterised by slipping, cascading, cataracting and centrifuging bodies of grains, where the regime depends on the rotation speed, fill fraction and the frictional properties of the particulates and the drum walls. The intermittent avalanching, continuously avalanching and cascading regimes are the most relevant to industrial mixing procedures, because producing any other flow regime requires either very weakly frictional walls (slipping, when no mixing occurs) or extreme rotation rates (Mellmann 2001). Intermittent avalanches comprise a repeatedly failing incline of granular material which is brought to rest by a shockwave propagating upslope upon impact with the downslope wall (Gray, Tai & Noelle 2003), which can create so-called Catherine wheel patterns (Gray & Hutter 1997; Gray & Chugunov 2006). It may be that frictional hysteresis (Edwards *et al.* 2019) and a yield stress are required to reproduce this effect in physical models, and numerical modelling has therefore mostly focused upon the continuous avalanches observed at faster rotation rates (Schlick *et al.* 2015; Liu, Gonzalez & Wassgren 2018; Brandao *et al.* 2020), which are also the focus here. While spherical rotating drum flows may reach a steady-state, Hill *et al.* (1999) demonstrated the complex transient pattern formations possible in square and elliptical geometries with mixtures of particles distinguished by size or density; here triangular drums are considered.

Schlick *et al.* (2015) prescribed a steady-state bulk velocity field for a circular drum based on fits to DEM data to derive strain-rate dependent segregation velocities. Liu *et al.* (2018) calculated the bulk flow field using a rate-independent constitutive law of a form prone to ill-posedness (Schaeffer 1987) and modelled self-diffusion of grains using the scaling observed by Utter & Behringer (2004), but did not consider segregation effects. Arseni *et al.* (2020) attempted to reproduce the rolling, cascading, cataracting and centrifuging regimes using monodisperse

simulations based on the original  $\mu(I)$ -rheology (Jop *et al.* 2005), although these results appeared to encounter issues with air trapping in the granular mixture, which is a common problem in computations utilising the volume-of-fluid method, as identified by Barker *et al.* (2021). Barker *et al.* (2021) resolved this air trapping issue and simulated square rotating drums containing a bidisperse granular mixture within a fully coupled framework. Here, experiments of triangular rotating drums are conducted for a range of fill fractions and mean particle concentrations, and the same coupled approach with the segregation-reduction factor suggested by Trehela *et al.* (2021) is used to perform equivalent numerical simulations, with no fitting parameters used. Confining sidewall friction is incorporated into the model, resulting in very accurate numerical simulations of the experimental data. Furthermore, a method of extracting concentration fields from the experimental images shows that the segregation intensity of the simulations closely matches that of the experiments. The evidence provided here strongly suggests that the partially regularised incompressible  $\mu(I)$ -rheology coupled with the segregation scaling law of Trehela *et al.* (2021) and the strain-rate dependent diffusivity scaling law is capable of capturing the complex dynamics of triangular rotating drum flows in the continuously avalanching regime.

## 2. Governing equations

### 2.1. Partially regularised $\mu(I)$ -rheology

Consider a body of granular material containing particles of differing sizes, shapes and frictional properties but with an assumed constant intrinsic grain density  $\rho_*$ . The solids volume fraction  $\Phi$  is further assumed to be constant and uniform throughout the grains, so that the bulk density  $\rho = \Phi\rho_*$  is also constant, and mass balance then implies that the bulk flow field  $\mathbf{u}$  is incompressible,

$$\nabla \cdot \mathbf{u} = 0, \quad (2.1)$$

where  $\nabla$  is the gradient operator and  $\cdot$  is the dot product. Although gravity-driven segregation relies on the formation of void spaces inside a flowing mixture, the bulk solids volume fraction in granular avalanches has been shown to remain approximately constant (Tripathi & Khakhar 2011) and incompressibility is therefore a

reasonable assumption. The momentum balance is

$$\rho \left( \frac{\partial \mathbf{u}}{\partial t} + \mathbf{u} \cdot \nabla \mathbf{u} \right) = -\nabla p + \nabla \cdot \boldsymbol{\tau} + \rho \mathbf{g}, \quad (2.2)$$

where  $p$  is the pressure,  $\boldsymbol{\tau}$  is the deviatoric stress tensor, and  $\mathbf{g}$  is the gravitational acceleration vector. Assuming alignment of the deviatoric stress and the strain rate, the  $\mu(I)$ -rheology (GDR MiDi 2004; Jop *et al.* 2005, 2006) gives the expression  $\boldsymbol{\tau} = 2\eta \mathbf{D}$  for the deviatoric stress in terms of a granular viscosity  $\eta$ , which is given by

$$\eta = \frac{\mu(I)p}{2\|\mathbf{D}\|}. \quad (2.3)$$

Here  $\mu$  is the internal friction coefficient,  $\mathbf{D} = \frac{1}{2} (\nabla \mathbf{u} + (\nabla \mathbf{u})^T)$  is the strain-rate tensor, and the second invariant of the strain-rate tensor is defined as

$$\|\mathbf{D}\| = \sqrt{\frac{1}{2} \text{tr}(\mathbf{D}^2)}. \quad (2.4)$$

The internal friction  $\mu$  is a function only of the non-dimensional inertial number  $I$  (GDR MiDi 2004), which is defined as

$$I = \frac{2d\|\mathbf{D}\|}{\sqrt{p/\rho_*}}, \quad (2.5)$$

where  $d$  is the grain diameter. The  $\mu(I)$ -rheology is an empirical law which was formulated using dimensional analysis alongside evidence from DEM simulations and experiments across a range of steady-state, monodisperse flow geometries (GDR MiDi 2004). A functional form for  $\mu(I)$  was first proposed by Jop *et al.* (2005), using a basal friction law (Pouliquen & Forterre 2002) to derive

$$\mu(I) = \frac{\mu_s I_0 + \mu_d I}{I_0 + I}, \quad (2.6)$$

where  $\mu_s$  is the static friction coefficient,  $\mu_d$  is the dynamic friction coefficient, and  $I_0$  is a material constant. However, Barker *et al.* (2015) found that this formulation led to unbounded growth of small perturbations in the high wavenumber limit for values of the inertial number that are either too low or too high. In practice, this has been shown to lead to grid-dependent numerical simulations (Barker *et al.* 2015; Martin *et al.* 2017; Barker & Gray 2017), and offers an indication that important physics are missing from the model. This problem of ill-posedness can be resolved by the inclusion of compressibility (Barker *et al.* 2017; Schaeffer



*et al.* 2019) but here a modified incompressible curve proposed by Barker & Gray (2017) is used, which guarantees well-posedness of the governing equations below an extreme high inertial number limit. This is known as the partially regularised  $\mu(I)$ -rheology, and is expressed as

$$\mu(I) = \begin{cases} \sqrt{\frac{\alpha}{\log\left(\frac{A_-}{I}\right)}}, & \text{for } I \leq I_1, \\ \frac{\mu_s I_0 + \mu_d I + \mu_\infty I^2}{I_0 + I}, & \text{for } I > I_1, \end{cases} \quad (2.7)$$

where  $\alpha \lesssim 2$  ensures well-posedness in the low  $I$  limit,  $\mu_\infty$  is a material constant, and

$$A_- = I_1 \exp\left(\frac{\alpha(I_0 + I_1)^2}{(\mu_s I_0 + \mu_d I_1 + \mu_\infty (I_1)^2)^2}\right). \quad (2.8)$$

This satisfies the condition that  $\mu(I = 0) = 0$ , which is necessary but not sufficient for a well-posed  $\mu(I)$  curve. It introduces a creep state for  $I \leq I_1$ , and consequently the partially regularised rheology does not have a yield stress. For the rheology to remain unconditionally well-posed while accommodating a yield stress, an incompressible theory with higher velocity gradients (Goddard & Lee 2017) or non-locality (Kamrin & Koval 2012; Kamrin 2019) may be used, or alternatively compressible rheologies (Barker *et al.* 2017; Schaeffer *et al.* 2019), but since these are relatively new theoretical developments it is sensible to use the better understood incompressible models for complex transient flows such as the rotating drum, particularly as they can also be coupled to incompressible segregation theories. Furthermore, the omission of a yield stress makes little practical difference to numerical simulations which already necessitate high viscosity regularisation, discussed in §3. Additionally, while for the original formulation (2.6)  $\mu \rightarrow \mu_d$  in the high inertial number limit (as  $I \rightarrow \infty$ ), for the partially regularised rheology  $\mu \rightarrow \mu_\infty I$ , as suggested by data from high speed chute flow experiments (Holyoake & McElwaine 2012; Barker & Gray 2017).

## 2.2. Generalized polydisperse segregation theory

The granular material is assumed to consist of  $n$  discrete particle species  $\nu$  with respective grain diameters  $d^\nu$  and an intrinsic grain density  $\rho_*$  which is constant across the entire granular material. Each species has a volume fraction per unit

granular volume  $\phi^\nu \in [0, 1]$  satisfying by definition the summation constraint

$$\sum_{\forall \nu} \phi^\nu = 1. \quad (2.9)$$

It is assumed that each species satisfies the standard form (Savage & Lun 1988; Gray & Thornton 2005; Gray & Chugunov 2006; Gray & Ancey 2011; Fan & Hill 2011; Schlick *et al.* 2015) of an advection-segregation-diffusion equation,

$$\frac{\partial \phi^\nu}{\partial t} + \nabla \cdot (\phi^\nu \mathbf{u}) + \nabla \cdot \mathbf{F}^\nu = \nabla \cdot \mathbf{D}^\nu, \quad (2.10)$$

where  $\mathbf{F}^\nu$  and  $\mathbf{D}^\nu$  are the segregation and diffusive flux vectors respectively. By summing (2.10) over each species and applying the summation constraint (2.9), incompressibility (2.1) is satisfied for independent segregation and diffusive fluxes provided

$$\sum_{\forall \nu} \mathbf{F}^\nu = 0, \quad \text{and} \quad \sum_{\forall \nu} \mathbf{D}^\nu = 0. \quad (2.11)$$

For a bidisperse mixture, the segregation flux function should satisfy the constraint that no segregation occurs when the volume fraction of either species of the sub-mixture is zero (Bridgwater *et al.* 1985). The simplest form therefore has a linear dependence on the species volume fractions, proposed for a bidisperse mixture by Gray & Thornton (2005). This was later generalised for a polydisperse mixture (Gray & Ancey 2011) which allows for variations in the segregation direction across the bidisperse sub-mixtures (Barker *et al.* 2021), taking the form

$$\mathbf{F}^\nu = \sum_{\forall \lambda \neq \nu} f_{\nu\lambda} \phi^\nu \phi^\lambda \mathbf{e}_{\nu\lambda}, \quad (2.12)$$

where  $f_{\nu\lambda}$  is the segregation velocity magnitude and  $\mathbf{e}_{\nu\lambda}$  is the unit segregation direction vector. This is simply the sum of the bidisperse segregation flux functions. It satisfies the summation constraint (2.11) provided

$$f_{\nu\lambda} = f_{\lambda\nu}, \quad \mathbf{e}_{\nu\lambda} = -\mathbf{e}_{\lambda\nu}. \quad (2.13)$$

The diffusive flux vector is defined by analogy with the Maxwell-Stefan equations (Maxwell 1867),

$$\mathbf{D}^\nu = \sum_{\forall \lambda \neq \nu} \mathcal{D}_{\nu\lambda} (\phi^\lambda \nabla \phi^\nu - \phi^\nu \nabla \phi^\lambda), \quad (2.14)$$

so that in general the diffusion rate  $\mathcal{D}_{\nu\lambda}$  may vary between sub-mixtures while still satisfying (2.11), provided  $\mathcal{D}_{\nu\lambda} = \mathcal{D}_{\lambda\nu}$ . When the diffusion rate is the same across all sub-mixtures, (2.14) reduces to the standard equation for Fickian diffusion.

### 2.3. Segregation induced feedback on the bulk flow

In polydisperse granular flows there is a complex interplay between the bulk flow properties and the evolving particle-size distributions. Differences in particle size between otherwise identical species are sufficient to induce frictional feedback of the particle distribution on the bulk flow (see e.g. Baker *et al.* 2016*b*). The coupled approach introduced by Barker *et al.* (2021) provides a theoretical and numerical framework for simultaneously solving the mass (2.1) and momentum balance equations (2.2), and the segregation-advection-diffusion equation (2.10), for the bulk velocity field  $\mathbf{u}$  and pressure  $p$ , and the particle concentrations  $\phi^\nu$ .

Each distinct particle species may be uniquely identified by its constituent particle size, shape and surface properties, which are quantified through the rheological parameters of the species. The evolving particle distributions may thus feedback onto the bulk flow through the granular viscosity, which captures the evolving frictional properties of the mixture. However, the definitions for the granular viscosity (2.3) and the inertial number (2.5) must first be extended for polydisperse mixtures. A volume fraction weighted average grain size  $\bar{d}$  has been proposed for bidisperse systems (Rognon *et al.* 2007; Tripathi & Khakhar 2011) and this may be trivially extended to a generalised polydisperse form (Barker *et al.* 2021),

$$\bar{d} = \sum_{\forall \nu} \phi^\nu d^\nu. \quad (2.15)$$

With this definition, the inertial number expression (2.5) can be re-defined for generalised polydisperse flows as

$$I = \frac{2\bar{d}\|\mathbf{D}\|}{\sqrt{p/\rho_*}}, \quad (2.16)$$

which increases as the volume fraction of larger particle species increases. This means that a mixture of larger particles is more frictional than a mixture of smaller particles, assuming that  $\mu(I)$  is a monotonically increasing function of  $I$ .

For monodisperse flows  $\bar{d} = d$ , and the original definition of  $I$  (2.5) is trivially recovered.

In addition to differing particle sizes, each species  $\nu$  may exhibit differing shape and surface properties. These can be quantified by the rheological parameters  $\mu_s^\nu$ ,  $\mu_d^\nu$ ,  $\mu_\infty^\nu$  and  $I_0^\nu$  to give a set of friction equations  $\mu^\nu(I)$  of the form (2.7) where  $I$  (2.16) is now dependent on the average grain diameter  $\bar{d}$ . The local effective friction of the mixture can then be defined as the volume fraction weighted average of the constituent frictions,

$$\bar{\mu}(I) = \sum_{\forall \nu} \phi^\nu \mu^\nu(I). \quad (2.17)$$

This leads naturally to a new granular viscosity definition (2.3) when included in place of the monodisperse friction law:

$$\bar{\eta} = \frac{\bar{\mu}(I)p}{2\|\mathbf{D}\|}. \quad (2.18)$$

If the non-dimensional rheological parameters are the same across each phase, as is often true when mixing together species of the same substance (such as glass), then the effective friction is also the same, i.e.  $\bar{\mu}(I) = \mu^\nu(I) = \mu(I)$ . In this case frictional feedback is introduced only through variations in the average grain diameter  $\bar{d}$ , and hence  $I$ .

#### 2.4. Bulk flow feedback on the segregation rate and diffusivity

The particle distributions are advected by the bulk flow due to the velocity transport term in (2.10). The segregation (2.12) and diffusion rates (2.14) are also coupled to the bulk flow through the functional dependence of the segregation velocity magnitude  $f_{\nu\lambda}$  and diffusion rate  $\mathcal{D}_{\nu\lambda}$ . This form of coupling is observed physically in rotating drum flows (Metcalf *et al.* 1995; Hill *et al.* 1999; Ottino & Khakhar 2000*a*; Gray 2001; Zuriguel *et al.* 2006), in which segregation is confined to an active layer of rapidly avalanching material above a substrate of quasi-static material in which no segregation occurs.

Consider a bidisperse mixture of small and large particles with respective grain diameters  $d^s$  and  $d^l$  undergoing a deviatoric (shear) stress  $\boldsymbol{\tau}$ , a pressure  $p$  with gravity  $g$ , resulting in a shear rate  $\dot{\gamma} = 2\|\mathbf{D}\|$ . The small particle concentration  $\phi^s = 1 - \phi^l$  and the solids volume fraction is  $\Phi$ . Trehwela *et al.* (2021) identified

six independent non-dimensional quantities for this system,

$$\mu = \frac{\tau}{p}, \quad I = \frac{\dot{\gamma}\bar{d}}{\sqrt{p/\rho_*}}, \quad \Phi, \quad P = \frac{p}{\rho_*g\bar{d}}, \quad R = \frac{d^l}{d^s}, \quad \phi^s, \quad (2.19a-f)$$

where  $P$  is the non-dimensional pressure and  $R$  is the particle-size ratio. Dimensional analysis demands that the diffusion rate scales with the shear rate and the particle size squared (Barker *et al.* 2021). This scaling was also implied by the analysis of Scott & Bridgwater (1975) on the relationship between particle percolation velocity and diffusion, and has been extensively confirmed by experimental observations (Bridgwater 1980; Natarajan, Hunt & Taylor 1995; Utter & Behringer 2004; Katsuragi, Abate & Durian 2010) and numerical simulations (Tripathi & Khakhar 2013; Fan *et al.* 2014; Cai *et al.* 2019). The simplest model for the diffusion rate is therefore

$$\mathcal{D}_{\nu\lambda} = 2\mathcal{A}\|\mathbf{D}\|\bar{d}^2, \quad (2.20)$$

where there is a factor of 2 since  $\|\mathbf{D}\|$  is half the shear rate. Here  $\mathcal{A}$  is a constant specified in table 1. Campbell (1997) found that diffusion in granular shear flows was anisotropic, and Utter & Behringer (2004) studied monodisperse Couette flow experiments using flat disc-shaped particles, from which they measured a radial diffusion coefficient of  $\mathcal{A} = 0.108$  and a tangential diffusion coefficient of  $\mathcal{A} = 0.223$ . However, there is strong evidence from bidisperse DEM shear cell simulations performed using spherical particles that the anisotropy is only slight, and that instead  $\mathcal{A} \in (0.03, 0.05)$  (Tripathi & Khakhar 2013; Cai *et al.* 2019; Bancroft & Johnson 2021; Artoni *et al.* 2021). Therefore isotropic diffusion can be reasonably assumed, and  $\mathcal{A} = 0.04$  is used here.

Dimensional analysis (Barker *et al.* 2021; Trehwela *et al.* 2021) furthermore suggests that the segregation velocity magnitude for a bidisperse mixture of large and small particles may scale as

$$f_{sl} \sim \dot{\gamma}\bar{d}\mathcal{G}(\mu, I, \Phi, P, R, \phi^s). \quad (2.21)$$

Trehwela *et al.* (2021) performed single intruder shear box experiments to derive

the segregation velocity scaling law

$$f_{sl} = \frac{2\mathcal{B}\rho_*g\|\mathbf{D}\|\bar{d}^2}{\mathcal{C}\rho_*g\bar{d} + p}\mathcal{F}(R, \phi^s), \quad (2.22)$$

where  $\mathcal{B}$  and  $\mathcal{C}$  are universal constants and  $\mathcal{F}(R, \phi^s)$  is some function of the grain size ratio and the small particle concentration. Based upon their single intruder experiments, Trewhela *et al.* (2021) initially suggested the form

$$\mathcal{F}(R, \phi^s) = (R - 1) + \mathcal{E}(1 - \phi^s)(R - 1)^2. \quad (2.23)$$

where  $\mathcal{E}$  is a universal constant. This encapsulates the observation of Trewhela *et al.* (2021) that in single intruder experiments, the large intruder velocity depended linearly on the size ratio  $R$ , whereas smaller intruders developed a quadratic dependence for larger size ratios. However, there is evidence from experiments and DEM simulations suggesting that for 50:50 mixtures of large and small particles in geometries for which the velocity and shear rate are functions of space and time, the segregation intensity is maximal near a grain-size ratio of  $R = 2$  (Golick & Daniels 2009; Thornton *et al.* 2012), whereas the formulation (2.23) is monotonically increasing with the size ratio. In DEM simulations of rotating drums (He *et al.* 2019; Zhang *et al.* 2017), it has been observed that while the final segregation intensity initially increases with the particle-size ratio  $R$ , drums containing a mixture with  $R = 3$  segregated less strongly than mixtures with  $R = 2$ , suggesting that the observations of Golick & Daniels (2009); Thornton *et al.* (2012) also hold for rotating drum geometries. Although the origins of this phenomenon are not yet fully understood, it is known that grains in a bidisperse mixture are able to pack more efficiently than those in monodisperse mixtures (Golick & Daniels 2009; Thornton *et al.* 2012), and increased packing efficiency impedes segregation since the probability of void spaces forming through which grains can percolate is reduced. A maximum segregation intensity near  $R = 2$  could therefore be related to the packing efficiency increasing with the grain-size ratio. Trewhela *et al.* (2021) suggested an alternative size-ratio dependency which captures this effect within the framework of incompressible segregation theory:

$$\mathcal{F}(R, \phi^s) = \frac{(R - 1) + \mathcal{E}\Lambda(\phi^s)(R - 1)^2}{1 + a(R - 1)^2\phi^s(1 - \phi^s)}, \quad (2.24)$$

$$\begin{array}{lll} \mathcal{A} = 0.108, & \mathcal{B} = 0.7125, & \mathcal{C} = 0.2712, \\ \mathcal{E} = 2.0957, & a = 9 & \phi_c^s = 0.2. \end{array}$$

TABLE 1. Non-dimensional, universal constants  $\mathcal{A}$ ,  $\mathcal{B}$ ,  $\mathcal{C}$ ,  $\mathcal{E}$  in the diffusivity (2.20) and segregation scaling laws of Trewela *et al.* (2021), as well the constants  $a$  and  $\phi_c^s$ , also suggested by the single intruder experiments of Trewela *et al.* (2021). The constant  $\mathcal{B}$  is corrected for the interstitial fluid present in the experiments of Trewela *et al.* (2021).

where  $a$  is a constant and the function  $\Lambda(\phi^s)$  is defined as

$$\Lambda(\phi^s) = \begin{cases} 1 - \frac{\phi^s}{\phi_c^s}, & \text{for } \phi^s \leq \phi_c^s, \\ 0, & \text{for } \phi^s > \phi_c^s. \end{cases} \quad (2.25)$$

This definition for  $\Lambda(\phi^s)$  means that increased segregation with a quadratic dependence on the grain-size ratio is now restricted to low small particle concentrations, where  $\phi_c^s$  is a constant which determines the point of transition between linear and quadratic dependencies. The denominator of the formulation (2.24) captures the idea that the packing efficiency becomes stronger with increasing grain-size ratio, and is only important for grains which are mixed together. The results from the single intruder experiments of (Trewela *et al.* 2021) are still accurately reproduced by this function since (2.23) and (2.24) are equivalent when  $\phi^s = 0$  or 1. The segregation Péclet number  $Pe = f_{sl}/D_{sl}$  (Wiederseiner *et al.* 2011) is now predicted to peak at  $R \simeq 1.66$ , which is very close to the maximum at  $R = 1.7$  observed in the DEM simulations of Thornton *et al.* (2012).

The bidisperse segregation velocity scaling law to be used in this paper can then be expressed in full as

$$f_{sl} = \left[ \frac{2\mathcal{B}\rho_*g\|\mathbf{D}\|\bar{d}^2}{\mathcal{C}\rho_*g\bar{d} + p} \right] \left[ \frac{(R-1) + \mathcal{E}\Lambda(\phi^s)(R-1)^2}{1 + a(R-1)^2\phi^s(1-\phi^s)} \right], \quad (2.26)$$

where the universal constants  $\mathcal{B}$ ,  $\mathcal{C}$  and  $\mathcal{E}$ , as well as  $a$  and  $\phi_c^s$ , are given in table 1. This can be trivially extended to pairwise segregation velocity magnitudes  $f_{\nu\lambda}$  for general polydisperse mixtures if  $\phi^s$  is replaced in the definition of  $\Lambda(\phi^s)$  (2.25) by the volume fraction of the species with smaller particle size from any given pair. The expression (2.26) is able to capture a variety of phenomena observed in bidisperse, sheared granular flows. The dominant mechanisms driving segregation in such flows are squeeze expulsion and kinetic sieving (Middleton

1970; Bridgwater *et al.* 1985; Savage & Lun 1988), a gravity driven process through which smaller grains percolate down through the mixture, and it has also been observed that segregation shuts off when gravity is effectively reduced through a density matched interstitial fluid (Vallance & Savage 2000; Thornton, Gray & Hogg 2006). The inclusion of the non-dimensional pressure  $P$  is therefore necessary since this is the only non-dimensional parameter from the set (2.19) which includes a dependence on gravity. Furthermore, Golick & Daniels (2009) observed a reduction in the segregation rate under increased pressure in a shear cell. The dependence on the average grain diameter also naturally gives rise to asymmetric flux functions, as suggested by annular shear cell experiments (Golick & Daniels 2009; Gajjar & Gray 2014) and oscillatory shear box DEM simulations (van der Vaart *et al.* 2015).

The segregation theory of Trehwela *et al.* (2021) used here in the form (2.26) is phenomenological, gravity-driven and derives from experiments focused upon determining the rise rate of large particles in the direction opposite gravity, but there is evidence that segregation induced by shear rate gradients can occur in other directions, even normal to gravity (Fan & Hill 2011), with large particles segregated towards regions of higher shear rate in dense flow regimes. However, gravity-induced avalanche experiments including rotating drum flows consistently demonstrate the segregation of large particles towards the free-surface, where the shear rate is lowest for Bagnold-like profiles. This is likely because the gravity-induced shear rate gradient drives segregation directly opposing but overwhelmed by the usual gravity-driven segregation, and which therefore goes undetected. The opposing influence of shear rate-induced segregation can therefore be considered to have been implicitly incorporated into measurements of the segregation parameter  $\mathcal{B}$  as a dampening effect in the experiments of Trehwela *et al.* (2021). For geometries in which the shear rate gradient and gravity diverge, the coupling theory makes use of arbitrary segregation directions (2.12) to allow for straightforward alteration within the same theoretical structure. In such cases the segregation scaling (2.26) would no longer hold, but it is suitable for the present study of rotating drum flows.



## 2.5. Sidewall friction

It has long been known that confining lateral sidewalls play an important role in granular flow experiments (Greve & Hutter 1993; Taberlet *et al.* 2003; Jop *et al.* 2005; Baker, Barker & Gray 2016*a*). In rotating drum flows the additional friction introduced by sidewalls results in avalanches which are significantly thinner and faster (Hill *et al.* 1999; Ottino & Khakhar 2000*a*; Jop *et al.* 2005; Mounty 2007) than those captured in the strictly two-dimensional drum simulations of Barker *et al.* (2021). Indeed, Mounty (2007) successfully reproduced patterns in square and triangular drum flows by collapsing the avalanche into an infinitesimal layer. The influence of sidewall friction may be incorporated into the governing equations through a simple modification of the momentum balance equation (2.2). Consider a three-dimensional granular flow confined within a narrow channel between  $y = 0$  and  $y = W$ , where zero velocity and velocity gradients are assumed in the  $y$ -direction. Proceeding in a similar manner to Jop *et al.* (2005), the boundary conditions at the lateral sidewalls are

$$\boldsymbol{\tau} \cdot \mathbf{n} = -\mu_W p \frac{\mathbf{u}}{|\mathbf{u}|} \quad \text{at } y = 0, W, \quad (2.27)$$

where  $\mathbf{n}$  is an outward pointing normal to the sidewall, the term  $-\mathbf{u}/|\mathbf{u}|$  ensures the wall friction acts against the flow, and  $\mu_W$  is a constant friction coefficient which models the wall friction effects using the assumption of Coulomb slip on the sidewalls. For rough sidewalls a no-slip condition may be more appropriate (Baker *et al.* 2016*b*) but the rotating drums used here have smooth acrylic sidewalls which allow slip. Three-dimensional mass and momentum balance equations, defined analogously with (2.1) and (2.2), may be integrated through the channel width in a similar fashion to the depth-averaged approach for a shallow system (Gray 2001; Gray & Edwards 2014). The resulting width-averaged system of equations, after applying the boundary conditions (2.27), may be stated as

$$\nabla \cdot \mathbf{u} = 0, \quad (2.28)$$

$$\rho \left( \frac{\partial \mathbf{u}}{\partial t} + \mathbf{u} \cdot \nabla \mathbf{u} \right) = -\nabla p + \nabla \cdot (2\eta \mathbf{D}) + \rho \mathbf{g} - \frac{2}{W} \mu_W p \frac{\mathbf{u}}{|\mathbf{u}|}, \quad (2.29)$$

where  $\nabla = (\partial/\partial x, \partial/\partial z)$ , the two-dimensional gradient operator, and the variables  $(\mathbf{u}, p, \eta, \mathbf{D})$  from this point onwards refer to width-integrated quantities. For a

more detailed derivation of these width-averaged equations, see appendix A. The final term in the momentum balance equation (2.29) models the influence of wall friction on the bulk flow. This alteration gives a straightforward method of capturing three-dimensional wall friction effects within a two-dimensional framework, and provides the necessary tools for computing numerical simulations of experimental configurations which utilise confining sidewalls.

### 3. Numerical method

The mass (2.28) and momentum balances (2.29) are solved in conservative form,

$$\nabla \cdot \mathbf{u} = 0, \quad (3.1)$$

$$\frac{\partial}{\partial t}(\varrho \mathbf{u}) + \nabla \cdot (\varrho \mathbf{u} \otimes \mathbf{u}) = -\nabla p + \nabla \cdot (2\eta \mathbf{D}) + \varrho \mathbf{g} - \frac{2}{W} \mu_{WP} \frac{\mathbf{u}}{|\mathbf{u}|}, \quad (3.2)$$

where  $\varrho$  is the mixture density and  $\otimes$  is the dyadic product. In addition to the granular mixture, it is also useful to include a Newtonian air phase for numerical simulations, and therefore the mixture density  $\varrho$  and the mixture viscosity  $\eta$  are now volume fraction weighted averages which include air,

$$\varrho = \sum_{\forall \nu} \varphi^\nu \varrho^\nu, \quad \eta = \sum_{\forall \nu} \varphi^\nu \eta^\nu. \quad (3.3)$$

The density of air  $\varrho^a$  is a constant, and  $\varrho^g = \Phi \rho_* \gg \varrho^a$ , where the superscript  $g$  denotes the granular phase. The granular viscosities  $\eta^g$  are derived from (2.18) and the viscosity of air  $\eta^a$  is assumed to be constant. All the relevant numerical parameters are specified in table 2.

The solids volume fraction  $\Phi$  remains unchanged throughout the mixture, with the excess air phase considered separately to the background, interstitial fluid of volume fraction  $1 - \Phi$  per unit mixture volume. For a bidisperse granular mixture of small and large particles with excess air there are volume fractions  $\varphi^s$ ,  $\varphi^l$  and  $\varphi^a$  respectively. The granular segregation aligns with gravity, as does the air-granular segregation. Zero diffusion between air and grains is assumed, and so the advection-segregation-diffusion equation (2.10) produces a system of three

---

$\mu_s = \tan(22^\circ)$	$\mu_d = \tan(34^\circ)$	$I_0 = 0.249$	$\mu_\infty = 0.04$
$\alpha = 1.9$	$I_1 = 0.02048$	$\rho_* = 2500 \text{ kg/m}^3$	$\Phi = 0.6$
$d^s = 0.35 \times 10^{-3} \text{ m}$	$d^l = 0.7 \times 10^{-3} \text{ m}$	$R = 2$	$\mathbf{e} = -\mathbf{g}/ \mathbf{g} $
$\varrho^a = 1 \text{ kg/m}^3$	$\eta^a = 10^{-3} \text{ kg/(ms)}$	$f_{ag} = 5 \text{ m/s}$	
$\mathcal{D}_{al} = \mathcal{D}_{al} = 0 \text{ m}^2/\text{s}$	$\mu_W = \tan(15.5^\circ)$	$W = 3 \times 10^{-3} \text{ m}$	

---

TABLE 2. Parameters for small and large glass beads, the air phase and the triangular drum. The physical parameters for glass beads are those adapted by Rocha *et al.* (2019) from the parameters used by Mangeney *et al.* (2007) to model the experiments of Félix & Thomas (2004). These parameters are used to determine  $I_0$  using the definition given by Jop *et al.* (2005), and  $\mu_\infty$  is chosen to ensure a well-posed partially-regularised  $\mu(I)$  curve up to  $I = 17.0189$ .

---

conservation laws

$$\frac{\partial \varphi^l}{\partial t} + \nabla \cdot (\varphi^l \mathbf{u}) + \nabla \cdot \left( -f_{ls} \varphi^l \varphi^s \frac{\mathbf{g}}{|\mathbf{g}|} + f_{ag} \varphi^l \varphi^a \frac{\mathbf{g}}{|\mathbf{g}|} \right) = \nabla \cdot \left( \mathcal{D}_{ls} (\varphi^s \nabla \varphi^l - \varphi^l \nabla \varphi^s) \right), \quad (3.4)$$

$$\frac{\partial \varphi^s}{\partial t} + \nabla \cdot (\varphi^s \mathbf{u}) + \nabla \cdot \left( f_{sl} \varphi^s \varphi^l \frac{\mathbf{g}}{|\mathbf{g}|} + f_{ag} \varphi^s \varphi^a \frac{\mathbf{g}}{|\mathbf{g}|} \right) = \nabla \cdot \left( \mathcal{D}_{sl} (\varphi^l \nabla \varphi^s - \varphi^s \nabla \varphi^l) \right), \quad (3.5)$$

$$\frac{\partial \varphi^a}{\partial t} + \nabla \cdot (\varphi^a \mathbf{u}) + \nabla \cdot \left( -f_{ag} \varphi^a \varphi^g \frac{\mathbf{g}}{|\mathbf{g}|} \right) = 0, \quad (3.6)$$

where the overall concentration of grains is

$$\varphi^g = \varphi^s + \varphi^l = 1 - \varphi^a. \quad (3.7)$$

The granular segregation velocity magnitude  $f_{sl}$  is defined by the scaling law (2.26) and  $f_{ag} = f_{as} = f_{al}$  is a constant specified in table 2. The system of equations (3.4)–(3.7) may be arbitrarily extended for  $n$  granular phases.

The system (3.1)–(3.6) is solved using the open source computational fluid dynamics package OpenFOAM, with the concentration equations (3.4)–(3.6) solved using the Multidimensional Universal Limiter for Explicit Solution (MULES) algorithm (Weller 2006). Numerical diffusion leads to diffuse interfaces in multiphase problems, which is usually counteracted in OpenFOAM using the in-built counter-gradient transport method (Rusche 2002; Weller 2008), but here the air segregation equation (3.6) is used instead. Barker *et al.* (2021) showed that whereas the standard, built-in method of OpenFOAM can frequently lead to the cumulative trapping of grid-dependent air bubbles inside the granular mixture, the air segregation equation avoids this potentially catastrophic issue by

having the excess air rapidly evacuate the mixture while maintaining sharp, grid resolved interfaces between phases. The air-grains segregation velocity magnitude is therefore physically unimportant and only needs to be sufficiently large to rapidly expel trapped air bubbles from the granular mixture (Barker *et al.* 2021).

The velocity solution and coupling to the mixture composition are calculated explicitly, leading to a Courant–Friedrichs–Lewy (CFL) criterion incorporating the local viscosity (Moukalled, Mangani & Darwish 2016), where the CFL number is defined as

$$\text{CFL} = \frac{|\mathbf{u}| \Delta t}{\Delta x} + \frac{\eta \Delta t}{\rho \Delta x^2}. \quad (3.8)$$

This should be limited to a characteristic value for the time integration scheme (such as 1 for forward Euler). In most multiphase flows the convective term dominates and the second, viscous term is neglected. The reverse is true for static granular material as the strain-rate tends to zero and the viscosity thus becomes infinite, with the resulting requirement that time steps become infinitesimally small. To avoid infinitesimal time steps, a high, constant cut-off value  $\eta_{\max}$  is used for the viscosity (see e.g. Lagr  e, Staron & Popinet 2011; Staron *et al.* 2012), which is redefined as

$$\eta = \min(\eta_{\max}, \eta). \quad (3.9)$$

This means that a Newtonian viscosity is activated as  $\|\mathbf{D}\| \rightarrow 0$  or  $p \rightarrow \infty$ . Smaller time steps are nevertheless required relative to low viscosity simulations as the viscosity continues to dominate the CFL number. Finally, since the partially regularised  $\mu(I)$ -rheology (2.7) does not have a yield stress and instead enters a creep regime for small values of the inertial number to maintain well-posedness (Barker & Gray 2017), it is not able to model static material, as detailed in §2.1. It is important to note here that although the  $\mu(I)$ -rheology of Jop *et al.* (2005) has a minimum yield stress of  $\mu_s$ , the granular viscosity definition (2.3) means that a creep regime would still be introduced numerically by the high viscosity regularisation (3.9) and so the partially regularised form is strongly preferable due its vastly extended region of well-posedness.

#### 4. Shear cell with sidewall friction

Before examining the influence of sidewall friction in rotating drums, an infinite shear cell is used as a validation case for the numerical implementation of the bulk mass and momentum with lateral sidewall friction, given by (3.1) and (3.2). Consider a monodisperse body of grains, in a Cartesian coordinate system  $Oxz$ , which is uniform and infinite in the  $x$ -direction, enclosed between confining sidewalls and driven by a top plate moving with velocity  $(V_0, 0)$  at  $z = 0$ . The top plate drives a velocity  $(u, 0)$  and the flow is assumed to be steady and gravity-free. The only non-zero component of the strain-rate tensor is  $D_{xz} = (1/2)du/dz$ , and since the velocity decreases away from the top plate the strain-rate magnitude  $\|\mathbf{D}\| = D_{xz}$ . Therefore the  $z$  momentum balance equation is satisfied if the pressure is equal to a constant,  $p = p_0$ . Since  $\mathbf{u}/|\mathbf{u}| = (1, 0)$  the  $x$  momentum balance then reduces to

$$\frac{\partial \mu}{\partial z} = \frac{2}{W} \mu_W, \quad (4.1)$$

where  $W$  is the channel width and  $\mu_W$  is the sidewall friction. Using the chain rule and the definition of the inertial number  $I$  (2.5), this can be transformed into an ordinary differential equation (ODE) for the velocity,

$$\frac{d^2 u}{dz^2} = \frac{1}{\mu'(I)} \frac{2\mu_W}{Wd} \sqrt{\frac{p_0}{\rho_*}}, \quad (4.2)$$

where  $d$  is the grain diameter,  $\rho_*$  is the intrinsic grain density and  $\mu'(I)$  is the derivative of  $\mu$  with respect to  $I$ . It is possible to obtain an exact solution by invoking the earlier  $\mu(I)$  curve (2.6) of Jop *et al.* (2005), and so here the partially-regularised  $\mu(I)$  curve (2.7) is temporarily neglected. In this case  $\mu$  can be differentiated to give

$$\mu'(I) = \frac{(\mu_d - \mu_s)I_0}{(I_0 + I)^2}, \quad (4.3)$$

and so after again using the definition of the inertial number (2.5), equation (4.2) becomes the second-order nonlinear ODE

$$\frac{d^2 u}{dz^2} = \beta \left( 1 + \gamma \frac{\partial u}{\partial z} \right)^2, \quad (4.4)$$

where  $\beta$  and  $\gamma$  are constants related to the parameters in (4.2), defined by

$$\beta = \frac{2\mu_W}{Wd} \frac{I_0}{\mu_d - \mu_s} \sqrt{\frac{p_0}{\rho_*}} \quad \text{and} \quad \gamma = \frac{d}{I_0} \sqrt{\frac{\rho_*}{p_0}}. \quad (4.5)$$

The equation (4.4) has the solution

$$u(z) = \frac{-\log(1 - \beta\gamma(z + h))}{\beta\gamma^2} - \frac{z + h}{\gamma}, \quad (4.6)$$

where  $h$  is the flow depth with  $u(z \leq -h) = 0$ . The flow depth can be located exactly using the boundary condition  $u(z = 0) = V_0$ , implying

$$\log(1 - \beta\gamma h) + \beta\gamma h = -\beta\gamma^2 V_0. \quad (4.7)$$

This equation has a solution in the form of a Lambert  $\mathcal{W}$  function, and the flow depth is therefore

$$h = \frac{\mathcal{W}(e^{-\beta\gamma^2 V_0 - 1}) + 1}{\beta\gamma}. \quad (4.8)$$

A numerical solution is computed in OpenFOAM using the modified conservative momentum balance equation (3.2), with a no-slip boundary condition at the base of the domain and periodic conditions on the left and right boundaries. A comparison between the numerical and analytic solutions is plotted in figure 2, and any new parameters used are specified in the caption. The remaining parameters are taken from table 2. The numerical solution matches very closely with the analytic solution, and significantly the numerical simulation is able to locate the avalanche depth very accurately regardless of the extent of the domain in the  $z$  direction, i.e. if the domain extends below the position  $z = -h$ , the velocity  $u$  will still reduce to approximately zero at the same position. It may also be noted that the influence of sidewall friction means that the velocity rapidly decays to zero below the driving top plate, and it is therefore important for the numerical method to reproduce this decay. These results strongly suggest that the numerical implementation of the sidewall friction is correct, and computations of rotating drum flows may now be considered.

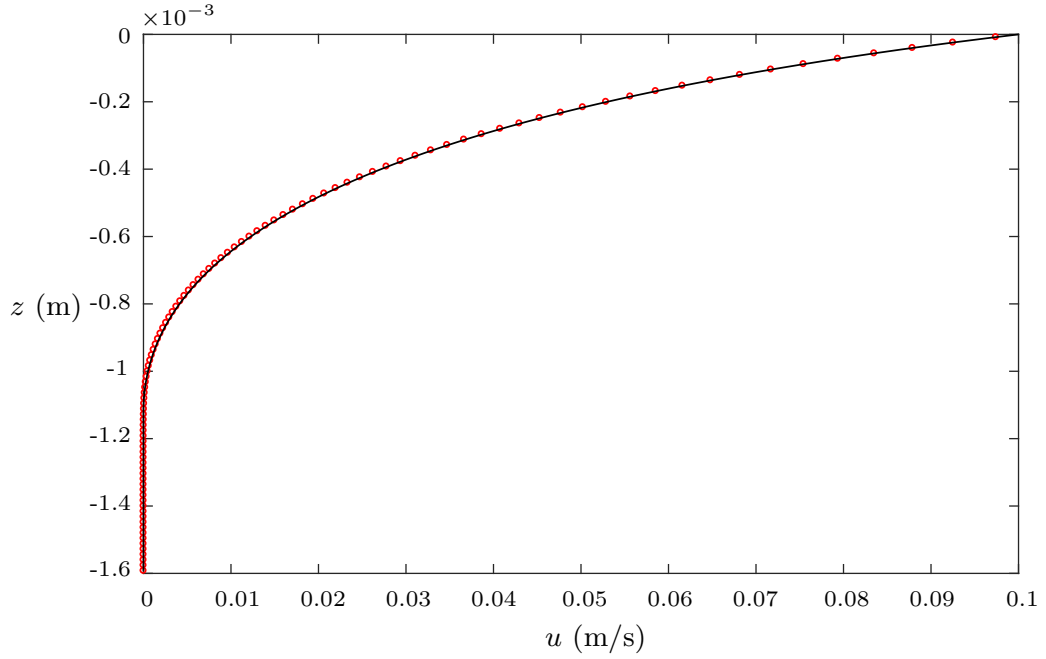


FIGURE 2. Comparison of the numerical solution computed in OpenFOAM by solving equations (3.1) and (3.2) (red open circles) to the exact solution (black curve) given by (4.6). The channel width  $W = 3$  mm and the wall friction coefficient  $\mu_W = \tan(15.5^\circ)$ . The constant pressure  $p_0 = 50$  N/m<sup>2</sup> and the top plate velocity  $V_0 = 0.1$  m/s. A particle diameter of  $d = d^s = 0.35 \times 10^{-3}$  m was used.

## 5. Bidisperse triangular rotating drum

Recent attempts at continuum modelling of rotating drum flows have used prescribed velocity fields obtained from DEM simulations (Schlick *et al.* 2015) or rate-independent rheologies (Liu *et al.* 2018) prone to ill-posedness. Elsewhere, DEM approaches to modelling circular drums (Yang, Sun & Chew 2018; Brandao *et al.* 2020; Yari *et al.* 2020) have achieved some success and provide useful evidence when considering the influence of parameters such as the grain-size ratio, fill fraction, rotation speed and particle shape. However, such methods are limited by the computational expense incurred when including many smaller sized particles, and so very large particles and/or low fill-fractions are typically needed. Zheng *et al.* (2019) coupled the  $\mu(I)$ -rheology (Jop *et al.* 2005) to a convection-diffusion equation to capture the mixing process in a monodisperse mixture with two colours of particles in a circular drum, building upon the work of Gray (2001). While studies which are restricted in focus to circular drums in the continuously avalanching (or rolling) regime may reveal useful parametric information, myriad unique particle pattern formations observed in other drum shapes or flow regimes (Hill *et al.* 1999; Mounty 2007) are excluded. Barker

*et al.* (2021) went significantly further by using the fully coupled system (3.1)–(3.6) to simulate a square rotating drum, although this model lacked a sidewall friction term. The importance of including confining sidewalls for modelling continuously avalanching rotating drum flows can be best understood through the study of polygonal drums. In contrast, the quasi-steady flow field produced by a continuously avalanching circular drum flow gives rise to radial segregation, where predominantly large or small particle annuli form around a central mixed region. In this case, feedback induced by changes to the avalanche depth and velocity only alters the radii of the distinct mixture regions and their segregation intensity, without affecting the geometrical structure of the overall particle distribution, unless another flow regime (Mellmann 2001) can be captured. However, the geometry of polygonal drums leads to continuous variation in the height, length and depth of the free-surface avalanche as the drum rotates, resulting in quasi-periodic, highly transient flow fields which can produce stunning patterns that are very sensitive to fill fraction, mixture composition and rotation rate, as well as the frictional properties of the grains and sidewalls. This means that numerical modelling attempts are naturally more sensitive to parameter changes which affect the bulk flow field. Square drums have been the focus of experimental observations (Hill *et al.* 1999; Ottino & Khakhar 2000*a*; Mounty 2007), and Mounty (2007) used a phenomenological affine mapping approach to accurately reproduce triangular and square drum patterns in the continuously avalanching regime. Here, experiments of bidisperse flow in an equilateral triangular rotating drum are undertaken with a range of volume fill fractions and mean particle concentrations. Furthermore, the coupled method of Barker *et al.* (2021) is used with the segregation reduction factor (2.24) and the modification (2.29) for lateral sidewall friction, represented in full by the system (3.1)–(3.6), to simulate triangular rotating drum flows which, due to the inclusion of sidewall friction effects, demonstrate an impressively strong qualitative and quantitative match to the experiments.

The drum flow is simulated in a fixed Cartesian coordinate system  $Oxz$  with the origin on the axis of rotation at the centre of the drum, where  $z$  is aligned opposite to gravity, as shown in figure 3. The drum frame is an equilateral triangle with side lengths  $L = 0.257$  m, and to begin with is filled to 70% of its total cavity volume



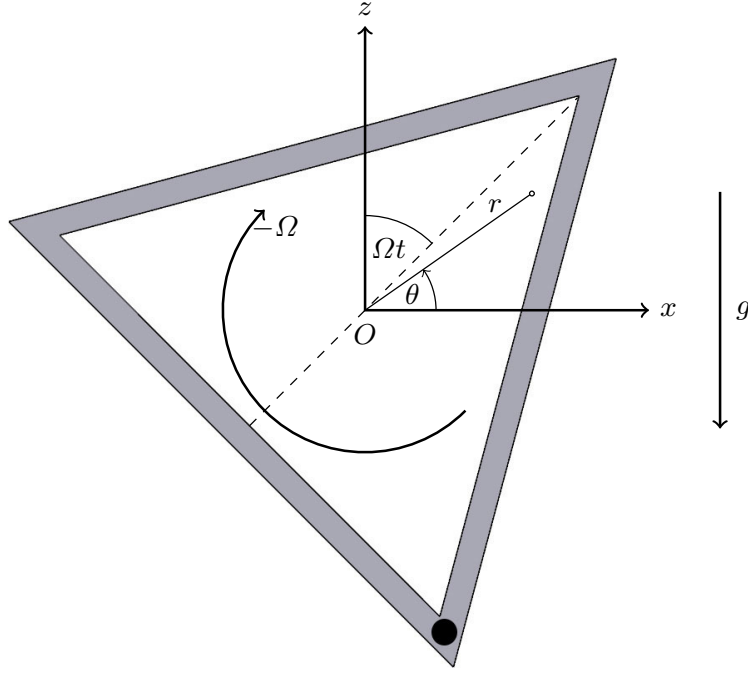


FIGURE 3. Schematic diagram of a rotating triangular drum. A fixed Cartesian co-ordinate system  $Oxz$  is defined, where the origin and centre of rotation  $O$  is at the centre of the equilateral triangle, and the  $z$  axis is orientated in the opposite direction to gravity  $g$ . The height of the triangle, represented by the dashed line, is initially aligned with the  $z$ -axis before it rotates away from the vertical position. For some arbitrary point of distance  $r$  from the origin,  $\theta$  is the angle it forms with the horizontal axis in the anticlockwise direction. A black dot is plotted on one corner of the drum frame so that the changing orientation may be easily tracked. The drum has rotated by an angle  $\Omega t$  from the starting position, with a clockwise rotation rate of  $\Omega = -\pi/12$  rad/s for every computation and experiment in §5, and a rotation rate of  $\Omega = -\pi/48$  rad/s for those in §9.

with an initially uniform granular mixture of 50:50 small and large particles, i.e. a mixture with mean small particle concentration  $\bar{\varphi}^s = 0.5$ , where  $\bar{\varphi}^s = \bar{\varphi}^l$ . All the material is initially assumed to perform solid body rotation

$$\mathbf{u}(t = 0) = \Omega r \boldsymbol{\theta}, \quad (5.1)$$

where  $\Omega$  is the rotation rate, the radial coordinate  $r = \sqrt{x^2 + z^2}$  and  $\boldsymbol{\theta} = (-\sin \theta, \cos \theta)$  is the azimuthal unit vector with  $\theta$  defined as in figure 3. A constant rotation rate of  $\Omega = -\pi/12$  rad/s is specified for each case discussed in this section, corresponding to one full revolution in the clockwise direction every 24 s. This places the drum flow in the continuously avalanching regime (Henein *et al.* 1983; Rajchenbach 1990; Gray 2001; Mellmann 2001; Ding *et al.* 2002; Yang *et al.* 2008) in which a free-surface avalanche forms with continuous erosion and deposition between the solid body of grains underneath.

It is useful to define a relative velocity field with the velocity of the rotating drum walls subtracted, defined as

$$\hat{\mathbf{u}} = \mathbf{u} - \Omega r \boldsymbol{\theta}. \quad (5.2)$$

No-slip and no-penetration conditions are imposed on the triangular walls which, using the relative velocity field, can be expressed as  $\hat{\mathbf{u}} = \mathbf{0}$  on the drum walls. These conditions are applied on the rotating mesh using OpenFOAM's mesh-motion routines, with a structured tetrahedral triangular mesh containing  $N^2 = 600^2$  cells. The frictional parameters for the large and small particles used throughout this section are specified in table 2, with the large grains twice the size of the small grains. Otherwise the rheological parameters are identical across each granular phase. Since the parameters for segregation (Trehwela *et al.* 2021) and diffusion (Tripathi & Khakhar 2013; Cai *et al.* 2019; Bancroft & Johnson 2021) are universal constants determined from experimental and DEM data, the rheological parameters for the granular phases correspond to those for glass beads used by (Rocha *et al.* 2019), and the parameters related to lateral sidewall friction are determined empirically as outlined below in §5.1, there are no fitting parameters used in the simulations. The simulations and experiments in this section run for two full revolutions, or 48 s.

### 5.1. *Experimental set-up*

The drum used for experiments can be seen in figure 4, rotating over two revolutions. It has a metal outer frame with three internal sides of lengths  $L = 0.257$  m, the same as the numerical simulations, and two lateral, transparent plates which confine the flow, made from Polymethyl Methacrylate (PMMA), an acrylic polymer. The transparent plates are screwed together with the metal frame lying between them, also screwed in place, so that they are separated by a cavity width measuring  $3 \times 10^{-3}$  m. The cavity is maintained and bounded along the edges of the equilateral triangle by the metal frame. Before assembly, the PMMA walls must be cleaned with anti-static spray and dried to prevent clinging of the smaller particles to the lateral walls. Glass beads sourced from Sigmund Lindner GmbH, coloured red and green, are sieved to diameters between approximately  $d^s = 300 - 400 \mu\text{m}$  and  $d^l = 600 - 800 \mu\text{m}$  respectively. They are poured into

the drum through a single gap in the metal frame, which is then plugged by a metal stopper and fixed firmly into the frame to prevent grains escaping. To ensure the correct volume of bidisperse granular material is used, the constituent large and small particle volumes are measured separately and then combined and mixed to account for small adjustments to the solids volume fraction, which will increase slightly upon mixing (Golick & Daniels 2009; Thornton *et al.* 2012) so that the total volume of the grains decreases. If necessary, additional grains are then added in the appropriately portioned quantities until the desired volume of mixed material is obtained.

The PMMA plates exert a Coulomb frictional force on the granular medium, and the wall friction parameter  $\mu_W = \tan(15.5^\circ)$  is a material property of both the glass beads and the PMMA, measured empirically as the angle of failure for static grains on a gradually inclined PMMA surface. A bidisperse mixture of the small and large grains is used to measure the wall friction. The parameters used in the numerical simulations are taken directly from these measurements, given in table 2. Since the beads used for experiments are sieved to encompass a specified range of grain diameters, in the simulations the median diameters are used. The back of the drum is then attached to a rotation mechanism, consisting of an ElectroCraft S642-1B/T stepper motor and a modulation speed control unit so that the rotation rate may be precisely calibrated between the experiments and simulations.

Finally, an initially homogeneous mixture must be approximated as closely as possible before the drum rotation begins. This initial condition is easily specified in a numerical simulation, but the natural propensity of grains to segregate based on particle size makes strictly controlling the experimental conditions challenging. This obstacle is overcome by orientating the drum horizontally, and shaking to induce segregation in the direction normal to the lateral transparent sidewalls. The large green beads can then be segregated to the front (observable) wall, with the small red beads concealed behind them against the rear wall. Any given cross section of the drum will thus contain an approximately 50:50 mixture of large and small particles. The particle size gradient in the direction normal to the sidewalls becomes approximately zero ( $d\varphi^s/dy \approx 0$ ) once material is entrained through the avalanche, and so the final pattern formation is approximately uniform in

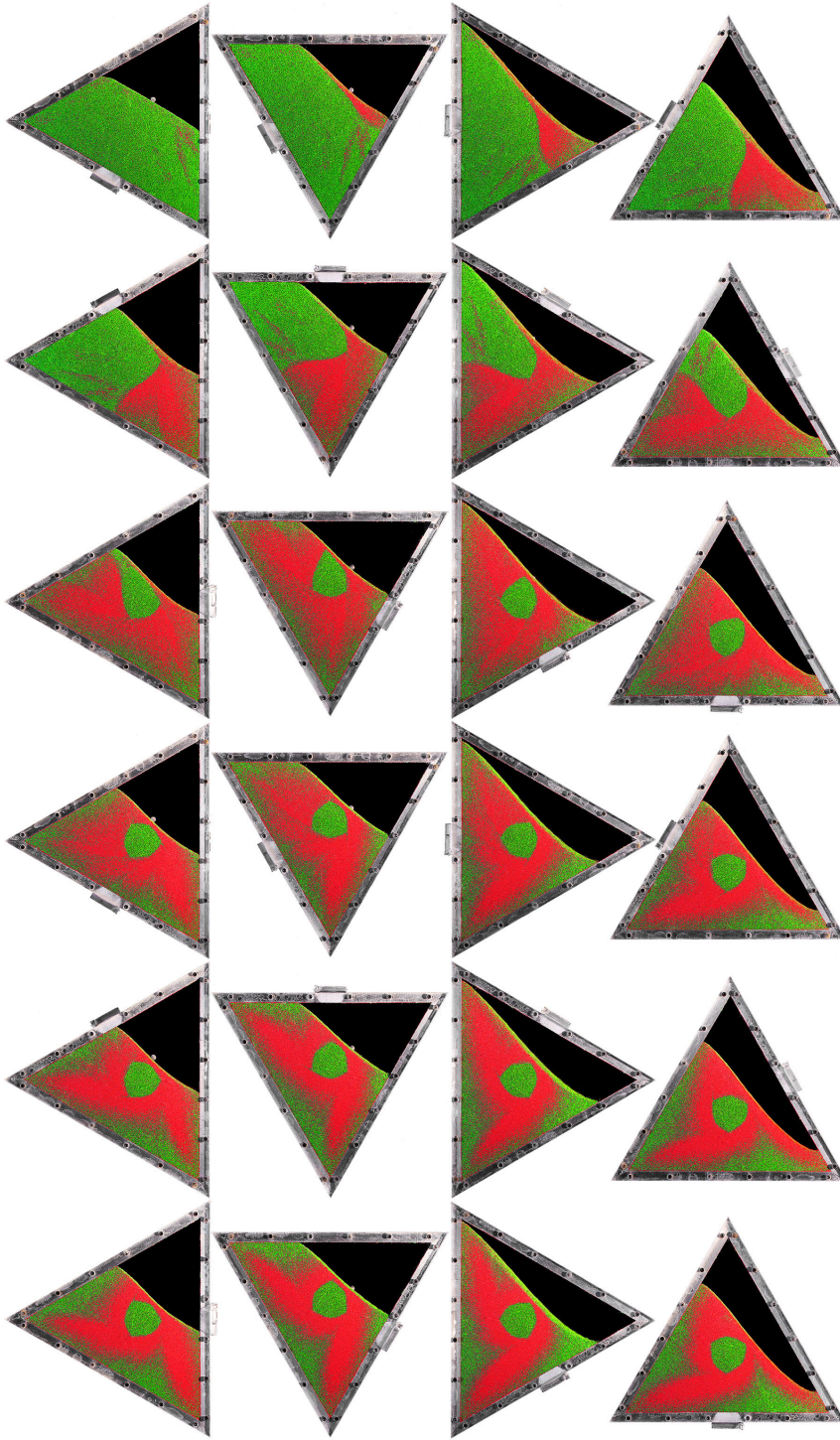


FIGURE 4. Images of a 70% filled triangular rotating drum experiment over two revolutions, beginning at  $t = 2$  s and progressing in increments of 2 s, from left to right, top to bottom, up to  $t = 48$  s. The drum is filled with an approximately homogeneous 50:50 mixture of small red and large green particles, and the free-surface is initially horizontal. Only solid body rotation occurs in the first 2 seconds and so the  $t = 0$  frame is omitted. Once the avalanche failure occurs between  $t = 2$  s and  $t = 4$  s, the mixture gradually segregates into a structure of small particle arms. The experimental procedure is described in §5.1. The protruding stopper, which plugs the cavity through which the drum is filled, provides a reference point for the rotation. A video is available in the online supplementary material.

this direction, excepting the central core, if present. There is also the additional advantage that the undisturbed core will appear to the observer from the front as a uniform region of green particles, providing a strong contrast with the predominantly small red particles which are deposited adjacent to the core.

To capture the images a light-emitting diode panel, a halogen lamp and an optical diffuser are positioned around the drum, with a black velvet sheet attached between the drum and the motor mechanism to provide a clean background, and another in front of the drum through which the camera protrudes to prevent reflections. A slotted circular wheel is affixed to the back of the drum with slots positioned in fixed increments around the perimeter of the wheel, with a light emitting diode and a sensor on opposite sides. In this way the sensor detects the light through the slots at periodic time intervals and hence signals to the camera to capture images at regular drum rotation intervals, and the rotation rate of the drum can be calibrated exactly with reference to the timestamps of the photographs. The slotted wheel or disc has twelve incisions, corresponding to twelve images per revolution. A Canon EOS 7D Mark II camera with a Canon EF 50mm f/2.5 Compact Macro lens is used. The camera shutter speed was chosen so as to produce some motion blur on the avalanching region of the flow, and it is therefore easily distinguishable from the region performing solid body rotation which remains in focus throughout. A full discussion of the experimental results is deferred until the particle distribution of the numerical simulation is introduced in §5.3.

## 5.2. Bulk flow fields

Initially the granular material is static and the free-surface is horizontally inclined, and as the drum begins to rotate the entire granular mixture performs solid body rotation. Due to the presence of sidewall friction the material forms a super-stable heap (Taberlet *et al.* 2003) with a free-surface inclination angle significantly exceeding the value of the static friction coefficient  $\zeta_s = \tan^{-1}(\mu_s)$ , which is the approximate angle of failure without sidewall friction (Barker *et al.* 2021). Once the material near the free-surface fails, a flowing layer is established as material avalanches downslope. After this the free-surface inclination remains relatively constant with only subtle periodic variations due to the continuously

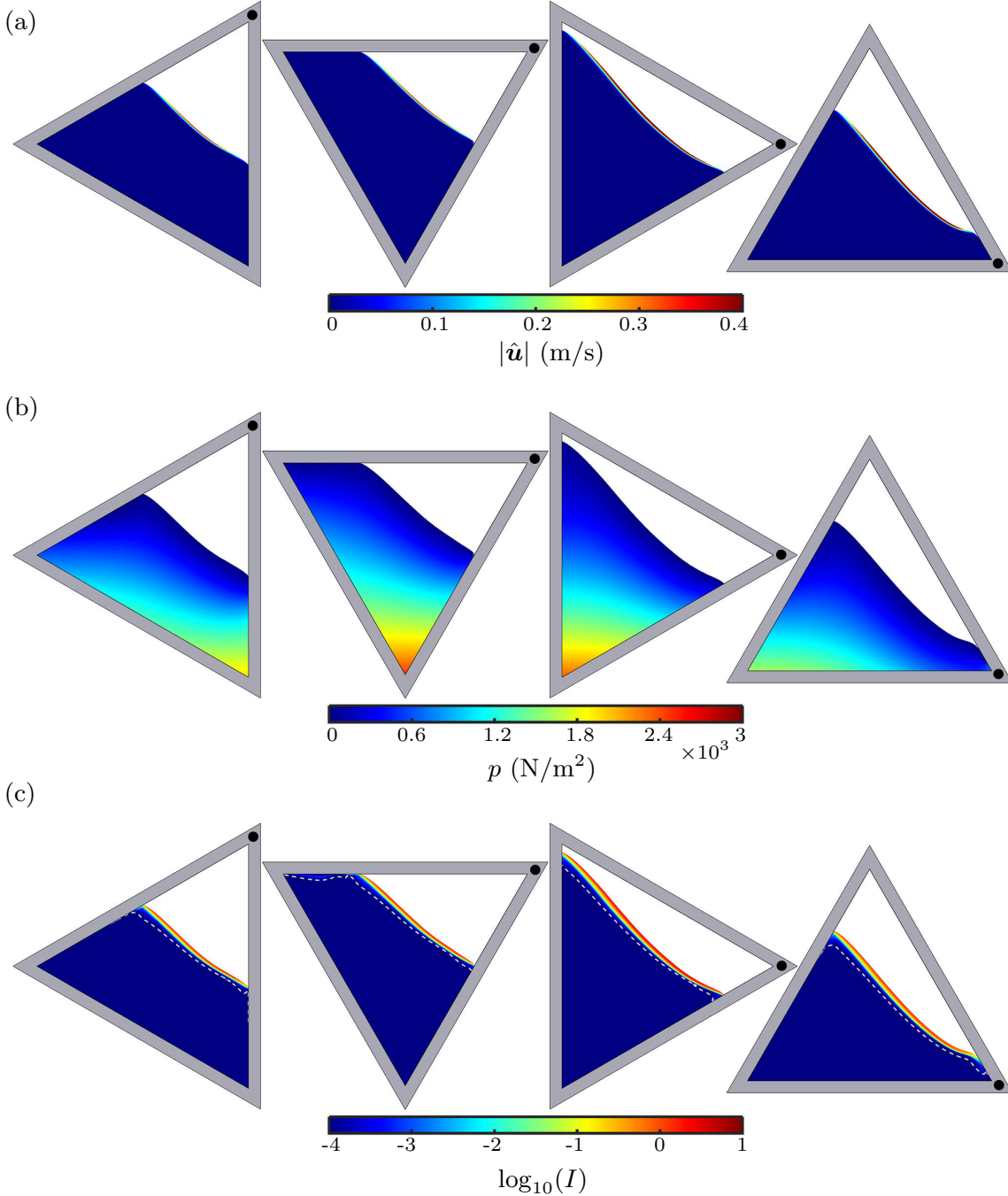


FIGURE 5. Approximately periodic motion of the bulk flow at four different orientations, for a triangular drum flow computed using the parameters from tables 1 and 2, for (a) the modulus of the relative velocity field, (b) pressure, and (c) the base 10 logarithm of the inertial number. Each field is plotted at  $t = 42$  s, 44 s, 46 s and 48 s, from left to right, corresponding to one third of a revolution. The white dashed line in (c) represents the position below which the high viscosity cut-off (3.9) becomes active. The granular mixture occupies 70% of the total area of the drum. The fields pulsate with the rotation of the drum as the free-surface periodically shortens and lengthens, rises and falls, altering the geometry of the region occupied by the granular mixture. The avalanche velocity is strongly dependent on the downslope length, flowing fastest when the free-surface is longest. Due to the presence of sidewall friction the avalanche is thin and rapid. Videos of the full evolution are available in the online supplementary material.

shifting geometry. For the numerical simulation, the free-surface is identified by plotting the contour  $\varphi^a = 1$  and then colouring the air region above the granular material white, as shown in figure 5. The simulation reproduces very closely the free-surface inclination observed experimentally and presented in figure 4, including the slight S-shape which becomes more pronounced when the free-surface is longest, and the subtle dip at  $t = 42$  s which occurs just past the halfway point of the avalanche. The entire flow then exhibits a quasi-periodic pulsating behaviour due to the rotation of the drum, as the free-surface intersection of the triangle produces a varying cross section occupied by the granular material. Figure 5 shows (a) the relative velocity field  $\hat{\mathbf{u}}$  defined by (5.2), (b) the pressure  $p$  and (c) the base 10 logarithm of the inertial number  $I$ . The period of the drum flow is 8 s, equivalent to a third of a revolution. Each field is therefore plotted through the final third of a rotation at  $t = 42$  s, 44 s, 46 s and 48 s, but once the flowing layer is established within the first third of a rotation the periodicity of the simulation means that any subsequent period would give very similar results, with the qualification that the feedback from the evolving mixture composition leads to subtle adjustments in the bulk flow. Videos showing the full evolution of the bulk flow fields in the numerical simulation are available in the online supplementary material. Feedback between the bulk flow and the mixture composition plays a more pivotal role at fill levels near 50%, when the strongly composition-dependent velocity field can lead to the formation of petal-like patterns in the particle distribution (Zuriguel *et al.* 2006) for circular drums, and more complex patterns in triangular and square drums (Mounty 2007) which have been linked to chaotic advection (Hill *et al.* 1999; Khakhar *et al.* 1999; Ottino & Khakhar 2000*b*).

The length of the avalanche depends on the orientation of the drum, and the longest avalanches at  $t = 46$  and 48 s, which occur when the free-surface is most closely aligned with the opposite, upper drum wall, are also the fastest flowing (see figure 5a) since the grains have a longer distance over which to accelerate. The acceleration of granular material in the free-surface occurs while the avalanche becomes deeper as more particles are entrained into the flowing region from the solid body below, resulting in peak velocities around halfway down the avalanche, after which particles are deposited back into the solid body and

the avalanche thins and decelerates. Due to the presence of sidewall friction this active avalanching layer is very thin in comparison with the simulations of Barker *et al.* (2021), and presents a good match with the blurred flowing region in the experiments of figure 4. Below the avalanching layer the velocity in the rotating frame rapidly decays into a quasi-static creep state. The pressure (figure 5b) has a lithostatic component, but with increasing depth the initially lithostatic pressure gradient becomes increasingly gravity-aligned as the pressure contours begin to divert towards the lower corner of the drum where the overburden is felt most strongly. Since both the segregation velocity magnitude and the inertial number are strain-rate dependent, the inertial number (figure 5c) gives an accurate identification of the active layer in which segregation takes place in the simulations. It appears slightly deeper than that implied by figure 5a since  $\log_{10}(I)$  is plotted, and also exhibits less variation in magnitude with changing orientation, in part due to the chosen logarithmic scale but also because the strain-rate dependent inertial number is tied to velocity gradients rather than velocity. The solid core of homogeneously mixed material develops below this zone. The flow is governed by the creep regime of the partially regularised  $\mu(I)$ -rheology (2.7) for  $I \leq I_1 = 0.0205$ , and  $I = I_1$  is attained above the white dashed line representing the point below which the numerical regularisation for high viscosities (3.9) is activated. Since the inertial number decreases with depth, this means that all of the granular material in the dynamic regime and some of the creeping material is modelled using the full granular rheology. The Newtonian viscosity is only applied in the quasi-static creeping region and therefore has little influence on the overall flow dynamics. It is notable that the inertial number very rapidly decays by orders of magnitude, from the free-surface avalanche to the peak viscosity region, which is due to the wall friction induced super-stable heap (Taberlet *et al.* 2003).

### 5.3. Particle-size distribution

Figure 4 shows the developing mixture composition over the entire process of segregation and diffusion in a 70% filled drum experiment using a 50:50 mix of small red grains and large green grains, and figure 6 shows the small particle concentration in the equivalent numerical simulation computed with the



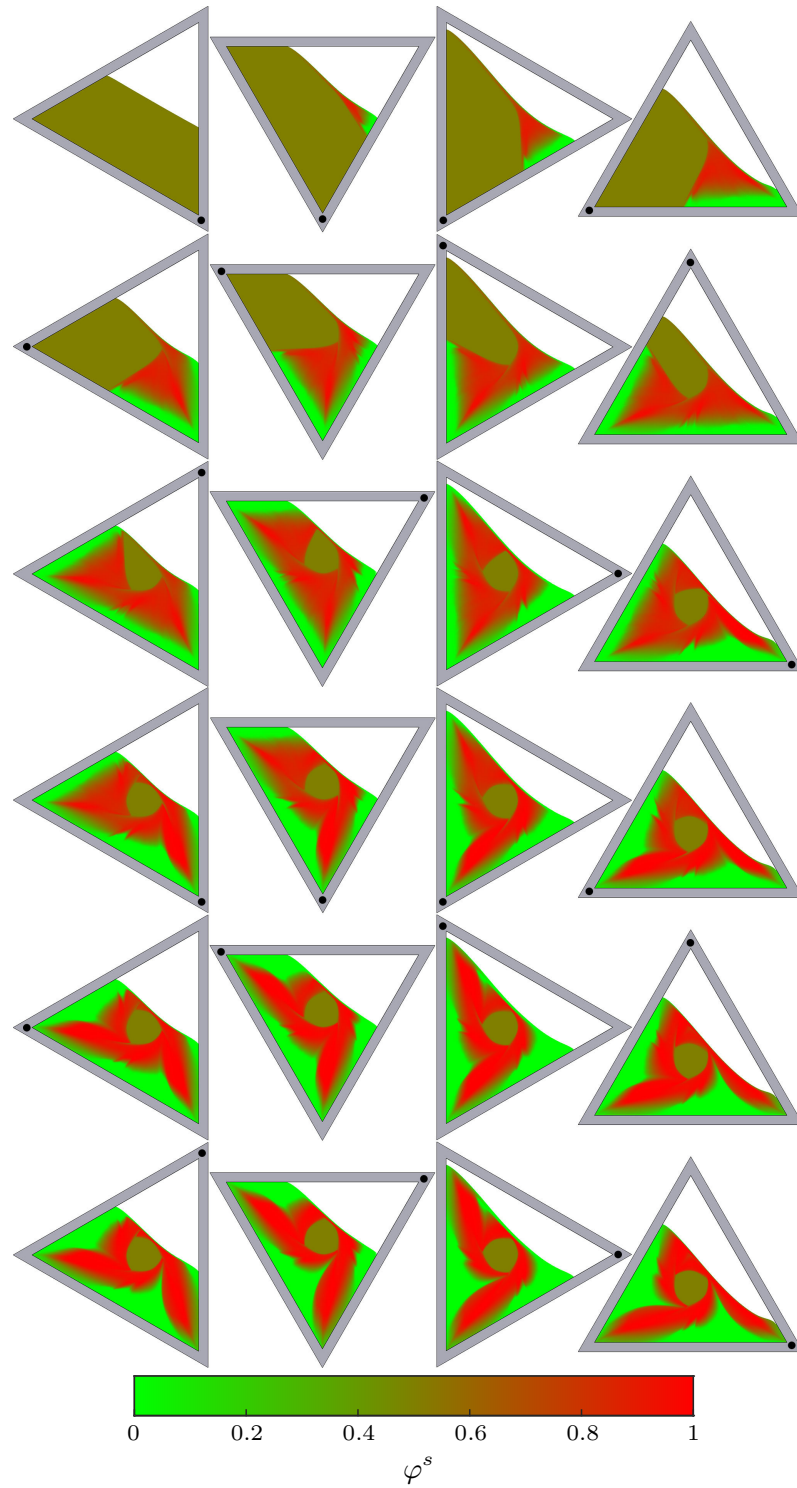


FIGURE 6. Small particle concentration in a 70% filled triangular rotating drum simulation with a 50:50 mixture of small and large particles, computed using the segregation, diffusion and rheological parameters specified tables 1 and 2. The simulation is shown over two full revolutions, beginning at  $t = 2$  s and progressing in increments of 2 s, or 1/12 of a revolution, from left to right, top to bottom, for comparison with the experiment presented in figure 4. A black dot is fixed to one corner of the triangle to provide a reference point for the progression of clockwise rotation. A video of the full numerical solution is available in the online supplementary material.

parameters from tables 1 and 2, with the frames moving in increments of two seconds or equivalently  $1/12$  of a revolution in both cases, beginning at  $t = 2$  s. Videos showing the full particle pattern evolution in the experiment and numerical simulation are available in the online supplementary material. The avalanche failure occurs between 2 s and 4 s. Before this failure, the grains are static and so cannot redistribute; this is captured by the numerical simulations since there is no shear on the particles and hence no segregation or diffusion occurs due to the strain-rate dependence in the segregation velocity magnitude (2.26) and the diffusion rate (2.20). The particle size distribution can therefore be seen evolving from the second frames. As the mixture flows down the avalanche, small particles can percolate down through void spaces opening throughout the mixture in a process known as kinetic sieving, and particles of both sizes are squeezed upwards towards the surface of the flow as a consequence of force imbalance, resulting in an inversely graded layer of large and small grains (Middleton 1970; Savage & Lun 1988). The functional form of the segregation velocity magnitude (2.26) means that segregation in the numerical simulation is confined to the sheared flowing region while material in the solid body remains in a mixed state, as observed experimentally here and elsewhere (Gray & Hutter 1997; Khakhar, McCarthy & Ottino 1997). The pressure dependence in (2.26) further acts to shut down the segregation process deeper into the drum (Golick & Daniels 2009; Fry *et al.* 2018; Trehwela *et al.* 2021). Segregation is therefore strongest at the free-surface, with the consequence that the large particle region is slightly more strongly segregated than the small particle region, although this is less obvious in the experiment. The effect is intensified by the fact that particles nearer the free-surface have longer trajectories through the avalanche before being deposited and hence spend longer in the active layer.

Since the fill level of the drum exceeds 50% there is a central core of homogeneously mixed material which is never entrained into the avalanche (Gray 2001; Mounty 2007), taking the approximate shape of a Reuleaux triangle, a three sided shape formed by the intersection of three circles. The presence of sidewall friction in the numerical simulations leads to a thin avalanche, and a central core is produced which matches very closely in both size and shape to that observed experimentally. This requires that (i) the partially regularised  $\mu(I)$ -rheology (2.7)

with lateral sidewall friction produces a free-surface avalanche with the correct flowing depth, and (ii) the segregation (2.26) and diffusion (2.20) formulations confine the particle-redistribution process to this avalanching region. In contrast, previous attempts at numerical simulation (Barker *et al.* 2021) which neglected sidewall friction possessed very deep, slow moving avalanches, and subsequently severely underestimated the core size and the segregation velocity magnitude relative to experimental observations (Hill *et al.* 1999; Ottino & Khakhar 2000*a*; Mounty 2007). For such computations it is necessary to scale the grain diameter with the flowing depth to achieve a greater intensity of segregation, whereas here no fitting parameters are required. The slightly S-shaped free-surface inclination of the experiments is also captured accurately by the numerical simulation, demonstrated by the strong qualitative match between each frame in figures 4 and 6. This represents a further validation of the partially regularised  $\mu(I)$ -rheology and the approach described in §2.5 to model the influence of sidewall friction.

The quasi-periodic pulsating avalanche leads to the formation of two small particle arms orientated towards the three corners of the drum which rotate in an impressive triskelion pattern, and strengthen in definition each time they are re-entrained into and then deposited from the avalanche. A triskelion is a shape with protruding arms exhibiting three-fold rotational symmetry. The particle composition deposited downslope by the avalanche is advected by the rotation of the drum back into the upslope position to be re-entrained into the avalanche, where there is another opportunity to segregate. Every time an arm is advected through the avalanche it is re-orientated towards the next drum corner in the clockwise direction, or by  $-2\pi/3$ , with the result that each of the two arms take 16 s to fully rotate around the drum, which is  $2/3$  of the time taken for a full revolution of the drum.

Over the first full rotation, the material separates out around the homogeneous core into distinct regions of predominantly large or small particles with a diffuse region separating them, in a triangular shape in which the partially-formed small particle arms are vaguely discernible. Over the second rotation, the pattern morphs into the full triskelion structure of small particle arms, and this pattern remains stable over subsequent revolutions omitted here. The timescale of this entire gradual formation is captured by the numerical simulation, as shown by the

excellent frame-by-frame match between figures 4 and 6. The arms exhibit a strong three-fold rotational symmetry, which is however incomplete since the pattern is interrupted by the free-surface. The pattern is necessarily incomplete since an avalanche will only form for a partially filled drum. The symmetry is particularly strong in the numerical simulation, which is demonstrated in figure 7 by plotting the contour for  $\varphi^s = 0.5$  around the two small particle arms, and rotating the original contour twice, by  $\pm 2\pi/3$ , to form a complete triskelion structure in which the two arms are overlaid. At  $t = 36$  s, the main body of the arms have almost perfect rotational symmetry, and only the free-surface interrupts the symmetry of the entire structure. This is because the arms have been entrained through the avalanche the same number of times. Interestingly, the lingering effects of the initial avalanche failure, which is not periodically repeated, do not appear to significantly affect the rotational symmetry. At  $t = 44$  s, one arm has had an additional opportunity to segregate, leading to a clearly defined crevice near the central core, while the arm itself is slightly different in shape. This weakens the rotational symmetry, as the other arm is unchanged in shape from  $t = 36$  s, since it has only performed solid body rotation during this time. The difficulty in obtaining a perfectly homogeneous initial mixture means that the rotational symmetry is inevitably weaker in the experiments, though still clearly evident. The arms emanate not from the undisturbed core as in the square rotating drum simulations of Barker *et al.* (2021) but from a position adjacent to the core, and individually form an asymmetrical structure in which the outer length of the arm is roughly parallel to the adjacent wall of the triangle, culminating in a flattened top. Furthermore, after the pattern formation has reached a certain stage, a small inner triangle can be distinguished above the undisturbed core as the upper arm is partially entrained through the avalanche, visible at  $t = 40$  s and 48 s. The small particle regions immediately adjacent to the core and in the avalanching arm encase a small triangular shaped zone with a higher concentration of large particles. This feature is also subtly present in the experimental images, and occurs once the small particle arms have achieved sufficient definition for a large particle-rich region to coalesce in a crevice near the core. This means that the numerical simulation successfully captures all of the key characteristics of the triangular drum experiment. Indeed, as will be demonstrated below, the arms do

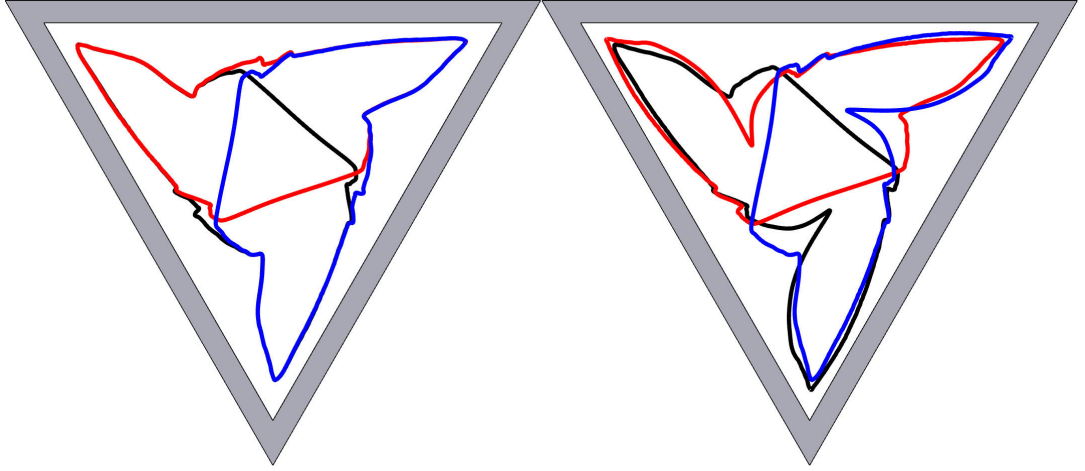


FIGURE 7. Contour for  $\varphi^s = 0.5$  around the small particle arms in the numerical simulations of a 70% filled triangular rotating drum containing a 50:50 bidisperse mixture (i.e. with  $\bar{\varphi}^s = 0.5$ ), demonstrating the rotational symmetry of the arms, at  $t = 36$  s on the left, and  $t = 44$  s on the right. In both cases, the original contour is plotted in black, the same contour rotated by  $-2\pi/3$  rad (i.e. rotation in the clockwise direction) in red, and the contour rotated  $2\pi/3$  rad (anticlockwise) in blue. At  $t = 44$  s, one arm has been entrained through the avalanche an additional time, leading to a crevice in this arm near the central core.

not form at all in numerical simulations without the presence of sidewall friction, when instead weak small and large particle regions coalesce in a triangular shape orientated with the outline of the drum walls, somewhat similar to the pattern which forms over the initial revolution here.

#### 5.4. Quantitative analysis and numerical convergence

As demonstrated above, the geometrical structure of small particle arms surrounding an undisturbed central core of homogeneous material is very accurately reproduced by the numerical simulation, as is the free-surface inclination and shape, but a quantitative method must be devised to precisely test the theoretical predictions and the accuracy of the numerical method.

Typically, quantitative comparisons for continuum simulations in recent years have been drawn with data from DEM simulations (Yang *et al.* 2018; Schlick *et al.* 2015), which accurately capture particle-level dynamics and therefore readily provide a data set against which continuum theory can be judged. However, there are disadvantages to this approach. The heavy computational expense incurred by DEM simulations, which must track each particle and compute each inter-particle interaction, can be severely limiting. As a consequence, particle numbers for rotating drums must be restricted to a practical order of magnitude by using

very large particle sizes or lower fill levels (Zhang *et al.* 2017; He *et al.* 2019; Yari *et al.* 2020; Brandao *et al.* 2020). The experiments presented in this paper are composed of many hundreds of thousands of tiny particles, up to approximately 1.2 million, and are therefore unsuitable for DEM simulations. This means that an alternative method of quantitative analysis must be established. Extracting quantitative data on particle-size distribution from granular flow experiments is notoriously difficult (Scott & Bridgwater 1975), particularly for the sealed containers handled here, where extractive sampling is laborious and possibly subject to systematic inaccuracies (Scott & Bridgwater 1975). Instead, a non-intrusive method of careful data extraction will be used.

The primary field of interest is the particle concentration field, which can be determined approximately from experimental images using the following method. First, the drum is filled with a mixture of known small particle concentration, shaken to achieve approximate uniformity and then photographed. The drum, containing this same mixture, is repeatedly shaken and photographed to improve reliability. This process is then repeated for a variety of mean small particle concentrations across the range  $\bar{\varphi}^s \in [0, 1]$ . All the images are cropped to remove the non-granular regions, and the colour profiles of the resulting raster images are processed in MATLAB to return a matrix giving the RGB (red-green-blue) intensities for each individual pixel. The ratio of the red intensity to the green intensity is determined for each pixel, and averaged over the entire domain. The red and green intensities exhibit a strong correlation with the small particle concentration since they correspond to the colours of the small and large particles respectively. This process returns a mean red to green pixel intensity ratio corresponding to each measured mean small particle concentration  $\bar{\varphi}^s$ , and the results for a given concentration can be reliably reproduced experimentally. The ratio can then be plotted against  $\varphi^s \in [0, 1]$  and a best fit curve drawn to give a complete set of unique expected intensity ratios for every possible concentration. In fact, here a strongly linear relationship was discovered between the intensity ratio and the particle concentration, and consequently the mapping can be further improved.

Once the relationship between the intensity ratio and the concentration is assumed to be linear, the appropriate linear fit can be determined using data taken from only two concentrations. When the mean small particle concentration

$\bar{\varphi}^s = 0$  or  $1$ , it follows that  $\varphi^s = \bar{\varphi}^s$  at every point in the granular mixture. Therefore, the images with these two mean particle concentrations can be divided into  $8 \times 8$  pixel cells, where the cell size is chosen to ensure a reasonable number of particles per cell, and the concentration in every cell is known *a priori*. The mean colour intensity ratio in each individual cell is then calculated, and the mean cell intensities when  $\varphi^s = 0$  and  $1$  can be used to produce the linear fit between intensity ratio and small particle concentration. This method has three major advantages over using a greater number of points for  $\bar{\varphi}^s$  and taking the mean pixel intensity ratio over the entire drum. First, since it uses data from  $8 \times 8$  pixel cells, it can be used to derive the concentration in cells of the same size from other drum images, without any additional assumption of validity. Second, since the concentration in every cell is known when  $\bar{\varphi}^s = 0$  or  $1$ , the standard deviation of the cell intensity ratio can be trivially calculated and used to plot a set of worst fit lines which facilitate accurate error estimation. Error is due to particle shadows and uneven light reflections (Hill *et al.* 1999), which may be reduced but not eradicated by an appropriately positioned lighting set-up. Finally, when the drums are filled with pure phases of small or large particles, attempts at attaining a relatively homogeneous mixture are not subject to inadvertent segregation and so the colour intensity data is more reliable than for intermediate particle concentrations.

Using the calculated mapping from colour intensity to concentration, images of the developing rotating drum patterns from figure 4 are divided into  $8 \times 8$  pixel cells, so that the mean red to green intensity ratio can be determined for the individual cell and a small particle concentration value assigned using the set of expected intensity ratios. To account for the undisturbed core, which appears to have  $\varphi^s = 0$  but in reality has  $\varphi^s = 0.5$  due to the method of attaining the initial mixture composition (see §5.1), this region is filled with black pixels for which an exception is made so that they are assigned the correct concentration value. Note that although some pixels elsewhere in the drum appear very dark due to gaps between particles adjacent to the clear walls, over the  $8 \times 8$  pixel cells there is sufficient saturation of colour to avoid confusion with the central core region. This results in a projected small particle concentration field for the entire drum. Using this method, the mean particle concentration of the experiments

using an approximately 50:50 mixture of small and large particles is calculated to be  $\bar{\varphi}^s = 0.49 \pm 0.03$ , matching very closely with the approximate true value of  $\bar{\varphi}^s = 0.5$ .

The concentration field for the 70% filled rotating drum after  $t=48$  s is shown in figure 8. The number of pixels per cell is chosen to give a detailed concentration field with strong image definition where each cell contains many particles. The subtle region of weaker small particle concentration above the core in the crevice of the arm being entrained into the avalanche is more clearly visible in this image than in the pre-processed image, which is shown in the final panel of figure 4. As predicted by the theory, the predominantly large particle regions adjacent to the drum walls are more strongly segregated than the small particle regions adjacent to the central core, since segregation is strongest at the free-surface, towards which the large particles are segregated. This was not evident in the pre-processed images, but has been verified by examining the field  $(\varphi^s - \bar{\varphi}^s)^2$ , which confirms that the predominantly large particle regions deviate further from the mean particle concentration than the predominantly small regions. The influence of particle size and mixture composition on segregation intensity will be examined further in §8.

To test the strength of the segregation and compare it directly to the simulation data, the segregation intensity is defined, analogously with Danckwerts (1952), as the standard deviation of  $\varphi^s$  normalised by the mean small and large particle concentrations,  $\bar{\varphi}^s(1 - \bar{\varphi}^s)$ ,

$$\mathcal{S} = \sqrt{\frac{\int_{\omega} (\varphi^s - \bar{\varphi}^s)^2 dX dZ}{\bar{\varphi}^s(1 - \bar{\varphi}^s) \int_{\omega} dX dZ}}, \quad (5.3)$$

where  $\omega$  is the part of the domain occupied by granular material. This definition for the segregation intensity means that  $\mathcal{S} = 0$  for an unsegregated mixture, and  $\mathcal{S} = 1$  for a fully segregated mixture.

The resulting data on the segregation intensity is presented in figure 9, over the full time for the simulation and after every third of a revolution, or 8 s, for the experiments. The intensity derived from the experiments is not dependent upon the number of pixels per cell because the map from intensity ratio to concentration is derived using cells of the same size, unless the cells used are



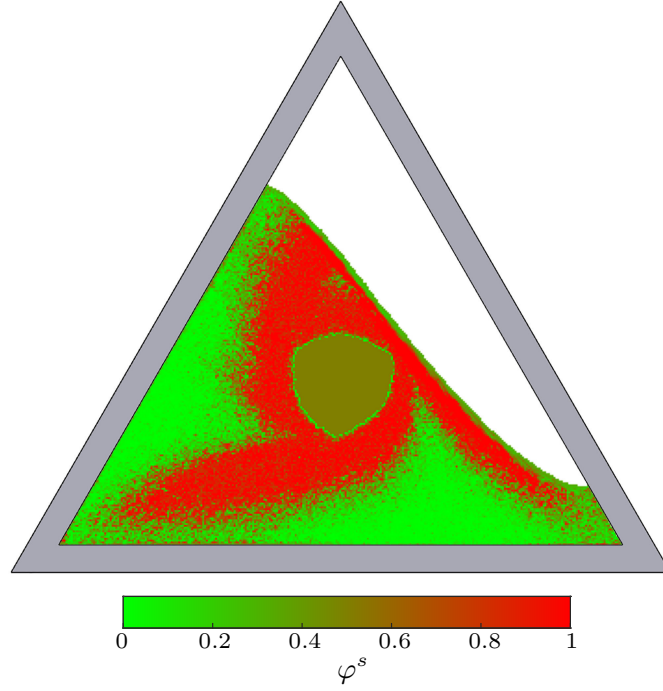


FIGURE 8. Approximated small particle concentration field at  $t = 48$  s for the experiment using a triangular drum 70% filled with an approximately 50:50 mixture of small and large particles. The small particle concentration is obtained using the projection method described in §5.4.

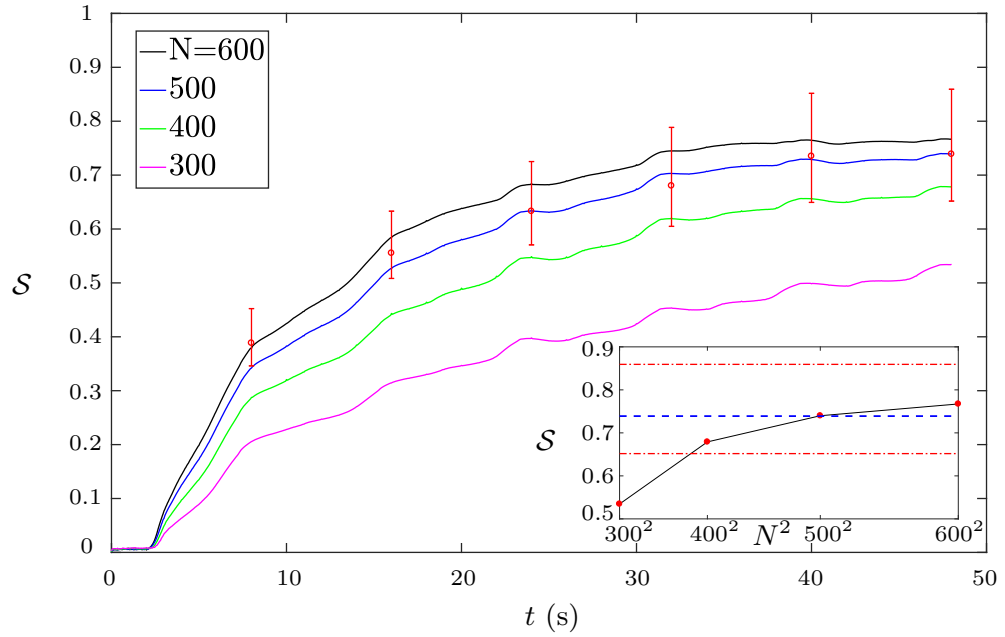


FIGURE 9. Comparison of the developing segregation intensity (5.3) over time in a 70% filled drum with a 50:50 mix of small and large particles, between the experiment (red circles with error bars) and the simulation data (solid colour lines) using a variety of grid resolutions, where the total number of cells is  $N^2$ . In the inset, the segregation intensity of the simulations at  $t = 48$  s is plotted against the grid resolution, with the segregation intensity calculated for the experiment represented by the dashed blue line for comparison, while the dot-dashed red lines represent the experimental error of the intensity.

excessively small (i.e. an order of magnitude similar to the grain size) or excessively large. The segregation intensity is plotted for numerical simulations computed at four different grid resolutions. Friction from the lateral sidewalls results in a very thin free-surface avalanche, which acts as a boundary layer within which all the segregation occurs. Therefore, to correctly predict the segregation and hence the overall pattern formation, this boundary layer must be adequately resolved, requiring a very fine mesh. For coarser meshes, the avalanche is under-resolved and numerical diffusion therefore leads to an underestimation of the segregation intensity. Although the finest resolution, which uses  $600^2$  tetrahedral cells, is not perfectly resolved, the two finest meshes yield similar results, and the time-evolution of the segregation intensities and the inset in figure 9 clearly demonstrate convergence of the solution with increasing refinement. Furthermore, the simulations appear to be converging on a solution close to the intensities derived from the experiments using the concentration field projection method, and are clearly converging on a solution within the estimated error. The comparison also confirms the earlier observation that the segregation takes place over a similar timescale in simulations and experiments, even when the avalanche is severely under-resolved. This means that the numerical simulations provide a strong qualitative and quantitative match with experimental data without the need for any fitting parameters.

Additionally, the simulation data shows periodic peaks and troughs in segregation intensity with a period of one third of a revolution, as expected given the variation in the avalanche dynamics with the shifting geometry (see §5.2, figure 5), producing higher strain-rates, longer particle trajectories and hence stronger segregation when the avalanche is at its longest. The intensity actually declines slightly after these peaks in the second rotation, while the arms are entrained through the avalanche. For the experiment and simulations the segregation intensity is stabilising by the end of the second revolution, with a final segregation intensity in the highest resolution simulation of  $S(t = 48 \text{ s}) = 0.77$ , although it may continue to plateau over many revolutions and will never become fully periodic (Mounty 2007).

## 6. The importance of lateral sidewall friction

The theoretical and numerical framework used to compute the rotating drum simulation in §5 uses width-averaged, two-dimensional mass and momentum equations with Coulomb slip assumed on the clear confining lateral sidewalls through which the evolving particle pattern is observed in the experiments (see §2.5). Jop *et al.* (2005) observed that sidewall friction effects control the dynamics of confined steady uniform granular flows on a pile, with narrower channel widths inducing faster and thinner free-surface avalanches, while Taberlet *et al.* (2003) demonstrated how flows atop a quasi-static heap can be stabilised at high inclination angles by confining sidewalls. The experimental and numerical results obtained in §5 demonstrate these same phenomena for a complex, transient non-uniform flow, and further insight may be gained by examining the effects of excluding lateral sidewall friction from the numerical computation.

Setting up the simulation is simple given the work described in the preceding sections. All the parameters used to compute the rotating drum simulation in §5 from tables 1 and 2 are retained, with the exception that sidewall friction effects are discarded by setting  $\mu_W = 0$ . The dimensions of the triangular drum walls are matched with the experimental values given in §5.1, and the drum rotation rate is again  $\Omega = -\pi/12$  rad/s.

A comparison between the particle distribution patterns in the experiment in figure 4 and the numerical simulations with and without sidewall friction effects is presented in figure 10a, at the end of two full revolutions. As discussed above, the simulation computed with sidewall friction matches excellently to the experimental results. However, without sidewall friction, almost no segregation has occurred. The segregation intensity at the end of two revolutions confirms this, with  $\mathcal{S}(t = 48 \text{ s}) = 0.0663$  indicating little deviation from the initial mixed state. A very thin region of large particles and a weaker region of small particles are discernible close to the drum walls, but in place of the complex geometrical structure which forms in the presence of sidewall friction there is a simple triangular shape. This indicates that sidewall friction is not only a necessary consideration for accurate modelling of rotating drum experiments, but is one of the dominant physical mechanisms determining the nature and extent of particle segregation in

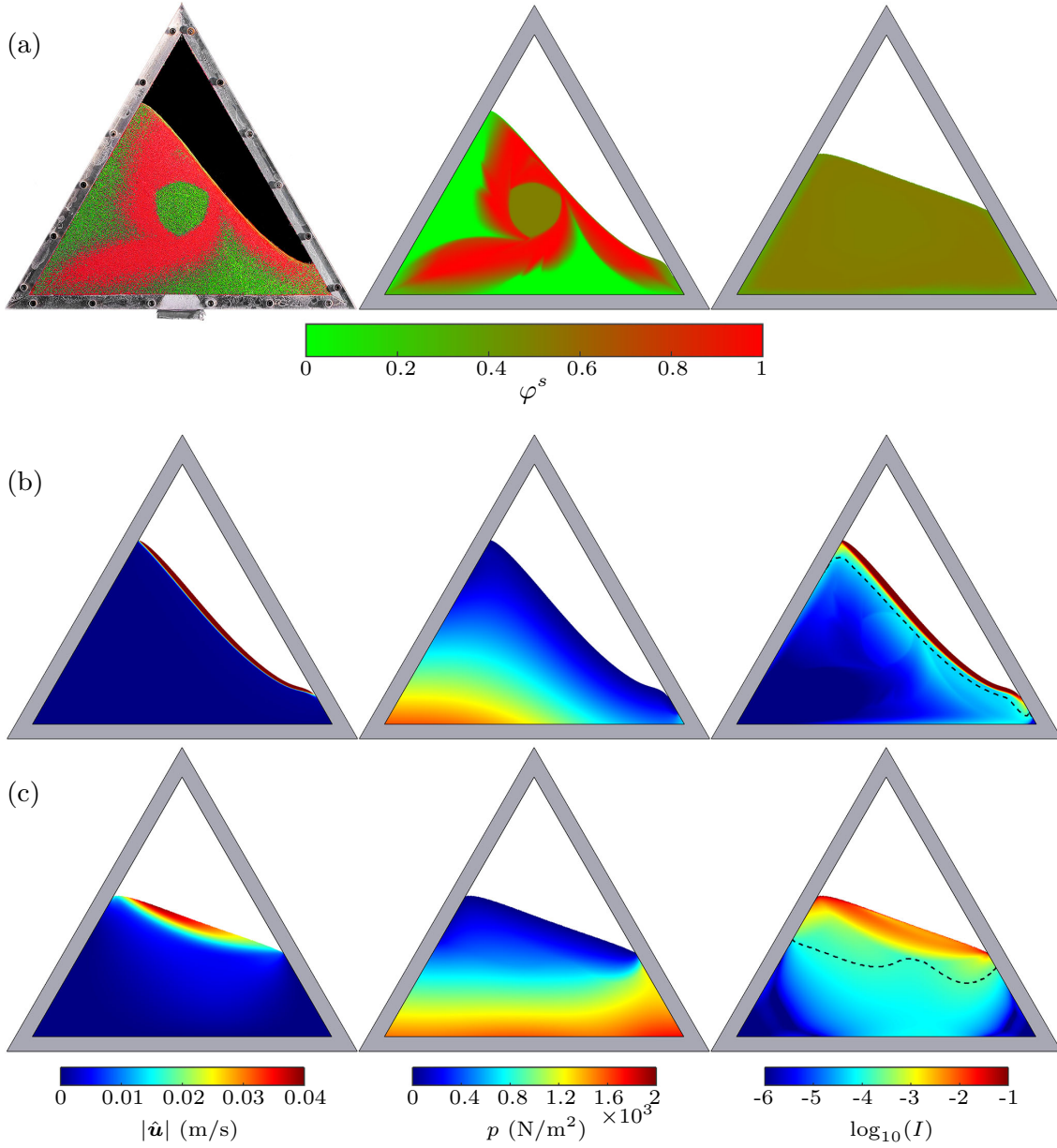


FIGURE 10. Particle-size distributions in bidisperse triangular rotating drum flows at  $t = 48$  s after two revolutions (a), for an experiment (left), the simulation incorporating lateral sidewall friction discussed in §5 (middle), and an otherwise identical simulation without sidewall friction (right), followed by the bulk flow fields for the triangular rotating drum simulation with sidewall friction (b) and without sidewall friction (c) at  $t = 48$  s. The fields plotted are the modulus of the relative velocity field (left), the pressure (middle) and the base 10 logarithm of the inertial number, where the black dashed line indicates the position below which the high viscosity cut-off (3.9) becomes active (right). The particle segregation is extremely weak and the free-surface inclination angle drastically reduced without sidewall friction, due to the slower and thicker free-surface avalanche.

narrow rotating drum flows. The particle distribution pattern aligned with the drum walls continues to intensify over subsequent revolutions, but even after 20 revolutions  $\mathcal{S}(t = 480 \text{ s}) = 0.3007$  and the segregation intensity has not reached a plateau, indicating an extreme overestimation of the segregation timescale. The

free-surface inclination is now straight rather than S-shaped, and the inclination angle is also severely reduced to a value close to the static friction angle of  $\zeta_s = \tan^{-1}(\mu_s) = 22^\circ$ , as observed in the rotating drum simulation of Barker *et al.* (2021). Therefore, the super stable heap phenomenon studied by Taberlet *et al.* (2003) is indeed produced by confined rotating drum flows.

The bulk flow fields with and without sidewall friction are plotted in figures 10b and c respectively, demonstrating the dynamics underpinning this weak segregation. The modulus of the relative velocity field in the free-surface avalanche is around an order of magnitude smaller without sidewall friction. The peak velocity magnitude, attained when the avalanche is parallel to the upper drum wall and hence at its longest, is  $|\hat{\mathbf{u}}| \approx 0.14$ , a fivefold reduction relative to the simulation computed with sidewall friction, for which the velocity peaks at  $|\hat{\mathbf{u}}| \approx 0.7$ . The avalanche is also much thicker, as predicted by the observations of Jop *et al.* (2005), and the velocity decays only gradually. The pressure field is similar, but the inertial number never approaches the high values with  $I \approx 1$  observed in the presence of sidewall friction. As an aside, a relationship between the inertial number and the particle distribution can also be discerned in figure 10b, since by definition  $I$  (2.16) depends on the concentration weighted particle diameter. The high viscosity cut-off is activated much deeper into the flow without sidewall friction, although still below the flowing layer, in part because sidewall friction induces a rapid decay below the flowing layer towards a quasi-static state. This reveals why the mixture segregates so weakly; the reduced strain-rate magnitude, owing to the thicker, slower flow, feeds back into the segregation scaling law (2.26) and inhibits the particle redistribution process. This issue can be circumvented by using particle sizes of a comparable order of magnitude to the avalanche depth, which compensates for the reduced strain-rate magnitude via the dependency of the segregation scaling law on the concentration weighted grain diameter (Barker *et al.* 2021). This results in a more strongly segregated mixture which nevertheless fails to predict the observed pattern formation of experiments with the accuracy of the computations presented in §5. Evidently, for rotating drum flows confined within a thin channel, it is essential that lateral sidewall friction be incorporated into continuum models for a realistic approximation of the dominant physics, which is demonstrated for the first time here.

## 7. Varying fill fractions

Here triangular drums are considered with varying fill fractions in relation to the 70% filled case discussed above, again with initially homogeneous 50:50 small and large particle mixtures in each case. The results from the experiments and the particle distribution from the numerical simulations are shown in figure 11, for (a) 30%, (b) 50%, (c) 70% and (d) 80% filled, after two full revolutions. The reader is referred to the supplementary material for videos showing the full particle pattern evolution in the experiments and numerical simulations at each fill level. In comparison with the 70% filled drum, the homogeneous central core for the 80% filled drum is much larger due to the relatively elevated position of the free-surface avalanche, whereas for the 30% and 50% filled drums no core forms as all the granular material is eventually entrained through the avalanche. In each case there is a region of the drum itself which never intersects with the free-surface, but this region is always outside the body of granular material when the fill level is at 50% and below.

Structurally, a similar pattern emerges for the 70% and 80% filled drums, although interestingly the homogeneous central cores appear to have opposite orientations. In fact, the corners of the central core in both drums are formed when the free-surface avalanche is longest, and therefore fastest and thickest, and the corners in the 80% filled drum are simply more subtle because the core region bulges outwards between corners. This is evident in the experiment and particularly in the numerical simulation shown in figure 11d, which successfully captures the broad features observed experimentally. The undisturbed core is slightly larger in the simulation, suggesting the free-surface avalanche thickness is underestimated, but it accurately reproduces the shape which develops in the experiment. Unlike the 70% filled drum, the core does not approximate a Reuleaux triangle as the curvature of the sides is not approximately constant - instead, the core is better described as the intersection of three ovals. The small particle lobes are less pronounced than for the 70% filled drum in figure 11c, and do not exhibit the flattened tip observed at 70% filled in either simulation or experiment, instead producing a pointed tip. As shown in the supplementary videos, the simulation at 80% filled correctly captures the time-evolution of the small particle arms,

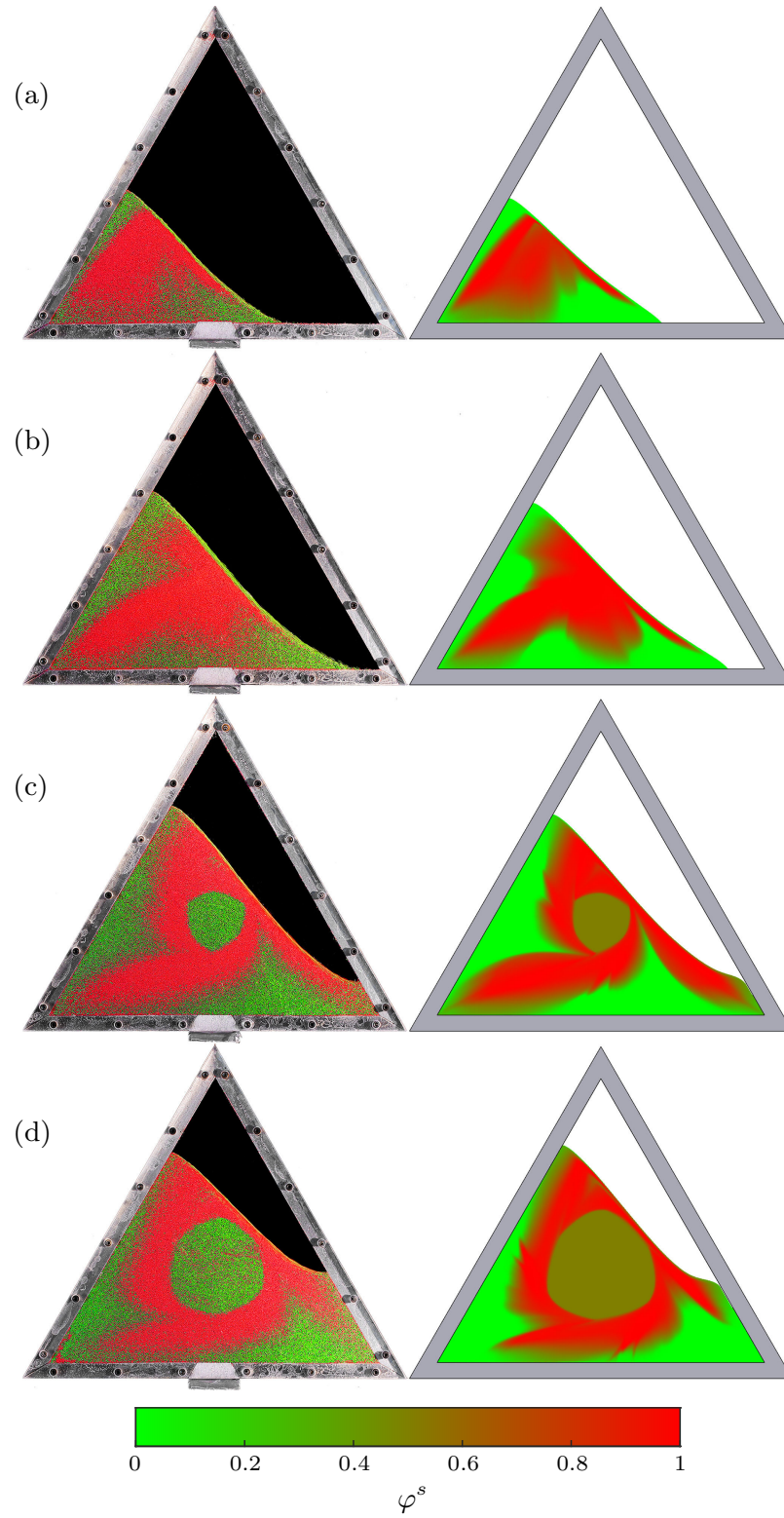


FIGURE 11. Comparison of triangular rotating drums at multiple fill fractions with  $\bar{\varphi}^s = 0.5$ , for experiments (left) and the small particle concentration in numerical simulations (right). The drums rotate over two full revolutions, with the final particle composition at  $t = 48$  s presented here. The drums are (a) 30% filled, (b) 50% filled, (c) 70% filled, and (d) 80% filled. Videos of the full pattern evolution in the experiments and simulations are available in the online supplementary material.

which form over the first drum revolution and become slightly shorter after subsequent re-entrainment in the second revolution. The S-shaped free-surface inclination angle is reproduced very accurately by the numerical simulation, with the curvature particularly pronounced around the downslope avalanche position.

The particle distributions in the 30% and 50% filled drums are qualitatively very different to those discussed so far. Both cases are apparently reduced to a single small particle lobe, with no central core, which is repeatedly entrained through the free-surface avalanche and re-orientated towards the second corner of the drum frame in the clockwise direction, or by  $-4\pi/3$ . Furthermore, the arms have a slight arc in the anti-clockwise direction, unlike the 70% and 80% filled drums for which the arms have a clockwise arc, which is also predicted by both numerical simulations. At both 30% and 50% filled, the numerical simulation accurately captures the structure of the particle distribution observed in the experiment, although the S-shape of the free-surface is weaker in the former simulation. At the 30% fill level, the small particle concentration is very strong on the outer, curved edge of the small particle arm and becomes relatively diffuse on the inner, right side. At the orientation presented in figure 11a, the arm is beginning to be re-entrained through the avalanche, and there is a crevice of large particles between the section of the arm which is either avalanching or has been deposited downslope, and the section yet to be re-entrained, similar to the subtle large particles regions enclosed above the core for fill fractions of 70% and 80%.

For the 50% filled drum, there are regions of high small particle concentration either side of the arm near the free-surface, which would eventually coalesce into a more obvious second arm if the fill level were increased. In fact, the particle distribution structure at 50% filled is a transitional stage between the structures observed at lower and higher fill fractions, and may be said to consist of two small particle arms. At orientations when the free-surface is approximately parallel to the lower drum wall, for example at  $t = 42$  s, plotted in figure 12, there are small particle regions orientated towards both the corners of the drum occupied by granular material. These regions may be interpreted as a single arm, partially deposited downslope and partially in the upslope position, re-orientated by  $-4\pi/3$  each time it passes through the avalanche. However, they should instead be identified as two genuinely distinct small particle arms re-orientated by  $-2\pi/3$



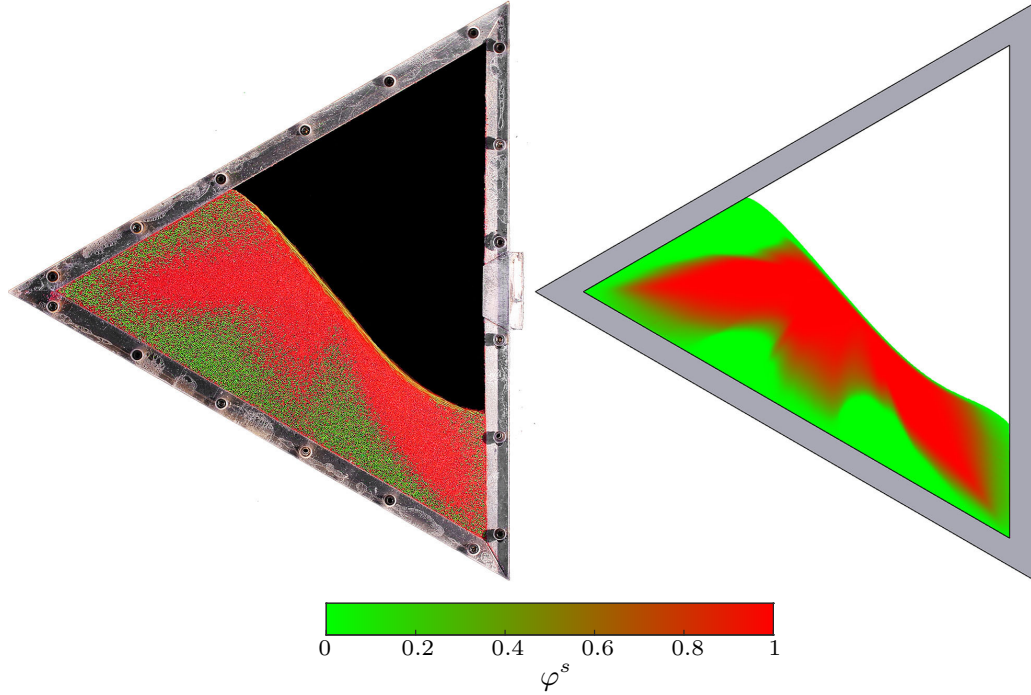


FIGURE 12. Particle distribution for the experiment (left) and the small particle concentration of the numerical simulation (right) of a 50% filled drum at  $t = 42$  s containing a mixture of large and small particles with  $\bar{\varphi}^s = 0.5$ . Two small particle arms are distinguishable when the free-surface is approximately parallel to the lower drum wall.

after each entrainment. In figure 11b, the second arm is undergoing entrainment through the avalanche, separated from the other by a more diffuse region.

A quantitative comparison between the segregation intensity (5.3) of the numerical simulations and the experiments is shown in figure 13. In each case, the timescale and intensity of segregation in the simulations matches very closely with the experimental data. For both experiments and simulations, the final segregation is weakest at 80% filled (where  $S(t = 48 \text{ s}) = 0.69$ , taken from the simulation data) and strongest at 50% filled ( $S(t = 48 \text{ s}) = 0.81$ ), while the 30% filled drum takes an intermediate value ( $S(t = 48 \text{ s}) = 0.73$ ). The segregation is weakest at 80% filled partly due the enlarged undisturbed central core, and may be highest at 50% filled due to the relatively small variation in the avalanche length, as can be seen in the supplementary videos. The intensity in the experiments is initially slightly stronger at 30% filled than 50% filled, before the latter case becomes significantly stronger in the second revolution of the drum, and this behaviour is also predicted in the simulations, where the curves intersect near  $t = 16$  s before diverging. While the 80% filled drum exhibits a relatively smooth increase with only small peaks and troughs of the segregation intensity, which very gradually plateaus, at 50%

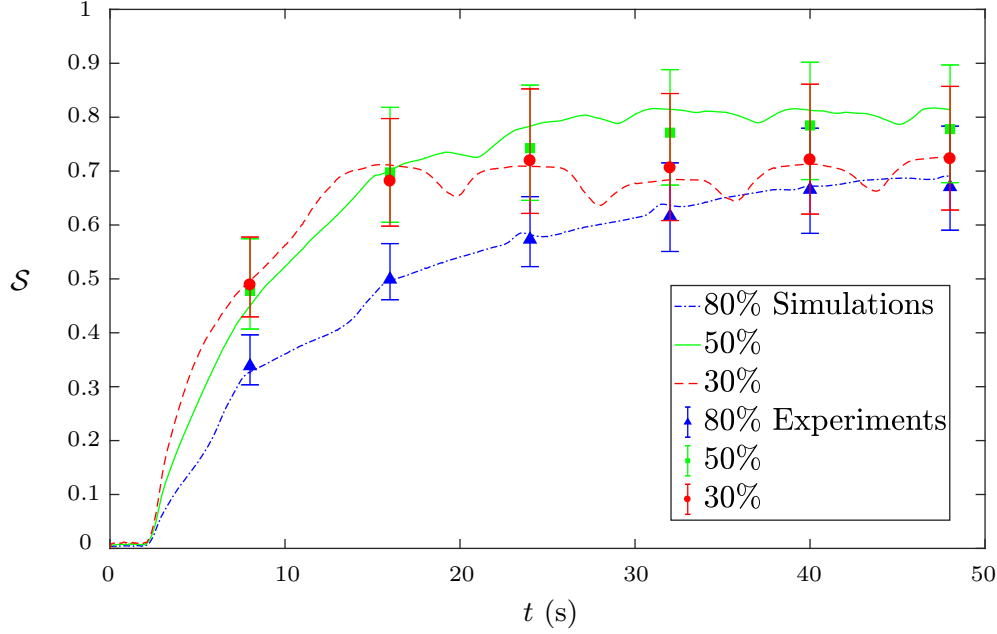


FIGURE 13. Comparison of the developing segregation intensity (5.3) over time, between experiments (symbols with error bars) and numerical simulations (curves), for 80%, 50%, and 30% filled drums. The mean small particle concentration  $\bar{\varphi}^s = 0.5$  in each case, and each simulation is performed with  $N^2 = 600^2$  grid points.

and particularly 30% filled the intensity fluctuates more erratically. At 30% filled each peak represents a brief plateau, which actually decrease in intensity before again increasing, and the estimated intensity of the experiments broadly confirms this phenomenon since the intensity is higher at  $t = 24$  s than  $t = 32$  s. The peak and trough shapes of the simulation curves are heavily dependent on the fill fraction, and they also become more pronounced at a 30% fill fraction because the rotation of the drum walls dramatically alters the geometry of the enclosed granular region.

## 8. Varying mean particle concentrations

Attention is now turned to the dependence of the particle-size distribution and bulk flow fields on the mixture composition. Initially two further cases are examined, both at fill levels of 70%, in addition to the original case of a bidisperse mixture with mean small particle concentration  $\bar{\varphi}^s = 0.5$ ; one with  $\bar{\varphi}^s = 0.3$ , and another with  $\bar{\varphi}^s = 0.7$ . The same technique described earlier of inducing segregation in the direction normal to the lateral sidewalls is used to produce an approximately homogeneous initial mixture, although in these two cases the

inversely graded layers of large and small particles are of differing thicknesses due to the uneven fill ratios.

Results from the experiments and numerical simulations are displayed for  $\bar{\varphi}^s = 0.3$  in figure 14a and  $\bar{\varphi}^s = 0.7$  in figure 14c, while the original  $\bar{\varphi}^s = 0.5$  case is shown in figure 14b. For videos of the developing particle concentration in the experiments and numerical simulations, see the supplementary material. Structurally the small particle arm patterns are similar, and develop over the same timescale for each of the three mean particle concentrations. The particle species separate out into somewhat diffuse regions over the first revolution, and then over the second revolution form a clear triskelion structure of small particle arms surrounding an undisturbed core. The different core colours in each of the numerical simulations represent the varying mean particle concentration. The small particle lobes, as one would expect, are larger when the small particle content is higher. Furthermore, the flattened top which is nearly parallel to the adjacent drum wall can be seen very clearly in figure 14c, while in figure 14a it is not obviously present at all. The small particle arms occupy a very wide region when  $\bar{\varphi}^s = 0.7$ , and then are much thinner for  $\bar{\varphi}^s = 0.3$ . Because of the thin particle arms in the latter case, the inner triangular region of high large particle concentration enclosed by the core and partially entrained arm can be seen more clearly than in the other drums, for both experiment and simulation. In both cases the numerical implementation of the coupling framework used here again produces simulations which not only accurately capture the final particle-size structures and free-surface inclination angles, but also the entire temporal evolution of these patterns.

As discussed above, the theoretical framework leads to greater segregation intensities in large particle-rich regions for the numerical simulations (due to the functional form of the segregation scaling law (2.26) and the longer particle trajectories towards the surface of the avalanche), and examining the projected concentration field of the experiment (see §5.4) indicated that this is a genuine physical phenomenon. Varying the mean particle concentration provides another perspective from which to consider this phenomenon. Figure 15a plots the segregation intensities at  $t = 48$  s for the experiments and simulations with  $\bar{\varphi}^s = 0.3, 0.5$  and  $0.7$ , as well as for two further extreme cases with

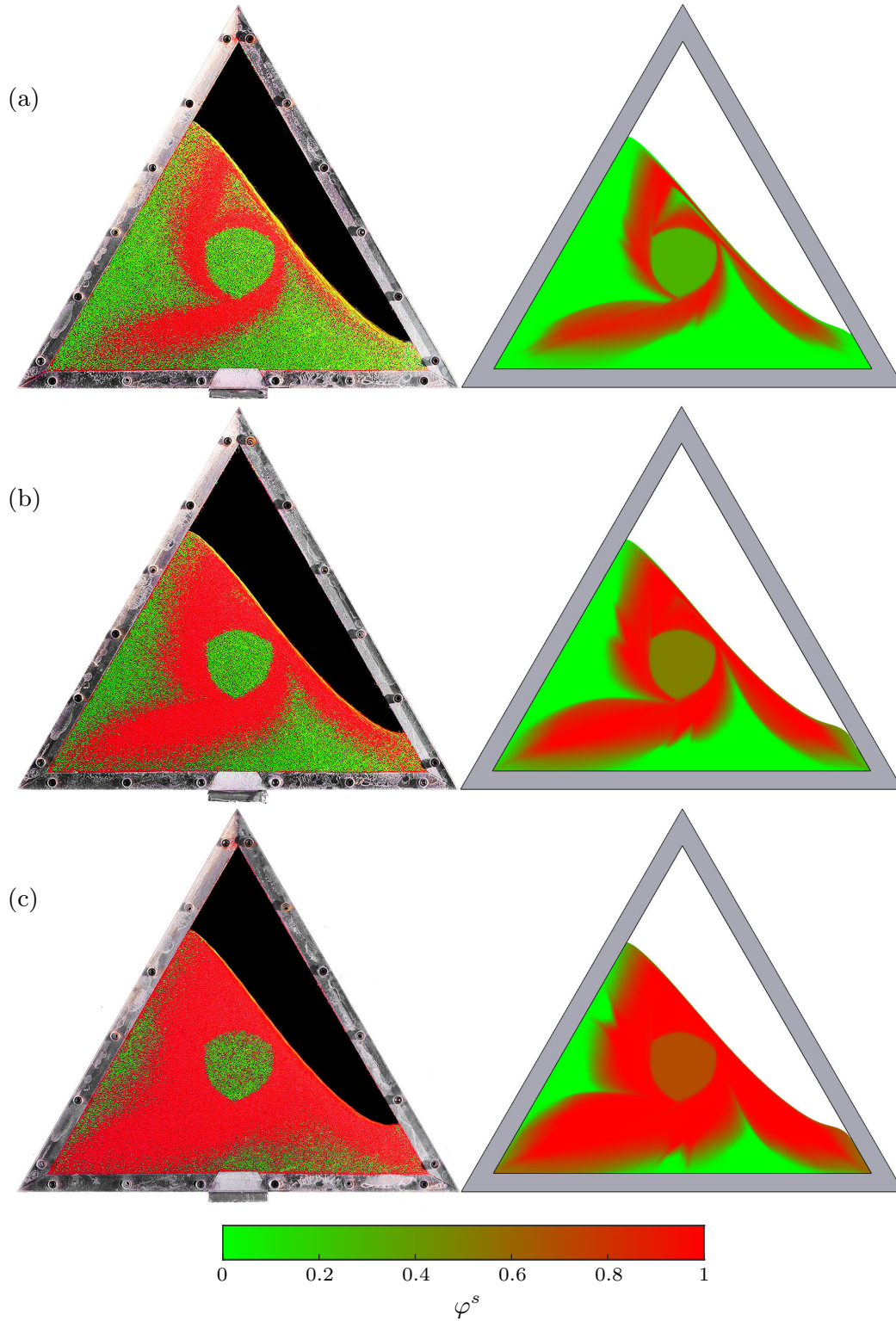


FIGURE 14. Comparison of 70% filled triangular rotating drums for experiments (left) and the small particle concentration in numerical simulations (right). The drums have mean small particle concentrations of (a)  $\bar{\varphi}^s = 0.3$ , (b)  $\bar{\varphi}^s = 0.5$ , and (c)  $\bar{\varphi}^s = 0.7$ . They rotate for two revolutions, with the final particle compositions at  $t = 48$  s presented here. Videos of the full pattern evolution in the experiments and simulations are available in the online supplementary material.

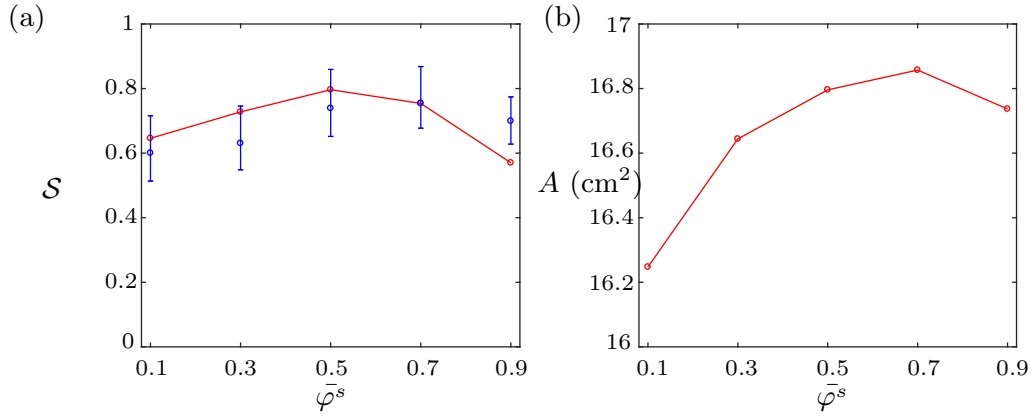


FIGURE 15. Variation of (a) the segregation intensity  $S$ , and (b) the total area of the homogeneous central core  $A$  with the mean small particle concentration, for 70% filled rotating drums with  $\bar{\varphi}^s = 0.1, 0.3, 0.5, 0.7$  and  $0.9$ , at  $t = 48$  s. The segregation intensity is plotted for the numerical simulations (solid red circles and lines) and experiments (blue circles). The mixture with  $\bar{\varphi}^s = 0.5$  segregates most strongly. The area of the homogeneous central core is plotted for the numerical simulations, and is generally smaller for flows with a higher mean concentration of large particles due to their lesser mobility, as implied by the experimental observations of Hill *et al.* (1999).

$\bar{\varphi}^s = 0.1$  and  $\bar{\varphi}^s = 0.9$ . As the mean small particle concentration increases, it may reasonably be expected that the reduced large particle content induces weaker segregation, but the observed behaviour is significantly more complex than this prediction. The segregation intensity initially increases with the mean small particle concentration, up to a maximal value at  $\bar{\varphi}^s = 0.5$ , before a severe decrease for  $\bar{\varphi}^s = 0.9$ . The segregation intensities derived from the simulation data also match closely with the experiments, confirming this general trend. The agreement between the simulations and experiments when  $\bar{\varphi}^s = 0.1$  and  $0.3$  suggests that the value  $\phi_c^s = 0.2$ , which determines the point below which the segregation velocity magnitude transitions to a quadratic dependence on the grain-size ratio, is accurate. The intensity is weaker for  $\bar{\varphi}^s = 0.9$  than  $\bar{\varphi}^s = 0.1$ , as predicted based on the respective large particle concentrations, but conversely is stronger for  $\bar{\varphi}^s = 0.7$  than  $\bar{\varphi}^s = 0.3$ . To discern the reasons for these seemingly counter-intuitive results, we must look beyond the functional dependence of the segregation scaling law and consider the more intricate nature of segregation-mobility feedback interactions.

According to the literature, the changing particle compositions through the free-surface avalanche should produce a feedback effect onto the bulk flow (Gray & Kokelaar 2010; van der Vaart *et al.* 2018a; Barker *et al.* 2021). Hill *et al.* (1999) performed experiments for different rotating drum geometries and observed that the avalanching layer was slower and deeper for flows with larger particles, which is

due to the lesser mobility of larger grains when other frictional properties remain unchanged. This effect can be captured by the framework used here since the effective friction  $\mu(I)$  (2.7) is monotonically increasing in the inertial number  $I$  (2.16) which depends linearly on the average particle size  $\bar{d}$  (2.15). This means that larger particles are more frictional than smaller particles, leading to a slightly slower-moving and deeper avalanche for an increased large particle presence (necessarily deeper so that the same mass of material can be advected through the slower avalanche). However, the variation away from the fields depicted in figure 5 is very slight and so a visualisation of the full bulk flow fields is omitted for the other mean particle concentrations.

Instead, because a deeper avalanche will result in a smaller homogeneous central core, comparing the core sizes of the numerical simulations provides another method of studying the feedback between the particle-size distribution and the bulk flow. Since the particle distribution in the core is approximately unchanged from the initial conditions, the small particle concentration in the core should be  $\varphi^s = \bar{\varphi}^s$ . The core region can then be identified as the region surrounding the origin with concentration lying within the range  $\varphi^s \in [\bar{\varphi}^s, \bar{\varphi}^s + \varepsilon)$ , where the one-sided limit reflects the fact that the core is surrounded by predominantly small particles, using

$$\varepsilon = \frac{\bar{\varphi}^s(1 - \bar{\varphi}^s)}{20}. \quad (8.1)$$

This is chosen to ensure that the core is accurately located for different mean particle concentrations, and to allow for a very small amount of segregation since quasi-static material is modelled by the high Newtonian viscosity cut-off (3.9). Once the core is located, its total area  $A$  can be calculated, and is plotted for the different mean particle concentrations in figure 15b. The core becomes larger for higher concentrations of small particles, successfully reproducing the experimental observations of Hill *et al.* (1999) and confirming predictions based on the functional dependence of the inertial number (2.16), until the core size decreases when  $\bar{\varphi}^s = 0.9$ . This latter result is likely related to the method by which the core is located, but the core is clearly larger when  $\bar{\varphi}^s = 0.9$  than when  $\bar{\varphi}^s = 0.1$ , which have equal values of  $\varepsilon$ . Nevertheless, the variation in core size is very slight (under 5%), and so a quantitative comparison to the

core size in the experiments is not undertaken due to the innate imprecision of, and sensitivity to, the initial conditions. This explains why the segregation intensity initially increases with  $\bar{\varphi}^s$ , as demonstrated in figure 15a. The increased concentration of small particles means that the free-surface avalanche is thinner and faster, which induces stronger segregation since the strain-rate is higher. This can clearly be seen via comparison with the rotating drum simulations of Barker *et al.* (2021), where despite very large grain diameters the segregation intensities are far weaker than in the simulations presented here, due to the very thick avalanching layer. The subsequent decrease in segregation intensity after  $\bar{\varphi}^s = 0.5$  is due to the interplay of competing effects related to the particle-size composition. The avalanche becomes increasingly thin up to  $\bar{\varphi}^s = 0.7$ , but since the rate of increase slows and the reduced large particle content simultaneously hinders segregation, the segregation intensity falls slightly between  $\bar{\varphi}^s = 0.5$  and  $\bar{\varphi}^s = 0.7$ . At  $\bar{\varphi}^s = 0.9$  the avalanche apparently becomes thicker, producing a more drastic fall in segregation intensity. The balance between avalanche thickness and particle composition in the 50:50 small and large particle mixture produces the strongest segregation. The magnitude of the relative velocity field at each mean particle concentration, plotted in figure 16, shows how higher large particle concentrations lead to slightly slower avalanches. Larger particles produce a slightly steeper free-surface inclination due to their reduced mobility, and so the free-surface position is not constant across different mean particle concentrations. Subsequently, the relative avalanche depths cannot be inferred directly from the velocity profile, justifying the use of the core size for this purpose. Nevertheless, it is notable that the velocity profiles are very similar for  $\bar{\varphi}^s = 0.7$  and  $\bar{\varphi}^s = 0.9$ , suggesting that the avalanche depth has altered very little.

The sensitivity of the core size to the initial particle-size composition in the numerical simulations is an example of two-way coupled feedback (Barker *et al.* 2021). First, because larger particles are less mobile, their increased presence results in a thicker, slower free-surface avalanche. This is feedback of the particle-size distribution onto the bulk flow, modelled through the inertial number definition (2.16). Once the thicker avalanche has formed, segregation is induced deeper into the flow, meaning that the undisturbed granular region is smaller. This is feedback of the bulk flow dynamics on the evolving particle mixture, and occurs

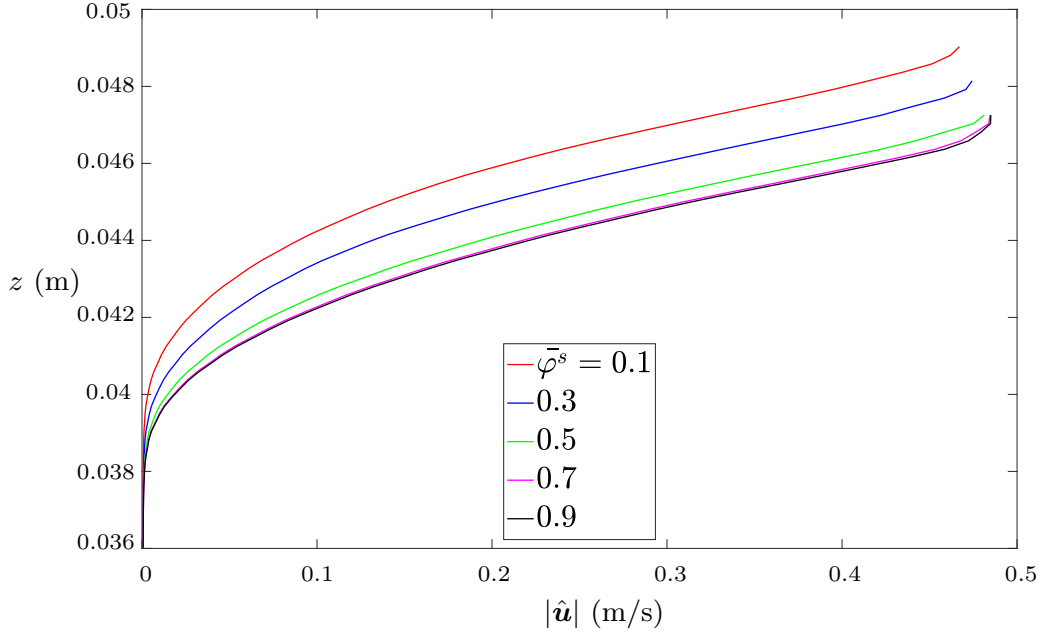


FIGURE 16. Magnitude of the relative velocity field (5.2) for 70% filled rotating drums with different mean particle concentrations. The velocity profiles are plotted up to the free-surface position, which is identified by examining the concentration of air,  $\varphi^a$ .

because of the segregation scaling law (2.24), which confines segregation to regions of high strain-rate. Simultaneously, higher values of the concentration weighted grain diameter  $\bar{d}$  (2.15) when the large particle content is higher induce stronger segregation since the segregation rate is an increasing function of  $\bar{d}$ . Within a continuum framework, the subtle interplay between distinct but related feedback effects demonstrated here can only be captured using a fully coupled model.

## 9. Tri-disperse triangular rotating drum

As discussed in §2, the theoretical framework throughout this paper is generalised for an arbitrary number of components, and this will now be demonstrated using a tri-disperse mixture, i.e. one with three distinct granular phases. The numerical method in OpenFOAM (see §3) is implemented for an arbitrary multi-component mixture and hence requires only the specification of an additional granular phase. Rather than describing the full set of equations, which are analogous to the system of equations (3.4)-(3.7), for brevity only the segregation and diffusive fluxes only will be specified. For small, medium and large granular phases



and an air phase, denoted by  $s$ ,  $m$ ,  $l$  and  $a$  respectively, the segregation fluxes are

$$\mathbf{F}^l = \left( -f_{ls}\varphi^l\varphi^s - f_{lm}\varphi^l\varphi^m + f_{ag}\varphi^l\varphi^a \right) \frac{\mathbf{g}}{|\mathbf{g}|}, \quad (9.1)$$

$$\mathbf{F}^m = \left( -f_{ms}\varphi^m\varphi^s + f_{ml}\varphi^m\varphi^l + f_{ag}\varphi^m\varphi^a \right) \frac{\mathbf{g}}{|\mathbf{g}|}, \quad (9.2)$$

$$\mathbf{F}^s = \left( f_{sm}\varphi^s\varphi^m + f_{sl}\varphi^s\varphi^l + f_{ag}\varphi^s\varphi^a \right) \frac{\mathbf{g}}{|\mathbf{g}|}, \quad (9.3)$$

$$\mathbf{F}^a = -f_{ag}\varphi^a\varphi^g \frac{\mathbf{g}}{|\mathbf{g}|}, \quad (9.4)$$

and the diffusive fluxes are

$$\mathcal{D}^l = \mathcal{D}_{ls} (\varphi^s \nabla \varphi^l - \varphi^l \nabla \varphi^s) + \mathcal{D}_{lm} (\varphi^m \nabla \varphi^l - \varphi^l \nabla \varphi^m), \quad (9.5)$$

$$\mathcal{D}^m = \mathcal{D}_{ms} (\varphi^s \nabla \varphi^m - \varphi^m \nabla \varphi^s) + \mathcal{D}_{ml} (\varphi^l \nabla \varphi^m - \varphi^m \nabla \varphi^l), \quad (9.6)$$

$$\mathcal{D}^s = \mathcal{D}_{sm} (\varphi^m \nabla \varphi^s - \varphi^s \nabla \varphi^m) + \mathcal{D}_{sl} (\varphi^l \nabla \varphi^s - \varphi^s \nabla \varphi^l), \quad (9.7)$$

$$\mathcal{D}^a = 0, \quad (9.8)$$

where the overall concentration of grains is now

$$\varphi^g = \varphi^s + \varphi^m + \varphi^l = 1 - \varphi^a. \quad (9.9)$$

In the experiment, the green large particle species is identical to the large particle species used in §5, the medium particles are white, and the small particles species are again red, but much smaller than the small particles used in §5. The grain diameter for each phase in the numerical simulation is specified in table 3. The segregation and diffusion is again modelled using the parameters in table 1, and all other rheological parameters are carried over from table 2. The grains used for the experiment, again sourced from Sigmund Lindner GmbH, are sieved to diameters in the ranges  $d^s = 120 - 180 \mu\text{m}$ ,  $d^m = 400 - 500 \mu\text{m}$ , and  $d^l = 600 - 800 \mu\text{m}$ . The drum is 70% filled with granular material in a 30:40:30 ratio of small:medium:large particles, and the rotation rate is reduced to  $\Omega = -\pi/48 \text{ rad/s}$  as the grains coalesce into clearly distinguishable regions at this speed, but the medium grains do not when  $\Omega = -\pi/12 \text{ rad/s}$ , for reasons discussed below. The final segregation intensity tends to decrease as the rotation rate increases, because faster rotation creates thicker free-surface avalanches where the strain-rates are weaker (He *et al.* 2019).

The simulation runs for two full revolutions, and the results from the experiment

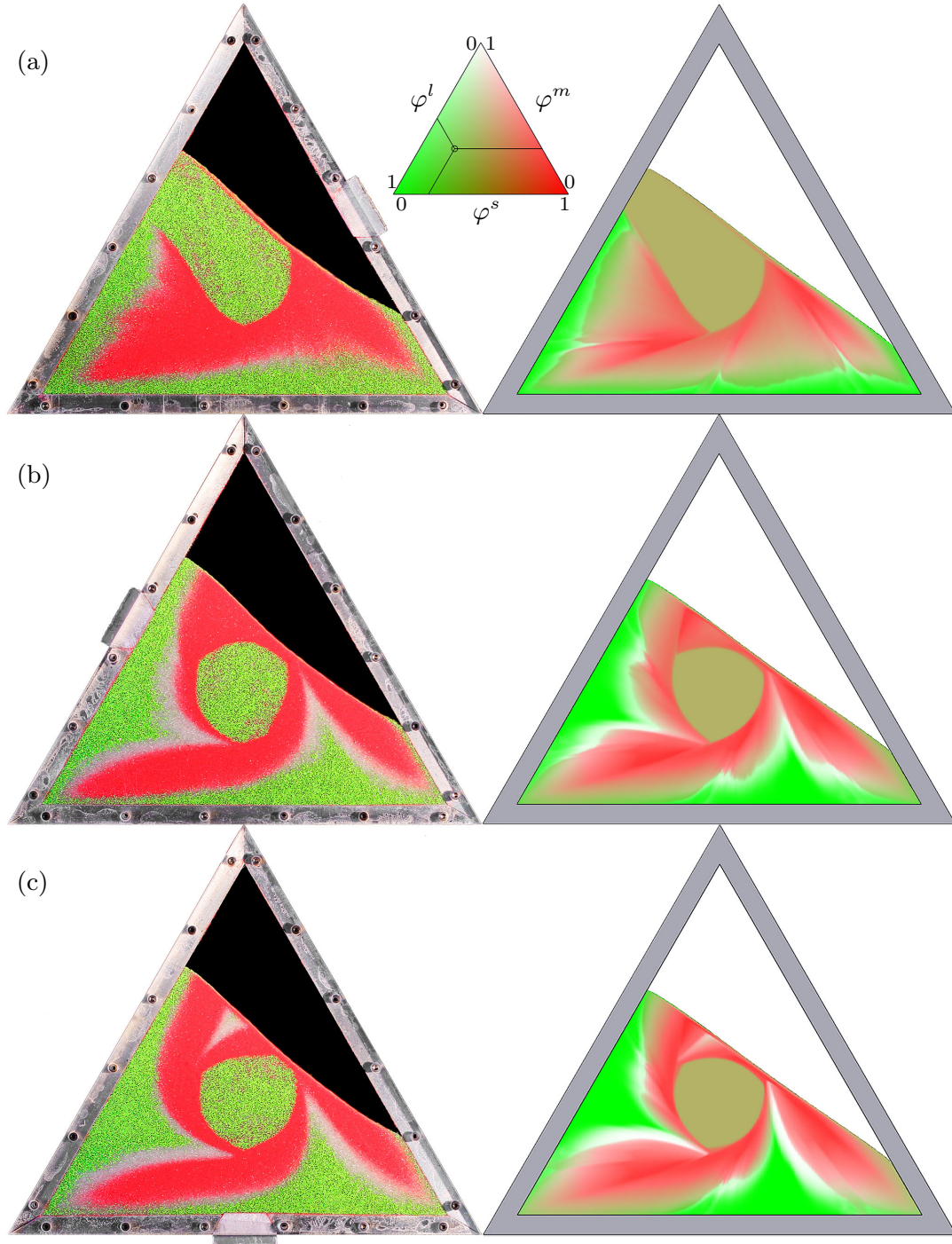


FIGURE 17. Comparison of the particle distribution in a 70% filled triangular rotating drum containing a tri-disperse mixture with a small:medium:large particle ratio of 30:40:30, for an experiment (left) and numerical simulation (right), at (a)  $t = 64$  s, (b)  $t = 128$  s, and (c)  $t = 192$  s. Each 64 s increment represents two thirds of a revolution. The numerical particle concentrations are represented by a three-way contour scale, where the phases go from  $\varphi^v = 0$  to 1 along their respective sides, and as a demonstrative example the concentration at the plotted point is determined by projecting along the lines towards each side, giving  $\varphi^s = 0.2$ ,  $\varphi^m = 0.3$  and  $\varphi^l = 0.5$ . The drums rotate over two full revolutions at a rotation rate of  $\Omega = -\pi/48$  rad/s. Videos of the full pattern evolution in the experiment and simulation are available in the online supplementary material.

---


$$d^s = 0.15 \times 10^{-3} \text{ m}, \quad d^m = 0.45 \times 10^{-3} \text{ m}, \quad d^l = 0.7 \times 10^{-3} \text{ m}.$$

TABLE 3. Grain diameters for the small, medium and large particle species used in the numerical simulations in §9.

---

and numerical simulation are presented in figure 17, with videos showing the full particle pattern evolution in the experiment and numerical simulation available in the online supplementary material. Initially, no region of predominantly medium sized particles is clearly discernible, although small and large particle regions begin to coalesce quickly. This is because the medium sized particles are in effect being simultaneously segregated in opposite directions by the other two species, due to their intermediate grain size. When interacting with large particles, medium particles segregate in the direction of gravity, but when interacting with small particles they segregate in the opposite direction to gravity. In practice they are regularly encountering grains of both other sizes, and so are subject to some reversal of the segregation direction. This is particularly true of the simulation since each point on the numerical grid has calculated concentration values which never reach perfectly pure phases (i.e. when  $\varphi^\nu = 1$  for some species) and so the medium mixture is genuinely being segregated in both directions simultaneously, and the net direction of segregation is determined by the respective grain-size ratios and concentrations. As a result, the medium particle regions, once formed, are smaller in the simulations than in the experiments. This effect is exacerbated by the different grain-size ratios, since  $R_{sl} = d^l/d^s = 4.\bar{6}$ , whereas  $R_{sm} = d^m/d^s = 3$  and  $R_{ml} = d^l/d^m = 1.\bar{5}$ , meaning that the small and large particles segregate more strongly relative to each other than to the medium sized particles, with which they remain in more diffuse mixtures. In the second revolution, regions of predominantly medium particles form, and the numerical simulations correctly predict that they are strongest adjacent to the inner length of the small particle arms, with weaker medium regions down the outer length. Overall, the simulations provide a good qualitative match to the experiments, but the small and medium particle arms are larger and less pointed than those in the experiments.

The slower rotation rate than the drums studied in §5 leads to a thinner avalanche and hence a larger undisturbed central core due to feedback of the

bulk flow onto the segregation, which is well approximated by the numerical simulation. The free-surface inclination is also accurately predicted by the simulation, although the small triangular region of predominantly medium particles above the central core, visible at  $t = 192$  s, is slightly weaker in the simulation. There is a reduction by a factor of four in the rotation rate relative to the drums studied in §5, and subsequently the free-surface inclination in the experiments and simulations is lower. This is expected since evidence from experiments and DEM simulations suggests that the inclination increases approximately linearly with the rotation rate (Yamane *et al.* 1998). The S-shaped free-surface present in the more rapidly rotating drums is also less pronounced in the experiment and simulation here.

## 10. Conclusions and discussion

In this paper, continuum simulations computed using the coupling framework developed by Barker *et al.* (2021) are used alongside experiments to investigate the flow of polydisperse granular material in triangular rotating drums. The mixing of distinct particle species which differ in grain size is captured by using the segregation scaling law derived by Trewthella *et al.* (2021), with a reduction factor (2.24) included so that the segregation Péclet number  $Pe = f_{sl}/D_{sl}$  is maximal near grain-size ratios close to 2, in line with observations from rotating drum DEM simulations (He *et al.* 2019; Zhang *et al.* 2017), as well as experimental and DEM data obtained from other geometries (Golick & Daniels 2009; Thornton *et al.* 2012). For the diffusion, the well-established result (see e.g. Utter & Behringer 2004) that the diffusion rate scales with the shear rate and the grain diameter squared is used. The bulk flow is modelled using the partially regularised incompressible  $\mu(I)$ -rheology (Barker & Gray 2017) which guarantees well-posed Navier-Stokes type equations below an extreme value of  $I$ , using a granular viscosity (2.3) dependent on the local concentration weighted grain-diameter, and hence on the evolving particle-size distribution. The rotating drum experiments conducted here as elsewhere (see e.g. Hill *et al.* 1999) rely on clear lateral sidewalls confining a thin channel of granular material, which exert a frictional force on the flow. This effect is incorporated into the bulk flow model by assuming a Coulomb slip on the sidewalls and then integrating the three-dimensional mass and momentum balance

equations through the channel width so that sidewall friction is represented by a single term in a two-dimensional momentum balance equation (2.29).

The numerical method developed in OpenFOAM by Barker *et al.* (2021) for solving fully coupled, polydisperse granular flow simulations is adapted here to include lateral sidewall friction. This implementation is tested in §4 using a two-dimensional infinite shear-cell with confining sidewalls. An exact steady-state solution is derived from the original  $\mu(I)$ -rheology (Jop *et al.* 2005), and the numerical solution gives an extremely close match to both the velocity profile and the precise depth of the flowing layer, shown in figure 2. It is important that the flowing layer depth is accurately predicted by the theoretical framework because one of the crucial effects of sidewall friction is that avalanches become thinner and faster (Jop *et al.* 2005).

The numerical method is then used to produce bidisperse triangular rotating drum simulations, which exhibit very thin free-surface avalanches within which the particle-size segregation is very strong (see figure 5). For a 70% filled drum containing a mixture with mean small particle concentration  $\bar{\varphi}^s = 0.5$ , the evolving particle-size distribution results in a triskelion pattern of small particle arms surrounding an undisturbed central core of granular material which is never entrained into the avalanche. The rotational symmetry of the small particle arms is assessed and presented in figure 7, and the symmetry is close to perfect when the arms have each been entrained through the avalanche an equal number of times. Laboratory experiments are performed, and an excellent qualitative match is found between experiment (figure 4) and computation (figure 6). All the parameters used for the simulations are obtained from empirical measurements of the parameters used for the drum experiments, or from independent studies, with no fitting parameters. A method of extracting quantitative data from the experiments is then devised, so that small particle concentration fields can be projected onto the laboratory images. This is used to measure the segregation intensity (5.3) of the experiments over time, and the timescale and magnitude match well with the simulation data, shown in figure 9. Grid convergence of the numerical solution is also demonstrated, although it should be noted that a very fine mesh is required to resolve the thin boundary layer avalanche where all the segregation occurs. This boundary layer must be resolved to correctly predict

the overall pattern formation and hence produce the converged solution. For this reason the simulations performed here incur considerable computational expense. A simulation with otherwise identical parameters but excluding sidewall friction effects is computed, producing a thick, slow moving avalanche which induces very little segregation. This shows that lateral sidewall friction is one of the dominant physical mechanisms on which particle redistribution in narrow rotating drums depends.

Triangular rotating drums at different fill levels are then examined, for 30%, 50%, 70% and 80% filled drums, and in each case the agreement between simulations and experiments is strong (see figure 11). The segregation intensity is again computed and demonstrates a close match between simulations and experiments, and the simulations reveal that peaks and troughs in the intensity are more pronounced at lower fill levels (see figure 13). Drums with fill fractions of 70% and mean small particle concentrations of  $\bar{\varphi}^s = 0.3$  and  $\bar{\varphi}^s = 0.7$  are considered against the original case with  $\bar{\varphi}^s = 0.5$ , shown in figure 14. The numerical simulations reveal a complex rheology-segregation coupling in which increasing the mean small particle concentration simultaneously inhibits and enhances the segregation rate via distinct physical mechanisms, by altering both the mixture composition and the bulk flow dynamics. While the segregation rate is higher for larger particles (2.26), Hill *et al.* (1999) observed that feedback from less mobile larger particles results in a thicker free-surface avalanche, and this phenomenon is reproduced by the numerical simulations, measured by assessing the size of the undisturbed central core (see figure 15). This is only possible because the coupling framework models mobility feedback onto the bulk flow from the evolving particle distribution. There is then feedback in the opposite direction, from the bulk flow onto the particle mixing process, as the segregation is weaker in the thicker avalanche, while the mixture segregates deeper into the flow and hence produces a smaller central core. A similar phenomenon can be expected in other industrially relevant polydisperse flows such as filling and emptying of storage silos, and this paper provides promising indications that they could be tackled using the fully coupled theory.

Finally, a 70% filled triangular drum containing a tridisperse mixture is considered. The presence of medium sized grains in the mixture reveals a different

type of particle interaction to those occurring within a bidisperse mixture, since they are simultaneously segregated in opposite directions by the small and large particles. This leads to a weakened net segregation rate for medium sized particles, observed in the experiments and predicted by the numerical simulations. This is likely to occur in other polydisperse granular flows, including geophysical flows where the wide distribution of particle sizes may inhibit segregation of those with intermediate sizes. Consequently, a slower rotation rate is chosen for the drum to induce a stronger final segregation intensity. A slower rotation rate leads to a reduction in the free-surface inclination angle, predicted by the numerical simulation and confirmed experimentally. More consideration is nevertheless needed to understand the relationship between free-surface inclination and rotation rate, which is expected to be linear (Yamane *et al.* 1998), but that is beyond the scope of this paper.

The results presented here demonstrate the power of the coupling method developed by Barker *et al.* (2021) and represent a strong validation of the partially regularised  $\mu(I)$ -rheology and the segregation scaling law of Trewella *et al.* (2021). The original incompressible  $\mu(I)$ -rheology was derived from observations of steady-state DEM simulations and experiments, including a circular rotating drum (GDR MiDi 2004), combined with a basal friction law (Pouliquen & Forterre 2002; Jop *et al.* 2005), and although it has been successfully applied to more complex geometries (Lacaze & Kerswell 2009; Staron *et al.* 2014) it is perhaps surprising that the partially regularised modification (Barker & Gray 2017) is able to predict the bulk flow dynamics in a highly transient triangular rotating drum with such accuracy. Both the avalanche depth and the free-surface shape and inclination in the experiments are reproduced very closely by this rheology. Furthermore, although the segregation scaling law of Trewella *et al.* (2021) was determined using data from refractive-index matched oscillatory shear box experiments with a single small or large particle intruder, the results presented here are only the latest successful application of this law to more complex geometries with less extreme particle concentrations (Trewella *et al.* 2021; Barker *et al.* 2021). These results therefore suggest that the fully coupled theory used here provides a sufficient approximation of the real physics for accurate modelling of polydisperse rotating drums in the continuously avalanching or rolling regime (Rajchenbach

1990) in general, representing a major breakthrough for continuum modelling of rotating drums. This could prove extremely useful in industrial settings where, for example, mixers fitted with segregation-inhibiting baffles (McCarthy 2009) could be tested numerically using continuum simulations before prototypes are produced.

Future work on rotating drums could use DEM simulations as a validation case for the continuum theory used here. This paper considers variations in the drum fill fraction, mean particle concentration and, to a minor extent, the rotation rate only, and further study is therefore required to examine the full parameter space over which this theory may be successfully applied. Such studies may take into account a wider range of drum rotation rates, cases where particle species have differing frictional properties (in addition to differing sizes), and a wider variety of drum geometries including baffled drums. Furthermore, attempts at continuum modelling of other flow regimes such as the intermittent avalanching or slumping regime (Rajchenbach 1990), which produces the Catherine wheel patterns observed by Gray & Hutter (1997), have so far been limited (Arseni *et al.* 2020). It is likely that some combination of frictional hysteresis (Edwards *et al.* 2019), compressibility (Schaeffer *et al.* 2019) and non-locality (Pouliquen & Forterre 2009; Kamrin 2019) is required to model intermittent avalanches within a continuum framework.

## Acknowledgements

This research was supported by NERC grants NE/E003206/1 and NE/K003011/1 as well as EPSRC grants EP/I019189/1, EP/K00428X/1 and EP/M022447/1. During the majority of the research J.M.N.T.G. was a Royal Society Wolfson Research Merit Award holder (WM150058) and an EPSRC Established Career Fellow (EP/M022447/1).

## Declaration of Interests

The authors report no conflict of interest.



## Supplementary material

Supplementary videos are available at <https://doi.org/10.17632/b36kh3w7xf.1>.

## Appendix A. Derivation of the width-averaged equations for flow in a confined channel

Consider a velocity field  $\mathbf{u} = (u, 0, w)$  in the co-ordinate system  $(x, y, z)$  confined within a narrow channel by sidewalls at  $y = 0$  and  $y = W$ . In full component form, the three-dimensional mass and momentum balance equations are

$$\frac{\partial u}{\partial x} + \frac{\partial w}{\partial z} = 0, \quad (\text{A } 1)$$

$$\rho \left( \frac{\partial u}{\partial t} + u \frac{\partial u}{\partial x} + w \frac{\partial u}{\partial z} \right) = -\frac{\partial p}{\partial x} + \frac{\partial \tau_{xx}}{\partial x} + \frac{\partial \tau_{xy}}{\partial y} + \frac{\partial \tau_{xz}}{\partial z}, \quad (\text{A } 2)$$

$$0 = -\frac{\partial p}{\partial y} + \frac{\partial \tau_{yx}}{\partial x} + \frac{\partial \tau_{yz}}{\partial z}, \quad (\text{A } 3)$$

$$\rho \left( \frac{\partial w}{\partial t} + u \frac{\partial w}{\partial x} + w \frac{\partial w}{\partial z} \right) = -\frac{\partial p}{\partial z} + \frac{\partial \tau_{zx}}{\partial x} + \frac{\partial \tau_{zy}}{\partial y} + \frac{\partial \tau_{zz}}{\partial z} - \rho g. \quad (\text{A } 4)$$

Assuming Coulomb friction on the sidewalls acting against the direction of flow, the stress on the boundary can be expressed as

$$(\tau_{xy}, 0, \tau_{zy}) = \mu_W p \frac{(u, 0, w)}{|\mathbf{u}|} \quad \text{at } y = 0, \quad (\text{A } 5)$$

$$(\tau_{xy}, 0, \tau_{zy}) = -\mu_W p \frac{(u, 0, w)}{|\mathbf{u}|} \quad \text{at } y = W, \quad (\text{A } 6)$$

where  $\mu_W$  is the constant wall friction coefficient. Consider some arbitrary variable  $f$ . Width-averaged variables are defined as

$$\bar{f} = \frac{1}{W} \int_0^W f dy, \quad (\text{A } 7)$$

for any  $f$ . If  $\partial f / \partial y = 0$ , then trivially  $\overline{fg} = \bar{f}\bar{g}$  for any second variable  $g$ . Jop *et al.* (2005) showed that confined flows approach uniformity in the  $y$ -direction as the channel becomes narrower, while Taberlet *et al.*'s (2003) investigations into confined heap flow suggest that flows of a few grain diameters in width are sufficiently narrow to be well approximated by the assumption of uniformity in the  $y$ -direction. For the rotating drum experiments in this paper, the channel width is  $W = 3$  mm, while the bidisperse granular mixtures contain particles of size  $d^s = 0.35$  mm and  $d^l = 0.7$  mm. Bidisperse flows can therefore be expected to occupy

between 4 and 8 grain diameters in width, and so uniform flow in the  $y$ -direction is assumed. The integrated mass and momentum balance equations are then, after utilising the Leibniz integral rule to exchange the order of differentiation and integration and applying the boundary conditions (A 5) and (A 6),

$$\frac{\partial \bar{u}}{\partial x} + \frac{\partial \bar{w}}{\partial z} = 0, \quad (\text{A } 8)$$

$$\rho \left( \frac{\partial \bar{u}}{\partial t} + \bar{u} \frac{\partial \bar{u}}{\partial x} + \bar{w} \frac{\partial \bar{u}}{\partial z} \right) = -\frac{\partial \bar{p}}{\partial x} + \frac{\partial \bar{\tau}_{xx}}{\partial x} - 2\mu_W p \frac{u}{|\mathbf{u}|} + \frac{\partial \bar{\tau}_{xz}}{\partial z}, \quad (\text{A } 9)$$

$$\rho \left( \frac{\partial \bar{w}}{\partial t} + \bar{u} \frac{\partial \bar{w}}{\partial x} + \bar{w} \frac{\partial \bar{w}}{\partial z} \right) = -\frac{\partial \bar{p}}{\partial z} + \frac{\partial \bar{\tau}_{zx}}{\partial x} - 2\mu_W p \frac{w}{|\mathbf{u}|} + \frac{\partial \bar{\tau}_{zz}}{\partial z} - \rho g. \quad (\text{A } 10)$$

Finally, the assumption  $\partial \mathbf{u} / \partial y = 0$  implies that  $\mathbf{u} / |\mathbf{u}| = \bar{\mathbf{u}} / |\bar{\mathbf{u}}|$  and  $\bar{\boldsymbol{\tau}} = 2\bar{\eta} \bar{\mathbf{D}}$ . After dropping the  $\bar{f}$  notation, the full width-averaged mass and momentum balances can thus be expressed in two-dimensional vector form as

$$\nabla \cdot \mathbf{u} = 0, \quad (\text{A } 11)$$

$$\rho \left( \frac{\partial \mathbf{u}}{\partial t} + \mathbf{u} \cdot \nabla \mathbf{u} \right) = -\nabla p + \nabla \cdot \boldsymbol{\tau} + \rho \mathbf{g} - 2\mu_W p \frac{\mathbf{u}}{|\mathbf{u}|}. \quad (\text{A } 12)$$

## REFERENCES

- ARSENI, A., MONACO, G. D., GRECO, F. & MAFFETTONE, P. 2020 Granular flow in rotating drums through simulations adopting a continuum constitutive equation. *Phys. Fluids* **32** (9), 093305.
- ARTONI, R., LARCHER, M., JENKINS, J. T. & RICHARD, P. 2021 Self-diffusion scalings in dense granular flows. *Soft Matter* **17** (9), 2596–2602.
- BAKER, J. L., BARKER, T. & GRAY, J. M. N. T. 2016*a* A two-dimensional depth-averaged  $\mu(I)$ -rheology for dense granular avalanches. *J. Fluid Mech.* **787**, 367–395.
- BAKER, J. L., JOHNSON, C. G. & GRAY, J. M. N. T. 2016*b* Segregation-induced finger formation in granular free-surface flows. *J. Fluid Mech.* **809**, 168–212.
- BANCROFT, R. S. J. & JOHNSON, C. G. 2021 Drag, diffusion and segregation in inertial granular flows. *J. Fluid Mech.* **924**, A3.
- BARKER, T. & GRAY, J. M. N. T. 2017 Partial regularisation of the incompressible  $\mu(I)$ -rheology for granular flow. *J. Fluid Mech.* **828**, 5–32.
- BARKER, T., RAUTER, M., MAGUIRE, E. S. F., JOHNSON, C. G. & GRAY, J. M. N. T. 2021 Coupling rheology and segregation in granular flows. *J. Fluid Mech.* **909**, A22.
- BARKER, T., SCHAEFFER, D. G., BOHORQUEZ, P. & GRAY, J. M. N. T. 2015 Well-

- posed and ill-posed behaviour of the  $\mu(I)$ -rheology for granular flow. *J. Fluid Mech.* **779**, 794–818.
- BARKER, T., SCHAEFFER, D. G., SHEARER, M. & GRAY, J. M. N. T. 2017 Well-posed continuum equations for granular flow with compressibility and  $\mu(I)$ -rheology. *Proc. Roy. Soc. A* **473** (2201).
- BRANDAO, R. J., LIMA, R. M., SANTOS, R. L., DUARTE, C. R. & BARROZO, M. A. S. 2020 Experimental study and dem analysis of granular segregation in a rotating drum. *Powder Technol.* **364**, 1–12.
- BRIDGWATER, J. 1980 Self-diffusion coefficients in deforming powders. *Powder Technol.* **25** (1), 129–131.
- BRIDGWATER, J., FOO, W. & STEPHENS, D. 1985 Particle mixing and segregation in failure zones - theory and experiment. *Powder Technol.* **41**, 147–158.
- CAI, R., XIAO, H., ZHENG, J. & ZHAO, Y. 2019 Diffusion of size bidisperse spheres in dense granular shear flow. *Phys. Rev. E* **99** (3), 032902.
- CAMPBELL, C. S. 1997 Self-diffusion in granular shear flows. *Journal of Fluid Mechanics* **348**, 85–101.
- COOKE, M., STEPHENS, D. J. & BRIDGWATER, J. 1976 Powder mixing — a literature survey. *Powder Technol.* **15** (1), 1–20.
- DANCKWERTS, P. V. 1952 The definition and measurement of some characteristics of mixtures. *Appl. Sci. Res. A* **3** (4), 279–296.
- DENISSEN, I. F. C., WEINHART, T., TE VOORTWIS, A., LUDING, S., GRAY, J. M. N. T. & THORNTON, A. R. 2019 Bulbous head formation in bidisperse shallow granular flow over an inclined plane. *J. Fluid Mech.* **866**, 263–297.
- DING, Y., FORSTER, R., SEVILLE, J. & PARKER, D. 2002 Granular motion in rotating drums: bed turnover time and slumping-rolling transition. *Powder Technol.* **124**, 18–27.
- DRAHUN, J. A. & BRIDGWATER, J. 1983 The mechanisms of free surface segregation. *Powder Technol.* **36** (1), 39–53.
- EDWARDS, A. N., RUSSELL, A. S., JOHNSON, C. G. & GRAY, J. M. N. T. 2019 Frictional hysteresis and particle deposition in granular free-surface flows. *J. Fluid Mech.* **875**, 1058–1095.
- EHRICHS, E., JAEGER, H., KARCZMAR, G. S., KNIGHT, J. B., KUPERMAN, V. Y. & NAGEL, S. R. 1995 Granular convection observed by magnetic resonance imaging. *Science* **267** (5204), 1632–1634.
- FAN, Y. & HILL, K. M. 2011 Theory for shear-induced segregation of dense granular mixtures. *New J. Phys.* **13** (9), 095009.
- FAN, Y., SCHLICK, C. P., UMBANHOWAR, P. B., OTTINO, J. M. & LUEPTOW, R. M.

- 2014 Modelling size segregation of granular materials: the roles of segregation, advection and diffusion. *J. Fluid Mech.* **741**, 252–279.
- FÉLIX, G. & THOMAS, N. 2004 Relation between dry granular flow regimes and morphology of deposits: formation of levées in pyroclastic deposits. *Earth Planet. Sci. Lett.* **221**, 197–213.
- FRY, A. M., UMBANHOWAR, P. B., OTTINO, J. M. & LUEPTOW, R. M. 2018 Effect of pressure on segregation in granular shear flows. *Phys. Rev. E* **97** (6), 062906.
- GAJJAR, P. & GRAY, J. M. N. T. 2014 Asymmetric flux models for particle-size segregation in granular avalanches. *J. Fluid Mech.* **757**, 297–329.
- GDR MiDi 2004 On dense granular flows. *Eur. Phys. J. E* **14** (4), 341–365.
- GODDARD, J. D. & LEE, J. 2017 On the stability of the  $\mu(I)$ -rheology for granular flow. *J. Fluid Mech.* **833**, 302–331.
- GOLICK, L. A. & DANIELS, K. E. 2009 Mixing and segregation rates in sheared granular materials. *Phys. Rev. E* **80** (4), 042301.
- GRAY, J. & ANCEY, C. 2011 Multi-component particle-size segregation in shallow granular avalanches. *Journal of Fluid Mechanics* **678**, 535–588.
- GRAY, J. M. N. T. 2001 Granular flow in partially filled slowly rotating drums. *J. Fluid Mech.* **441**, 1–29.
- GRAY, J. M. N. T. 2018 Particle segregation in dense granular flows. *Annu. Rev. Fluid Mech.* **50**, 407–433.
- GRAY, J. M. N. T. & ANCEY, C. 2009 Segregation, recirculation and deposition of coarse particles near two-dimensional avalanche fronts. *J. Fluid Mech.* **629**, 387–423.
- GRAY, J. M. N. T. & ANCEY, C. 2015 Particle-size and -density segregation in granular free-surface flows. *J. Fluid Mech.* **779**, 622–668.
- GRAY, J. M. N. T. & CHUGUNOV, V. A. 2006 Particle-size segregation and diffusive remixing in shallow granular avalanches. *J. Fluid Mech.* **569**, 365–398.
- GRAY, J. M. N. T. & EDWARDS, A. N. 2014 A depth-averaged  $\mu(I)$ -rheology for shallow granular free-surface flows. *J. Fluid Mech.* **755**, 503–534.
- GRAY, J. M. N. T. & HUTTER, K. 1997 Pattern formation in granular avalanches. *Continuum Mech. Thermodyn.* **9** (6), 341–345.
- GRAY, J. M. N. T. & KOKELAAR, B. P. 2010 Large particle segregation, transport and accumulation in granular free-surface flows. *J. Fluid Mech.* **652**, 105–137.
- GRAY, J. M. N. T., TAI, Y.-C. & NOELLE, S. 2003 Shock waves, dead-zones and particle-free regions in rapid granular free surface flows. *J. Fluid Mech.* **491**, 161–181.
- GRAY, J. M. N. T. & THORNTON, A. R. 2005 A theory for particle size segregation in shallow granular free-surface flows. *Proc. Royal Soc. A* **461**, 1447–1473.

- GREVE, R. & HUTTER, K. 1993 Motion of a granular avalanche in a convex and concave curved chute: experiments and theoretical predictions. *Philos. Trans. R. Soc. London, Ser. A* **342** (1666), 573–600.
- HE, S., GAN, J., PINSON, D., YU, A. & ZHOU, Z. 2019 Radial segregation of binary-sized ellipsoids in a rotating drum. *Powder Technol.* **357**, 322–330.
- HENEIN, H., BRIMACOMBE, J. & WATKINSON, A. 1983 Experimental study of transverse bed motion in rotary kilns. *Metall Trans. B* **14**, 191–205.
- HILL, K. M., KHAKHAR, D. V., GILCHRIST, J. F., MCCARTHY, J. J. & OTTINO, J. M. 1999 Segregation-driven organization in chaotic granular flows. *Proceedings of the National Academy of Sciences* **96** (21), 11701–11706.
- HILL, K. M. & TAN, D. S. 2014 Segregation in dense sheared flows: gravity, temperature gradients, and stress partitioning. *J. Fluid Mech.* **756**, 54–88.
- HOLYOAKE, A. J. & MCELWAINE, J. N. 2012 High-speed granular chute flows. *J. Fluid Mech.* **710**, 35–71.
- IVERSON, R. M. 1997 The physics of debris-flows. *Rev. Geophys.* **35**, 245–296.
- IVERSON, R. M. 2003 The debris-flow rheology myth. In *Debris-flow hazards mitigation: mechanics, prediction, and assessment*, pp. 303–314. IOS Press.
- IVERSON, R. M. & VALLANCE, J. W. 2001 New views of granular mass flows. *Geology* **29** (2), 115–118.
- JENKINS, J. T. & YOON, D. K. 2002 Segregation in binary mixtures under gravity. *Phys. Rev. Letters* **88** (19), 194301.
- JOHNSON, C. G., KOKELAAR, B. P., IVERSON, R. M., LOGAN, M., LAHUSEN, R. & GRAY, J. M. N. T. 2012 Grain-size segregation and levee formation in geophysical mass flows. *J. Geophys. Res. Earth Surf.* **117** (F01032).
- JOP, P., FORTERRE, Y. & POULIQUEN, O. 2005 Crucial role of sidewalls in granular surface flows: consequences for the rheology. *J. Fluid Mech.* **541**, 167.
- JOP, P., FORTERRE, Y. & POULIQUEN, O. 2006 A constitutive relation for dense granular flows. *Nature* **44**, 727–730.
- JOSEPH, D. D. & SAUT, J. C. 1990 Short-wave instabilities and ill-posed initial-value problems. *Theor. Comput. Fluid Dyn.* **1**, 191–227.
- KAMRIN, K. 2019 Non-locality in granular flow: Phenomenology and modeling approaches. *Front. Phys.* **7**, 116.
- KAMRIN, K. & KOVAL, G. 2012 Nonlocal constitutive relation for steady granular flow. *Phys. Rev. Lett.* **108** (17), 178301.
- KATSURAGI, H., ABATE, A. & DURIAN, D. 2010 Jamming and growth of dynamical heterogeneities versus depth for granular heap flow. *Soft Matter* **6** (13), 3023–3029.
- KHAKHAR, D. V., MCCARTHY, J. J., GILCHRIST, J. F. & OTTINO, J. M. 1999 Chaotic

- mixing of granular materials in two-dimensional tumbling mixers. *Chaos* **9** (1), 195–205.
- KHAKHAR, D. V., MCCARTHY, J. J. & OTTINO, J. M. 1997 Radial segregation of granular mixtures in rotating cylinders. *Phys. Fluids* **9** (12), 3600–3614.
- LACAZE, L. & KERSWELL, R. R. 2009 Axisymmetric granular collapse: a transient 3d flow test of viscoplasticity. *Phys. Rev. Lett.* **102** (10), 108305.
- LAGRÉE, P.-Y., STARON, L. & POPINET, S. 2011 The granular column collapse as a continuum: validity of a two-dimensional Navier–Stokes model with a  $\mu(I)$ -rheology. *J. Fluid Mech.* **686**, 378–408.
- LIU, Y., GONZALEZ, M. & WASSGREN, C. 2018 Modeling granular material blending in a rotating drum using a finite element method and advection-diffusion equation multiscale model. *AIChE Journal* **64** (9), 3277–3292.
- MAKSE, H. A., HAVLIN, S., KING, P. R. & STANLEY, H. E. 1997 Spontaneous stratification in granular mixtures. *Nature* **386**, 379–382.
- MANGENEY, A., BOUCHUT, F., THOMAS, N., VILOTTE, J. P. & BRISTEAU, M. O. 2007 Numerical modeling of self-channeling granular flows and of their levee-channel deposits. *J. Geophys. Res.* **112**, F02017.
- MARTIN, N., IONESCU, I. R., MANGENEY, A., BOUCHUT, F. & FARIN, M. 2017 Continuum viscoplastic simulation of a granular column collapse on large slopes:  $\mu(I)$  rheology and lateral wall effects. *Phys. Fluids* **29**, 013301.
- MAXWELL, J. C. 1867 Iv. on the dynamical theory of gases. *Philos. Trans. R. Soc. London* **157**, 49–88.
- MAY, L. B. H., GOLICK, L. A., PHILLIPS, K. C., SHEARER, M. & DANIELS, K. E. 2010 Shear-driven size segregation of granular materials: Modeling and experiment. *Phys. Rev. E* **81** (5), 051301.
- MCCARTHY, J. J. 2009 Turning the corner in segregation. *Powder Technol.* **192** (2), 137–142.
- MELLMANN, J. 2001 The transverse motion of solids in rotating cylinders—forms of motion and transition behavior. *Powder Technol.* **118** (3), 251–270.
- METCALFE, G., SHINBROT, T., MCCARTHY, J. & OTTINO, J. M. 1995 Avalanche mixing of granular solids. *Nature* **374** (6517), 39–41.
- MIDDLETON, G. V. 1970 Experimental studies related to problems of flysch sedimentation. In *Flysch Sedimentology in North America* (ed. J. Lajoie), pp. 253–272. Business and Economics Science Ltd, Toronto.
- MOUKALLED, F., MANGANI, L. & DARWISH, M. 2016 *The finite volume method in computational fluid dynamics*. Springer.
- MOUNTY, D. 2007 *Particle size-segregation in convex rotating drums*. PhD Thesis, The University of Manchester (United Kingdom).

- NATARAJAN, V., HUNT, M. & TAYLOR, E. 1995 Local measurements of velocity fluctuations and diffusion coefficients for a granular material flow. *J. Fluid Mech.* **304**, 1–25.
- OTTINO, J. M. & KHAKHAR, D. V. 2000*a* Mixing and segregation of granular materials. *Annu. Rev. Fluid Mech.* **32**, 55–91.
- OTTINO, J. M. & KHAKHAR, D. V. 2000*b* Mixing and segregation of granular materials. *Annu. Rev. Fluid Mech.* **32** (1), 55–91.
- POULIQUEN, O., DELOUR, J. & SAVAGE, S. B. 1997 Fingering in granular flows. *Nature* **386** (6627), 816.
- POULIQUEN, O. & FORTERRE, Y. 2002 Friction law for dense granular flows: application to the motion of a mass down a rough inclined plane. *J. Fluid Mech.* **453**, 133–151.
- POULIQUEN, O. & FORTERRE, Y. 2009 A non-local rheology for dense granular flows. *Phil. Trans. R. Soc. A* **367**, 5091–5107.
- POULIQUEN, O. & VALLANCE, J. W. 1999 Segregation induced instabilities of granular fronts. *Chaos* **9** (3), 621–630.
- RAJCHENBACH, J. 1990 Flow in powders: From discrete avalanches to continuous regime. *Phys. Rev. Lett.* **65** (18), 2221–2224.
- ROCHA, F. M., JOHNSON, C. G. & GRAY, J. M. N. T. 2019 Self-channelisation and levee formation in monodisperse granular flows. *J. Fluid Mech.* **876**, 591–641.
- ROGNON, P. G., ROUX, J.-N., NAAÏM, M. & CHEVOIR, F. 2007 Dense flows of bidisperse assemblies of disks down an inclined plane. *Phys. Fluids* **19** (5), 058101.
- RUSCHE, H. 2002 *Computational fluid dynamics of dispersed two-phase flows at high phase fractions*. PhD Thesis, University of London.
- SAVAGE, S. B. & LUN, C. K. K. 1988 Particle size segregation in inclined chute flow of dry cohesionless granular solids. *J. Fluid Mech.* **189**, 311–335.
- SCHAEFFER, D. G. 1987 Instability in the evolution-equations describing incompressible granular flow. *J. Differ. Equ.* **66** (1), 19–50.
- SCHAEFFER, D. G., BARKER, T., TSUJI, D., GREMAUD, P., SHEARER, M. & GRAY, J. M. N. T. 2019 Constitutive relations for compressible granular flow in the inertial regime. *J. Fluid Mech.* **874**, 926–951.
- SCHLICK, C. P., FAN, Y., UMBANHOWAR, P. B., OTTINO, J. M. & LUEPTOW, R. M. 2015 Granular segregation in circular tumblers: theoretical model and scaling laws. *J. Fluid Mech.* **765**, 632–652.
- SCHRÖTER, M., ULRICH, S., KREFT, J., SWIFT, J. B. & SWINNEY, H. L. 2006 Mechanisms in the size segregation of a binary granular mixture. *Phys. Rev. E* **74** (1), 011307.
- SCHULZE, D. 2008 Powders and bulk solids. *Behaviour, characterization, storage and flow*. Springer **22**.

- SCOTT, A. M. & BRIDGWATER, J. 1975 Interparticle percolation: a fundamental solids mixing mechanism. *Ind. Eng. Chem. Fundam.* **14** (1), 22–27.
- STARON, L., LAGRÉE, P.-Y. & POPINET, S. 2012 The granular silo as a continuum plastic flow: The hour-glass vs the clepsydra. *Phys. Fluids* **24**, 103301.
- STARON, L., LAGRÉE, P.-Y. & POPINET, S. 2014 Continuum simulation of the discharge of the granular silo. *Eur. Phys. J. E* **37** (1), 5.
- TABERLET, N., RICHARD, P., VALANCE, A., LOSERT, W., PASINI, J. M., JENKINS, J. T. & DELANNAY, R. 2003 Superstable granular heap in a thin channel. *Phys. Rev. Lett.* **91** (26), 264301.
- THORNTON, A. R., GRAY, J. M. N. T. & HOGG, A. J. 2006 A three-phase mixture theory for particle size segregation in shallow granular free-surface flows. *J. Fluid Mech.* **550**, 1–25.
- THORNTON, A. R., WEINHART, T., LUDING, S. & BOKHOVE, O. 2012 Modeling of particle size segregation: calibration using the discrete particle method. *Int. J. Mod. Phys. C* **23** (08), 1240014.
- TREWHELA, T., ANCEY, C. & GRAY, J. 2021 Scalings laws for gravity driven particle size segregation in dense sheared granular flows. *J. Fluid Mech.* .
- TRIPATHI, A. & KHAKHAR, D. V. 2011 Rheology of binary granular mixtures in the dense flow regime. *Phys. Fluids* **23** (11), 113302.
- TRIPATHI, A. & KHAKHAR, D. V. 2013 Density difference-driven segregation in a dense granular flow. *J. Fluid Mech.* **717**, 643–669.
- UTTER, B. & BEHRINGER, R. P. 2004 Self-diffusion in dense granular shear flows. *Phys. Rev. E* **69**, 031308.
- VAN DER VAART, K., GAJJAR, P., EPELY-CHAUVIN, G., ANDREINI, N., GRAY, J. M. N. T. & ANCEY, C. 2015 Underlying asymmetry within particle size segregation. *Phys. Rev. Lett.* **114** (23), 238001.
- VAN DER VAART, K., VAN SCHROJENSTEIN LANTMAN, M. P., WEINHART, T., LUDING, S., ANCEY, C. & THORNTON, A. R. 2018*a* Segregation of large particles in dense granular flows suggests a granular saffman effect. *Phys. Rev. Fluids* **3** (7), 074303.
- VAN DER VAART, K., THORNTON, A. R., JOHNSON, C. G., WEINHART, T., JING, L., GAJJAR, P., GRAY, J. M. N. T. & ANCEY, C. 2018*b* Breaking size-segregation waves and mobility feedback in dense granular avalanches. *Granular Matter* **20** (3), 46.
- VALLANCE, J. W. & SAVAGE, S. B. 2000 Particle segregation in granular flows down chutes,. In *IUTAM Symposium on segregation in granular materials* (ed. A. D. Rosato & D. L. Blackmore). Kluwer.
- WELLER, H. G. 2006 Bounded explicit and implicit second-order schemes for scalar transport, report tr/hgw/06. *Tech. Rep.*. OpenCFD Ltd.



- WELLER, H. G. 2008 A new approach to vof-based interface capturing methods for incompressible and compressible flow, report tr/hgw/04. *Tech. Rep.*. OpenCFD Ltd.
- WIEDERSEINER, S., ANDREINI, N., EPELY-CHAUVIN, G., MOSER, G., MONNEREAU, M., GRAY, J. M. N. T. & ANCEY, C. 2011 Experimental investigation into segregating granular flows down chutes. *Phys. Fluids* **23**, 013301.
- WILLIAMS, S. C. 1968 The mixing of dry powders. *Powder Technol.* **2**, 13–20.
- WOODHOUSE, M. J., THORNTON, A. R., JOHNSON, C. G., KOKELAAR, B. P. & GRAY, J. M. N. T. 2012 Segregation-induced fingering instabilities in granular free-surface flows. *J. Fluid Mech.* **709**, 543–580.
- YAMANE, K., NAKAGAWA, M., ALTOBELLI, S., TANAKA, T. & TSUJI, Y. 1998 Steady particulate flows in a horizontal rotating cylinder. *Phys. Fluids* **10** (6), 1419–1427.
- YANG, R. Y., YU, A. B., MCELROY, L. & BAO, J. 2008 Numerical simulation of particle dynamics in different flow regimes in a rotating drum. *Powder Technol.* **188** (2), 170–177.
- YANG, S., SUN, Y. & CHEW, J. W. 2018 Simulation of the granular flow of cylindrical particles in the rotating drum. *AIChE Journal* **64** (11), 3835–3848.
- YARI, B., BEAULIEU, C., SAURIOL, P., BERTRAND, F. & CHAOUKI, J. 2020 Size segregation of bidisperse granular mixtures in rotating drum. *Powder Technol.* **374**, 172–184.
- YU, H.-S. 2007 *Plasticity and Geotechnics*. Springer Science & Business Media.
- ZHANG, Z., GUI, N., GE, L. & LI, Z. 2017 Numerical study of mixing of binary-sized particles in rotating tumblers on the effects of end-walls and size ratios. *Powder Technol.* **314**, 164–174.
- ZHENG, Q., BAI, L., YANG, L. & YU, A. 2019 Continuum modeling of granular mixing in a rotating drum. *Ind. Eng. Chem. Res.* **58** (41), 19251–19262.
- ZURIGUEL, I., GRAY, J. M. N. T., PEIXINHO, J. & MULLIN, T. 2006 Pattern selection by a granular wave in a rotating drum. *Phys. Rev. E* **73**, 061302.

# Chapter 4

## Conclusions

This thesis has developed a method for coupling rheology and segregation in polydisperse granular flows, and investigated rotating drum flows in which rheology-segregation feedback interactions are particularly important. In chapter 2, the partially regularised incompressible  $\mu(I)$ -rheology in a Navier-Stokes framework is coupled with segregation and diffusion rates dependent on the strain-rate, pressure, particle size and particle-size ratio for flows containing an arbitrary number of particle species. A numerical method for handling air-grain interfaces in volume-of-fluid solvers is also developed, giving superior results to the default counter-gradient transport method of interface sharpening used by OpenFOAM. The numerical method accurately reproduces exact solutions for bidisperse inclined plane flows, and is able to predict the formation of a large particle-rich bulbous head at the flow front due to frictional feedback of the particle distribution onto the bulk flow. The numerical implementation is also tested against the DEM simulations of Tripathi & Khakhar (2011). It is then used to compute a bidisperse square rotating drum flow, and successfully predicts the formation of small particle lobes surrounding an undisturbed central core of mixed material, because the segregation and diffusion rates limit particle redistribution to the free-surface avalanche where the strain-rates are high and the pressure low. However, the segregation is underestimated and the avalanche is too thick relative to experiments since lateral sidewall friction is not included in the theoretical model.

Chapter 3 is dedicated to a rigorous application of the coupling approach to triangular rotating drum flows. For certain transient flows, including those in rotating drums, experimental and DEM data shows that the segregation intensity is maximal

near a grain-size ratio of  $R = 2$ , and the segregation rate is adapted to reflect this using the reduction factor suggested by Trehwela *et al.* (2021). Rotating drum experiments are performed for bidisperse mixtures at different fill fractions and mean particle concentrations, where the granular material is confined in a very thin channel by clear lateral sidewalls which exert a frictional force on the flow. To incorporate this into the theoretical and numerical method, three-dimensional mass and momentum balance equations are width-averaged with Coulomb slip assumed on the sidewalls, returning a two-dimensional system containing an additional momentum term representing sidewall friction. The adapted numerical method is tested against an exact solution for an infinite shear cell with sidewall friction, showing very precise agreement.

Rotating drum flows are then computed, with all appropriate parameters matched to the experiments and no fitting parameters used. The timescale and pattern formation of the experiments is predicted by the numerical simulations with excellent accuracy. A method for quantitative analysis of the experiments is developed, in which pixel intensity data is used to project a concentration field onto laboratory images. This data can then be used to compute segregation intensities, and strong quantitative agreement is observed between the simulations and experiments. This is only possible because of the inclusion of lateral sidewall friction in the theoretical model. Sidewall friction leads to a very thin, rapidly flowing boundary layer avalanche at the free-surface where all the segregation occurs, in which the strain-rates and hence segregation intensity are very high. This also means that a very fine mesh is required to fully resolve the boundary layer, and so the computational expense is significant.

Changes in the particle distribution structure are observed as the fill fraction of the drum varies, and competing feedback interactions between rheology and segregation lead to subtle and surprising variations in the segregation intensity as the mean small particle concentration increases. The latter is clarified by careful examination of the simulation data, which shows that increased large particle concentrations enhance the segregation rate but also induce thicker, slower avalanches and so simultaneously inhibit segregation. Finally, a tridisperse triangular drum flow is analysed. The timescale and pattern formation gives good qualitative agreement with an experiment, and demonstrates successful application of the coupling method to mixtures of more than two particles species.

All the important features of rotating drum flows in the continuously avalanching regime are captured here using a fully coupled, incompressible continuum framework, but intermittent avalanche flows are also commonly observed at slower drum rotation rates. The periodic collapse of the rotating free-surface has not yet been captured using continuum modelling, and may be due to frictional hysteresis (see e.g. Edwards *et al.*, 2019). Hysteresis has been studied using depth-averaged models, but in a non-depth averaged, local incompressible framework this may require non-monotonic  $\mu(I)$  curves, which Barker *et al.* (2015) showed to be ill-posed. Compressible or non-local models, which can incorporate a yield stress and non-monotonicity while remaining well-posed (Kamrin & Koval, 2012; Bouzid *et al.*, 2013; Schaeffer *et al.*, 2019), engender exciting possibilities as they continue to develop. Nevertheless, it is significant that hysteresis, compressibility, non-locality and other physics excluded from the incompressible  $\mu(I)$ -rheology are apparently unnecessary for a satisfactory physical description of the phenomena observed in chapter 3.

For mixtures containing a great number of particles, the coupling approach saves computational expense relative to DEM simulations, but computing time remains an issue. For rotating drums flows in which a very fine mesh is required to resolve the boundary layer avalanche, adaptive meshing techniques which reduce the cell size in regions requiring greater resolution may drastically reduce the computational expense, as could computations performed using the material point method (MPM) which forgo a mesh altogether and also provide advantages for modelling solid-like granular material (Dunatunga & Kamrin, 2015). Another limitation to the current numerical implementation of the coupling theory is presented by the air segregation method of interface sharpening, which is very useful for the flows investigated here but becomes problematic when studying free-falling grains due to interference from the air phase. The air bubble trapping observed with the default counter-gradient transport method used in OpenFOAM becomes very severe in free-falling flows and in such cases a new interface handling method is therefore needed.

It is hoped that the rheology-segregation coupling developed here provides a useful theoretical and numerical tool for polydisperse granular flow modelling in multiple contexts. Fully coupled computations may provide new insights into geophysical phenomena such as the inter-relatedness of bulbous head formation (Denissen *et al.*, 2019),

levee formation (Johnson *et al.*, 2012; Edwards *et al.*, 2017; Rocha *et al.*, 2019), and fingering instabilities (Woodhouse *et al.*, 2012; Baker *et al.*, 2016). For industries handling polydisperse granular materials, whether the aim is mixing, segregation or transportation, the coupling method detailed here can be expected to provide insight into a number of different geometries. For example, a similar approach to that described in chapter 3 may be applied to filling and draining silo flows (Staron *et al.*, 2012, 2014), where segregation is also potentially problematic and difficult to control. Furthermore, segregation minimisation methods for rotating drums (see chapter 1.3.3) could in future be developed and tested using fully coupled simulations.

# Bibliography

- ANCEY, C., COUSSOT, P. & EVESQUE, P. 1999 A theoretical framework for granular suspensions in a steady simple shear flow. *J. Rheol.* **43** (6), 1673–1699.
- ANDREOTTI, B., FORTERRE, Y. & POULIQUEN, O. 2013 *Granular media: between fluid and solid*. Cambridge University Press.
- ARMANINI, A., LARCHER, M., NUCCI, E. & DUMBSER, M. 2014 Submerged granular channel flows driven by gravity. *Advances in Water Resources* **63**, 1–10.
- BAGNOLD, R. A. 1954 Experiments on gravity-free dispersion of large solid spheres in a newtonian fluid under shear. *Proc. Roy. Soc. Lond. A* **225**, 49–63.
- BAKER, J., JOHNSON, C. G. & GRAY, J. M. N. T. 2016 Segregation-induced finger formation in granular free-surface flows. *J. Fluid. Mech.* **809**, 168–212.
- BANCROFT, R. S. J. & JOHNSON, C. G. 2021 Drag, diffusion and segregation in inertial granular flows. *J. Fluid Mech.* **924**, A3.
- BARALE, L. 2015 Footstep-triggered grain flows on the lee side of a desert sand dune (Erg Chebbi, Morocco). *Int. J. Earth Sci.* **104** (8), 2213.
- BARKER, T. & GRAY, J. M. N. T. 2017 Partial regularisation of the incompressible  $\mu(I)$ -rheology for granular flow. *J. Fluid. Mech.* **828**, 5–32.
- BARKER, T., SCHAEFFER, D. G., BOHÓRQUEZ, P. & GRAY, J. M. N. T. 2015 Well-posed and ill-posed behaviour of the  $\mu(I)$ -rheology for granular flows. *J. Fluid. Mech.* **779**, 794–818.

- BARTELT, P., GLOVER, J., FEISTL, T., BÜHLER, Y. & BUSER, O. 2012 Formation of levees and en-echelon shear planes during snow avalanche run-out. *J. Glaciol.* **58** (211), 980–992.
- BOUZID, M., TRULSSON, M., CLAUDIN, P., CLÉMENT, E. & ANDREOTTI, B. 2013 Nonlocal rheology of granular flows across yield conditions. *Phys. Rev. Lett.* **111**, 238301.
- BREU, A. P. J., ENSNER, H.-M., KRUELLE, C. A. & REHBERG, I. 2003 Reversing the brazil-nut effect: competition between percolation and condensation. *Phys. Rev. Lett.* **90** (1), 014302.
- BRIDGWATER, J. 1994 Mixing and segregation mechanisms in particle flow. In *Granular matter*, pp. 161–193. Springer.
- BRIDGWATER, J., FOO, W. & STEPHENS, D. 1985 Particle mixing and segregation in failure zones - theory and experiment. *Powder Technol.* **41**, 147–158.
- BRILLIANTOV, N. V. & PÖSCHEL, T. 2004 *Kinetic theory of granular gases*. Oxford University Press.
- CAMPBELL, C. S. 1990 Rapid granular flows. *Annu. Rev. Fluid Mech.* **22** (1), 57–90.
- CHENG, X., XU, L., PATTERSON, A., JAEGER, H. M. & NAGEL, S. R. 2008 Towards the zero-surface-tension limit in granular fingering instability. *Nat. Phys.* **4** (3), 234–237.
- CONWAY, S. L., LIU, X. & GLASSER, B. J. 2006 Instability-induced clustering and segregation in high-shear couette flows of model granular materials. *Chem. Eng. Sci.* **61** (19), 6404–6423.
- COOKE, M. H., STEPHENS, D. J. & BRIDGWATER, J. 1976 Powder mixing — a literature survey. *Powder Technol.* **15** (1), 1–20.
- DE COULOMB, C. A. 1773 Essay on the application of the rules of maxima and minima to certain statics problems relevant to architecture. *Memoires presentes a l'Academie* pp. 343–384.

- CRASSOUS, J., METAYER, J., RICHARD, P. & LAROCHE, C. 2008 Experimental study of a creeping granular flow at very low velocity. *J. Stat. Mech: Theory Exp.* **2008** (03), P03009.
- DA CRUZ, F., EMAM, S., PROCHNOW, M., ROUX, J. & CHEVOIR, F. 2005 Rheo-physics of dense granular materials: Discrete simulation of plane shear flows. *Phys. Rev. E* **72** (2), 021309.
- DAMIÁN, S. M. 2013 An extended mixture model for the simultaneous treatment of short and long scale interfaces. PhD thesis, National University of the Littoral.
- DAVIS, M. 2006 *Planet of slums*. Verso.
- DENISSEN, I. F. C., WEINHART, T., TE VOORTWIS, A., LUDING, S., GRAY, J. M. N. T. & THORNTON, A. R. 2019 Bulbous head formation in bidisperse shallow granular flow over an inclined plane. *J. Fluid Mech.* **866**, 263–297.
- DOLGUNIN, V. N. & UKOLOV, A. A. 1995 Segregation modelling of particle rapid gravity flow. *Powder Technol.* **83**, 95–103.
- DRUCKER, D. C. & PRAGER, W. 1952 Soil mechanics and plastic analysis or limit design. *Q. Appl. Math.* **10** (2), 157–165.
- DUNATUNGA, S. & KAMRIN, K. 2015 Continuum modelling and simulation of granular flows through their many phases. *J. Fluid Mech.* **779**, 483—513.
- EDWARDS, A. N., RUSSELL, A. S., JOHNSON, C. G. & GRAY, J. M. N. T. 2019 Frictional hysteresis and particle deposition in granular free-surface flows. *J. Fluid. Mech.* **875**, 1058–1095.
- EDWARDS, A. N., VIROULET, S., KOKELAAR, B. P. & GRAY, J. M. N. T. 2017 Formation of levees, troughs and elevated channels by avalanches on erodible slopes. *J. Fluid Mech.* **823**, 278–315.
- EHRICHS, E. E., JAEGER, H. M., KARCZMAR, G. S., KNIGHT, J. B., KUPERMAN, V. Y. & NAGEL, S. R. 1995 Granular convection observed by magnetic resonance imaging. *Science* **267** (5204), 1632–1634.



- FAN, Y. & HILL, K. M. 2010 Shear-driven segregation of dense granular mixtures in a split-bottom cell. *Phys. Rev. E* **81** (4), 041303.
- FAN, Y. & HILL, K. M. 2011 Theory for shear-induced segregation of dense granular mixtures. *New J. Phys.* **13** (9), 095009.
- FÉLIX, G. & THOMAS, N. 2004 Relation between dry granular flow regimes and morphology of deposits: formation of levées in pyroclastic deposits. *Earth Planet. Sci. Lett.* **221**, 197–213.
- FORTERRE, Y. & POULIQUEN, O. 2008 Flows of dense granular media. *Ann. Rev. Fluid Mech.* **40**, 1–24.
- GAJJAR, P. & GRAY, J. M. N. T. 2014 Asymmetric flux models for particle-size segregation in granular avalanches. *J. Fluid Mech.* **757**, 297–329.
- GDR-MiDi 2004 On dense granular flows. *Eur. Phys. J. E* **14**, 341–365.
- GODDARD, J. D. 1986 Dissipative materials as constitutive models for granular media. *Acta Mech.* **63** (1), 3–13.
- GODDARD, J. D. & LEE, J. 2018 Regularization by compressibility of the  $\mu(I)$  model of dense granular flow. *Phys. Fluids* **30** (7), 073302.
- GOLICK, L. A. & DANIELS, K. E. 2009 Mixing and segregation rates in sheared granular materials. *Phys. Rev. E* **80** (4), 042301.
- GRAY, J. M. N. T. 2001 Granular flow in partially filled slowly rotating drums. *J. Fluid Mech.* **441**, 1–29.
- GRAY, J. M. N. T. 2018 Particle segregation in dense granular flows. *Annu. Rev. Fluid Mech.* **50**, 407–433.
- GRAY, J. M. N. T. & ANCEY, C. 2011 Multi-component particle size-segregation in shallow granular avalanches. *J. Fluid Mech.* **678**, 535–588.
- GRAY, J. M. N. T. & ANCEY, C. 2015 Particle-size and-density segregation in granular free-surface flows. *J. Fluid Mech.* **779**, 622–668.

- GRAY, J. M. N. T. & CHUGUNOV, V. A. 2006 Particle-size segregation and diffusive remixing in shallow granular avalanches. *J. Fluid Mech.* **569**, 365–398.
- GRAY, J. M. N. T. & HUTTER, K. 1997 Pattern formation in granular avalanches. *Continuum Mech. Thermodyn.* **9**, 341–345.
- GRAY, J. M. N. T. & KOKELAAR, B. P. 2010*a* Large particle segregation, transport and accumulation in granular free-surface flows. *J. Fluid Mech.* **652**, 105–137.
- GRAY, J. M. N. T. & KOKELAAR, B. P. 2010*b* Large particle segregation, transport and accumulation in granular free-surface flows – erratum. *J. Fluid Mech.* **657**, 539.
- GRAY, J. M. N. T. & THORNTON, A. R. 2005 A theory for particle size segregation in shallow granular free-surface flows. *Proc. Roy. Soc. A* **461**, 1447–1473.
- GREENSHIELDS, C. & WELLER, H. 2022 *Notes on computational fluid dynamics: General principles*. CFD Direct Ltd.
- HEYMAN, J. & DE COULOMB, C. A. 1972 *Coulomb’s memoir on statics: an essay in the history of civil engineering*. Cambridge University Press.
- HEYMAN, J., DELANNAY, R., TABUTEAU, H. & VALANCE, A. 2017 Compressibility regularizes the  $\mu(I)$ -rheology for dense granular flows. *J. Fluid Mech.* **830**, 553–568.
- HILL, K. M., GIOIA, G. & AMARAVADI, D. 2004 Radial segregation patterns in rotating granular mixtures: Waviness selection. *Phys. Rev. Lett.* **93**, 224301.
- HILL, K. M., KHAKAR, D. V., GILCHRIST, J. F., MCCARTHY, J. J. & OTTINO, J. M. 1999 Segregation driven organization in chaotic granular flows. *Proc. Natl Acad. Sci. USA* **96**, 11701–11706.
- HILL, K. M. & TAN, D. S. 2014 Segregation in dense sheared flows: gravity, temperature gradients, and stress partitioning. *J. Fluid Mech.* **756**, 54–88.
- HIRSCH, C. 2007 *Numerical Computation of Internal and External Flows Volume 1: Fundamentals of Computational Fluid Dynamics*. John Wiley & Sons, Ltd.
- HOLYOAKE, A. J. & MCELWAINE, J. N. 2012 High-speed granular chute flows. *J. Fluid Mech.* **710**, 35–71.

- HONG, D. C., QUINN, P. V. & LUDING, S. 2001 Reverse brazil nut problem: competition between percolation and condensation. *Phys. Rev. Lett.* **86** (15), 3423.
- ISSA, R. I. 1986 Solution of the implicitly discretised fluid flow equations by operator-splitting. *Journal of Computational Physics* **62** (1), 40–65.
- IVERSON, R. M. 1997 The physics of debris-flows. *Rev. Geophys.* **35**, 245–296.
- JAEGER, H. M., NAGEL, S. R. & BEHRINGER, R. P. 1996 Granular solids, liquids, and gases. *Rev. Mod. Phys.* **68**, 1259.
- JASAK, H. 1996 Error analysis and estimation for the finite volume method with applications to fluid flows. PhD thesis, Imperial College London.
- JASAK, H., WELLER, H. G. & GOSMAN, A. D. 1999 High resolution nvd differencing scheme for arbitrarily unstructured meshes. *Int. J. Numer. Meth. Fl.* **31** (2), 431–449.
- JENKINS, J. T. 2007 Dense inclined flows of inelastic spheres. *Granular matter* **10** (1), 47–52.
- JENKINS, JAMES T & BERZI, DIEGO 2010 Dense inclined flows of inelastic spheres: tests of an extension of kinetic theory. *Granular Matter* **12** (2), 151–158.
- JOHNSON, C. G., KOKELAAR, B. P., IVERSON, R. M., LOGAN, M., LAHUSEN, R. G. & GRAY, J. M. N. T. 2012 Grain-size segregation and levee formation in geophysical mass flows. *J. Geophys. Res.* **117**, F01032.
- JOP, P., FORTERRE, Y. & POULIQUEN, O. 2005 Crucial role of sidewalls in granular surface flows: consequences for the rheology. *J. Fluid Mech.* **541**, 167–192.
- JOP, P., FORTERRE, Y. & POULIQUEN, O. 2006 A constitutive relation for dense granular flows. *Nature* **44**, 727–730.
- KAMRIN, K. 2019 Non-locality in granular flow: Phenomenology and modeling approaches. *Front. Phys.* **7**, 116.
- KAMRIN, K. & KOVAL, G. 2012 Nonlocal constitutive relation for steady granular flow. *Phys. Rev. Lett.* **108**, 178301.

- KHAKHAR, D. V., MCCARTHY, J. J., GILCHRIST, J. F. & OTTINO, J. M. 1999 Chaotic mixing of granular materials in two-dimensional tumbling mixers. *Chaos* **9** (1), 195–205.
- KHAKHAR, D. V., MCCARTHY, J. J. & OTTINO, J. M. 1997 Radial segregation of granular mixtures in rotating cylinders. *Phys. Fluids* **9**, 3600–3614.
- KHAKHAR, D. V., ORPE, A. V. & OTTINO, J. M. 2001 Continuum model of mixing and size segregation in a rotating cylinder: concentration-flow coupling and streak formation. *Powder Technol.* **116** (2-3), 232–245.
- KNIGHT, J. B., JAEGER, H. M. & NAGEL, S. R. 1993 Vibration-induced size separation in granular media: the convection connection. *Phys. Rev. Lett.* **70** (24), 3728.
- KOMATSU, T. S., INAGAKI, S., NAKAGAWA, N. & NASUNO, S. 2001 Creep motion in a granular pile exhibiting steady surface flow. *Phys. Rev. Lett.* **86**, 1757–1760.
- LACAZE, L. & KERSWELL, R. R. 2009 Axisymmetric granular collapse: a transient 3d flow test of viscoplasticity. *Phys. Rev. Lett.* **102** (10), 108305.
- LAGRÉE, P.-Y., STARON, L. & POPINET, S. 2011 The granular column collapse as a continuum: validity of a two-dimensional navier-stokes model with a  $\mu(I)$ -rheology. *J. Fluid Mech.* **686**, 378–408.
- LI, H. & MCCARTHY, J. J. 2005 Phase diagrams for cohesive particle mixing and segregation. *Phys. Rev. E* **71** (2), 021305.
- LUN, C. K. K. 1991 Kinetic theory for granular flow of dense, slightly inelastic, slightly rough spheres. *J. Fluid Mech.* **233**, 539–559.
- MCCARTHY, J. J. 2009 Turning the corner in segregation. *Powder Technol.* **192** (2), 137–142.
- METCALFE, G., SHINBROT, T., MCCARTHY, J. & OTTINO, J. M. 1995 Avalanche mixing of granular solids. *Nature* **374** (6517), 39–41.

- MIDDLETON, G. V. 1970 Experimental studies related to problems of flysch sedimentation. In *Flysch Sedimentology in North America* (ed. J. Lajoie), pp. 253–272. Toronto: Business and Economics Science Ltd.
- MORLAND, L. W. 1992 Flow of viscous fluids through a porous deformable matrix. *Surv. Geophys.* **13**, 209–268.
- MOUNTY, D. 2007 Particle size-segregation in convex rotating drums. PhD thesis, The University of Manchester (United Kingdom).
- OTTINO, J. M. & KHAKHAR, D. V. 2000 Mixing and segregation of granular materials. *Annu. Rev. Fluid Mech.* **32** (1), 55–91.
- POULIQUEN, O. 1999a Scaling laws in granular flows down rough inclined planes. *Phys. Fluids* **11**, 542–548.
- POULIQUEN, O., DELOUR, J. & SAVAGE, S. B. 1997 Fingering in granular flows. *Nature* **386**, 816–817.
- POULIQUEN, O. & FORTERRE, Y. 2002 Friction law for dense granular flows: application to the motion of a mass down a rough inclined plane. *J. Fluid Mech.* **453**, 133–151.
- POULIQUEN, O. & FORTERRE, Y. 2009 A non-local rheology for dense granular flows. *Phil. Trans. Roy. Soc. A* **367** (1909), 5091–5107.
- POULIQUEN, O. & VALLANCE, J. W. 1999 Segregation induced instabilities of granular fronts. *Chaos* **9** (3), 621–630.
- RAJCHENBACH, J. 1990 Flow in powders: From discrete avalanches to continuous regime. *Phys. Rev. Lett.* **65** (18), 2221–2224.
- ROCHA, F. M., JOHNSON, C. G. & GRAY, J. M. N. T. 2019 Self-channelisation and levee formation in monodisperse granular flows. *J. Fluid Mech.* **876**, 591–641.
- ROSHKO, A. & LIEPMANN, H. W. 1957 *Elements of Gas Dynamics*. Wiley.
- SAMADANI, A. & KUDROLLI, A. 2000 Segregation transitions in wet granular matter. *Phys. Rev. Lett.* **85** (24), 5102.

- SAVAGE, S. B. 1983 Granular flows down rough inclines-review and extension. *Stud. Appl. Math.* **7**, 261–282.
- SAVAGE, S. B. & LUN, C. K. K. 1988 Particle size segregation in inclined chute flow of dry cohesionless granular solids. *J. Fluid Mech.* **189**, 311–335.
- SAVAGE, S. B. & SAYED, M. 1984 Stresses developed by dry cohesionless granular materials sheared in an annular shear cell. *J. Fluid Mech.* **142**, 391–430.
- SCHAEFFER, D. G. 1987 Instability in the evolution equations describing incompressible granular flow. *J. Differ. Equ.* **66** (1), 19–50.
- SCHAEFFER, D. G., BARKER, T., TSUJI, D., GREMAUD, P., SHEARER, M. & GRAY, J. M. N. T. 2019 Constitutive relations for compressible granular flow in the inertial regime. *J. Fluid Mech.* **874**, 926–951.
- SCHRÖTER, M., ULRICH, S., KREFT, J., SWIFT, J. B. & SWINNEY, H. L. 2006 Mechanisms in the size segregation of a binary granular mixture. *Phys. Rev. E* **74** (1), 011307.
- SCHULZE, D. 2008 *Powders and Bulk Solids*. Springer Berlin Heidelberg, 10.1007/978-3-540-73768-1.
- SCOTT, A. M. & BRIDGWATER, J. 1975 Interparticle percolation: A fundamental solids mixing mechanism. *Ind. Eng. Chem. Fundam.* **14** (1), 22–27.
- SHI, D., ABATAN, A. A., VARGAS, W. L. & MCCARTHY, J. J. 2007 Eliminating segregation in free-surface flows of particles. *Phys. Rev. Lett.* **99** (14), 148001.
- SHINBROT, T. & MUZZIO, F. J. 2000 Nonequilibrium patterns in granular mixing and segregation. *Phys. Today* **53** (3), 25–30.
- SHINOHARA, K., SHOJI, K. & TANAKA, T. 1970 Mechanism of segregation and blending of particles flowing out of mass-flow hoppers. *Ind. Eng. Chem. Process Des. Dev.* **9** (2), 174–180.
- STARON, L., LAGRÉE, P.-Y. & POPINET, S. 2012 The granular silo as a continuum plastic flow: The hour-glass vs the clepsydra. *Phys. Fluids* **24**, 103301.

- STARON, L., LAGRÉE, P.-Y. & POPINET, S. 2014 Continuum simulation of the discharge of the granular silo. *Eur. Phys. J. E* **37**, 5.
- STARON, L. & PHILLIPS, J. C. 2015 Stress partition and microstructure in size-segregating granular flows. *Phys. Rev. E* **92** (2), 022210.
- TANG, P. & PURI, V. M. 2004 Methods for minimizing segregation: a review. *Part. Sci. Technol.* **22** (4), 321–337.
- THORNTON, A. R. & GRAY, J. M. N. T. 2008 Breaking size-segregation waves and particle recirculation in granular avalanches. *J. Fluid Mech.* **596**, 261–284.
- THORNTON, A. R., GRAY, J. M. N. T. & HOGG, A. J. 2006 A three-phase mixture theory for particle size segregation in shallow granular free-surface flows. *J. Fluid Mech.* **550**, 1–25.
- TREWHELA, T., ANCEY, C. & GRAY, J. M. N. T. 2021 An experimental scaling law for particle-size segregation in dense granular flows. *J. Fluid Mech.* **916**.
- TRIPATHI, A. & KHAKHAR, D. V. 2011 Rheology of binary granular mixtures in the dense flow regime. *Phys. Fluids* **23** (11), 113302.
- TRIPATHI, A. & KHAKHAR, D. V. 2013 Density difference-driven segregation in a dense granular flow. *J. Fluid Mech.* **717**, 643–669.
- VAN DER VAART, K., GAJJAR, P., EPELY-CHAUVIN, G., ANDREINI, N., GRAY, J. M. N. T. & ANCEY, C. 2015 Underlying asymmetry within particle size segregation. *Phys. Rev. Lett.* **114** (23), 238001.
- VAN DER VAART, K., THORNTON, A. R., JOHNSON, C. G., WEINHART, T., JING, L., GAJJAR, P., GRAY, J. M. N. T. & ANCEY, C. 2018 Breaking size-segregation waves and mobility feedback in dense granular avalanches. *Granular Matter* **20** (3), 1–18.
- VALLANCE, J. W. & SAVAGE, S. B. 2000 Particle segregation in granular flows down chutes. In *IUTAM Symposium on segregation in granular materials* (ed. A. D. Rosato & D. L. Blackmore). Kluwer.

- WOODHOUSE, M. J., THORNTON, A. R., JOHNSON, C. G., KOKELAAR, B. P. & GRAY, J. M. N. T. 2012 Segregation-induced fingering instabilities in granular free-surface flows. *J. Fluid Mech.* **709**, 543–580.
- YU, H.-S. 2007 *Plasticity and Geotechnics*. Springer Science & Business Media.
- ZALESAK, S. T. 1979 Fully multidimensional flux-corrected transport algorithms for fluids. *J. Comput. Phys.* **31** (3), 335–362.
- ZURIGUEL, I., GRAY, J. M. N. T., PEIXINHO, J. & MULLIN, T. 2006 Pattern selection by a granular wave in a rotating drum. *Phys. Rev. E* **73**, 061302.